# Pressure Sensing Microsystems for Energy Industry Applications

by

Partha Pratim Dutta

A dissertation submitted in partial fulfillment
of the requirements for the degree of
Doctor of Philosophy
(Electrical and Computer Engineering)
in the University of Michigan
2022

Doctoral Committee:

Dr. Alexander C. Benken, Co-Chair
Professor Yogesh B. Gianchandani, Co-Chair
Professor Wei Lu
Professor Khalil Najafi

Partha Pratim Dutta
pdutta@umich.edu
ORCID iD: 0000-0002-1545-8044

© Partha Pratim Dutta 2022

## ACKNOWLEDGEMENTS

I would like to express utmost gratitude to my advisor, Prof. Yogesh Gianchandani for his guidance and support over the past five years of my doctoral study at University of Michigan. I thank him for all the excellent learning opportunities and wide array of experiences across multiple projects, for ensuring constant research funding through a pandemic, and for critical appreciation of my work which has led me become a better researcher. I am grateful to Professor Tao Li, who helped me immensely to get started with my research work during the initial years of my study. My sincerest gratitude to Dr. Alexander Benken, who has been a firsthand mentor, and certainly the most actively involved individual in my doctoral pursuits. I thank him for his time and effort as well as his constant encouragement, which has made this journey intellectually challenging but emotionally fulfilling. I would also like to thank the other committee members, Prof. Wei Lu and Prof. Khalil Najafi, for their constructive comments and feedback.

The research described by this dissertation was funded in part by the Advanced Energy Consortium (AEC) and by TOTAL Energies (Pau, France). I would like to thank Mr. John-Richard ORDONEZ-VARELA who has been instrumental in facilitating industrial adaptation and evaluation of the work presented, thus enabling pathways for impact in real world applications. All corporate laboratory and field tests were performed by researchers from TOTAL Energies (Pau, France) in corporate laboratories and in the energy fields at Democratic Republic of Congo (Africa). The pressure transducers used in this work were developed by Dr. Alexander Benken and fabricated at the Lurie Nanofabrication Facility at University of Michigan. I would like to thank Dr. Neeharika Vellaluru, for introducing me to her research on downhole monitoring applications,

which served as a great platform and inspiration for this work. The PGM system readout electronics was investigated and realized in collaboration with Prof. Tao Li's research team at University of Cincinnati. In addition, Mr. Aditya Verma, Mr. Hanfei Zheng, Mr. Yifan Yang, Mr. Zechao Li, and Mr. Ziyan Wang have contributed to certain 3D modelling and software investigation efforts described within this dissertation. The ELM9 packaging effort was aided by Dr. Alexander Benken.

I would like to extend my gratitude to former and current members of our research group and EECS 2001 office space – Adrienne, Daniel, Declan, Ester, Johnny, Leo, Neeharika, Ramprasad, Sajal, Tsenguun, Weilin, Yutao, Zeyu, and others. I have been fortunate to interact with and befriend a lot of awesome and interesting people across these five years at University of Michigan. Thank You to everyone who helped make these five years a cherished memory of my life.

At last, and most importantly, I want to thank my parents – my mother, Banani Dutta who has been an epitome of love and encouragement, my father, Pranab Dutta, who exemplifies drive and passion, and my dear sister, Bratati Dutta, who inspires goodness, and has been great company to grow up with. I would also sincerely thank my girlfriend, Stuti Patel, who has been a constant through these five years, with her love, support, and appreciation for what I do – she inspires me every day to be a better version of myself. I would like to thank my best friend, Vikramjit Lahiri, for help in making these years in Michigan an incredible journey.

# TABLE OF CONTENTS

**Acknowledgements** ..... **ii**
**List of Figures** ..... **vi**
**List of Tables** ..... **xi**
**Abstract** ..... **xii**
**Chapter 1: Introduction** ..... **1**
1.1 Motivation and Background ..... 1
1.2 Challenges for Pressure Sensing in Space Constrained Environments ..... 3
1.3 Pressure Sensing Opportunities in the Energy Industry ..... 8
1.3.1 Laboratory Application: Sensor confinement requirement ..... 9
1.3.2 Field Application: System Confinement Requirement ..... 14
1.4 Research Goals and Objectives ..... 18
1.5 Organization of Dissertation ..... 21
**Chapter 2: Distributed Pressure Measurement Microsystem for Core Samples with Feedthrough Technology** ..... **24**
2.1 System Concept and Design ..... 25
2.1.1 System Hardware ..... 26
2.1.2 System Software ..... 32
2.2 System Implementation ..... 34
2.3 Experimental Setup, Results and Discussion ..... 40
2.3.1 Static Pressure Response ..... 40
2.3.2 Distributed Pressure Test Setup Design ..... 41
2.3.3 Dynamic Pressure Response ..... 50
2.4 System Deployment and Field Test Results ..... 51
2.4.1 System Calibration ..... 51
2.4.2 Flow Test Results ..... 52
2.5 Chapter Summary ..... 53
**Chapter 3: Passive Wireless Pressure Gradient Measurement System for Fluid Flow Analysis** ..... **55**
3.1 System Concept and Design ..... 56
3.1.1 LC Sensor Circuit Model ..... 58
3.1.2 LC Sensor Electrical Design ..... 60
3.1.3 Readout Circuit ..... 63
3.2 System Fabrication ..... 65
3.3 LC Sensor Packaging ..... 67
3.4 Software Control and User Interface ..... 71
3.4.1 Micro-controller Unit (MCU) State Machine ..... 72

3.4.2 External Unit Back-end Software ..... 75
3.4.3 Remote Desktop User Interface (UI) Front-end ..... 76
3.5 System Testing and Validation ..... 77
3.5.1 Static Pressure and Thermal Response ..... 78
3.5.2 Conversion of Resonant Frequency to Pressure: ..... 79
3.5.3 Pressure Resolution: ..... 80
3.5.4 Dynamic Pressure Response and Flow Test: ..... 82
3.6 Chapter Summary ..... 85
**Chapter 4: Optimizing Minimum Resolvable Pressure Resolution in a Wireless LC Sensor System ..... 88**
4.1 Inductor-Capacitor (LC) Sensor Model ..... 89
4.2 Design Refinement Method of LC Sensor ..... 94
4.3 Impact of Packaging Materials on LC Sensor Design ..... 101
4.4 Verification of Proposed LC Sensor Design Refinement Method ..... 104
4.5 Readout Circuitry and Frequency Sweeping Factors Impacting Resolution ..... 106
4.6 Chapter Summary ..... 109
**Chapter 5: Environmental Logging Microsystem for Downhole Monitoring ..... 112**
5.1 System Design ..... 116
5.1.1 System Hardware ..... 117
5.1.2 Power Management Unit ..... 127
5.1.3 System Software ..... 129
5.2 System Integration ..... 138
5.3 System Packaging ..... 141
5.4 System Fabrication and Testing ..... 147
5.4.1 ELM8 Fabrication ..... 147
5.4.2 Laboratory Testing of Packaged ELM8 microsystem ..... 150
5.4.3 Functionality and Current Characterization of ELM9 microsystem ..... 151
5.5 Chapter Summary ..... 154
**Chapter 6: Conclusions and Future work ..... 157**
6.1 Summary and Major Contributions ..... 157
6.2 Future Work ..... 162
6.2.1 Alternate Applications of Passive Wireless Pressure Gradient Measurement system for Fluid Flow Analysis ..... 163
6.2.2 Node to Node Acoustic Communication ..... 164
**References ..... 166**

# LIST OF FIGURES

Fig. 1.1: The pressure sensor market ecosystem in 2022. ..... 1
Fig. 1.2: Schematic of a typical pressure sensing microsystem. ..... 2
Fig. 1.3: IC packaging vs MEMS pressure sensor packaging, duplicated from [One99]. ..... 5
Fig. 1.4: Summary of wireless pressure sensing microsystem opportunities in energy industry. .. 9
Fig. 1.5: (a) Schematic of a typical core-flood experiment setup. (b) Cross sectional view of a test cell with typical dimensions ..... 11
Fig. 1.6: (a) A laboratory core-flood experiment setup with X-ray CT scanner [Wij20]; (b) Pressure changes recorded across test cell for limestone core, flooded with $CO_2$ saturated brine in a typical core-flood experiment. Pressure changes are in the range of a few 100 mbar over the course of this experiment [Ott12]. ..... 13
Fig. 1.7: Illustrated deployment of free flowing ELM systems in borehole fractures (ELM systems are shown using yellow dots); duplicated from [Sui17]. ..... 15
Fig. 1.8: Packaged ELM systems (a) ELM1; (b) ELM2; (c) ELM3; and (d) ELM7 [Ma16, Sui17, Vel20]. ..... 17
Fig. 2.1: Concept diagram for the distributed pressure measurement system utilizing a wired feed-through technology for core-flood experiments. ..... 25
Fig. 2.2: (left) 3D drawing [Mur13] and (right) photo of the commercial Murata SCB10H capacitive pressure sensor. ..... 27
Fig. 2.3: DPSCore flexible PCB circuit schematic. ..... 30
Fig. 2.4: Flexible PCB layout. ..... 31
Fig. 2.5: Cross sectional view of the LP-HP chamber feedthrough, showing perforated steel bolt with PCB tab. ..... 32
Fig. 2.6: Software flowchart for external computer. ..... 33
Fig. 2.7: A snapshot of the DPSCore user interface during system operation. ..... 33
Fig. 2.8: Design of flexible PCB layers for rigid region (left) and flexible region (right). ..... 34
Fig. 2.9: DPSCore flexible PCB post fabrication. ..... 35
Fig. 2.10: (a) Temperature dependance characterization test setup; (b) Variation of $\Delta C$ response with temperature at constant atmospheric pressure for all 4 sensing channels. ..... 36
Fig. 2.11: (a) 3D view of COMSOL model for Murata sensor package assembled on flexible PCB substrate; (b) bottom and side view of sensor model; (c) Modelled thermal stress results at 125°C showing a maximum stress of 67.5 MPa near sensor diaphragm. ..... 37
Fig. 2.12: Improvement in sensor baseline capacitance at 125°C with anneal time (in hours). ... 38
Fig. 2.13: Through hole drilled in the steel bolt. The hole diameter $d_H$ is 3.2 mm. ..... 39

Fig. 2.14: (a) Polymer sheath with steel nuts; (b) Fabricated 3D printed inserts; (c) PCB tab integrated with 3D printed insert; (d) PCB tab integrated with 3D-printed insert within the perforation in steel bolt; (e) Cover plate attachment to complete feedthrough. ..... 39
Fig. 2.15: Completely assembled PCB with all four tabs inserted into steel bolts mounted on the polymer sheath. ..... 40
Fig. 2.16: (a) Test setup for static pressure test (b) Variation of ΔC response with chamber pressure at room temperature for DPSCore system. ..... 41
Fig. 2.17: Distributed pressure test setup schematic. ..... 42
Fig. 2.18: Capacitive response of reference capacitor and pressure sensor in no flow state. The table on the right shows the range and standard deviation of the plotted response. ..... 47
Fig. 2.19: (a) CDC temperature variation in a no flow state (b) Reference capacitor response as a function of the CDC temperature variation, data points averaged over 3 sec time intervals. ..... 48
Fig. 2.20: Percent variation in syringe pump flow rate at 25 mL/min setpoint. ..... 49
Fig. 2.21: Percent variation in syringe pump flow rate at 5 mL/min setpoint. ..... 49
Fig. 2.22: (a) Pressure response of Murata SCB10H pressure sensors recorded during flow test at room temperature. Theoretically estimated bounds for each pressure sensor response are indicated by dashed lines; (b) Differential pressure between different test capsules (tabs) recorded during the flow test at room temperature. ..... 50
Fig. 2.23: DPSCore test cell with the integrated system in Total laboratory, Pau. ..... 51
Fig. 2.24: (a) Pressure calibration test data for DPSCore system #DPS18.1.02 at 60°C; (b) Pressure calibration function along with fitted 3rd order calibration equation for DPSCore system #DPS18.1.02 at 60°C. ..... 52
Fig. 2.25: (a) Flow test data for DPSCore system #DPS18.1.02 at 60°C; (b) The difference in pressure between different Murata sensors during flow test at 60°C. ..... 53
Fig. 3.1: Cross-sectional view of the implemented solution for a passive wireless pressure gradient measurement (PGM) system. The system can be scaled to have n LC Sensors and readout nodes, with n = 4 in this work. ..... 57
Fig. 3.2: Wireless Inductive Pressure Gradient Measurement (PGM) System circuit model illustrating the LC Sensor and Readout coil and circuitry. ..... 58
Fig. 3.3: Two $Re\{Z_{in}\}$ datasets at minimum $(P_{Min})$ and maximum $(P_{Max})$ applied pressure illustrating important parameters such as bandwidth, $\sigma$, resonant frequency, $f_0$, $f_0$ shift due to applied pressure, $\Delta f_0$, and fitted gaussian approximation, $F_{Zin}$, used to extract $f_0$ via interpolation. ..... 59
Fig. 3.4: Studied 2D axisymmetric FEA model geometry of the LC Sensor coil and readout coil in COMSOL Multiphysics (left) Magnetic field distribution of the sensor and readout coil assembly under excitation at 13 MHz (right). ..... 61
Fig. 3.5: FEA modelling results showing variation in coupling coefficient and mutual inductance with interrogation gap (*IG*). ..... 62
Fig. 3.6: (a) MATLAB model result showing variation in input impedance magnitude, $\Delta Z_{in}$ with inductor trace width and parallel capacitance for a two-layer PCB. (b) Variation in *DOF* with inductor trace width and parallel capacitance for two-layer PCB, with one and two pressure transducers. ..... 63
Fig. 3.7: Circuit schematic of readout node on Readout PCB. ..... 64

Fig. 3.8: (a) Image of LC Sensor flexible PCB coil with one capacitive pressure transducers (P. XDCR) mounted at the center, placed on an US penny. An inset image shows the diaphragm structure of P. XDCR [Ben21]. (b) Typical capacitive pressure response of pressure transducer over 25 MPa (250 bar) of applied pressure. ..... 65
Fig. 3.9: Layout of the flexible readout PCB. ..... 66
Fig. 3.10: Image of the fabricated flexible readout PCB next to an US penny. ..... 66
Fig. 3.11: Cross sectional view of LC Sensor with proposed packaging method. ..... 67
Fig. 3.12: (a) 3D printed bottom metal stiffener (left) and top metal cover (right) on an US penny (b) Image of a fully packaged LC Sensor on an US penny. ..... 68
Fig. 3.13: Liquid polyimide thin film coated LC Sensor (left) as fabricated and (right) after 24-hour toluene soak on an US penny. ..... 69
Fig. 3.14: 2D axisymmetric FEA modelling result showing von Mises stress distribution in LC Sensor packaging aluminum top metal cover, polyimide substrate, and aluminum bottom metal substrate stiffener under applied pressure of 230 bar. ..... 69
Fig. 3.15: $Re\{Z_{in}\}$ datasets for LC Sensors in unpackaged and packaged configurations with aluminum, magnetic stainless steel (15-5), and non-magnetic stainless steel (316L) top metal cover and bottom metal substrate stiffener. ..... 70
Fig. 3.16: PGM system software requirement. ..... 71
Fig. 3.17: MCU State Diagram. ..... 72
Fig. 3.18: Software flowchart for Raspberry Pi based external unit. ..... 76
Fig. 3.19: (a) Resonant frequency, $f_0$, shift of four LC Sensors over the full-scale temperature range of 25°C – 125°C, at zero applied pressure. (b) $f_0$ shift of four LC Sensors for an applied static pressure over the full-scale pressure range of 0 – 20 bar, at 25°C. ..... 79
Fig. 3.20: Measured improvement in resolution of integrated Pressure Gradient Measurement (PGM) system when oversampling and averaging is utilized. ..... 81
Fig. 3.21: (a) Illustration of axial misalignment (*AM*) and interrogation gap (*IG*) (b) Measured relative impact on LC Sensor pressure resolution with non-ideal *AM* up to 4 mm and *IG* of 3 mm, 4 mm, and 5 mm. ..... 82
Fig. 3.22: Flow test setup schematic illustrating 4 LC Sensors ($LC_n$) located at 4 different locations along a flow path. 4 wired pressure gauges (PG) are located adjacent to the LC Sensors. Check valves ($CV_n$) create pressure drop along the flow path. Readout nodes ($RN_n$) wirelessly couple with individual LC Sensors for pressure readout. ..... 83
Fig. 3.23: (a) Raw resonant frequency shift, $\Delta f_0$ recorded from the PGM system during flow test (b) Temperature data recorded from PGM system during flow test (c) Pressure recorded by LC Sensors ($LC_n$) during flow experiment in custom setup (Fig. 3.22) at room temperature (25°C). The flow rate is increased in four discrete steps of 0 mL/min, 14 mL/min, 24 mL/min, and 32 mL/min. (d) Pressure measurements recorded by four wired pressure gauges ($PG_n$) during flow experiment, placed adjacent to the LC Sensors. ..... 84
Fig. 4.1: Block diagram of LC Sensor readout system with the four major element blocks highlighted and how most sub-elements overlap within each major block. ..... 89
Fig. 4.2: Circuit model illustrating an LC Sensor and Readout coil and circuitry. ..... 89
Fig. 4.3: Two $Re\{Z_{in}\}$ datasets at minimum $(P_{Min})$ and maximum $(P_{Max})$ applied pressure illustrating important parameters such as bandwidth, $\sigma$, resonant frequency, $f_0$, $f_0$ shift due to

applied pressure, $\Delta f_0$, *and* fitted gaussian approximation, $F_{Zin}$, used to extract $f_0$ via interpolation. ..... 93
Fig. 4.4: Comparison of example $Re\{Z_{in}\}$ datasets at 0 and 20 bar applied pressure for three different LC Sensor designs with varying absolute and relative LC Sensor Response, $R_A$ and $R_R$, and Design Optimization Factor, *DOF*. All datasets are plotted over their respective bandwidth (i.e. bandwidth normalized); $Re\{Z_{in}\}$ datasets at 0 applied pressure are represented with dashed lines; $Re\{Z_{in}\}$ datasets at 20 bar applied pressure are represented with solid lines. ..... 96
Fig. 4.5: Impact of sensor and readout coil diameter on relative coupling, with varying *IG*. ..... 99
Fig. 4.6: Full circuit model for LC Sensor showing all parasitic resistances and capacitances. 101
Fig. 4.7: Measured results of LC Sensors unpackaged, packaged with non-magnetic (316L), and packaged magnetic (15-5) stainless steel top metal cover with two parallel pressure transducers and varying dummy ceramic capacitors ($C_{DUMMY}$). Simulation curves are obtained using the circuit from Fig. 4.6 and the values given in Table 4.3. ..... 102
Fig. 4.8: Fig. 1: (a)-(d) Analytical simplification of example LC Sensor circuit model. ..... 103
Fig. 4.9: (a) LTSPICE simulated input impedance of circuit model in Fig 4.7(a). (b) LTSPICE simulated input impedance of circuit model in Fig 4.8(d). ..... 104
Fig. 4.10: Measured and simulated resolution of LC Sensor with and without top metal covers using equation 4.17 with a proportionality factor, P=45, and the fitted LC Sensor values as presented in Table 4.4. ..... 105
Fig. 5.1: ELM9 Block Diagram. ..... 116
Fig. 5.2: Circuit Schematic of ELM9 microsystem. ..... 118
Fig. 5.3: Measured quiescent current variation with temperature for Linear Technology LTC2941-1 battery gauge in (a) Active mode; (b) Sleep mode of operation. ..... 123
Fig. 5.4: (a) ADG819 leakage current with rising temperature in “OFF” state. (b) Relay configuration used over temperature characterization. ..... 125
Fig. 5.5: Images of ELM9 piezoresistive pressure sensor [Mer22]. ..... 126
Fig. 5.6: Configuration of designed power switching SPDT relay when wireless power transfer is inactive (state 1, battery power only), during switch to wireless power (state 2, both power sources present) and active (state 3, microsystem recovery with depleted battery). ..... 129
Fig. 5.7: Typical operational flowchart for ELM9. ..... 130
Fig. 5.8: ELM9 B-MCU state machine diagram. ..... 131
Fig. 5.9: Custom BLE data transfer redundancy check algorithm. ..... 134
Fig. 5.10: CMOS relays controlled by the B-MCU. ..... 135
Fig. 5.11: Operation flowchart of B-MCU in detection state. ..... 136
Fig. 5.12: ELM9 Graphical User Interface on laptop. ..... 137
Fig. 5.13: (a) Example illustration of ELM9 microsystem stack (b) FEA study showing ELM9 stack arrangement with minimum PCB deformation under uniformly applied load of 50 MPa. 139
Fig. 5.14: (a) PCB design layout of the mother board with 3 metal layers (top – layer 1, layer 2, and bottom – layer 16) (b) PCB design layout of the daughter board with 2 metal layers (top, and bottom). ..... 140
Fig. 5.15: (a) Picture of acid stimulation bench used to study ELM package in simulated borewell environment at TOTAL Energies, France (b) Pictures of affected ELM7 packages from laboratory and field testing with potential issues identified. ..... 142

Fig. 5.16: (a) Illustration showing ELM8 packaging approach (b) ELM8 package after 72 hour in HPHT oil bath (c) ELM8 dummy package (no electronics) after $CH_4$ gas intrusion test at 34 MPa, 90°C for 6 hours. ..... 144
Fig. 5.17: Packaging concept of ELM9 microsystem – includes ELM9 microsystem stack injection molded into a sphere of HNBR with small flat area for placement onto Qi wireless power transfer pad..... 147
Fig. 5.18: Unpackaged Environmental Logging Microsystem 8 (ELM8): (a) top and (b) bottom view (without primary battery) and (c) HT primary battery connected to ELM8 microsystem. Major components labelled are detailed in Table 5.8. ..... 148
Fig. 5.19: Collected data from packaged ELM8 microsystems (up to 7,250 psi and 100°C). (a) ELM8-0001 is packaged using flexible epoxy and cenosphere composite. (b) ELM8-0002 is packaged in oil filled nylon bag [Vel20]. ..... 151
Fig. 5.20: (a) ELM9 current draw during BLE radio advertising (b) ELM9 current draw during BLE connection and handshaking with GUI (c) ELM9 current draw during one sensor measurement routine in B-MCU detection state with only capacitive pressure sensor active (d) ELM9 current draw during one sensor measurement routine in B-MCU detection state with capacitive pressure sensor and IMU active in single mode (e) ELM9 current draw during external Flash erase operation (f) ELM9 current draw during standby mode/B-MCU placed in EM4 shutoff; average current is 0.27 µA. All measurements performed at 25°C..... 153
Fig. 6.1: Operating regimes of ELM microsystems..... 160
Fig. 6.2: Illustration of acoustic communication between sensing nodes with a multiple tethered acoustic transponder..... 165

# LIST OF TABLES

Table 1.1: Comparison of Capacitive pressure sensors. ..... 3
Table 1.2: Comparison of communication protocols [Sui17, Glo17, Vel20]. ..... 6
Table 1.3: Key challenges in microsystem design based on application domain. ..... 7
Table 1.4: List of fluids which have been used in prior core-flood experiments. ..... 12
Table 1.5: Summary of prior microsystem work for downhole applications [Vel22]. ..... 16
Table 1.6: Summary of previous generations of ELM [Ma16, Sui17, Vel20]. ..... 18
Table 1.7: Design targets of this dissertation. ..... 21
Table 2.1: Preferred performance targets for DPSCore system. ..... 26
Table 2.2: Summary of three miniature high resolution CDC chips for capacitance conversion. 28
Table 2.3: Comparison of estimated p-p pressure resolution when using the Murata SCB10H-B250 pressure sensor with the three identified CDC chips. ..... 28
Table 2.4: COTS component list for the DPSCore flow test setup. ..... 42
Table 2.5: Theoretical estimation of channel 4 pressure response. ..... 45
Table 2.6: Theoretical estimation of channel 3 pressure response. ..... 45
Table 2.7: Theoretical estimation of channel 2 pressure response. ..... 45
Table 2.8: Theoretical estimation of channel 1 pressure response. ..... 46
Table 2.9: Theoretical estimation of pressure response for all sensor channels. ..... 46
Table 2.10: Estimated pressure error for all sensor channels due to pump flow variation. ..... 49
Table 3.1: Design constraints for LC Sensor and readout coil for PGM system. ..... 60
Table 3.2: Assumed material properties in FEA model. ..... 61
Table 3.3: Design parameters for LC Sensor. ..... 63
Table 3.4: Layer stack of flexible readout PCB. ..... 66
Table 3.5: Weight of fully packaged LC Sensor during Toluene resistance validation test ..... 69
Table 4.1: LC Sensor specifications used in SPICE circuit simulation of Fig. 4.4. ..... 96
Table 4.2: $R_{CS}$ for varying number of transducers, $ESR_{XDCR}$'s, and $C_{PS}$ values. ..... 101
Table 4.3: Fitted component values for measured results. ..... 102
Table 4.4: Resolution results of LC Sensor ..... 106
Table 5.1: Major ELM9 components. ..... 119
Table 5.2: Comparison of MCUs for B-MCU. ..... 121
Table 5.3: Available energy modes during B-MCU operation. ..... 121
Table 5.4: List of GUI sections with their functionality. ..... 137
Table 5.5: Potential options for ELM9 package material. ..... 145
Table 5.6: Dimensional and weight changes of Viton and HNBR, after $CH_4$ migration test. ..... 146
Table 5.7: ELM8 microsystem specifications ..... 148
Table 5.8: Descriptions of major components of ELM8. ..... 149
Table 5.9: ELM9 microsystem specifications. ..... 154
Table 6.1: Comparison of results with design targets of this dissertation. ..... 162

## ABSTRACT

Over the past decade, significant interest has gathered toward studying robust microsystem technologies for deployment in harsh environments. This research is directed at investigating sensing microsystems for high pressure and high temperature (≥20 MPa, ≥100°C) environments that are encountered in the energy industry in two contexts: i) laboratory studies of geological samples and ii) downhole energy exploration and production.

Laboratory studies involve assessing rock core samples for the transport of fluids in experiments that can last months. The results are used to predict energy recovery processes for geological formations and study flooding strategies. The existing assessment methodology does not facilitate *in-situ* measurement of pressure gradients along the length of the rock core; however, incorporating distributed pressure sensors along the seam of the rock core, without disturbing fluid transport, can greatly enhance the quality and impact of the data gathered. In this work, the readout electronics were located exterior to the polymer sheath that hugs the rock core within the test cell that is maintained at elevated pressure (up to 25 MPa) and temperature (up to 125°C). Two microsystem configurations were investigated – a wired version using feedthroughs in the polymer sheath, and a wireless version using passive, wireless, inductive capacitive (LC) pressure sensors embedded in the polymer sheath. The wired version provided a pressure resolution of 30 Pa over a 2 MPa full-scale range. The wireless LC Sensor-based microsystem provided a pressure resolution better than 100 Pa over a 2 MPa full-scale range. To minimize pressure resolution of a passive LC sensing microsystem, a figure of merit, termed *Design Optimization Factor* was defined, and evaluated using finite element analysis and 3D modelling. Application-driven

constraints, including a customized pressure transducer, the choice of packaging, alignment tolerances, and commercial manufacturing limits were considered in an optimization effort, and the results were experimentally verified using fabricated LC Sensors.

In energy exploration and production, as well as in other applications, downhole environments are routinely monitored with wireline logging tools. These macro-scale tools can be expensive, and lead to multi-day production shortfall, and slickline interventions. To miniaturize wireline tools and facilitate untethered sensing, autonomous microsystems are being developed with temperature, pressure, inertial, and magnetic sensing. This work investigated challenges in hardware/software codesign, power and performance limits, and operating modalities of an environment logging microsystem for high pressure high temperature operation. A microsystem was designed to sense pressure over a 50 MPa full-scale range (with 0.5 kPa resolution), temperatures up to 150°C (0.1°C resolution), and inertial parameters (acceleration and magnetic field) at bandwidths >10 Hz. Multi-day deployment with high sensing bandwidth was achieved with a large non-volatile memory, while fast wireless sensor data readout was achieved with minimum impact on battery capacity using a Bluetooth low energy (BLE, v5.2) communication module activated in presence of Qi wireless power. Microsystem standby current was reduced to 0.27 µA @ 25°C through investigation of a dynamic power management module, increasing microsystem shelf-life to >5 years, primarily limited by self-discharge of primary battery. An integration and packaging methodology was investigated to enable buoyant deployment of microsystem in narrow wellbores; designed microsystem package has an overall volume <32 $cm^3$ and density 1.39 $g/cm^3$.

# Chapter 1: Introduction

## 1.1 Motivation and Background

Over the past few decades, Micro-Electromechanical Systems (MEMS) have been able to offer many benefits over conventional, macro-scale sensor designs, as the need for wireless, compact, and cost-effective solutions rise in demand [Par99, Gri01, Tak04, Cha12]. Considered one of the greatest successes of the microsensor industry, pressure sensors have been widely utilized in the industrial, automotive, and healthcare sectors [Gia06]. Over the last decade, the introduction of pressure sensors in consumer electronics such as smartphones and gaming units has further propelled the $13 billion pressure sensing industry, which is expected to grow up to $21 billion by 2026 [Mar20]. Fig. 1.1 illustrates the pressure sensor market ecosystem and the many interconnected areas within it as of 2022; this work aims to contribute in the sectors highlighted in red.

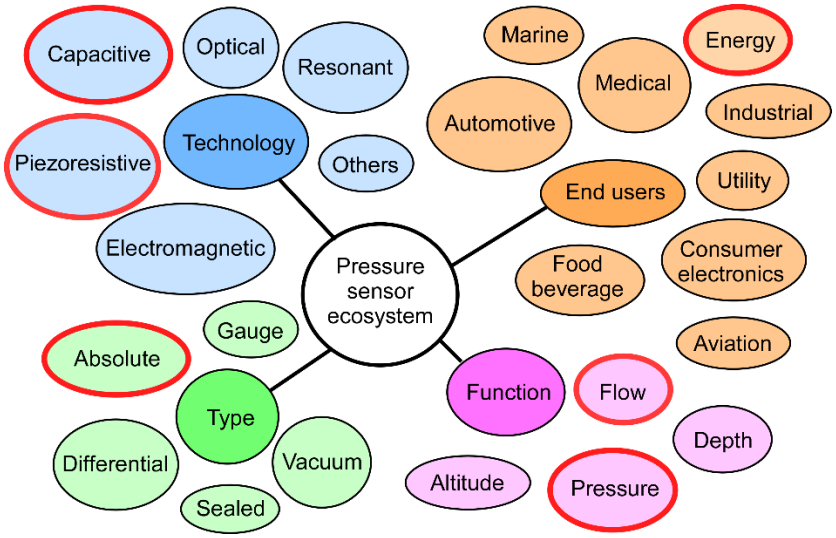



Fig. 1.1: The pressure sensor market ecosystem in 2022.

A typical pressure sensing microsystem, shown in Fig. 1.2, consists of, at minimum, the pressure sensor, transduction circuit, micro-controller, memory, power module / microbattery, communication module, and system package. A variety of transduction approaches have been utilized in the past to realize pressure sensing capability, the most popular being piezoresistive [Sam73] and capacitive [San80]. Piezoresistive pressure sensors traditionally have a more linear output response (change in resistance with applied pressure) and low output impedance, but can be limited by dimensional scaling constraints, large temperature coefficients, [Kan82] and higher power budgets [Cha87]. Capacitive pressure sensors can offer higher sensitivity and scalability, lower noise, smaller power budgets, and lower temperature coefficients, but their high output impedance poses challenges to design of the transduction circuit [Gia83, Ji92, Wan97] and requires that the sensor and circuit remain in close proximity. While commercial microfabrication methods have advanced to permit the production of smaller pressure sensors with footprints <2 $mm^2$ using both piezoresistive and capacitive transduction methods [Mer22, Mur13], design of a pressure sensing microsystem which preserves the performance of the sensor in varying environments is fraught with challenges and limitations.

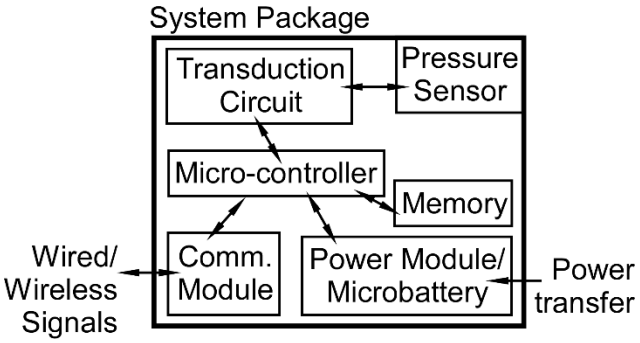


Fig. 1.2: Schematic of a typical pressure sensing microsystem.

## 1.2 Challenges for Pressure Sensing in Space Constrained Environments

Prior art in microfabricated pressure sensors has focused primarily on reducing size of the sensing element – often aiming for an ideal tradeoff (for the desired application) between several sensing parameters such as full-scale range, noise, sensitivity, resolution, and temperature coefficients [Hes17, Son20]. Table 1.1 lists prior work of capacitive pressure sensors and their performance characteristics. However, creating an entire pressure sensing microsystem involves much more than just the sensing element itself; one must consider the transduction circuitry, control methodology (microcontroller, programming), data storage, power source, communication mode, energy harvesting and package design module. Each of these modules have their own energy and operational constraints often governed by the application domain, different methods of inter-communication, and occasionally their own volatile/non-volatile memory. Efficient dimensional and performance enhancement of each system module in association with other modules is, therefore, necessary to fully refine overall system performance and footprint. The following paragraphs in this section shed light on the importance of some of these modules and the challenges they present in microsystem design.

Table 1.1: Comparison of Capacitive pressure sensors.

| Work | Size [$mm^3$] | $C_0$ [pF] | Cap. Rsp. [fF/kPa] | Sensitivity [ppm/kPa] | Range [MPa] | Resol. [kPa] (1 fF/code) | Resol. [bits] | TCO [ppm/°C] |
|---|---|---|---|---|---|---|---|---|
| Cho92 | 2.2 | 6 | 4575 | 762k | 0.001 | 0.0002 | 12.6 | 841 |
| Cha88 | 0.15 | 0.5 | 5.47 | 10.9k | 0.04 | 0.183 | 7.8 | -3071 |
| Par00 | 0.17 | 3.75 | 1.5 | 400 | 1.5 | 0.67 | 11.1 | 405 |
| Cha01 | 3.0 | 8.34 | 231.4 | 27.7k | 0.01 | 0.004 | 11.2 | 3900 |
| Mic08 | 0.6 | 9.8 | 13.1 | 1340 | 0.8 | 0.08 | 13.7 | - |
| Mur13 | 1.67 | 7.3 | 2.64 | 362 | 2.5 | 0.4 | 12.7 | 560 |
| Ben21 | 0.7 | 3.6 | 0.45 | 125 | 50 | 2.22 | 14.5 | 420 |

☐ (*Used in this work)*

First, we must understand the fundamental difficulties, and differences in dimensional scaling of a sensing microsystem, in comparison to the integrated circuit (IC) industry. While the

IC industry has successfully reduced transistor gate nodes from 1000 nm in 1990 [Che14] to the highly compact 5 nm in 2022 [Lia22], the progress in dimensional scaling of pressure sensing microsystems has not shared the same rate of size reduction. Although significant effort has been directed towards leveraging advancements of the IC industry into pressure sensing microsystem designs, such as monolithically integrated pressure sensors using an IC foundry compatible process [Yan14], the philosophical differences related to physically sensing the environment (i.e. diaphragm scaling), as well as in packaging technology of IC devices have consistently posed a significant challenge in dimensional scaling of these microsystems. First, microfabricated pressure sensors encounter several roadblocks in release / stiction, stress, dicing and die handling, outgassing, and testing constraints which pose challenges at the die and device level packaging [Gia06]. Second, while standardized IC packages provide only physical support, electrical interfacing, and isolation from the environment, the pressure sensing microsystem needs to be intimately coupled to the environment while simultaneously being either protected from it (e.g. harsh environments in down-hole monitoring) or be insulated to protect the environment from the sensor itself (e.g. biocompatibility in *in vivo* healthcare devices) [One99]. Application environment plays a major role in material selection and design of pressure sensor microsystem package, which is often heavily customized. CMOS compatibility and monolithic integration of sensors is achieved through limitations in sensor material, processes and integration challenges heavily affecting yield, repeatability, and performance of the sensor [Ped97].

At present, the average assembly, packaging, and testing budget for MEMS pressure sensors in production is 80% of the total production cost; despite this, though, the cause of most microsystem failures is traced back to inadequate packaging [Bha13]. Hence, significant effort is

needed in achieving a low cost, volume scalable, and modular packaging solution for pressure sensing microsystems.

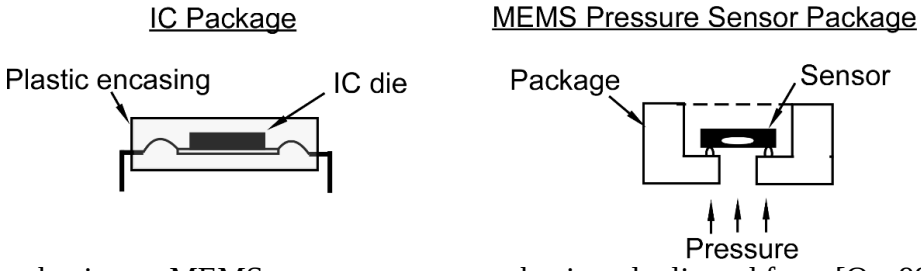



Fig. 1.3: IC packaging vs MEMS pressure sensor packaging, duplicated from [One99].

In addition to packaging constraints, power availability and hardware/software codesign also play a critical role in design of miniaturized sensing systems. Space constrained environments may require the sensing system to be untethered and autonomous, thus necessitating an on-board battery. Choice of battery in a microsystem is heavily governed by the environment, nature of application, and total power draw characteristics of the microsystem. The average power budget for a sensing system decreases with reduction in battery size and increase in desired lifetime of operation [Bla14]. Therefore, pressure sensing microsystems must have nanowatt power budgets unlike larger systems which can afford average power consumption rates on the order of milliwatts. In low duty cycle sensing systems, standby power becomes the dominant component. However, in high bandwidth systems, increased sensor and communication module operation may result in them becoming the dominant consumers of system power. A dynamic software driven control of oscillators and sensor hardware peripherals based on microsystem performance necessities with configurable duty cycles may lead to a power and performance optimized design; this type of approach is detailed in Chapter 5.

A transduction circuit is required to effectively convert sensor signals (such as capacitance or resistance) to a signal more easily digitizable, such as an analog voltage. For interfacing with a capacitive pressure sensor, an analog front end (AFE) along with an analog to digital converter

(ADC) is commonly utilized. AFE choices include switched-capacitor sampling [Gia06, Yam92], capacitance to time [Mon17], capacitance to frequency [Mat14], etc… whereas the ADC may be dual-slope [Phi14, Zou16], successive-approximation [Lee14], delta-sigma [Pet05], etc. Each AFE and ADC choice contributes their own complexity, power and footprint requirements affecting overall system performance. An oscillation frequency-based transduction is sometimes used to eliminate the use of an ADC for highly space constrained passive applications at the disadvantages of reduced sensitivity and reduced stray capacitance immunity [Aka01, Ben19, Zha20].

Additionally, the microsystem must interface with the external world using a communication module for data, command, and possible power transfer. The communication module plays an important role in limiting system scalability and power budget, typically being the largest consumer of system power [Hea08]. High power consumption leads to heat production in a microsystem which may be detrimental to performance. A variety of wired and wireless communication protocols used in microsystems have been summarized in Table 1.2. Wired protocols provide reliability, security, and high data transfer rates while wireless protocols strive to meet all necessities of an untethered deployment in a space-constrained environment [Glo17].

Table 1.2: Comparison of communication protocols [Sui17, Glo17, Vel20].

| Protocol Type | Wired | | | Wireless | | | |
|---|---|---|---|---|---|---|---|
| Feature | SPI | $I^2C$ | RS232 | Wi-Fi | Bluetooth | Zigbee | BLE |
| Data Rate [Mbps] | 20 | 0.1 | 0.02 | 11 | 1 | 0.25 | 1-2 |
| Frequency [GHz] | - | - | - | 2.4 | 2.4 | 2.4 | 2.4 |
| Range [m] | 100 | 10 | 15 | 1-100 | 10-100 | 10-100 | 10-100 |
| Peak current [mA] | - | - | - | 100-350 | 1-35 | 1-10 | 0-15 |
| Complexity | Medium | Low | Low | High | Medium | Medium | Medium |
| Security | - | - | - | WPA2 | 128 bit | 128 bit | 128 bit |

The intended application domain necessitates its own set of requirements. For example, the biomedical domain sets additional limitations on biocompatibility, materials, and battery; energy industry domains require packaging for extreme environments and enhanced security of

collected sensor data. Table 1.3 summarizes some of the major challenges faced in designing a pressure sensing microsystem based on its intended application domain.

Table 1.3: Key challenges in microsystem design based on application domain.

| **Application Industry** | **Application areas** | **Key Design Challenges** | **Reference** |
|---|---|---|---|
| Aerospace and Automobile | Flight data systems, hydraulics, structural monitoring, safety and diagnostics, tire pressure, etc. | - Device centered sensor design<br>- Safety and reliability<br>- Rugged to withstand high shear, tensile and normal forces<br>- Temperature and environment | [Fle01, Son20, Wu06, Tiw12] |
| Biomedical | Blood pressure, intraocular pressure, Intracranial pressure, GI tract monitoring, etc. | - Biocompatibility<br>- Rugged to withstand sterilization process<br>- Cost due to their disposable nature<br>- Characterization and classification algorithms<br>- Wireless interfaces<br>- Power consumption<br>- High frequency response and feedback mechanisms<br>- Safety and reliability, <2°C temperature rise for in vivo systems<br>- Ergonomics | [Ben19, Che08, Eat97, Gia06, Gop93] |
| Consumer products | Electronics, altimeter, microphone, sports, wearables, etc. | - User acceptance and convenience<br>- Wear resistance and reliability<br>- Cost and market reach<br>- Rugged to bear abuse, durability<br>- Power constraints | [Cai16, Hor07] |
| Energy | Downhole monitoring, core flood, ocean imaging, etc. | - Extreme environment robustness<br>- High pressure and high temperature<br>- Chemical resistance and compatibility<br>- Data security<br>- Power constraints<br>- Scalability and reliability<br>- Heavy machinery and vibrations | [Ott12, Sui17, Vel20] |
| Food | Human tactile system monitoring and kinematics research, process control, level and flow, packaging | - Safety and reliability<br>- Hygiene and guidelines<br>- Contamination and food compatibility<br>- Machinery and vibrations | [Koh15], [Kre01] |
| Marine | Flow dynamics, auto-steering and navigation, obstacle detection | - Electrical isolation and water resistance<br>- Robust packaging<br>- Reliability and durability<br>- Small pressure gradient measurements<br>- Instrument calibration | [Dev15], [Sha18], [Gao12] |

## 1.3 Pressure Sensing Opportunities in the Energy Industry

Global energy demand is expected to increase by 50% over the next 20 years and renewable energy sources, though steadily maturing, may only play a complimentary and supplementary role to the use of traditional hydrocarbon-based sources. In order to meet the world's growing energy needs over the next few decades, the energy industry requires major breakthroughs in its core science and engineering technologies in order to improve their efficiency and reduce their impact on the environment [Kon10].

The hydrocarbon energy industry involves a wide range of indusial operations, which can be categorized into four major sectors: upstream (exploration and production), midstream (storage and transportation), downstream (refining), and analytics/support technology (R&D). Since most industry assets are in remote and hard to access areas, continuous remote monitoring of all equipment and processes in the first three sectors become increasingly important [Kha16]. Although several wired sensing technologies have been historically used in the energy industry, their bulky structure and low flexibility, high maintenance costs, deployment difficulties in harsh environments, and vulnerability to data breaches have increasingly made them a less attractive option compared to wireless sensing microsystems [Sav13]. However, major challenges in design of these miniaturized wireless microsystems originate from a large variety of operational and environmental conditions across the four sectors discussed above, raising questions of cost, security, energy consumption, reliability, scalability, and robustness of the designed microsystem [Aal18]. Fig. 1.4 identifies different microsystem-based pressure sensing opportunities in the four major operation sectors of the energy industry. This work investigates three design approaches for pressure sensing microsystems to enhance research, performance, and monitoring activities in two separate sectors of the industry — upstream and analytics.

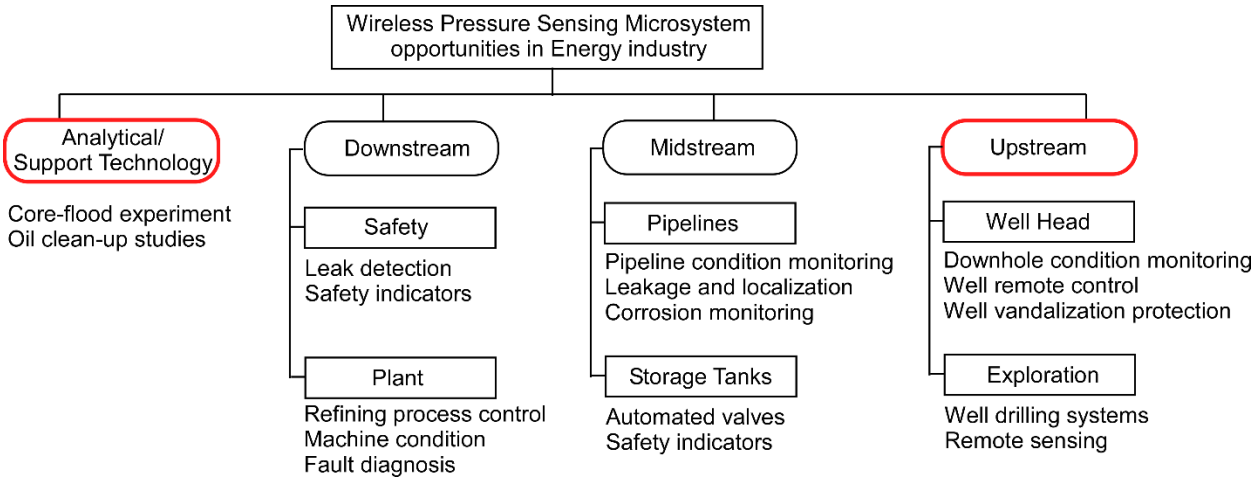



Fig. 1.4: Summary of wireless pressure sensing microsystem opportunities in energy industry.

### 1.3.1 Laboratory Application: Sensor confinement requirement

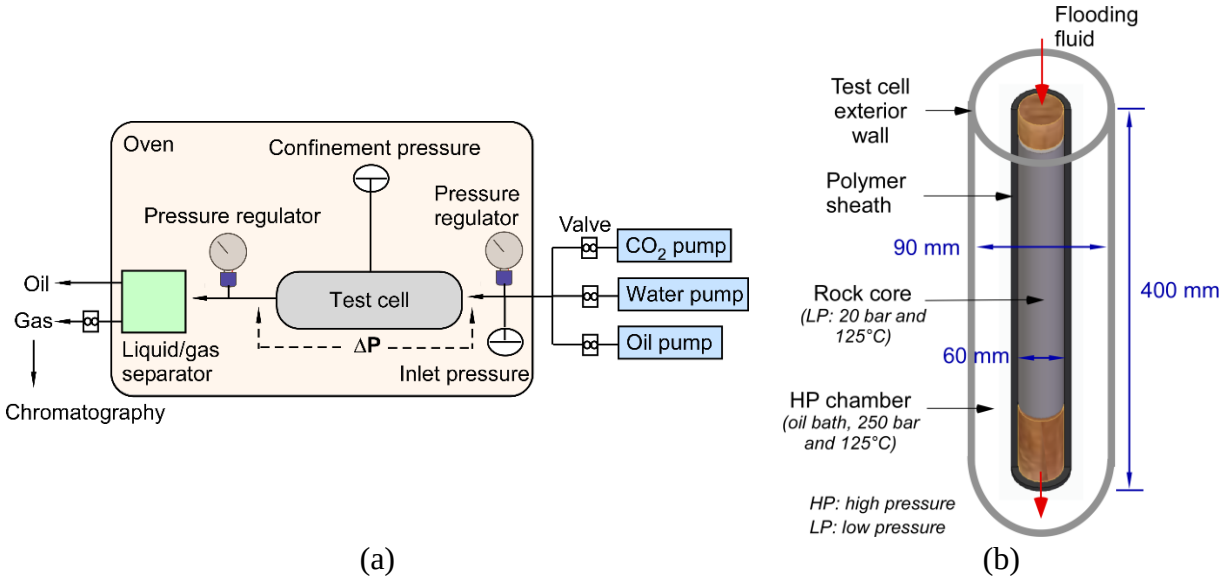
The technology sector of the energy industry for analytics and support includes advanced testing centers and research laboratories which study and advance the field of energy extraction [Aal18]. Deployment of a pressure sensing microsystem in this domain requires sensing pressure inside research equipment in laboratories for testing and monitoring purposes. These applications often require designing sensor and transduction methodologies to access and extract critical pressure data from highly confined spaces within the machinery without the sensing element affecting the pressure to be measured and without affecting the performance of the machine. In addition to dimensional constraints, the sensing environment inside the equipment can be saturated with corrosive and conductive fluids and/or be subjected to high temperature and pressure levels contributing to complexity in sensor access strategies, sensor performance, and package design. However, since the equipment is typically located in an indoor facility, there may be reduced restrictions on power availability and computation capabilities, thus allowing some control electronics to be located outside the sensing environment. One primary laboratory application explored in this work is a core-flood experiment, discussed below.

#### 1.3.1.1 Core-flood Experiments

The ever pressing need to explore new hydrocarbon resources in unexplored regions of the world has led the energy industries to investigate ever more efficient extraction processes [Bal14]. USA alone spends approximately $15 billion per year in energy exploration efforts which can involve site selection, drilling operations, and production wells [Sta20]. In recent years, there has been significant interest in the use of different flooding fluids (brine, chemicals, surfactants, polymers, etc.) to displace resident energy phase in underground porous rocks to enhance energy production [Oil14]. Therefore, laboratory testing facilities (and their corresponding test and monitoring equipment) to predict energy recovery processes of new geological formations and the applicability of new flooding strategies without embarking a costly venture of direct drilling in the field [Bal14] is required. To address this need, energy industries have traditionally relied on laboratory core-flood experiments which play a critical role in energy production; however, improvements in the sensing capabilities of these core-flood experiments is required to enhance their predictive capabilities to better elucidate the proposed drilling and flooding strategies.

Fig. 1.5 (a) shows the schematic of a typical core-flood experiment setup and Fig. 1.5 (b) shows a cross-section of the test cell. In a typical experiment, a rock core sample representing the porous natural reservoir in question is prepared with consolidated (e.g. rock, sandstone, carbonate outcrops) or unconsolidated materials (e.g. sand) and placed within a test cell. The rock core sample, also referred to as the rock core, is placed in the center of the test cell wrapped in a polymer sheath. The interior of the test cell is filled with a non-conductive fluid pressurized up to ≈250 bar to create confinement pressure and is referred to as the high pressure (HP) chamber. Flooding fluid is pumped into the rock core encased by a polymer sheath which forms the low pressure (LP) chamber. Pressure inside the LP chamber can be as high as ≈20 bar while temperature of the entire

test cell can be raised up to 125°C during a core-flood experiment; these test conditions are chosen to simulate reservoir environment. Pumps and piston accumulators supply a variety of flooding fluids to one end of the core sample which flow through it and are then collected using fraction collectors or phase separators [Nas11]. These flooding fluids can be both corrosive and electrically conductive in nature; Table 1.4 shows a list of fluids which have been used in prior reports core-flood experimental efforts. The flow rate and differential pressure drop (ΔP) observed across the ends of the rock core, as well as the chemical analysis of the collected fluids, reveal important information on porosity, permeability, and chemical compatibility of the reservoir with the proposed flooding strategies. Incompatible flooding would lead to chemical reactions within the core material causing trapping / blockage inside the core which, if transpired in an energy well, could render the entire extraction activity fruitless. Additionally, collected data can be analyzed using artificial intelligence algorithms to estimate efficiency of the tested oil recovery method [Pet08]. Therefore, the more data that can be extracted from the experiment, the better the estimates can become.




(a) (b)

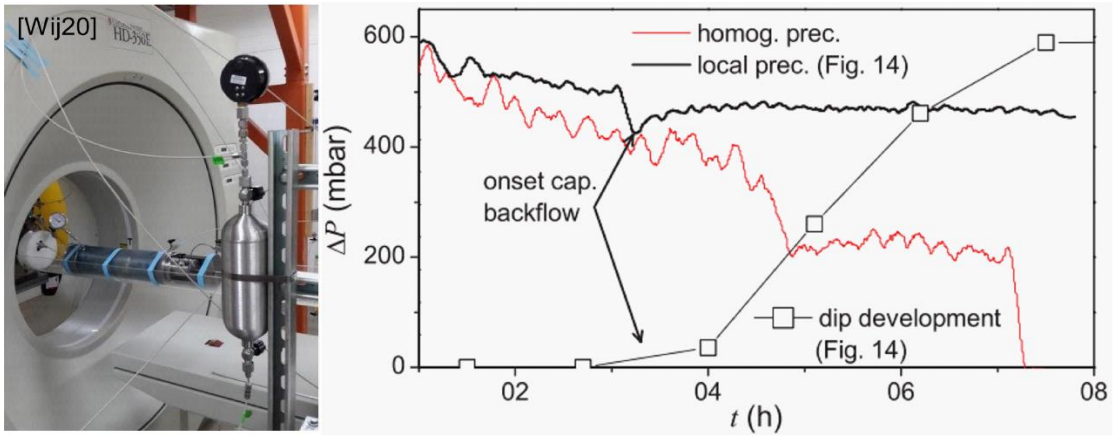
Fig. 1.5: (a) Schematic of a typical core-flood experiment setup. (b) Cross sectional view of a test cell with typical dimensions

Table 1.4: List of fluids which have been used in prior core-flood experiments.

| Work | Year | Flooding fluid |
|---|---|---|
| [Hor87] | 1987 | isooctane, brine, water, and oil |
| [Cha94] | 1994 | $CO_2$, brine, oil, and surfactant solution |
| [Bag01] | 2001 | water, oil, and different microbial cultures |
| [Sol04] | 2004 | steam, $CH_4$, and heavy oil |
| [Nob07] | 2007 | crude oil, and $CO_2$ |
| [Man10] | 2010 | oil-in-water emulsion, oil, and water |
| [Sam12] | 2012 | oil, brine, and chemical slug |
| [Ko14] | 2014 | brine, oil, and surfactant |

In order to make the core flooding experiment more robust and efficient, great effort has been directed towards mapping pressure gradient and fluid saturation characteristics inside the rock core (i.e., to obtain a better understanding of the inside the core material) during the core-flood experiment. This challenge is exacerbated by the fact that experiments may run for up to several months at a time [Sun16]. Data obtained from inside the core material can help by improving both accuracy and turnaround time of core-flood experiments and open new pathways for mapping underground wells and reservoirs. X-ray CT scan has historically been used to map fluid saturation data inside rock cores during a core-flood experiment [Ott12]. An X-ray CT scan setup with a test cell has been shown in Fig. 1.6(a). Apart from being complex and difficult to operate, this approach is very expensive, does not enable continuous data collection, is not scalable, performs measurements *ex situ* to the rock core, and occupies a large space. Due to these difficulties, a sensing system opportunity was identified for investigation of an *in situ* high resolution distributed pressure measurement microsystem to continuously monitor flow induced pressure gradients in the rock core during a core flood experiment. This approach would provide a reusable, low cost, and continuous pressure gradient monitoring tool, as part of the core flood experiment setup, thus opening new pathways for understanding geological samples using MEMS pressure sensors. As shown in Fig. 1.6 (b), the pressure changes across a test cell over a typical

core-flood experiment, using a limestone core flooded with $CO_2$ saturated brine, ranges from 0 to 600 mbar. Although core-flood experiments have been utilized for decades, and continue to be an essential tool in energy production, a core-flood experiment's success rate is only ≈50% and the experiment often fails up to 3 months after it has been started. Therefore, in addition to the benefits discussed previously, a continuous measurement of the rock core may be able to better detect these pressure gradients formed across small sub-sections of the core and aid in early failure detection of the experiment, saving valuable time, cost, and effort in energy production studies.




(a) (b)

Fig. 1.6: (a) A laboratory core-flood experiment setup with X-ray CT scanner [Wij20]; (b) Pressure changes recorded across test cell for limestone core, flooded with $CO_2$ saturated brine in a typical core-flood experiment. Pressure changes are in the range of a few 100 mbar over the course of this experiment [Ott12].

### 1.3.2 Field Application: System Confinement Requirement

In contrast to the analytics sector, the upstream sector of the energy industry is comprised of production wells and drilling sites, often spread across remote and rugged terrain, greatly increasing the difficulty in travelling to and maintaining a human presence [Kha16]. Deployment of a pressure sensing microsystem in this domain necessitates sensing pressure in production wells or downhole environments to help monitor and control well operations. Therefore, major challenges lie in designing an autonomous and untethered sensing microsystem which will have all the microsystem components from the sensor to power and communication module integrated within a single sealed package compatible with the designed system functionalities and the sensing environment. In addition to dimensional and environmental constraints for the system package, the remote location of deployment, combined with the autonomous and untethered nature of these systems, lead to increased restrictions on power budget, computation, sensor data storage, and communication capabilities.

#### 1.3.2.1 Environmental Logging Microsystem (ELM) for Downhole Monitoring

Acquisition of well monitoring data such as temperature, pressure, resistivity, and chemical concentration, is necessary in hydraulic fracturing operations for increasing well efficiency and safety, extending well life, and lowering operational cost [Cha12, Fin10, Wod11, Yu12]. Traditional wireline well monitoring involves lowering long cables with integrated sensors into the wellbore [Ell07]. However, wired monitoring systems are bulky, costly, difficult to operate and maintain, and are often limited in maximum depth of the well to which they can be extended. Unlike wired approaches, untethered, autonomous microsystems can provide distinct advantages in seamlessness of usage, cost, and scalability and in reaching greater reservoir depths, thus providing better access to horizontal wellbores and fractures. As illustrated in Fig. 1.7, often these

autonomous environment logging microsystems can be deployed into wellbores in large numbers using a fluid medium, to continuously record well data and location. The microsystems are later pumped out of the well and interrogated for the recorded data.

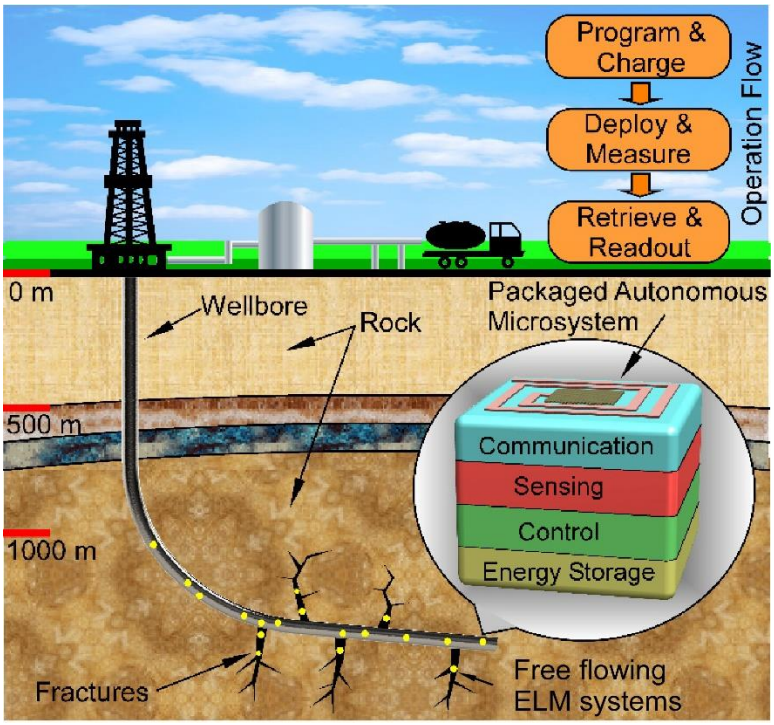



Fig. 1.7: Illustrated deployment of free flowing ELM systems in borehole fractures (ELM systems are shown using yellow dots); duplicated from [Sui17].

There has been limited prior work on microsystems for downhole environmental monitoring. A summary of prior microsystem work for downhole applications has been provided in Table 1.5. The University of Tulsa and Saudi Aramco have investigated a research prototype using customized electronic chips encapsulated in a ø8 mm polymer sphere which monitors temperature and pressure in downhole environments [Yu12, Shi15]. The system successfully operated in a wellbore for 1 hour at temperature up to 115°C and pressure up to 69 MPa. However, the system had a short lifetime, limiting maximum deployment intervals, and high density, which may cause problems in system recovery. OpenField$^{TM}$ Technology investigated a pressure and temperature micro recorder for drill stem testing encased in an Inconel shell [Ope14]. The system's

large size, wired communication, and high density however may limit its deployment in smaller wellbores.

Table 1.5: Summary of prior microsystem work for downhole applications [Vel22].

| Work | Density [g/cm$^3$] | Package | $H_2S$ Compat? | Size [mm] | Diag. [mm] | IMU[#] | Comm. | Life [hrs] | Battery Recharge | Max. Pres. [MPa] | Max. Temp. [°C] |
|---|---|---|---|---|---|---|---|---|---|---|---|
| [Ope14] | >2 | Inconel | Yes | ø19×184 | 185 | N | USB (Wired) | 24 | No | 100 | 150 |
| [ING21] | 0.6-2.0 | HDPE | Yes | ø57 | 57 | MAG | --- | 24 | --- | 10 | 60 |
| [Ser17] | 0.9 | Syntatic Foam | No | ø43 | 43 | N | Wired | 10 | Wired | 10 | 100 |
| [Buz20] | 0.9 | Syntatic Foam + Plastic | No | ø64×66 | 92 | N | Inductive Coupling (Wireless) | 4 | Wireless | 24 | 100 |
| [Yu12, Shi15] | --- | --- | --- | ø8 | 8 | N | Magnetic (Wireless) | 1 | Wireless | 69 | 115 |

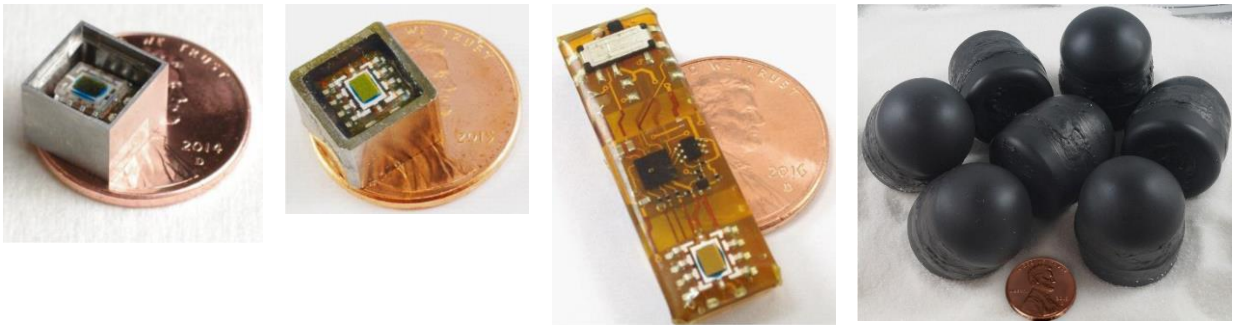
---: *Data not provided*

#: M: *Magnetometer*, A: *Accelerometer*, G: Gyroscope, N: *None*

For application in energy well logging, multiple considerations must be accounted for in designing a pressure logging microsystem. Small form factors to access narrow fractures, sufficient full-scale range of pressure measurement (up to 70 MPa preferred), endurance to high temperature (up to 150°C preferred), and immunity to harsh chemical environments (containing high concentrations of brine and $H_2S$) are required for such a microsystem. Other capabilities which increase the microsystems usefulness include geolocation monitoring, nanowatt power budget for extended system lifetime, wireless power transfer and communication, and high resolution continuous sensor data logging.

Previous Environmental Logging Microsystems (ELM1, ELM2, ELM3 and ELM7) were designed for downhole monitoring application to monitor data in high-temperature, high-pressure and high-salinity subsurface environments, such as the wellbore of an oil well [Vel20]. These microsystems had data logging capabilities and were intended to be retrieved after data collection

for interrogation by the client. ELM1-3 systems used optical methods for charging and communication while ELM7 used resonant inductive Qi-charging for power transfer and a Bluetooth Low Energy (BLE4.0) platform for wireless communication. All systems consisted of off-the-shelf electronic and battery components that were compatible with assembly on a rigid or flexible printed circuit board (PCB). Fig. 1.8 shows pictures of the packaged ELM systems.



(a) (b) (c) (d)

Fig. 1.8: Packaged ELM systems (a) ELM1; (b) ELM2; (c) ELM3; and (d) ELM7 [Ma16, Sui17, Vel20].

ELM1-3 systems focused on reducing the exterior dimensions of the packaged systems, resulting in a final volume of <1 $cm^3$; however, the systems exhibited a limited lifetime (<1 day) due to the use of a small coin cell battery. The ELM7 microsystems increased in size to approximately ø30 x 35 $mm^3$ in order to reduce overall density to <1.2 $g/cm^3$ and improve lifetime through the use of a larger battery. However, during field trials, these systems could only operate up to 85°C, exhibited issues with the packaging, and had a larger than desired standby current which reduced lifetime. Table 1.6 presents a summary of the prior ELM generations.

Table 1.6: Summary of previous generations of ELM [Ma16, Sui17, Vel20].

| Features | ELM1 | ELM2 | ELM3 | ELM7 |
|---|---|---|---|---|
| Pressure logging | No | Yes | Yes | Yes |
| Pres. range [MPa / psi] | - | 50 / 7200 | 50 / 7200 | 42 / 6092 |
| Theoretical Pres. resolution [kPa / psi] | - | 2 / 0.3 | 2 / 0.3 | 0.5/0.07 |
| Operated Temp. range [°C] | 25 - 125 | 25 - 125 | 25 - 125 | 25 - 85 |
| Communication | LED | LED | LED | BLE4.0 |
| Battery recharging | Optical | Optical | Optical | Resonant inductive (Qi) |
| Standby current [μA] | 12 @ 125°C | 12 @ 125°C | 12 @ 125°C | 400 @ 85°C |
| Max stored data points | 1270 | 1270 | 1270 | 4200 |
| Lifetime [hours] | 12 @ 125°C | 24 @ 125°C | 24 @ 125°C | 96 @ 85°C |
| Unpackaged system dimensions [mm] | 6.5 × 6.3 × 4.5 | 6.5 × 6.5 × 5.8 | 8.8 × 8.6 × 7.2 | ø27 × 1.5 |
| Packaged system dimensions [mm] | 8.9 × 8.9 × 6.85 | 9.5 × 9.5 × 6.5 | 29 × 8.8 × 3.0 | ≈ø30 × 35 |

## 1.4 Research Goals and Objectives

This work is aimed at investigating critical elements of building easily volume scalable, low-cost, and modular sensing microsystems with application in the energy industry. The energy industry presents many different pressure sensing opportunities across its different production sectors, with different sets of design challenges and application requirements. The primary research goals of this work are the following:

1. Investigate new system and packaging technology in deploying multiple pressure sensor nodes in a space constrained chemical environment, to measure very low pressure gradients induced by transport of fluid through a porous material, over a large baseline pressure, with application in core flood experiment.
    a. Achieve pressure measurement across full-scale range up to 20 bar (2 MPa), with a preferred measurement resolution of <1 mbar (100 Pa).

b. Design sensor nodes and system electronics to preferably withstand a large baseline pressure of up to 250 bar (25 MPa or 3,625 psi) and operating temperatures up to 125°C in fluid saturated environments such as synthetic oil, 15% brine, organic solvents, and/or gas.

c. Sensor nodes must preferably remain $\leq$ø15 x 3 $mm^3$ to ensure rock core remains flush with the sheath and no leakage flow paths exist along the rock boundary.

d. Investigate methods to interface between sensors and readout electronics placed across a polymer sheath.

    i. Study a wired feedthrough technology to provide lead transfer across a large pressure difference up to 25 MPa preferred.

    ii. Investigate a passive wireless inductive-capacitive (LC) based transduction approach to interrogate untethered pressure sensor nodes across a 5 mm thick polymer sheath housing the rock core inside a test cell.

2. Investigate design methodology and investigate pathways to maximize pressure measurement resolution of a LC Sensor with design constraints governed by the specific application requirements.

3. Investigate system level design challenges in dimensional scaling, relationship between building blocks, and environment specific performance limits of an autonomous environment logging microsystem for downhole application.

    a. Achieve functional full-scale pressure measurement range of 50 MPa (500 bar) with preferred operating temperatures up to 150°C.

    b. Investigate challenges in microsystem hardware/software codesign and operating modality to permit continuous recording of multiple sensing parameters such as

pressure (preferably with <1.5 kPa resolution), temperature (preferably with 0.1°C resolution), inertial measurement data (at >10 Hz frequency to extract meaningful geolocation information) while having a low standby current consumption (<0.5 µA @ 25°C preferred to ensure system shelf life is primarily limited by self-discharge of primary battery).

4. Investigate an autonomous ELM package (maximum diameter <ø45 mm) to enable deployment into narrow wellbores with the following features:
    a. Achieve density-matched package buoyancy (<1.5 g/cm$^3$) to allow free flowing deployment, retrieval, and reusability of the system.
    b. Allow low energy wireless communication and wireless power transfer for secure access to recorded sensor data upon retrieval and incorporate battery power conservation methodologies during system interrogation and storage.
    c. Be capable of preserving all sensor and system functionalities while providing protection to system in a high pressure high temperature (HPHT) and chemically harsh environment (15% brine, raw diesel fuels, methane, and $H_2S$ concentration up to 2,500 ppm).

Goal 1 has been addressed in Chapters 2 and 3, goal 2 has been addressed in Chapter 4, and goals 3 and 4 have been jointly addressed in Chapter 5 of this dissertation.

The functional thresholds and preferred targets of this dissertation are summarized in Table 1.7.

Table 1.7: Design targets of this dissertation.

| Goals | Tasks | Parameters | Functional Threshold | Preferred Target |
|---|---|---|---|---|
| Design in situ distributed pressure measurement microsystem to record pressure gradients and flow characteristics along the seam of a rock core | Investigate system hardware, automation, and integration strategies | Max. operating pressure | 150 bar (15 MPa) | 250 bar (25 MPa) |
| | | Max. operating temperature | 100°C | 125°C |
| | | Max. full-scale pressure measurement range with offset | 10 bar (1 MPa) | 20 bar (2 MPa) |
| | | Pressure measurement resolution | <10 mbar (1 kPa) | <1 mbar (100 Pa) |
| | Investigate wired feedthrough sensing technology | Upper limit of feedthrough pressure difference | 150 bar (15 MPa) | 250 bar (25 MPa) |
| | Investigate passive wireless LC sensing technology | Max. LC Sensor package thickness | 4 mm | 3 mm |
| | | Max. LC Sensor package diameter | ø20 mm | ø15 mm |
| Design of an autonomous environment logging microsystem for downhole monitoring application | Investigate system level design challenges, and performance limits | Max. operating pressure | 400 bar (40 MPa) | 700 bar (70 MPa) |
| | | Max. operating temperature | 100°C | 150°C |
| | | Pressure measurement resolution | <70 mbar (7 kPa) | <15 mbar (1.5 kPa) |
| | | Max. standby current | <5.0 µA @ 25°C | <0.5 µA @ 25°C |
| | | Min. deployment lifetime | 5 days (100°C) 1 day (150°C) | 10 days (100°C) 2 days (150°C) |
| | Investigate an autonomous ELM package | Packaged system diameter | <ø45 mm | ø25 mm |
| | | Packaged system volume | <48.0 $cm^3$ | 8.2 $cm^3$ |
| | | Packaged system density | <1.5 $g/cm^3$ | 1.0 $g/cm^3$ |

## 1.5 Organization of Dissertation

This dissertation is arranged into six Chapters. Chapter 1 introduces the topics, including the pressure sensing market ecosystem, the different challenges of pressure sensing in space constrained applications and specific requirements of sensing microsystem based on application domain. The broad opportunities for deploying a pressure sensing microsystem in different sectors of the energy industry has been highlighted. This work focuses on the analytics and upstream

sectors of the energy industry in further detail, where the background, prior work, challenges and opportunities in designing a pressure sensing microsystem for core-flood experiment and down-hole environment applications has been discussed.

Chapter 2 describes the design and implementation of the first high-resolution distributed pressure measurement system for core-flood experiments (DPSCore). A series of microfabricated pressure sensors are embedded in bolts at the seam of the rock core along its length for in situ measurements. A feedthrough technology has been investigated to provide lead transfer between the sensors and system electronics across a 230 bar (23 MPa) pressure difference, and an anneal protocol has been studied to address variations resulting from assembly stress. The system has been successfully tested in an in-house custom-made distributed pressure test setup as well as in corporate core-flood testing facilities at TOTAL S.A. (Pau, France) with flooding fluids such as synthetic oil and/or gas. Pressure measurements have been recorded over a full-scale range of 20 bar (2 MPa) with a resolution as small as 0.3 mbar (30 Pa).

Chapter 3 introduces a passive LC tank based wireless sensing approach (LC Sensor) for distributed pressure gradient measurement in core flood experiments. The investigated pressure gradient measurement (PGM) system has been successfully tested over the full-scale pressure range of 20 bar (2 MPa), and temperature up to 125°C. A packaging and integration methodology for the LC Sensor has been evaluated for sensor application in a high temperature chemical environment. A custom test setup was built to provide pressure differentials during fluid flow, the microsystem was integrated into this setup and demonstrated a pressure resolution of <1 mbar (100 Pa).

Chapter 4 discusses an LC Sensor design methodology to maximize pressure measurement resolution. A figure of merit, termed Design Optimization Factor (DOF), for LC Sensors has been

analytically derived to maximize overall LC Sensor performance in context of this application. The proposed design optimization approach has been experimentally verified. Physical design parameters which impact sensor input impedance magnitude has been studied. The impact of readout circuitry design and frequency sweeping factors on LC Sensor resolution has been discussed.

Chapter 5 introduces the design and integration methodology of an environment logging microsystem (ELM) to support downhole monitoring applications up to 150°C. Microsystem hardware, and software controls have been codesigned to measure pressure over a full-scale range of 50 MPa with 0.5 kPa measurement resolution, alternatively using a capacitive and a piezoresistive pressure sensor. In addition, the system is capable of continuously recording temperature (with 0.1°C resolution), acceleration, magnetic field (at a frequency of >10 Hz) for geolocation. A power management module has been investigated to cut down standby current and eliminate use of the system's primary battery in presence of Qi wireless power, i.e., in all operating scenarios other than during downhole deployment. Challenges in design of a HPHT, and flow compatible packaging methodology for the ELM system for downhole deployment in narrow wellbores has been investigated.

Chapter 6 provides the conclusions from this dissertation, summarizes major contributions, and proposes future work.

The following references used across this work carry the understated assumptions: high temperature (HT) is any temperature above 100°C, low pressure (LP) is any pressure between 0 and 2 MPa, and high pressure (HP) is any pressure above 20 MPa.

# Chapter 2: Distributed Pressure Measurement Microsystem for Core Samples with Feedthrough Technology

This Chapter describes the design and implementation of an *in situ* high-resolution **D**istributed **P**ressure measurement **S**ystem for **Core**-flood experiments (DPSCore) [Dut19]. Investigation of the transport of fluids through porous rocks in core-flood experiments is pursued in several areas of science with promising applications in geology, hydrogeology and petroleum engineering [Ott12]. Fluid flow in the pressurized rock core in a typical core flood experiment setup introduces small pressure gradients along its length, providing information on the permeability of the rock core at various pressure and temperature conditions [Gil94]. While current core flood experiment setups allow for pressure measurements only at the inlet and outlet of the rock core assembly; with additional pressure measurement capability along the entire length of the rock core, more insight into the geological sample and the energy reservoir may be obtained. Furthermore, these measurements shall make the core flood experiment more efficient, with increase in ability of an early detection of experiment failure, as well as protect from time and monetary losses. Previously reported core flood studies have used X ray CT scan to obtain fluid saturation and rock porosity information [Pin13]. However, this approach is expensive, does not enable continuous data collection, and requires a large space to house the equipment. This Chapter describes the system design and integration concepts of the DPSCore system to perform pressure measurements along the length of a rock core using a wired feedthrough technology.

## 2.1 System Concept and Design

The system concept of the high-resolution distributed pressure measurement system utilizing a wired feed-through technology for core-flood experiments is shown in Fig. 2.1. A typical test cell used for the core-flood experiments houses a rock core sample pressurized in a polymeric sheath. The interior of the sheath is labelled as the low pressure (LP) chamber; the pressure here can be up to 20 bar. This sheath is located within an oil bath in a high pressure (HP) chamber, where pressure and temperature levels can be as high as 250 bar and 125°C, respectively [Puy17]. The polymer sheath isolates the rock core from an oil bath within the HP chamber. A gaseous or liquid phase fluid is transported through the rock core in the LP chamber in the longitudinal direction; these permeability experiments can continue for up to three months in duration. The DPSCore measurement system consists of four sets of a pressure sensor, a reference capacitor, and a capacitance to digital converter (CDC) on a flexible printed circuit board (PCB) backbone. A Raspberry Pi based external unit serially communicates with the four CDCs through a multiplexer, while wirelessly interfacing with a user interface running on a computer.

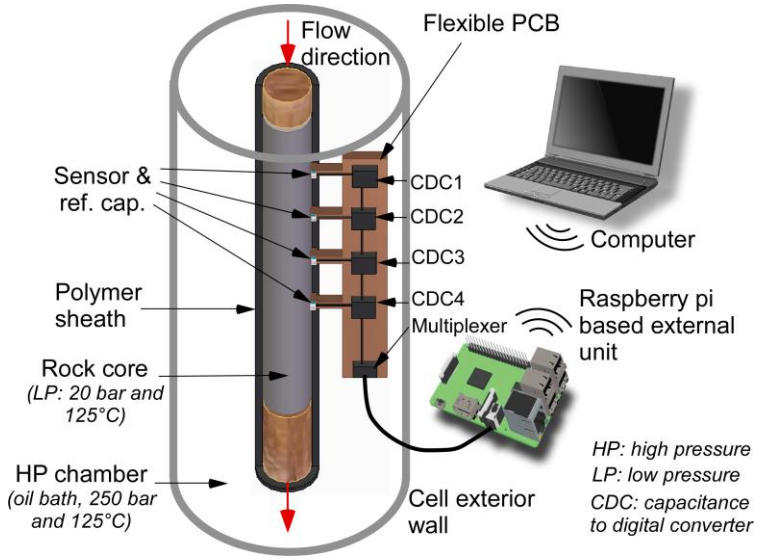



Fig. 2.1: Concept diagram for the distributed pressure measurement system utilizing a wired feed-through technology for core-flood experiments.

### 2.1.1 System Hardware

The measurement system consists of a flexible printed circuit board (PCB), an external readout unit based on the Raspberry Pi® (Raspberry Pi 3, Raspberry Pi Foundation, UK), and a remote computer. The flexible PCB includes four pressure sensors located on tabs and interface electronics located along a backbone. The sensors on the PCB tabs are positioned along the length of the rock core within feedthroughs in the polymeric sheath, whereas the electronics on the backbone of the PCB are in the HP chamber. Another feedthrough on the exterior cell wall connects the flexible PCB to an external readout unit based on Raspberry Pi (R-Pi), which reads and records sensor data through an $I^2C$ bus and provides power to the flexible PCB. Upon request, the recorded data is wirelessly transferred from the external readout unit through a Wi-Fi network to a remote computer for data processing and user interfacing. The preferred performance targets of the measurement system are listed in Table 2.1.

Table 2.1: Preferred performance targets for DPSCore system.

| **Pressure Measurement Targets** | |
|---|---|
| Resolution | <1 mbar (100 Pa) |
| Full-scale range | 20 bar (2 MPa) |
| Measurement duty cycle | A few minutes per day |
| **Operating Environment Conditions** | |
| Temperature | 20°C - 125°C |
| Pressure (electronics) | Up to 250 bar (25 MPa) |
| Fluids | Synthetic oil, and/or gas |

Commercial off-the-shelf (COTS) components and standard manufacturing practices were chosen to reduce cost and enhance scalability of the proposed solution. Important system components, including the microsensor and CDC have been discussed below.

*Microsensor:*

A variety of microscale pressure sensing technologies have been explored in the past five decades, of which the most widely used are piezoresistive and capacitive pressure sensors [Gia06]. Although piezoresistive sensors have low output impedance enabling larger flexibility in sensor readout circuit design and sensor placement relative to the readout electronics, these sensors typically have large dimensions and exhibit high temperature coefficients, which are both undesirable for this application. The smallest commercially available capacitive pressure sensor is the Murata SCB10H-B250 (Murata Manufacturing Co., Ltd., Japan), shown in Fig. 2.2; it provides a full-scale pressure range of 25 bar. The capacitance change over the full-scale pressure range is 6.6 pF (with an offset capacitance, $C_0$, of 7.3 pF) [Mur13]. The operating temperature range is -55°C to 125°C. The sensor has dimensions of 1.4×1.4 ×1.0 $mm^2$. These characteristics (e.g. full-scale pressure and temperature range) are suitable for this application; therefore, the Murata SCB10H-B250 sensor was chosen.

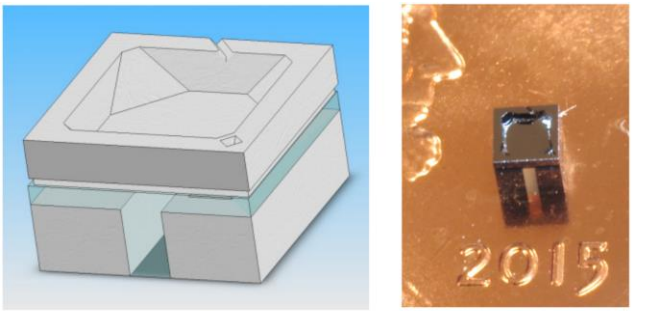



Fig. 2.2: (left) 3D drawing [Mur13] and (right) photo of the commercial Murata SCB10H capacitive pressure sensor.

*Capacitance-to-Digital Converter (CDC):*

In order to interrogate the capacitive pressure sensor, a CDC is required to convert capacitance change to a more easily digitizable signal. A broad investigation of commercially

available miniature CDC chips was performed. Three of the most suitable options were identified and examined, shown in Table 2.2 [Ana05, Fdc15, Sil14]. The theoretically estimated pressure resolution of the Murata SCB10H sensor, when used with each CDC chip, has been given in Table 2.3. The Analog Devices AD7746 (Analog Devices Inc., USA) was selected as it has a peak-to-peak noise limited resolution of 0.1 fF/code, the highest among all commercially available CDC chips. The chip has an input capacitance range of ±4 pF and programmable offset capacitance of up to 17 pF, allowing the actual input capacitance to vary between 0–21 pF. The chip has an integrated temperature sensor with a 0.1°C resolution that can be used for temperature compensation of the measurement system. The operating temperature range of the CDC is -40°C – 25°C. The size of the chip is 6.4 × 5.0 × 1.2 $mm^3$. The data output of the CDC chip can be retrieved through an $I^2C$ standard communication bus.

Table 2.2: Summary of three miniature high resolution CDC chips for capacitance conversion.

| | Silicon Labs C8051F990 | Texas Instruments FDC1004Q | Analog Devices AD7746 |
|---|---|---|---|
| Resolution (ENOB[#]) | 16 bits | 16 bits | 21 bits (p-p: 16.3 bits*) |
| Resolution (fF/code) | 1 fF/code | 0.5 fF/code | 4 aF/code (p-p: 0.1 fF/code*) |
| Input capacitance range of CDC | 45 pF | 30 pF | 8 pF (programmable $C_0$ offset of ≤21 pF) |
| Operating Temperature | -40 – 85°C | -40 – 125°C | -40 – 125°C |
| Embedded temperature sensor | Yes | No | Yes |
| Footprint | 4 x 4 $mm^2$ | 3 x 3 $mm^2$ | 6.4 x 5.0 $mm^2$ |

[#] *ENOB: Effective number of bits.*
** Resolution values limited by peak-to-peak (p-p) noise.*

Table 2.3: Comparison of estimated p-p pressure resolution when using the Murata SCB10H-B250 pressure sensor with the three identified CDC chips.

| | Silicon Labs C8051F990 | Texas Instruments FDC1004Q | Analog Devices AD7746 |
|---|---|---|---|
| CDC resolution (fF/code) | 1 fF/code | 0.5 fF/code | 0.1 fF/code |
| Pres. resolution @ 1 bar, 1.2 fF/kPa | 8.3 mbar | 4.2 mbar | 0.83 mbar |
| Pres. resolution @ 20 bar, 4 fF/kPa | 2.5 mbar | 1.3 mbar | 0.25 mbar |

*Flexible PCB:*

As shown in Fig. 2.1, the PCB consist of a main body along with four narrow tabs, each of which contain a pressure sensor and reference capacitor at the distal tip of the tab. The reference capacitor is used to compensate any common mode noise or parasitic capacitance in the measurement. The AD7746 CDC chip is located on the main PCB near each tab for capacitance readout. The tabs are designed to be curved and inserted into the holes on the polymer sheath so that the tip of the side strip can reach the rock core surface for pressure measurement. An $I^2C$ multiplexer (LTC4306, Linear Technology Corp., USA) [Lin05] is used to switch between each CDC to permit data to be recorded from the each sensor tab (e.g. sensor channel). Fig. 2.3 shows the PCB circuit schematic of the DPSCore system. The flexible PCB is powered through the power output port of the Raspberry Pi (Vcc and Gnd), which provides an output voltage of 3.3 V and up to 50 mA current. The $I^2C$ multiplexer typically consumes a current of 5.2 mA (maximum 8 mA) and each CDC chip typically consumes 0.7 mA, resulting in a total current consumption of $6.6 \pm 1.4$ mA + (0.7 mA × 4) = $9.4 \pm 1.4$ mA, which is well within the driving current limit of the Raspberry Pi. The 4 wires in the cable between the Raspberry Pi and the flexible PCB are for Vcc, Gnd, SCL and SDA. The latter two are clock and data lines of the $I^2C$ bus.

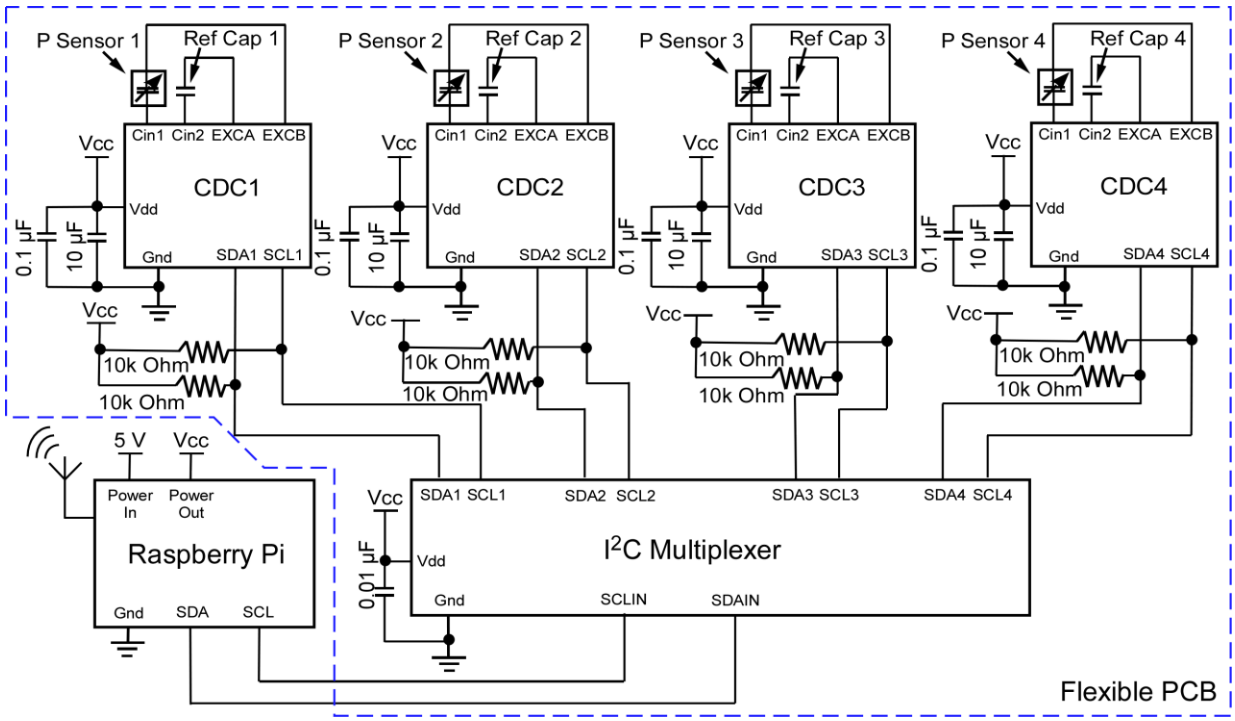



Fig. 2.3: DPSCore flexible PCB circuit schematic.

Fig. 2.4 shows the layout of the flexible PCB with four side strips. The magnified view shows the details of the layout for one of the side strips. The dimensions of the main PCB as well as the side strips are listed in the table embedded within the figure. The separations between side strips (L2, L3, and L4) are chosen to be 50.3 mm. A variation of up to ±1 mm in the separations between insertion holes on the sheath can be accommodated by slightly bending the flexible PCB as needed when inserting the side strips into the holes.

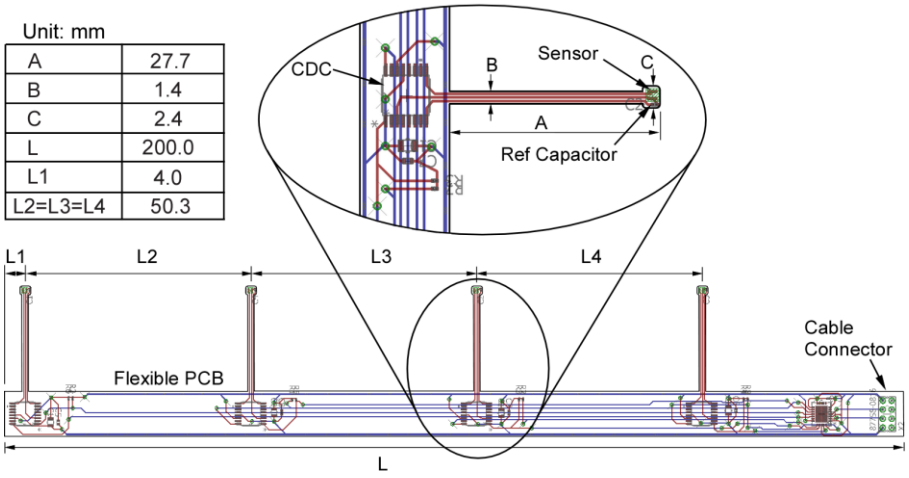



Fig. 2.4: Flexible PCB layout.

*Feedthrough:*

As shown in Fig. 2.1, pressure sensors record data from the surface of a rock core placed inside a polymer sheath while the PCB main body resides outside the polymer sheath in the high pressure chamber. The pressure difference across the polymer sheath is ≈230 bar (23 MPa or 3,335 psi). A customized feedthrough is necessary to provide lead transfer between the sensor and the interface electronics through the polymer sheath. The polymer sheath normally incorporates steel nuts that are sealed with steel bolts. The steel bolt must be perforated to allow the PCB side strip to be inserted into the LP chamber. Fig. 2.5 shows the design of the side strip and how it has been bent and inserted into the perforation drilled in the steel bolt. The distal end of the side strip with the pressure sensor and reference capacitor has been bent 90° to orient the sensing surface to face the LP chamber. To ensure that the sensing tip of the PCB side strip is accurately folded and held firmly at this 90° angle, the requirement of a support structure inside the through-hole is deemed necessary. Built using 3D printing technique, this support structure (3D printed plug) acts as a platform to the sensors (Fig. 2.5), and a long-slit structure designed along the length of this 3D printed plug is optimized to enhance the seal between the two pressure chambers by allowing easy epoxy application during system integration without contaminating the pressure sensor diaphragm.

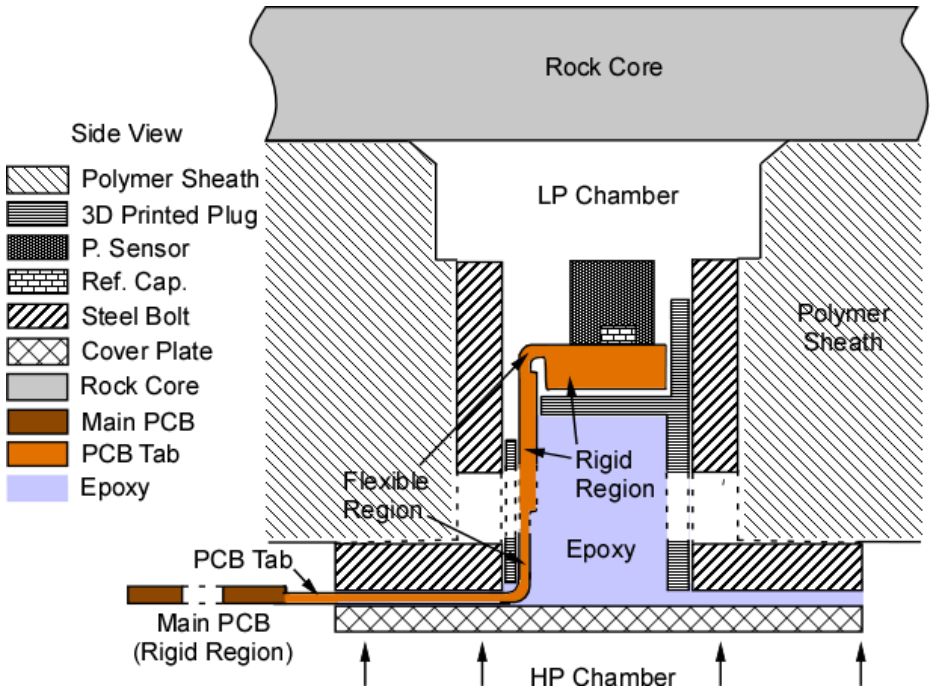



Fig. 2.5: Cross sectional view of the LP-HP chamber feedthrough, showing perforated steel bolt with PCB tab.

### 2.1.2 System Software

Software was designed using Python programming language for the external computer (R-Pi, Raspberry Pi 3, Raspberry Pi Foundation, UK) to retrieve sensor data. The flowchart for the designed software is shown in Fig. 2.6. The software executing on the R-Pi sequentially triggers different CDC chips through the $I^2C$ multiplexer to retrieve individual pressure sensor, reference capacitor, and temperature sensor data. The collected data is then locally stored, processed, and shared over a wireless network or uploaded online to a cloud-based server for remote retrieval. The R-Pi is programmed to interface wirelessly with a remote laptop running a graphical user interface (GUI) for command and data transfer.

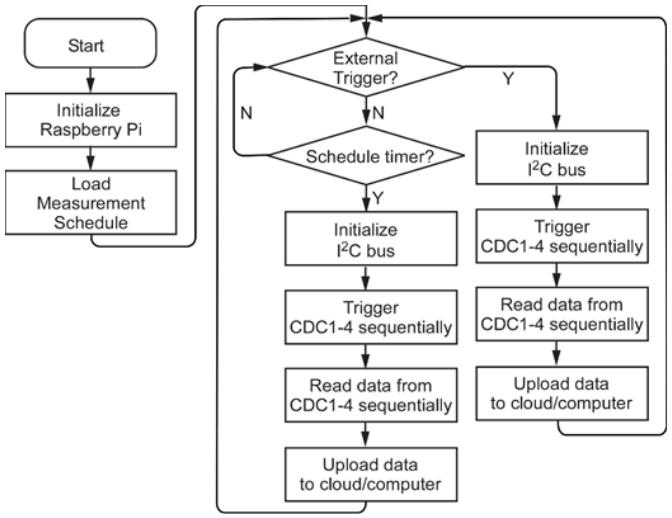



Fig. 2.6: Software flowchart for external computer.

A snapshot of the designed GUI[1] on the remote laptop while in operation is shown in Fig. 2.7. The interface allows the user to remotely manage the DPSCore system, start and stop scheduled measurement, request an instant measurement, update calibration coefficients, retrieve sensor data from cloud storage and plot both sensor capacitance and pressure data in real time.

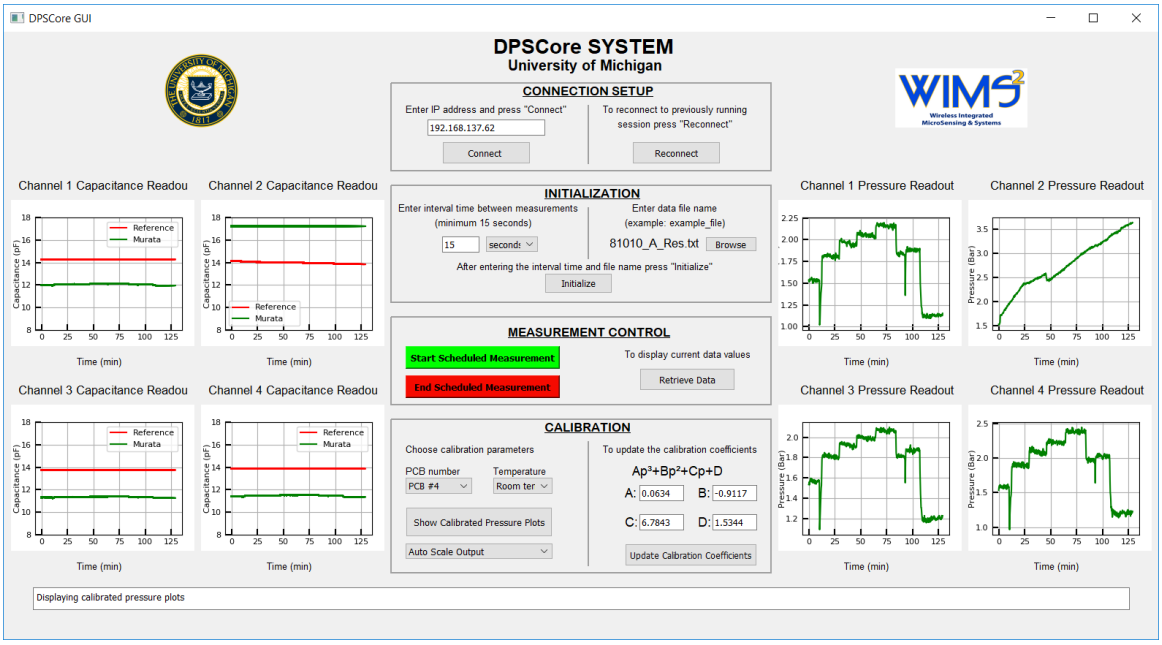



Fig. 2.7: A snapshot of the DPSCore user interface during system operation.

[1] GUI was developed with contribution from Mr. Aditya Varma Muppala, ECE, University of Michigan.

## 2.2 System Implementation

*PCB Fabrication:*

The flexible PCB uses standard flexible polyimide as the substrate material (Flex PCB, Santa Ana, USA). The layer composition of the substrate can be adjusted within selectable options, and the selections for the DPSCore flexible PCB are shown in Fig. 2.8. The regions of the PCB where components are attached need to be more rigid and have a larger thickness by using an extra stiffener layer; these regions are labelled "rigid region". The stiffener layer has a thickness of either 20 mil or 5 mil (1 mil = 1/1000th inch = 25.4 µm) depending on the size of the region and the types of components to be mounted, giving a total thickness of 32.8 or 12.8 mil (833 or 325 µm) for the rigid region. The regions of the PCB that will be bent and folded do not have the stiffener layer, and have a total thickness of 6.8 mil (172.7 µm); these regions are labelled "flexible region."

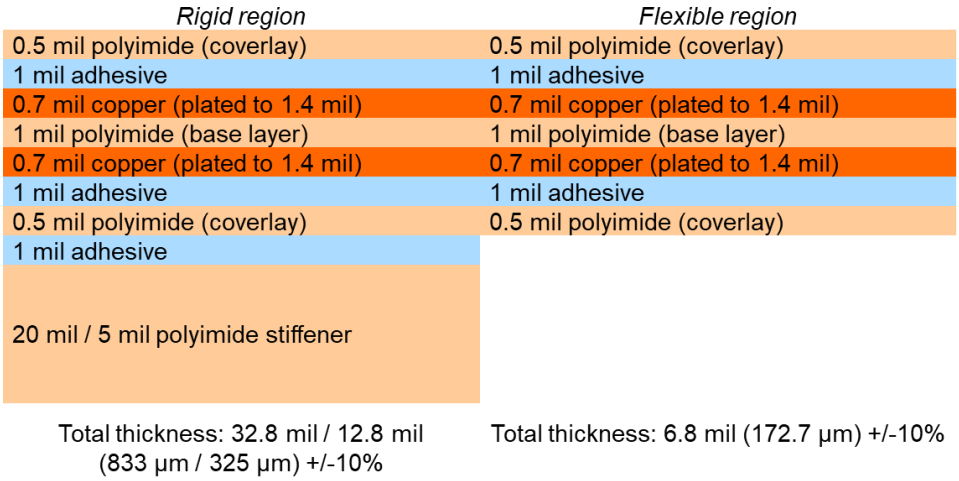



Fig. 2.8: Design of flexible PCB layers for rigid region (left) and flexible region (right).

In the DPSCore flexible PCB design, there are two flexible regions, both on the tabs: one near the tip and one beside the main PCB as shown in Fig. 2.5. All other regions of the flexible PCB are rigid regions, including the main PCB (5 mil thick stiffener), center portions of tabs (5 mil thick stiffener), and the tips of tabs (20 mil thick stiffener). Fig. 2.9 shows a picture of the commercially fabricated DPSCore PCB (Flex PCB, Santa Ana, USA).

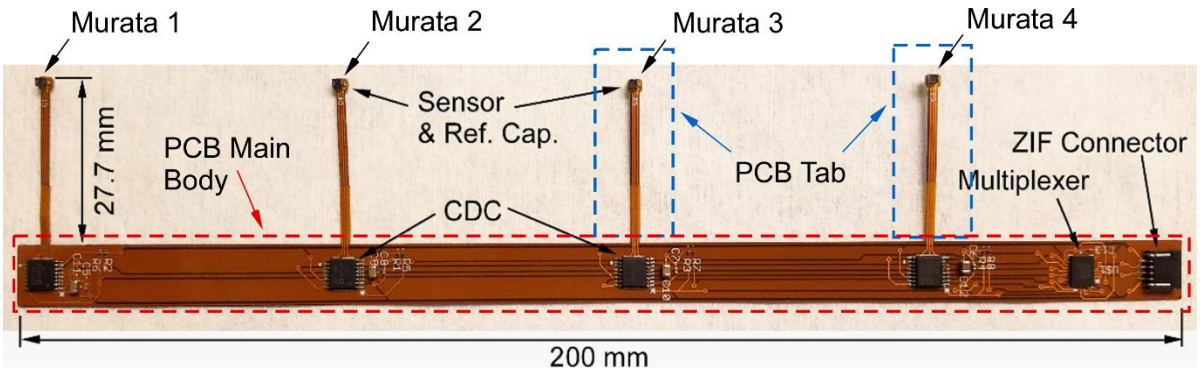
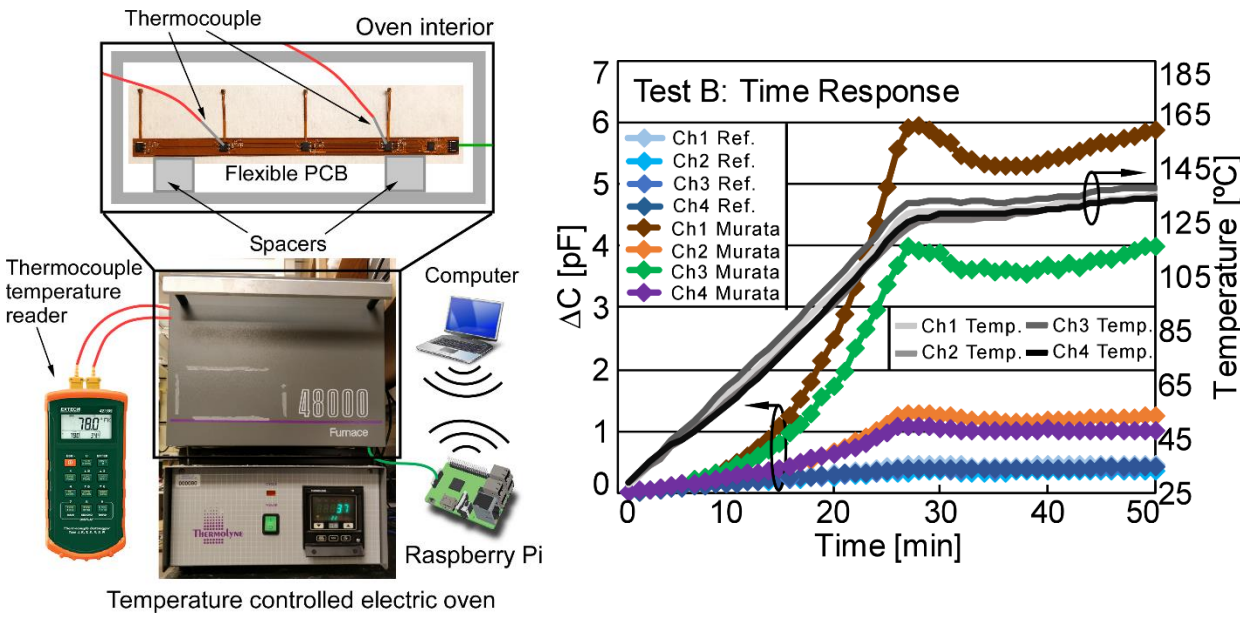



Fig. 2.9: DPSCore flexible PCB post fabrication.

*Anneal to Reduce System Temperature Dependence:*

To perform temperature characterization at atmospheric pressure, the fabricated DPSCore PCB was suspended inside a PID temperature controlled oven and the oven temperature is ramped up to 125°C at a constant rate of 3°C/min. The oven temperature was then held at 125°C for 20 min following which the system is air-cooled back to room temperature. All four Murata sensor capacitive responses are constantly recorded through the experiment. The temperature dependance characterization test setup has been shown in Fig. 2.10(a). Over the experiment at constant atmospheric pressure shown in Fig. 2.10(b), there is a large variation in the capacitive output (ΔC response) amongst the four Murata sensors with ΔC variation up to 6 pF at 125°C for channel 1 Murata, which is comparable to the 6.6 pF full-scale response of the Murata pressure sensor over their full-scale pressure of 20 bar. The variation in ΔC response of the four reference capacitors were low (<0.5 pF at 125°C) and overlapped with each other, thus verifying the observed variability in Murata sensor response was from the sensor and not from the readout electronics. This large variability in baseline capacitance of four pressure sensors, when subjected to the same elevated temperature at atmospheric pressure, presented a research opportunity to understand and address thermal stress in diaphragm-based pressure sensors.




(a) (b)

Fig. 2.10: (a) Temperature dependance characterization test setup; (b) Variation of ΔC response with temperature at constant atmospheric pressure for all 4 sensing channels.

A detailed theoretical study and modelling of the Murata pressure sensor package in COMSOL Multiphysics® (COMSOL Inc., USA) was performed. The materials used to realize the model as shown in Fig. 2.11(a) and (b) were silicon and glass for sensor package, solder (Young's modulus: 10 GPa, Poisson's ratio: 0.4, CTE: 21.0 ppm/°C), polyimide and copper for flexible PCB. Study of thermal stress formed at several key nodal locations of the sensor package revealed that the thermal response of the system is significantly affected by residual stress in the solder joints that bonds the sensor contacts to the metal pads on top of the flexible PCB. Solder when applied manually and when heated to varying temperatures on cool down produces varying stress characteristics which results in varying thermal dependence of the baseline capacitance for different pressure sensors. As shown in Fig. 2.11(c), the modelled thermal stress reaches a maximum of 67.5 MPa near the sensor diaphragm at 125°C thus gravely affecting sensor diaphragm operation.

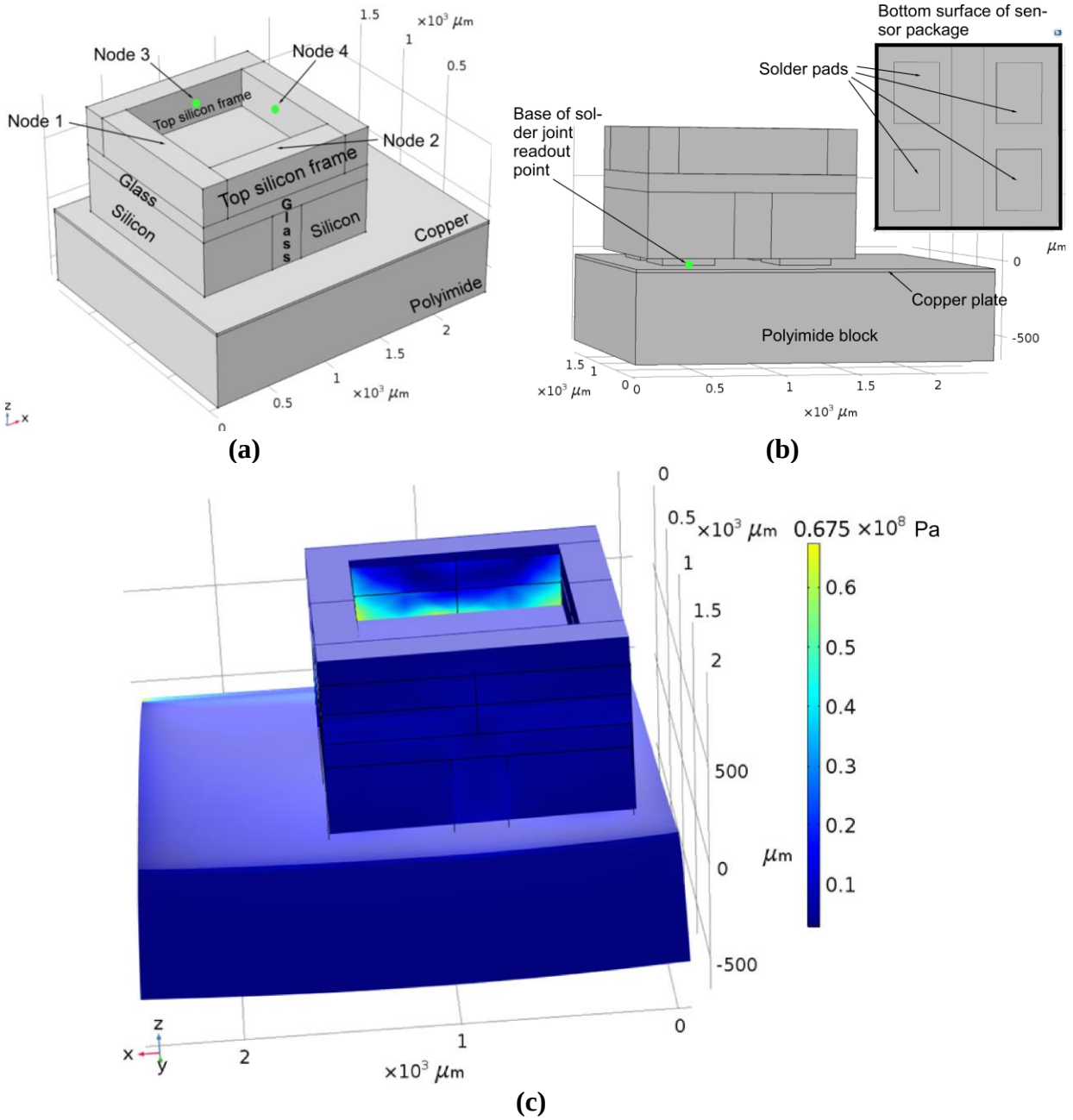



Fig. 2.11: (a) 3D view of COMSOL model for Murata sensor package assembled on flexible PCB substrate; (b) bottom and side view of sensor model; (c) Modelled thermal stress results at 125°C showing a maximum stress of 67.5 MPa near sensor diaphragm.

To reduce the residual thermal stress in sensor package, an anneal protocol has been investigated. The DPSCore system is suspended inside a tightly sealed oven. The oven temperature is ramped up to 170°C at a constant rate of 3°C/min and then held for 5 hr at 170°C. After this step, the system is slowly air cooled over an additional 5 hr duration. The high temperature is

enough to soften the solder bonds and the gradual cooling releases majority of the residual stress from the joints. The improvement in sensor baseline capacitance ($\Delta C_{Murata}$ - $\Delta C_{Ref.}$) measured at 125°C across the 4 sensor channels with anneal duration (in hours) is shown in Fig. 2.12. The large sensor response variations (≈6 pF) across the 4 channels, after undergoing 5-6 hours of anneal, show up to 10-fold reduction in capacitance response with all 4 channel responses overlapping each other. These lower and predictable thermal responses are highly desirable to establish any temperature calibration methodology for system deployment in high temperature applications. Notably the post-anneal thermal responses were consistent across different units.

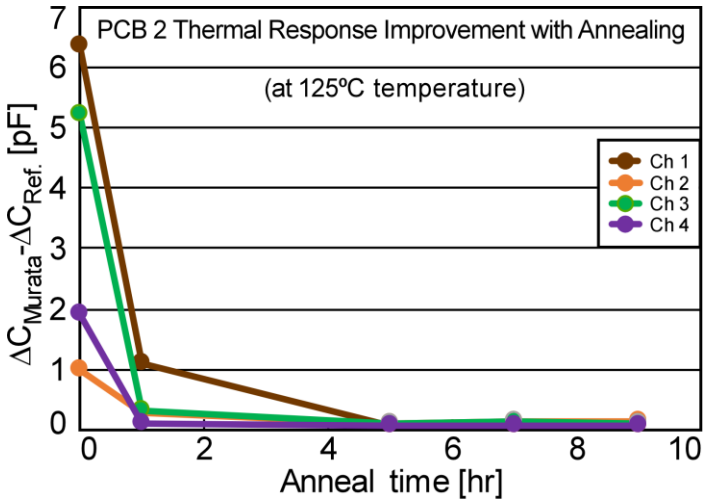



Fig. 2.12: Improvement in sensor baseline capacitance at 125°C with anneal time (in hours).

*Feedthrough manufacture and integration:*

As described in previous section, the tabs of the flexible PCB are inserted into perforations drilled through steel bolts which are mounted on the polymer sheath. A high-speed steel round-shank reamer (McMaster #2777A19) with 3.193 mm diameter was used to perform the perforation and leave a smooth surface finish. The lateral surface of the bolts was protected by epoxy coating during this procedure. A perforated bolt is shown in Fig. 2.13. The diameter of the perforation $d_H$ is 3.2 mm.

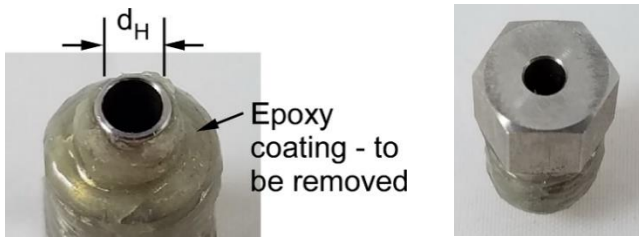



Fig. 2.13: Through hole drilled in the steel bolt. The hole diameter $d_H$ is 3.2 mm.

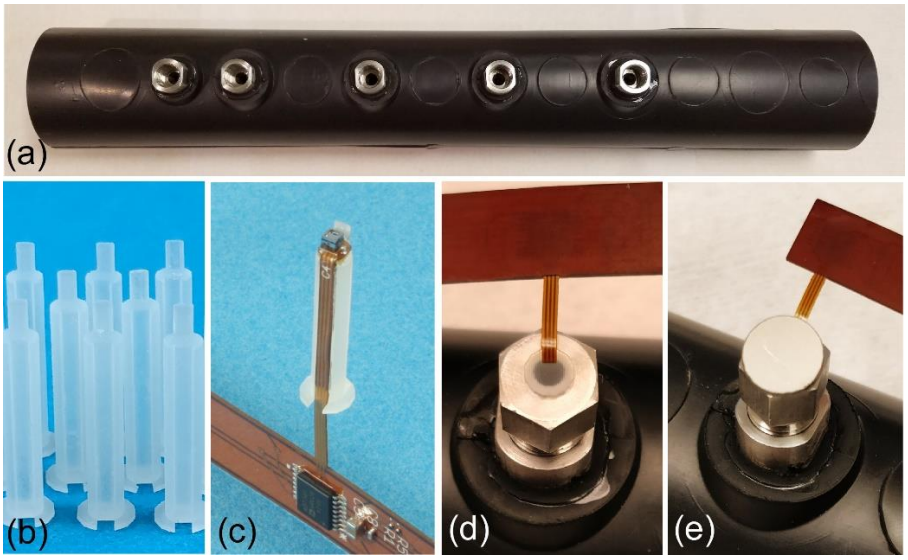



Fig. 2.14: (a) Polymer sheath with steel nuts; (b) Fabricated 3D printed inserts; (c) PCB tab integrated with 3D printed insert; (d) PCB tab integrated with 3D-printed insert within the perforation in steel bolt; (e) Cover plate attachment to complete feedthrough.

The polymer sheath used in a typical core-flood test cell is shown in Fig. 2.14(a). The 3D-printed plug (Fig. 2.14) is made from M3 crystal resin using the ProJet® 3500 HDMax 3D printer (3D Systems, Rock Hill, USA). The distal end of the PCB tab with the pressure sensor and the reference capacitor is bent at 90° such that the sensing diaphragm faces the LP chamber as shown in Fig. 2.14(c). The tab is inserted into the perforation on the steel bolt (Fig. 2.14d). Epoxy is used to fill the interior of the 3D-printed insert, and a steel cover plate machined using a computer numerical control (CNC) waterjet cutter is placed over the perforation to isolate the pressure from the HP chamber (Fig. 2.14e). Fig. 2.15 shows a completely assembled PCB with all four tabs inserted into steel bolts mounted on the polymer sheath.

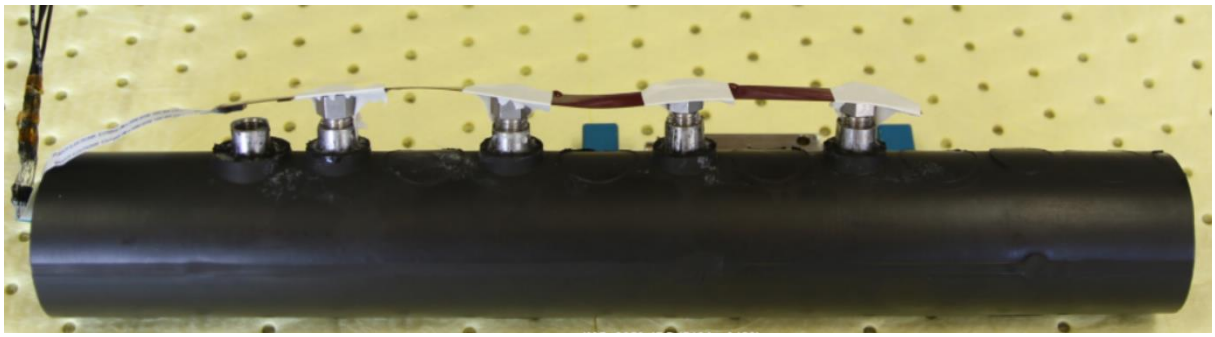


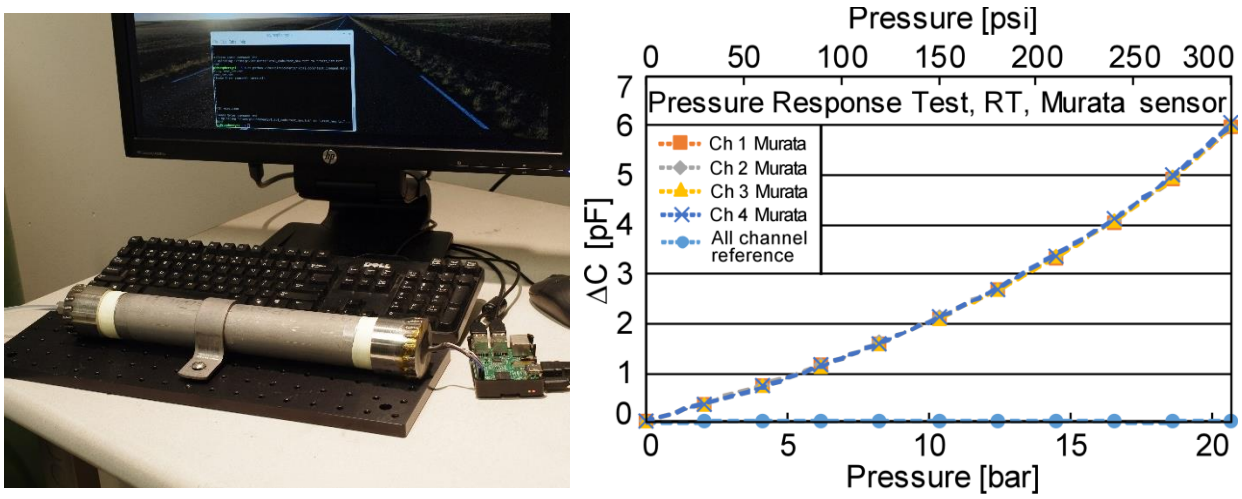
Fig. 2.15: Completely assembled PCB with all four tabs inserted into steel bolts mounted on the polymer sheath.

## 2.3 Experimental Setup, Results and Discussion

This section reports the static and full-scale pressure response of the DPSCore system obtained using custom designed test setups along with uncertainty and noise analysis of the microsystem and test setup.

### 2.3.1 Static Pressure Response

The static pressure response of the DPSCore system has been recorded at room temperature. A custom-made 35.6 mm long stainless-steel chamber with lead transfer capabilities has been designed for the pressure tests as shown in Fig. 2.16(a). Chamber pressure is ramped from 0-21 bar (0-2 MPa) in steps of 2.1 bar with the chamber pressure being held constant for 5 min at each pressure step. The recorded capacitive ($\Delta C$) response with pressure is shown in Fig. 2.16(b). All four pressure sensors show overlapping $\Delta C$ responses while the reference sensors show negligible variation over full pressure range at room temperature.




(a) (b)

Fig. 2.16: (a) Test setup for static pressure test (b) Variation of ΔC response with chamber pressure at room temperature for DPSCore system.

### 2.3.2 Distributed Pressure Test Setup Design

A DPSCore flow test setup was designed and built to perform distributed pressure measurement and flow tests on the DPSCore system prior to deployment in corporate facilities. The test setup (Fig. 2.17) includes a syringe pump, fluidic channel, and feedthrough chambers located along the length of the channel, where pressure sensors from the DPSCore sensor array can be inserted to perform a measurement. Between adjacent feedthroughs is a spring-operated check valve (CV) designed for a specific opening pressure. The check valves act as small pressure relief elements which cause the fluid pressure to drop between adjacent feedthroughs. The flow test system was implemented using commercial-off-the-shelf (COTS) components as shown below in Table 2.4.

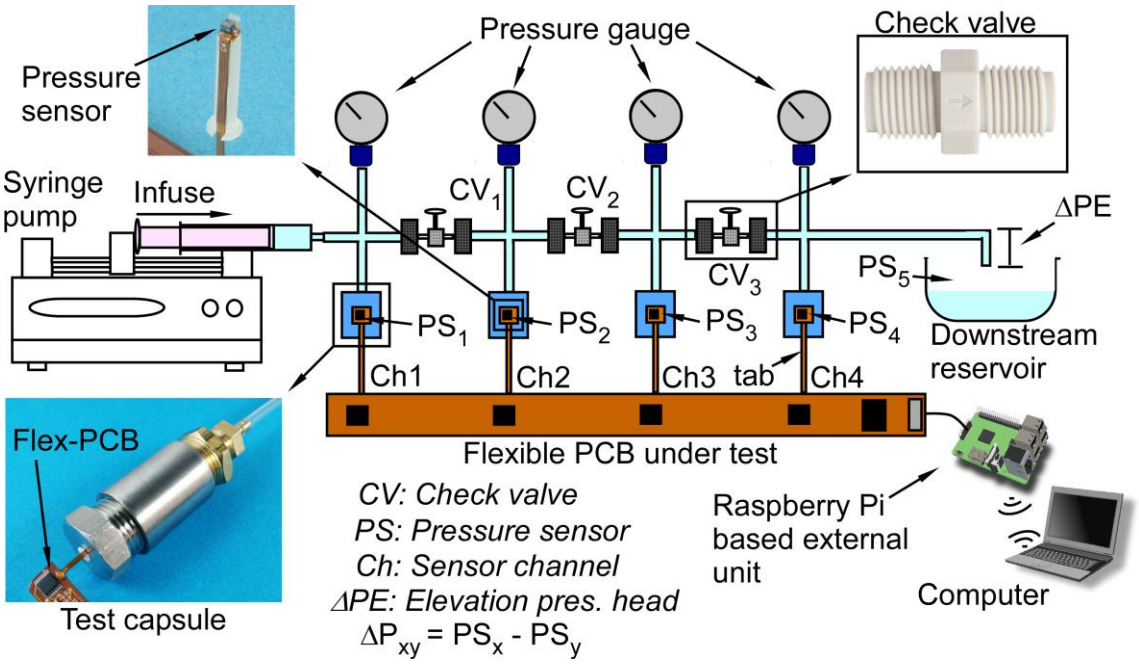



Fig. 2.17: Distributed pressure test setup schematic.

Table 2.4: COTS component list for the DPSCore flow test setup.

| Item | Manufacturer | Manuf. Part No. | Description |
|---|---|---|---|
| Syringe pump | kd Scientific | LEGATO® 100 | Single syringe infusion pump, max. linear force 30 lb, max. volume 60 mL |
| Syringe | BD Biosciences | 43217-9983 | 60 mL, leur-lock tip |
| Syringe – tube adapter | Cole-Parmer | AO-45502-04 | Female luer x 1/8" hose barb adapter, nylon |
| CV 1- 4 | Smart Products Inc. | 214214PB | 1/8” x 1/8” MNPT Check Valve; Opening pressures: 0.09 psi, 0.45 psi, 1.03 psi |
| Pressure Gauge | Winters Instruments | PEM1300 | 0-30 psi, 1-1/2" Dial Display, 1/8" NPT Bottom Mount |
| Tubing | ATP Pneumatics | PU316AC | 1/8" ID x 3/16" OD polyurethane plastic tubing |
| Tube connector | Cole-Parmer | VV-40610-96 | PVDF 1/8” barbed tube cross fitting |

The COTS components were assembled to realize the DPSCore flow test setup illustrated in Fig. 2.17. A DPSCore PCB #DPS18.1.09 was prepared to verify the flow test setup operation. The DPSCore PCB tabs integrated with 3D printed plugs were inserted into through-holes in the feedthrough chamber. After this step, the through-holes were sealed using 5-minute epoxy to ensure a leakage free lead transfer. Under a fluid infusion rate of 25 mL/min, check valves CV1

and CV2 had a characterized opening pressure of 6 ± 1 mbar (0.09 ± 0.01 psi) while valve CV3 had an opening pressure of 146.1 ± 29 mbar (2.1 ± 0.4 psi). The commercial check valves created a known pressure drop between adjacent pressure sensors. Pressure gauges with a measurement range of 0-30 psi were included to provide reference readings. White mineral oil (Crystal Plus, 70FG) was used as test fluid.

*Theoretical estimation of differential pressure response:*

The pressure drop across each check valve (PCVx) was estimated using the formula:

$$PCV_x = ( PD1 - PD2 ) - \Delta PC \quad (x = 1,2,3) \tag{2.1}$$

where, PD1 and PD2 are the digital pressure gauge readouts at the two ends of the check valve and ΔPC is the pressure drop in the associated connectors, estimated to be ≈3 mbar at 25 mL/min fluid infusion rate and ≈1 mbar at 5 mL/min infusion rate.

Assuming a laminar fluid flow inside the polyurethane tube used in the test setup, the tubing pressure drop for white mineral oil flow was estimated using the simplified Hagen-Poiseuille's equation [Lou99],

$$\Delta PT_{12} = \frac{128 \mu L Q}{\pi D^4} \tag{2.2}$$

where, $\Delta PT_{12}$ is the pressure drop in the tube between points 1 and 2, μ is the dynamic viscosity of white mineral oil, L is the tube length, Q is the flow rate, and D is the tube inner diameter. For a tube length of 2.54 cm, tube inner diameter of 3.175 mm, mineral oil density of 838 g/cm$^3$, dynamic viscosity of 0.0103 N-s/m$^2$ and flow rate of 25 mL/min, the calculated pressure drop is 0.437 mbar. Using the same assumptions but substituting in a 5 mL/min flow rate, the pressure drop per is 0.0873 mbar. These values have been used later to calculate the tubing pressure drop between adjacent pressure sensors.

In case of gain or loss in elevation by the flexible tubing, the static head pressure (ΔPE) can be calculated by [Hyd19],

$$\Delta PE = \rho g h \tag{2.3}$$

where, ρ is fluid density, g is acceleration of gravity, and h is elevation. For white mineral oil, the pressure gradient is 2.08 mbar for a 1-inch gain in elevation.

The total pressure-drop between two sensor channels x and y ($\Delta PS_{xy}$) is given by,

$$\Delta PS_{xy} = \Delta PT_{xy} + PCV_z + \Delta PE_{xy} + \Delta PC \tag{2.4}$$

where, $\Delta PT_{xy}$ is the tube resistance induced pressure drop in tube length $TL_{xy}$ calculated with equation (1) between channels x and y, $PCV_z$ is the opening pressure of the check valve $CV_z$ located between channels x and y, $\Delta PE_{xy}$ is the elevation pressure head calculated using equation (3) and ΔPC is the estimated flow rate dependent pressure drop in associated connectors between channels x and y.

The pressure read by an imaginary absolute pressure sensor ($PS_5$) placed in the downstream reservoir will be the current atmospheric pressure at the location of the test setup. Ann Arbor has a standard atmospheric pressure of 983 mbar (assuming an altitude of 840 feet above sea level and ambient temperature of 20°C) [Noa19]. Due to fluctuations in local atmospheric pressure, air drafts inside the building, and other factors such as air conditioning, an error margin of ±40 mbar was assumed for atmospheric pressure fluctuations inside the laboratory in which the test setup is housed. Therefore, the absolute pressure measurement at the downstream reservoir made by pressure sensor PS5 is 983 ± 40 mbar.

Because the channel 4 pressure sensor ($PS_4$) has a 21.6 cm length of tube between it and the atmosphere ($PS_5$), the pressure recorded by $PS_4$ can be estimated by adding the pressure drop

($\Delta PT_{45}$) due to the tube length ($TL_{45}$) at specific flow rate and pressure drop due to gain in tube elevation ($\Delta PE_{45}$) to $PS_5$. The theoretical pressure shown below in Table 2.5 vindicates that pressure sensor $PS_4$ shall record values that are slightly higher than the atmospheric pressure with an uncertainty of ± 40 mbar resulting from unmeasured fluctuations in atmospheric pressure.

Table 2.5: Theoretical estimation of channel 4 pressure response.

| Flow Rate (mL/min) | $TL_{45}$ (cm) | $\Delta PT_{45}$ (mbar) | $\Delta PE_{45}$ (mbar) | $\Delta PS_{45}$ (mbar) | $PS_4 = PS_5 + \Delta PS_{45}$ (mbar) |
|---|---|---|---|---|---|
| 25 | 21.6 | 3.7 | 4.4 | 8 | 991 ± 40 |
| 5 | | 0.7 | | 5 | 988 ± 40 |

The pressure sensor responses of channels 3, 2 and 1 have been estimated using equation (3) and are shown below in Table 2.6, Table 2.7, and Table 2.8 respectively. In addition to the uncertainty resulting from atmospheric pressure fluctuation, an error margin of ±20% for CV3 opening pressure has been considered as prescribed by manufacturer which increases the total error margin to ±69 mbar and ±64 mbar at 25 mL/min and 5 mL/min flow rates respectively. As seen in Table 2.6-2.8, the theoretical pressure change between consecutive sensors is largely governed by the opening pressure of the respective check valves. The theoretical pressure increases with the addition of each flow resistive element (check valve, tubing, etc.) to 1170 mbar and 1121 mbar at $PS_1$ for 25 mL/min and 5 mL/min respective flow rates.

Table 2.6: Theoretical estimation of channel 3 pressure response.

| Flow Rate (mL/min) | $TL_{34}$ (cm) | $\Delta PT_{34}$ (mbar) | $PCV_3$ (mbar) | $\Delta PE_{34}$ (mbar) | $\Delta PC$ (mbar) | $\Delta PS_{34}$ (mbar) | $PS_3 = PS_4 + \Delta PS_{34}$ (mbar) |
|---|---|---|---|---|---|---|---|
| 25 | 16.5 | 2.8 | 146.1 ± 29 | - | 3 | 152 ± 29 | 1143 ± 69 |
| 5 | | 0.6 | 120.1 ± 24 | | 1 | 122 ± 24 | 1110 ± 64 |

Table 2.7: Theoretical estimation of channel 2 pressure response.

| Flow Rate (mL/min) | $TL_{23}$ (cm) | $\Delta PT_{23}$ (mbar) | $PCV_2$ (mbar) | $\Delta PE_{23}$ (mbar) | $\Delta PC$ (mbar) | $\Delta PS_{23}$ (mbar) | $PS_2 = PS_3 + \Delta PS_{23}$ (mbar) |
|---|---|---|---|---|---|---|---|
| 25 | 17.8 | 3.1 | 6 | - | 3 | 12 | 1155 ± 69 |
| 5 | | 0.6 | 2 | | 1 | 4 | 1114 ± 64 |

Table 2.8: Theoretical estimation of channel 1 pressure response.

| Flow Rate (mL/min) | $TL_{12}$ (cm) | $\Delta PT_{12}$ (mbar) | $PCV_1$ (mbar) | $\Delta PE_{12}$ (mbar) | $\Delta PC$ (mbar) | $\Delta PS_{12}$ (mbar) | $PS_1 = PS_2 + \Delta PS_{12}$ (mbar) |
|---|---|---|---|---|---|---|---|
| 25 | 17.1 | 3.0 | 6 | 3.1 | 3 | 15 | 1170 ± 69 |
| 5 | | 0.6 | 2 | | 1 | 7 | 1121 ± 64 |

Table 2.9 below shows a summary of the theoretically estimated pressure sensor responses for all 4 sensor channels. The pressure in $PS_4$ is very close to atmospheric pressure and the pressure in each sensor sequentially increases from $PS_4$ to $PS_1$ with the addition of each flow resistive element, check valves being the largest contributor. It is important to note that the uncertainty assumed due to unmeasured fluctuation in atmospheric pressure and manufacturer prescribed check valve opening pressure variation is an error margin and is not representative of noise in the test setup. These sources of uncertainty can be reduced to some extent with superior manufacturing and appropriate characterization of relevant elements.

Table 2.9: Theoretical estimation of pressure response for all sensor channels.

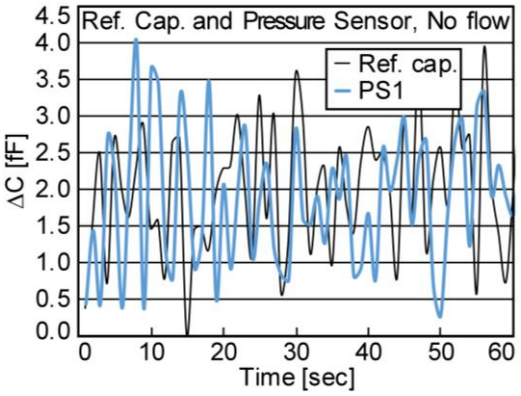
| Flow Rate (mL/min) | $PS_1$ (mbar) | $PS_2$ (mbar) | $PS_3$ (mbar) | $PS_4$ (mbar) |
|---|---|---|---|---|
| 25 | 1170 ± 69 | 1155 ± 69 | 1143 ± 69 | 991 ± 40 |
| 5 | 1121 ± 64 | 1114 ± 64 | 1110 ± 64 | 988 ± 40 |

*Noise Analysis:*

In order to better understand noise in DPSCore flow test setup, experimental evaluation and analysis of the possible sources were performed. Three possible sources of noise and/or uncertainty in the DPSCore system were identified and separately analyzed which are: (a) noise in the interface circuit readout, (b) temperature effects, and (c) variation in syringe pump flow rate. These sources are presented in the following subsections.

*Circuit Noise:*

To evaluate DPSCore readout circuit noise, the system shown in Fig. 2.17 was filled with mineral oil and a zero flow infusion rate (i.e. no flow state) was established. In this no flow state, the channel 1 pressure sensor capacitance (i.e. $PS_1$) and channel 1 reference capacitor (i.e. Ref. cap.), which is a fixed ceramic capacitor located adjacent to the pressure sensor were recorded and are shown below in Fig. 2.18. The range and standard deviation of capacitive outputs over the duration of the test for both the Ref. cap. and $PS_1$ are tabulated in Fig. 2.18. The fluctuations of $PS_1$ in a no flow state was comparable to the fluctuations of Ref. cap., suggesting that the source of the observed fluctuation is limited by the readout circuit and not the capacitive pressure sensor. As shown, the fluctuation in the readout circuit is estimated to be ≈±1.8 fF which corresponds to ≈±17 mbar of pressure uncertainty. This reveals that the readout circuit noise floor is much higher than the estimated noise floor for the pressure sensors (≈0.8 mbar) making the circuit a significant contributor of uncertainty in sensor readout.



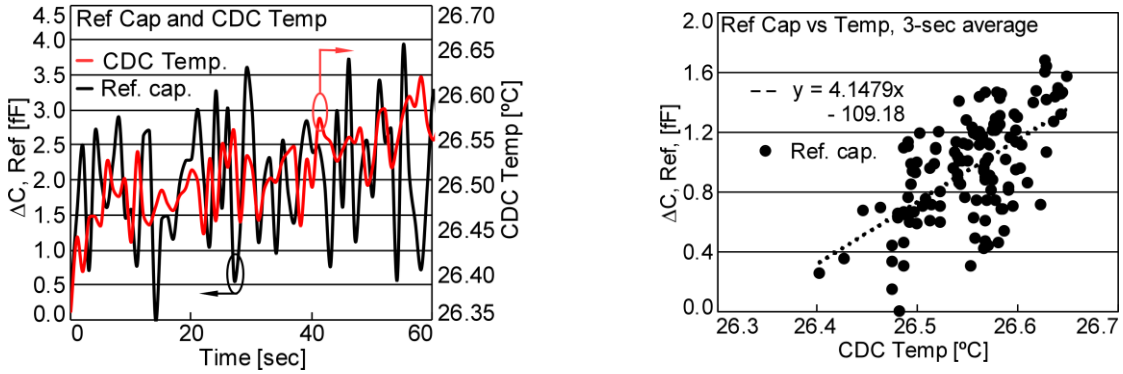

Range and standard deviation of response.

| | Range [fF] | Std. Dev. [fF] |
|---|---|---|
| Ref. cap. | 3.92 | 0.82 |
| PS1 | 3.98 | 0.92 |

Fig. 2.18: Capacitive response of reference capacitor and pressure sensor in no flow state. The table on the right shows the range and standard deviation of the plotted response.

*Temperature Effects:*

To further understand the source of uncertainty, the temperature readout from the capacitance to digital converter (CDC) used in the circuit was analyzed and plotted along with the reference capacitor response for channel 1, as shown below in Fig. 2.19(a). The results showed an increasing trend with CDC temperature. Fig. 2.19(b) shows ≈4 fF/°C dependence of the reference capacitor readout on the CDC temperature. The temperature increased by ≈0.3°C over the course of the test, contributing to a rise in capacitance output of ≈1.3 fF or ≈12 mbar in pressure uncertainty.




(a) (b)

Fig. 2.19: (a) CDC temperature variation in a no flow state (b) Reference capacitor response as a function of the CDC temperature variation, data points averaged over 3 sec time intervals.

*Variation in pump flow rate:*

In order to characterize the fluctuation in syringe pump flow rate, a digital liquid flow sensor (SLF3S-1300F, Sensirion, Switzerland) was used [Slf19]. DI water was infused using the syringe pump at room temperature through the flow sensor which has a stated measurement resolution of 0.05 mL/min and sampling frequency of 5 ms. The measured percent variation in pump flow rate for both 25 mL/min and 5 mL/min setpoints with time have been shown below in Fig. 2.20 and Fig. 2.21 respectively.

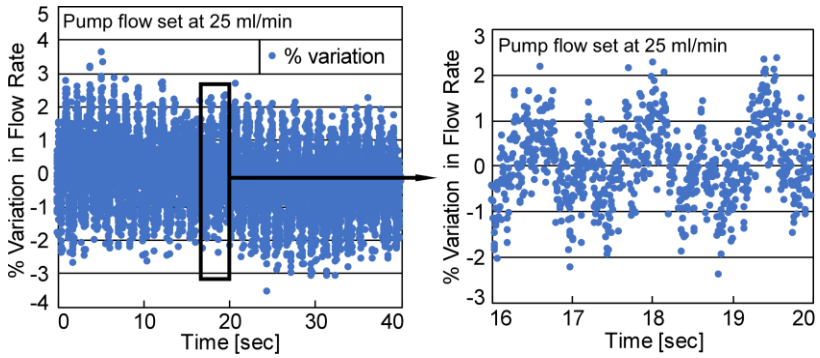



Fig. 2.20: Percent variation in syringe pump flow rate at 25 mL/min setpoint.

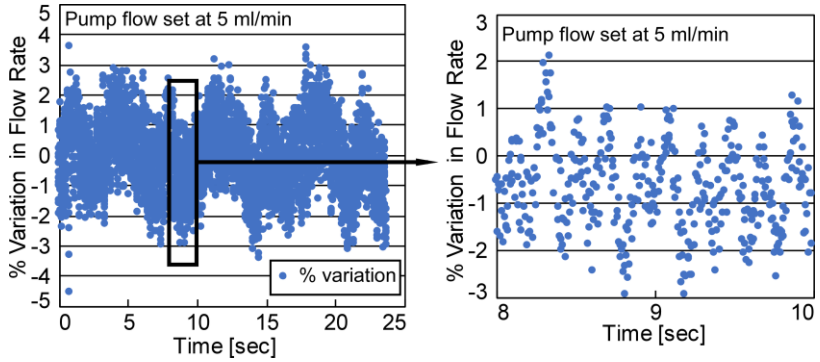



Fig. 2.21: Percent variation in syringe pump flow rate at 5 mL/min setpoint.

Table 2.10 contains the range and standard deviation of flow rate variation over the duration of the tests along with the corresponding pressure uncertainty estimated in the pressure sensor readouts due to this variation. The pressure uncertainty has been estimated using equations discussed in earlier section of this report considering ≈8% variation in actual flow rate of the syringe pump. The length of the tube between the syringe pump outlet and $PS_1$ as shown in Fig. 2.17 is 30 cm.

Table 2.10: Estimated pressure error for all sensor channels due to pump flow variation.

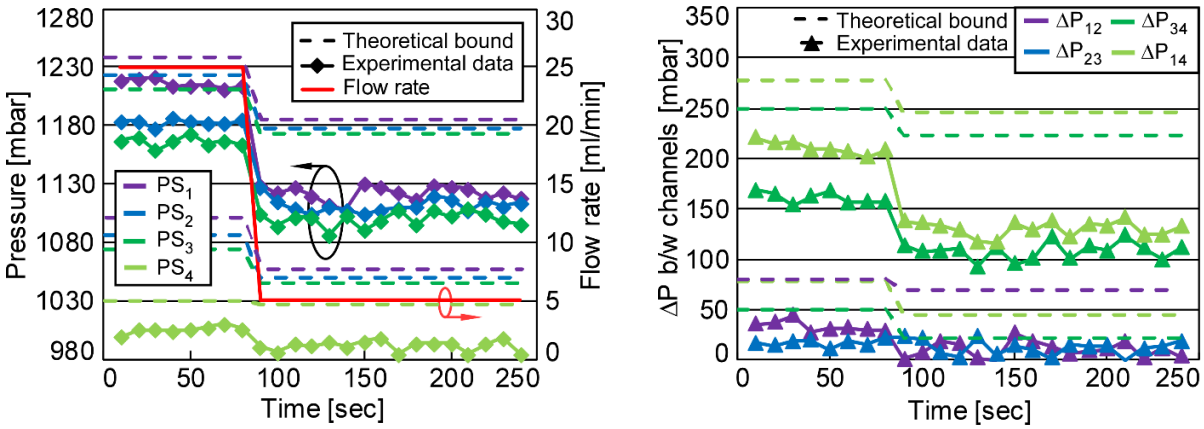
| Flow rate setpoint (mL/min) | Flow rate variation (%) | Standard deviation (%) | Estimated pressure error [mbar] | | | |
|---|---|---|---|---|---|---|
| | | | $PS_1$ (mbar) | $PS_2$ (mbar) | $PS_3$ (mbar) | $PS_4$ (mbar) |
| 25 | ± 4 | ± 0.55 | ± 0.4 | ± 0.9 | ± 1.4 | ± 7.5 |
| 5 | | | ± 0.1 | ± 0.3 | ± 0.5 | ± 5.4 |

To conclude the noise and uncertainty analysis, the uncertainty in DPSCore interface circuit readout was estimated to be ≈±1.8 fF which corresponds to ≈±17 mbar of pressure

uncertainty. The observed temperature variation (≈0.3°C) is likely to account for about ≈±0.6 fF (33%) of the observed uncertainty contributed by the interface circuit. This source of variation can be possibly reduced with a precise temperature calibration curve. The remaining uncertainty in interface circuit readout at no flow state (≈±1.2 fF) needs further evaluation and understanding. A study of the syringe pump revealed ≈8% variation in actual pump flow rate which can contribute up to ±7.5 mbar in pressure uncertainty.

### 2.3.3 Dynamic Pressure Response

In a typical experiment using the distributed pressure measurement system, a fluid infusion rate of 25 mL/min was maintained for the first 90 sec followed by a reduced infusion rate of 5 mL/min through the rest of the experiment. Fig. 2.22(a) shows a time-series of pressure measurements, sampled at 10 sec intervals from the four channels. The flow rate during the experiment is also plotted. Fig. 2.22(b) shows the differential pressure between different test capsules (tabs).




(a) (b)

Fig. 2.22: (a) Pressure response of Murata SCB10H pressure sensors recorded during flow test at room temperature. Theoretically estimated bounds for each pressure sensor response are indicated by dashed lines; (b) Differential pressure between different test capsules (tabs) recorded during the flow test at room temperature.

The theoretically estimated bounds for the response based on the test setup configuration and experimental conditions previously discussed are also plotted. The measured pressure gradients were well within the theoretically estimated bounds. These results demonstrated the capability of this system to measure pressure gradient with a resolution as small as 0.3 mbar.

## 2.4 System Deployment and Field Test Results

Two DPSCore systems have been deployed in the energy industry and tested in corporate laboratory (TOTAL S.A., France). These systems have been successfully integrated with test cells that use different core materials, such as rock or sand. The high pressure chamber was saturated with mineral oil at confinement pressure while two different flooding test fluids were used in the low pressure chamber for flow testing: Isopar™ (Exxon Mobil Corp., USA) for the rock core system and white oil (Marcol™, Exxon Mobil Corp., USA) for the sand core system. A picture of the integrated test cell used during the corporate laboratory testing is shown in Fig. 2.23.

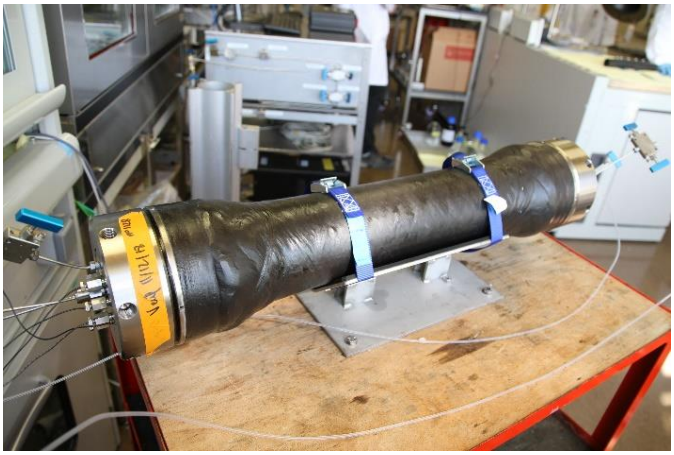
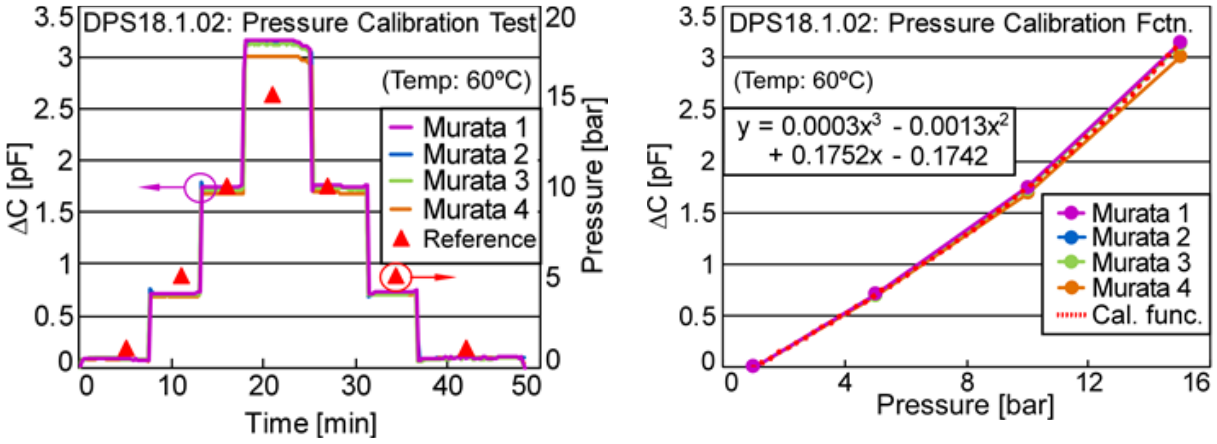


Fig. 2.23: DPSCore test cell with the integrated system in Total laboratory, Pau.

### 2.4.1 System Calibration

Each of the two deployed systems in corporate laboratory is calibrated over the full pressure dynamic range (up to 20 bar) at two operating temperatures: room temperature and 60°C. Tests at higher operating temperatures up to 125°C are planned for a later schedule. The calibration

data recorded at 60°C for a DPSCore system #DPS18.1.02 with a sand core is shown in Fig. 2.24(a). The pressure inside the core chamber is increased in approximate step sizes of 6 psi up to 18 psi and again brought down in similar step sizes to 1 psi. The recorded data is used to investigate a calibration function as shown in Fig. 2.24(b) by comparing with manually read reference pressure data from a pressure gauge attached to the core chamber. A 3rd order polynomial fitting is performed to obtain the calibration function. The coefficients of this polynomial are then updated on the user interface program for calculating and displaying calibrated pressure outputs for all future system measurements at 60°C. A similar calibration approach has been followed for each system for different ambient temperature operation up to 125°C.



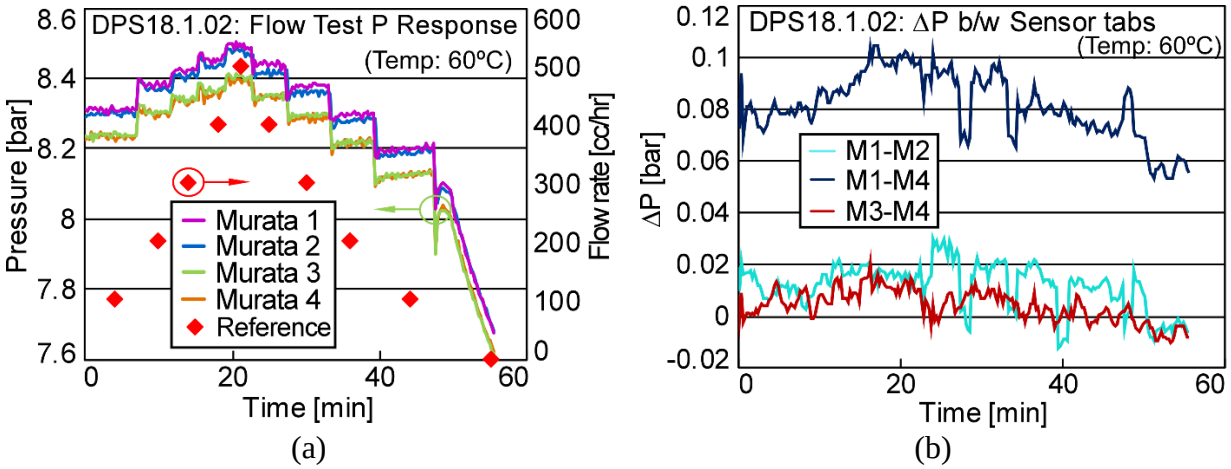

(a) (b)

Fig. 2.24: (a) Pressure calibration test data for DPSCore system #DPS18.1.02 at 60°C; (b) Pressure calibration function along with fitted 3rd order calibration equation for DPSCore system #DPS18.1.02 at 60°C.

### 2.4.2 Flow Test Results

Flow tests at different ambient temperatures for the DPSCore system were performed at corporate laboratory facilities (TOTAL S.A., France). For the flow test, a constant flow rate is established inside the LP chamber of the test cell containing the rock core. The flow rate is then increased in steps of 100 cc/hr being held for 4-5 min at each flow rate step. The calibrated pressure

response from the different sensor channels for DPSCore system #DPS18.1.02 during the flow test at 60°C is shown in Fig. 2.25(a). As observed, the pressure data follows the step changes in input reference flow rate. The difference in pressure measured ($\Delta P_{xy}$) between different sensor tabs has been plotted in Fig. 2.25(b). A pressure difference in the order of milli-bar is observed between the different sensor tabs of the DPSCore system with the maximum pressure recorded by the sensor located at the input side of fluid flow with subsequent drops in pressure picked up by sensors along the flow direction. This confirms successful operation and performance of the designed DPSCore system. A similar approach is employed to characterize flow in DPSCore systems at different operating temperatures when assembled with different core materials.




(a) (b)

Fig. 2.25: (a) Flow test data for DPSCore system #DPS18.1.02 at 60°C; (b) The difference in pressure between different Murata sensors during flow test at 60°C.

## 2.5 Chapter Summary

This Chapter investigated design and implementation of the first *in situ* high resolution distributed pressure measurement system for core-flood experiments. A series of microfabricated pressure sensors are embedded in bolts located at the seam of the rock core within a polymer sheath that encases the rock core. In order to ensure the rock core remains flush with the sheath the interface electronics are located outside the sheath in a high pressure chamber. A compact,

hermetic lead transfer through the bolts was successfully designed to electrically connects the sensors to the interface electronics, traversing a 230-bar pressure difference. The impact of post-package stress on the performance of pressure sensors was modelled, characterized, and mitigated by using a customized anneal protocol which showed a 10-fold improvement in baseline capacitance variation of sensors, caused due to temperature fluctuations up to 125°C.

System electronic design was realized on a flexible PCB, largely using commercial off-the-shelf components to reduce cost and increase scalability. A Raspberry-Pi (R-Pi) based external computer was programmed to operate the flexible PCB and serially interrogate each pressure sensing node over a $I^2C$ bus. The R-Pi was also programmed to upload processed sensor data over Wi-Fi to the cloud and interact with a remote desktop running a customized graphical user interface for data and command transfer.

A distributed pressure testing setup was designed and built to understand dynamic response of the DPSCore system with an in-depth theoretical understanding of measurement uncertainty and experimental noise analysis of the designed test setup and system components. The system has been successfully tested using customized test setup over a full-scale range of 20 bar and 0.3 mbar pressure resolution, verifying the validity of the design and the feasibility of the implementation. Two DPSCore systems were successfully deployed at corporate facilities in the energy industry (TOTAL S.A., Pau, France) where both units were successfully integrated with commercial core-flood experiment setups, calibrated, and tested at 60°C using multiple core materials and flooding fluids at varying flow rates. This confirmed successful operation and performance of the designed DPSCore system in field environments. Future work will focus on characterization of sensor size and noise limits and investigate a passive wireless sensing solution to eliminate the need for lead transfer through the polymer sheath.

# Chapter 3: Passive Wireless Pressure Gradient Measurement System for Fluid Flow Analysis

This Chapter reports the design and realization of a passive wireless distributed pressure gradient measurement (PGM) system for fluid flow analysis. Pressure gradients are generated in fluidic systems when fluid flow encounters resistance, governed by Darcy's law in the presence of a porous medium [Mus43, Whi86]. Study and measurement of these flow induced pressure gradients are critical in many engineering systems, such as core-flood experiments for geological studies [Dut19], high pressure liquid chromatography (HPLC) columns [Pod19], and navigation of unmanned underwater vehicles [Dev15]. Improving the ability to measure these gradients, especially by designing systems in which sensors have a minimal effect on flow, can allow a better understanding of the sensed environment.

As presented in Chapter 2, core-flood experiments refer to the study of rock core samples by subjecting them to pressurized fluid flow; these experiments are routinely used in the energy industry to predict oil and natural gas recovery potential and the applicability of new extraction strategies before embarking on costly ventures [Kam15]. A rock core sample of a potential extraction site is taken in order to measure its porosity and permeability [Gil94], which can provide critical information on the nature of the reservoir. The core sample is prepared for testing by encasement in a polymer sheath to form a low pressure (LP) chamber, where pressure and temperature can be up to 20 bar, and 125°C, respectively. The assembly is then placed inside a test cell, referred to as the high pressure (HP) chamber. Conditions in the test cell are simulated to

match the environment of the reservoir by raising temperature and confinement pressure up to 125°C and 250 bar, respectively. A mixture of fluids found in the reservoir (e.g. oil, water, gas, etc.) are pumped into the rock core and flow through it.

While Chapter 2 addresses the system design and integration concepts of a distributed pressure sensing system with a wired feedthrough technology, this Chapter presents the system design and integration concepts of a passive wireless PGM system uses an inductive-capacitive (LC) measurement approach. This new approach shall address three primary challenges: 1) miniaturization of the pressure sensing element, 2) lead transfer from sensor to interrogation electronics through the flow path boundary, and 3) a robust package to protect the sensing element from a chemical environment. The proposed LC measurement approach utilizes a fully passive sensing element, permitting a great reduction in size by eliminating the need for the largest and most sensitive system components (e.g. battery and electronics) to be present in the sensing environment [Fon02]. Furthermore, it removes the requirement of a direct wired connection between sensor and readout electronics, permitting sensing in applications where lead transfer may be difficult or impossible, such as in rotating systems [Hen05]. However, designing a packaging approach and system integration strategy is still critical, as LC Sensors must be designed to permit operation in a high temperature, and/or chemically corrosive environment, such as those prevalent in core-flood experiment setups.

## 3.1 System Concept and Design

The proposed PGM system, illustrated in Fig. 3.1, consists of multiple wireless LC pressure sensing elements (LC Sensors, $LC_n$) distributed along longitudinal axis of the rock core. Each LC Sensor includes a custom capacitive pressure transducer [Ben21] and planar inductive coil. The resonant peak of an inductor-capacitor circuit is altered by pressure induced changes in capacitance

[Col67]. LC Sensors are on the interior surface of the polymer sheath *in situ* to the sensing environment, permitting pressure measurements along the rock core to be made. Multiple readout nodes on a printed circuit board (PCB) are located outside the polymer sheath in the high pressure (HP) chamber to remotely interrogate individual LC Sensors. Each node consists of a readout inductor coil, standing wave ratio bridge circuit, and sinusoidal excitation circuitry; a microcontroller unit (MCU) controls each node, digitizing the collected data with an embedded ADC, temporarily holding data after each pressure measurement. An external Raspberry Pi™ (R-Pi) microcomputer (Raspberry Pi™ Foundation, UK) interfaces with the MCU; it collects data temporarily stored in the MCU and runs data processing algorithms for extraction of pressure dependent resonant frequency. A laptop remotely connected to the R-Pi via Wi-Fi permits user control of the system through a graphical user interface (GUI) and can upload processed data to the cloud for further processing and retrieval.

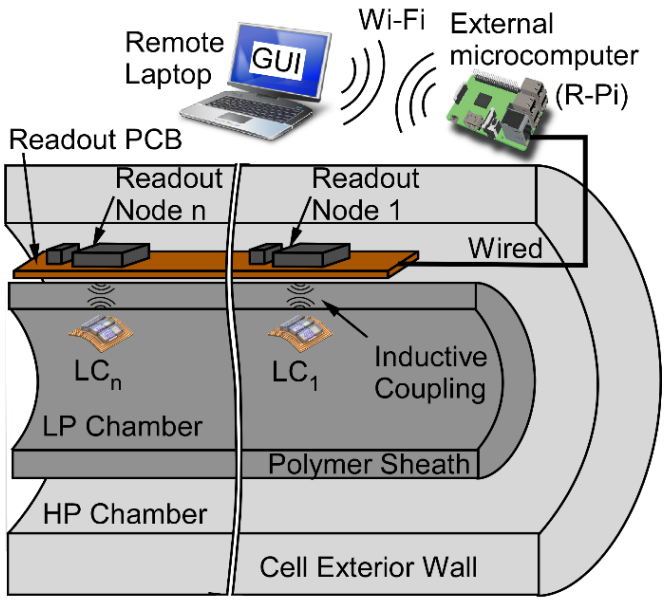



Fig. 3.1: Cross-sectional view of the implemented solution for a passive wireless pressure gradient measurement (PGM) system. The system can be scaled to have *n* LC Sensors and readout nodes, with $n = 4$ in this work.

### 3.1.1 LC Sensor Circuit Model

The pressure sensing element of the PGM system is the LC Sensor, comprised of a capacitive pressure transducer, $C_{XDCR}$, and inductive coil, $L_S$; a simplified LC Sensor circuit model is shown in Fig. 3.2. The parallel capacitance, $C_{PS}$, is due to any parasitic capacitance of the LC Sensor, $C_P$ as well as any additional capacitance, $C_{DUMMY}$ added in parallel with $C_{XDCR}$. Total capacitance of LC Sensor, $C_S$ is due to summation of $C_{PS}$ and $C_{XDCR}$. The parasitic series resistance, $R_S$, is due to the resistance of the inductor coil and the equivalent series resistance, *ESR*, of the capacitive pressure transducer, resulting from the resistance of the thin film metal electrodes.

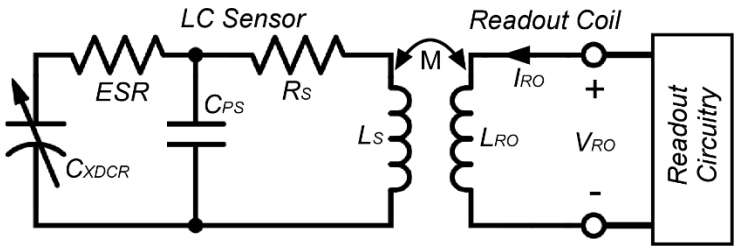



Fig. 3.2: Wireless Inductive Pressure Gradient Measurement (PGM) System circuit model illustrating the LC Sensor and Readout coil and circuitry.

When the readout, $L_{RO}$, and LC Sensor, $L_S$, coils are in close proximity, they will become coupled, resulting in a mutual inductance, *M*. The pressure-dependent resonant frequency, $f_0$, of the LC Sensor, equation (3.1), will manifest as a peak in the real part of the input impedance, $Re\{Z_{in}\}$, of the readout coil, where $Z_{in}$ is the complex input impedance of $L_{RO}$ calculated from $V_{RO}$ and $I_{RO}$, the complex input voltage and current, equation (3.2). $Re\{Z_{in}\}$ is monitored by the readout circuitry, described in Section 3.1.2.

$$f_0 \approx \frac{1}{\sqrt{(L_S) \cdot (C_{XDCR} + C_{PS})}} \approx \frac{1}{\sqrt{L_S C_S}} \tag{3.1}$$

$$Z_{in} = \frac{V_{RO}}{I_{RO}} \tag{3.2}$$

In order to extract $f_0$, a set of discrete data points is collected, where each data point is the magnitude of $Re\{Z_{in}\}$ at a specific frequency. A typical captured dataset of $Re\{Z_{in}\}$ of the LC Sensor circuit is shown in Fig. 3.3; a fitted Gaussian curve, referred to as the fitted frequency response waveform, $F_{Zin}$ is fit to each dataset. Bandwidth ($BW = \sigma$) is defined as $f_0/Q$, and mean ($\mu$) is defined as $f_0$. In this work, $\sigma$ is defined as the full width at half maximum ($FWHM$), which is the frequency span of the $Re\{Z_{in}\}$ dataset measured between the points which are half the input impedance magnitude, $\Delta Z_{in}$. Input impedance magnitude, $\Delta Z_{in}$, is the difference in height between the maximum value of $Re\{Z_{in}\}$, found at approximately $f_0$, and the minimum value of $Re\{Z_{in}\}$, found far away from $f_0$ (at approximately $f_0/10$); it can also be estimated using $M$, $Q$, $L_{RO}$, and $L_S$. Quality factor, $Q$, is $f_0$ divided by $\sigma$; it can also be estimated using $R_S$, $L_S$, and total capacitance ($C_S = C_{XDCR} + C_{PS}$). The shift in resonant frequency, $\Delta f_0$, with applied pressure, $\Delta P$, (due to the change in capacitance, $\Delta C$, of the pressure transducer over the full-scale pressure range, $\Delta P_{FS}$) is defined as *Absolute Response*, $R_A$. A further detailed understanding of this $f_0$ extraction method, along with all relevant design equations, has been provided in Chapter 4 of this dissertation.

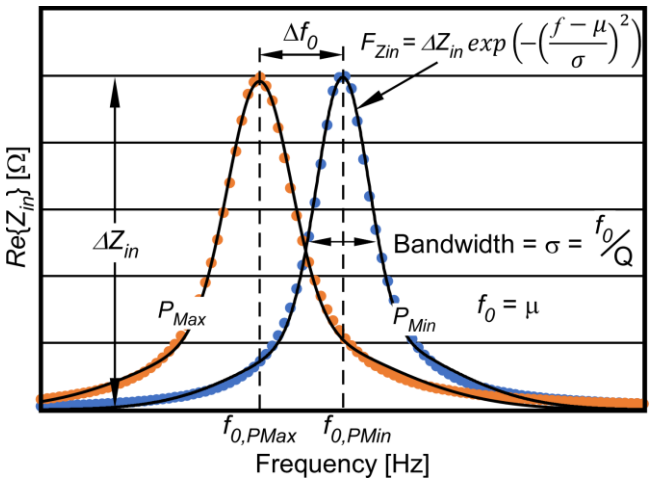



Fig. 3.3: Two $Re\{Z_{in}\}$ datasets at minimum ($P_{Min}$) and maximum ($P_{Max}$) applied pressure illustrating important parameters such as bandwidth, $\sigma$, resonant frequency, $f_0$, $f_0$ shift due to applied pressure, $\Delta f_0$, and fitted gaussian approximation, $F_{Zin}$, used to extract $f_0$ via interpolation.

### 3.1.2 LC Sensor Electrical Design

To realize electrical design of the LC Sensor, an LC Sensor design optimization model was investigated in MATLAB (MathWorks, USA) to sweep the physical design parameters of the LC Sensor and readout coil within their boundary conditions, required by the core flood experiment application (Table 3.1) and the resulting output of the Design Optimization Factor, *DOF* was calculated. The derivation of this figure of merit, termed Design Optimization Factor, to analytically predict LC Sensor pressure resolution has been described in Chapter 4 of this dissertation, including all relevant LC Sensor design equations used in this model study.

Table 3.1: Design constraints for LC Sensor and readout coil for PGM system.

| **Design Parameter** | **Dimension** | **Comments** |
|---|---|---|
| LC Sensor, max. diameter | <13 mm | In order to maintain a packaged LC Sensor diameter of ≤15 mm |
| Readout coil, max. diameter | <25 mm | Pitch between adjacent LC Sensors is 50 mm |
| Minimum *L* trace width | 0.125 mm | Minimum manufacturable dimension |
| Minimum *L* trace spacing | 0.125 mm | Minimum manufacturable dimension |
| LC Sensor PCB thickness | 0.250 mm | Minimum fabricable thickness of PCB |
| Nominal Interrogation gap (*IG*) of $L_S$ and $L_{RO}$ coils | 4 mm | Typical thickness of polymer sheath in a core-flood experiment |
| Full-scale pressure, $\Delta P_{FS}$ | 20 bar | Full-scale pressure range of core-flood experiments |
| Pressure Transducer (P. XDCR) size | $1.8 \times 1.0 \times 0.5$ mm$^3$ | Dimensions of custom microfabricated P. XDCR |
| P. XDCR offset cap, $C_0$ | 4.0 pF | P. XDCR capacitance at 0 applied pressure |
| Transducer cap. change, $\Delta C_{FS}$ | 3.2 pF | Total capacitance change of P. XDCR over $\Delta P_{FS}$ |
| P. XDCR *ESR* | 200 Ω | Equivalent Series Resistance (*ESR*) of P. XDCR |

Mathematical estimation of mutual inductance, *M* is difficult; simplified closed form equations to determine *M* (equation 4.9, Chapter 4) often do not accurately estimate the impact of magnetic coupling and leakage flux; furthermore, the magnetic behavior of sensor materials and other nonidealities may significantly impact this value. Therefore, a finite element analysis (FEA)

model was investigated in COMSOL Multiphysics® to more accurately extract *M* between the LC Sensor and readout coil inductors. Fig. 3.4 shows the 2D axisymmetric model geometry, including packaging materials of the LC Sensor (discussed later in section 3.3) to the left, and resulting magnetic field lines generated between the readout coil and LC Sensor at an excitation frequency of 13 MHz, to the right. The magnetic field is most intense at the innermost windings of the readout coil, approximately 0.10 mT. Key material properties used in the study are listed in Table 3.2.

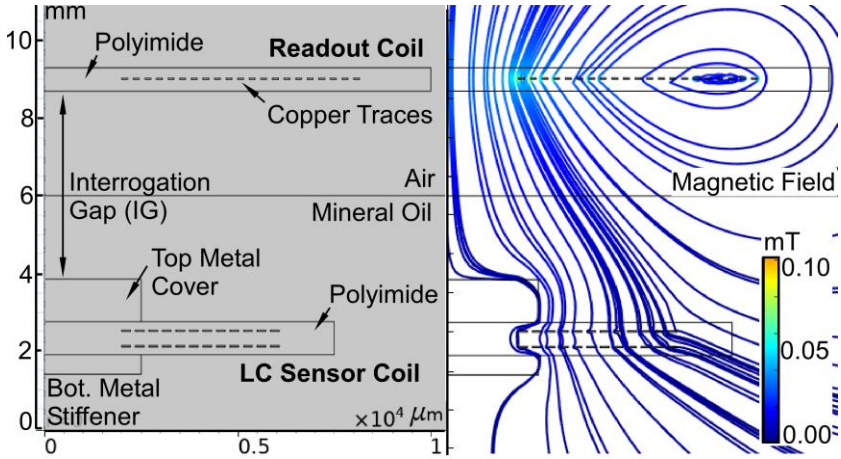



Fig. 3.4: Studied 2D axisymmetric FEA model geometry of the LC Sensor coil and readout coil in COMSOL Multiphysics (left) Magnetic field distribution of the sensor and readout coil assembly under excitation at 13 MHz (right).

Table 3.2: Assumed material properties in FEA model.

| **Material** | **Density [g/cm$^3$]** | **Young's Modulus [GPa]** | **Poisson's Ratio** | **Electrical Conductivity [S/m]** |
|---|---|---|---|---|
| Air | - | - | - | 1.00e-2 |
| Aluminum | 2700 | 70.0 | 0.33 | 3.77e7 |
| Copper | 8700 | 130 | 0.34 | 5.99e7 |
| Mineral oil | - | - | - | 1.75e-1 |
| Polyimide | 1300 | 3.10 | 0.34 | 6.66e-16 |
| Viton$^{TM}$ | 1840 | 0.01 | 0.47 | 2.1e-9 |

Fig. 3.5 shows the FEA results obtained for *k* and *M* with a varying separation between the two inductors, referred to as interrogation gap (*IG*); as *IG* increases, *k* and *M* decrease. Results from the FEA study was used to perform empirical adjustments to analytical equations of *k* and *M*, studied in the MATLAB model to calculate *DOF*.

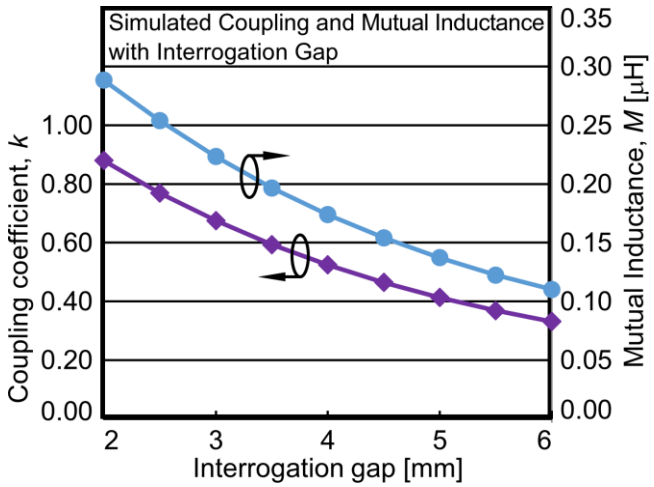
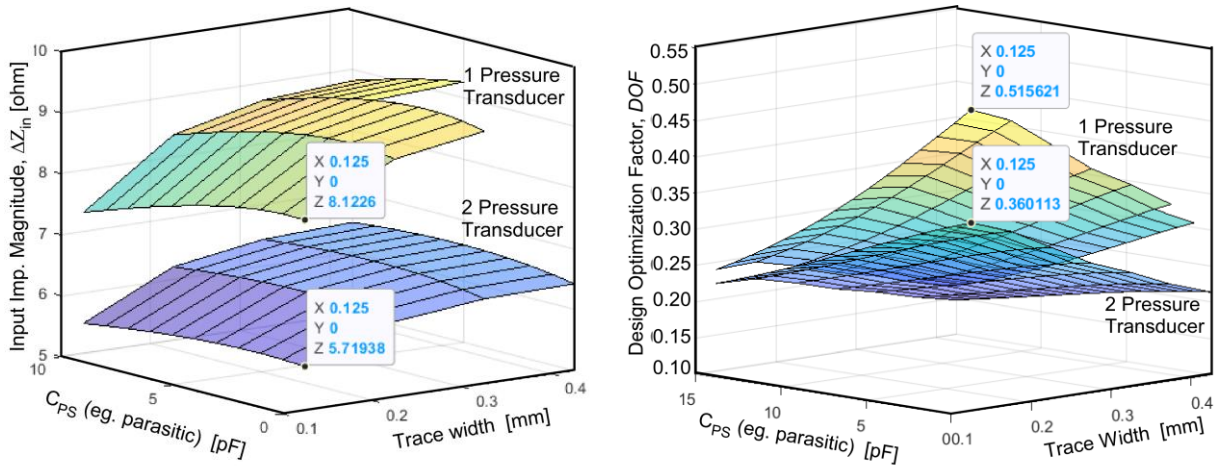



Fig. 3.5: FEA modelling results showing variation in coupling coefficient and mutual inductance with interrogation gap (*IG*).

Multiple LC Sensor electrical design factors were evaluated in the MATLAB model within the boundary conditions listed in Table 3.1, including sensor inductor trace width, number of pressure transducers, addition of a dummy capacitor in parallel with the pressure transducers (to reduce effective series resistance of the pressure transducer), number of PCB layers, etc. Fig. 3.6(a) shows the model predicted values of LC Sensor input impedance magnitude ($\Delta Z_{in}$) for a two-layer PCB design, with varying inductor trace width and value of total parallel capacitance ($C_{PS}$) at an interrogation gap, *IG* of 5 mm. As can be observed, the input impedance magnitude is higher when a single pressure transducer (P. XDCR), and no parallel capacitance is present. Fig. 3.6(b) shows the calculated *DOF* for the same one and two pressure transducer designs, on a two-layer PCB with varying inductor trace width. As shown in Fig. 3.6(b), the study yielded the optimum LC Sensor design (i.e. maximization of *DOF*) to be a double layer inductor with a diameter of 13 mm, trace width and spacing of 0.125 mm, and one capacitive pressure transducer. The parasitic capacitance of the inductor coil was measured to be 14 pF on a 0.250 mm thick flexible polyimide substrate. The corresponding readout inductor design used a diameter of 17.5 mm with trace width and spacing of 0.15 mm. Final design parameters of LC Sensor are summarized in Table 3.3.




(a) (b)

Fig. 3.6: (a) MATLAB model result showing variation in input impedance magnitude, $\Delta Z_{in}$ with inductor trace width and parallel capacitance for a two-layer PCB. (b) Variation in *DOF* with inductor trace width and parallel capacitance for two-layer PCB, with one and two pressure transducers.

Table 3.3: Design parameters for LC Sensor.

| **Parameter** | **Dimensions** | **Comments** |
|---|---|---|
| Inductor Trace Width | 0.125 mm | Produces optimum coil design, analytically studied |
| Inductor Trace Spacing | 0.125 mm | Produces optimum coil design, analytically studied |
| LC Sensor PCB thickness | 0.250 mm | Minimum thickness of PCB fabricable |
| LC Sensor Inductance | 10.5 µH | Inductance of fabricated LC Sensor inductor |
| $C_P$ | 14.0 pF | Measured parasitic capacitance of LC Sensor inductor |
| No. of P. XDCR | 1 | Number of pressure transducers |
| $C_{DUMMY}$ | 0 pF | Additional dummy cap. in parallel with P. XDCR |

### 3.1.3 Readout Circuit

The Readout Circuit was designed with contribution from Dr. Tao Li's research team at University of Cincinnati, USA. Individual LC Sensors are wirelessly coupled to specific readout inductor coils integrated into each corresponding readout circuit node (Readout Node *n*, Fig. 3.1). A schematic of the readout node is given in Fig. 3.7.

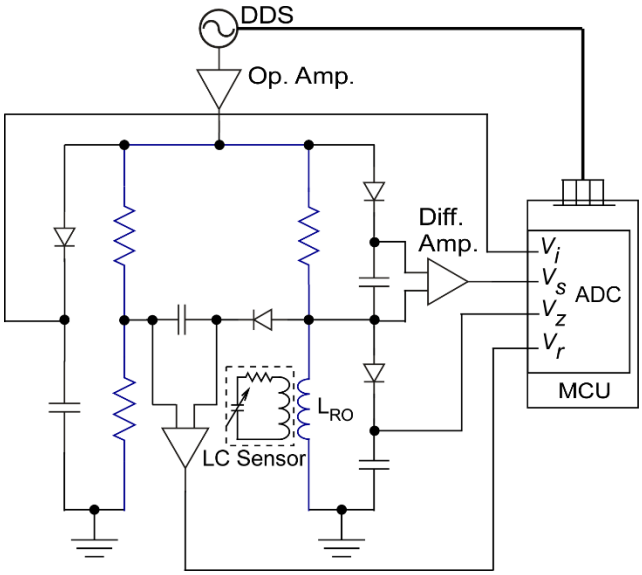



Fig. 3.7: Circuit schematic of readout node on Readout PCB.

Each readout node is controlled by an individual MCU (C8051F990, Silicon Laboratories, Inc., USA) with an embedded 12-bit analog to digital converter (ADC). A direct digital synthesizer (DDS) (AD9850, Analog Devices, Inc., USA) generates a sinusoidal signal to excite a standing wave ratio bridge circuit. The readout coil, with varying impedance due to the coupled LC Sensor, forms one branch of the standing wave ratio bridge circuit; the remaining branches are realized with a fixed value resistor. Four voltages of each branch of the standing wave ratio bridge circuit, $\overrightarrow{V_z}$, $\overrightarrow{V_s}$, $\overrightarrow{V_r}$, and $\overrightarrow{V_i}$, are amplified through individual differential amplifiers, realized with ADA4891 operational amplifiers (Analog Devices, Inc., USA). The amplified signals are then digitized using the embedded ADC. $Re\{Z_{in}\}$ is calculated within the MCU using equation (3.3). $|Z_{in}|$ and SWR are defined in equation (3.4) and (3.5), respectively, where $|\overrightarrow{V_z}|$, $|\overrightarrow{V_s}|$, $|\overrightarrow{V_r}|$, and $|\overrightarrow{V_i}|$ represent peak values of the four voltages $\overrightarrow{V_z}$, $\overrightarrow{V_s}$, $\overrightarrow{V_r}$, and $\overrightarrow{V_i}$ [Zha14].

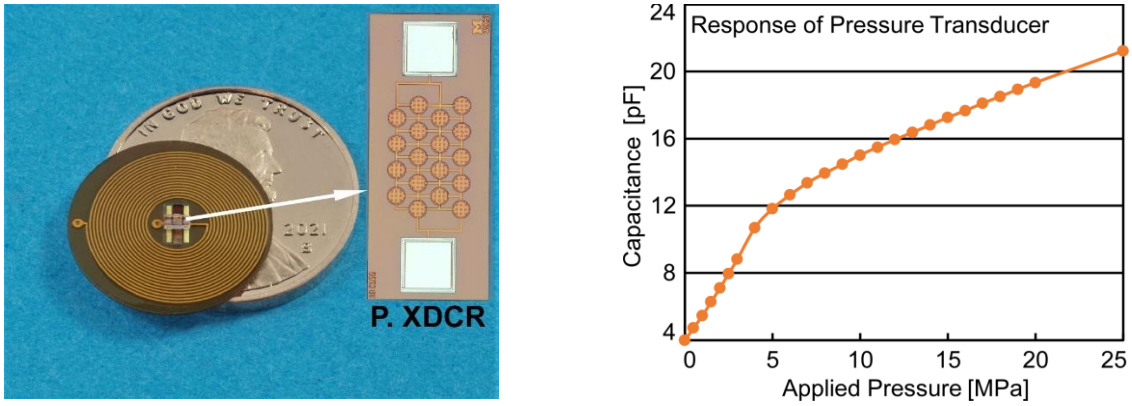
$$Re(Z_{in}) = \frac{(|Z_{in}|^2 + 50^2) \cdot SWR}{50 \cdot (SWR^2 + 1)} \tag{3.3}$$

$$|Z_{in}| = 50\frac{|\overrightarrow{V_Z}|}{|\overrightarrow{V_s}|} \tag{3.4}$$

$$SWR = \frac{\left|\frac{1}{2}\overrightarrow{V_i}\right| + |\overrightarrow{V_r}|}{\left|\frac{1}{2}\overrightarrow{V_i}\right| - |\overrightarrow{V_r}|} \tag{3.5}$$

## 3.2 System Fabrication

The LC Sensor inductor coil is fabricated on a polyimide substrate flexible printed circuit board (PCB), fabricated by FlexPCB (Santa Ana, CA, USA), Fig. 3.8(a). It is an inductor coil with electrical mounting contact pads at the center for the capacitive pressure transducers and additional parallel capacitance, as required. The capacitive pressure transducer, P. XDCR, [Ben21] is electrically connected to the LC Sensor using Duralco 120, a high temperature silver epoxy from Cotronics (Brooklyn, NY, USA). A typical capacitance response of the pressure transducer with applied pressure is given in Fig. 3.8(b).




(a) (b)

Fig. 3.8: (a) Image of LC Sensor flexible PCB coil with one capacitive pressure transducers (P. XDCR) mounted at the center, placed on an US penny. An inset image shows the diaphragm structure of P. XDCR [Ben21]. (b) Typical capacitive pressure response of pressure transducer over 25 MPa (250 bar) of applied pressure.

The designed flexible readout PCB, shown in Fig. 3.9, contains four sets of readout circuit nodes, such as described in Fig. 3.7. In addition to four readout nodes, the PCB also includes a 5-pin cable connector for power supply and serial communication with each individual readout node through an $I^2C$ bus. The spiral readout coils are placed on the four side tabs of the PCB. All

components used on the flexible PCB are surface mount to minimize the size of the PCB. The final dimension of the readout PCB is 210 × 61 $mm^2$.

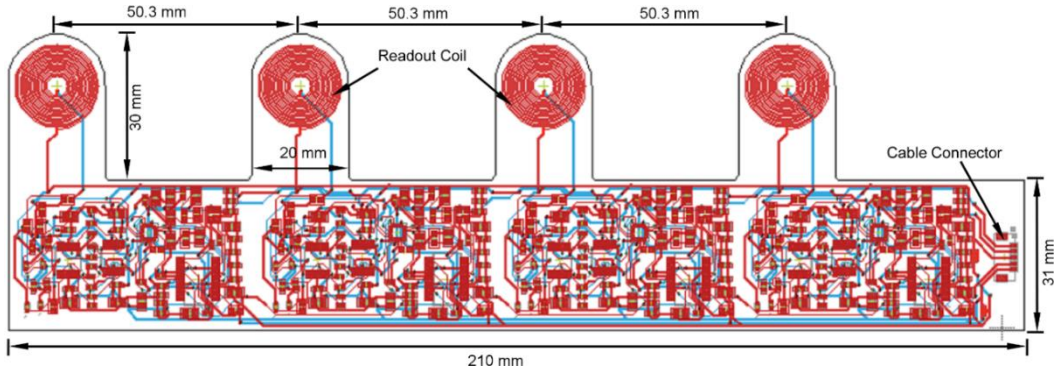



Fig. 3.9: Layout of the flexible readout PCB.

The layer configuration of the flexible readout PCB is shown in Table 3.4. The stiffener layers are only used in the main body of the PCB but not in the side tabs with the readout coils to allow the readout coil to wrap around the circumference of the polymer sheath. The fabricated flexible readout PCB, manufactured by FlexPCB (Santa Ana, CA, USA), is shown in Fig. 3.10.

Table 3.4: Layer stack of flexible readout PCB.

| | |
|---|---|
| .0005" Top polyimide coverlay | Solder mask Amber |
| .001" adhesive | |
| .0007" copper (plated to .0014") | |
| .002" polyimide | Dupont 2FPD2005JA |
| .0007" copper (plated to .0014") | |
| .001" adhesive | |
| .0005" Bottom polyimide coverlay | Solder mask Amber |
| .001" adhesive | |
| .007" polyimide Stiffener | LF0150 stiffener |

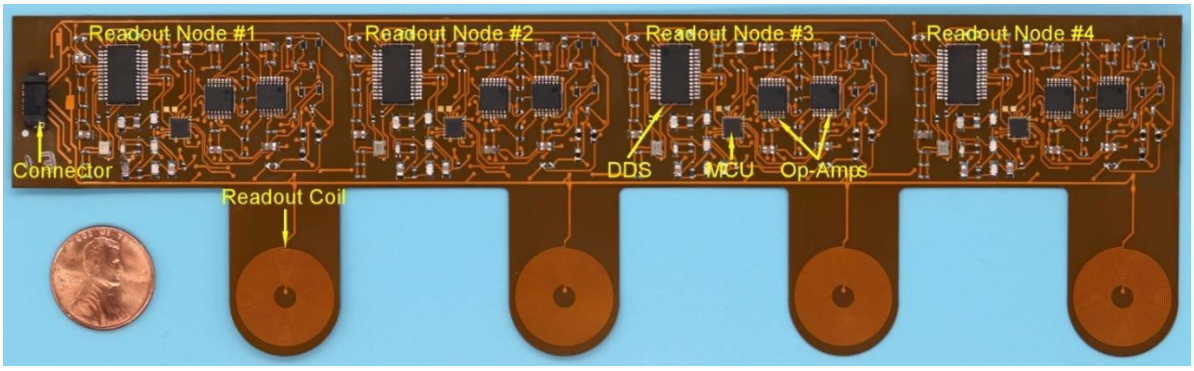



Fig. 3.10: Image of the fabricated flexible readout PCB next to an US penny.

## 3.3 LC Sensor Packaging

The LC Sensor packaging must be sufficiently robust to provide protection against mechanical forces and withstand environments inside core-flood equipment (containing corrosive chemicals and temperatures up to 125°C) while still permitting pressure transmission to the transducer. To limit any disturbance in the fluid flow during a core-flood experiment, the packaged sensor should be less than 3 mm in thickness. The proposed packaging method is composed of a top metal cover and bottom metal substrate stiffener, Viton$^{TM}$ rubber encapsulation, and thin film polyimide coating; a cross section is shown in Fig. 3.11.

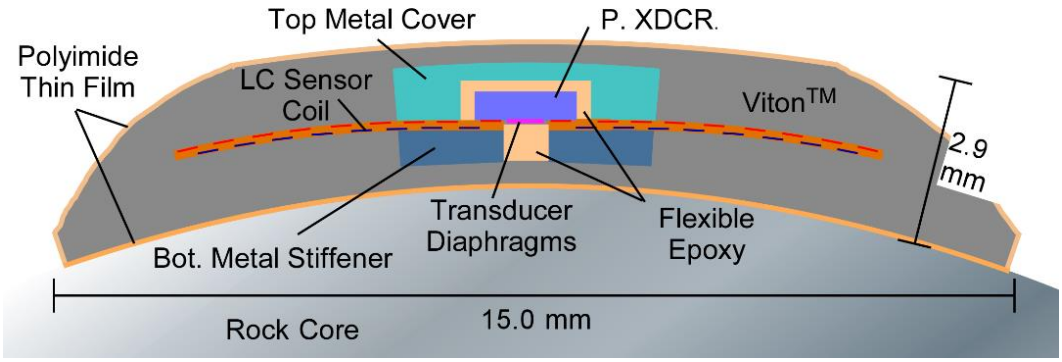



Fig. 3.11: Cross sectional view of LC Sensor with proposed packaging method.

The top metal cover and bottom metal substrate stiffener, shown in Fig. 3.12(a), are used to protect the capacitive pressure transducer, providing mechanical support to prevent any shear forces or static high pressure from causing delamination. They are fabricated by Fathom Advanced Manufacturing (Oakland, CA, USA) using Direct Metal Laser Sintering (DMLS) 3D printing process with an AlSi10Mg aluminum alloy [Eos22] to both minimize size and reduce impact on the LC Sensor coupling to the readout coil while still providing maximum support and protection. The top of the top metal cover and bottom of the bottom metal substrate stiffener are curved to match the curvature radius of the rock core for the core-flood application. To secure them to the LC Sensor, a high temperature flexible epoxy (Duralco 4538, Brooklyn, NY, USA) is employed.

This flexible epoxy also surrounds the transducer and transducer diaphragms to provide additional protection while still permitting pressure transduction to the diaphragms.




(a) (b)

Fig. 3.12: (a) 3D printed bottom metal stiffener (left) and top metal cover (right) on an US penny (b) Image of a fully packaged LC Sensor on an US penny.

After the top metal cover and bottom metal substrate stiffener are secured, the LC Sensor is then encapsulated in Viton$^{TM}$ rubber, known to be resistant to most harsh environments [Dup20]. This is accomplished by using a custom mold and Fluorodyn Viton$^{TM}$ Caulk from Thermodyn Global Sealing (Houston, TX, USA). As Viton$^{TM}$ is incompatible with certain organic solvents used in core-flood experiments, such as toluene, a 100 µm thin film polyimide coating (PI 2610, HD MicroSystems, Wilmington, DE, USA) is applied to the outer Viton$^{TM}$ surface. The fully packaged LC Sensor is shown in Fig. 3.12 (b). To verify effectiveness of the polyimide coating approach, a fully packaged LC Sensor was placed into pure toluene for 25 hours, showing no degradation to the film or Viton with minimal (<0.7%) change in weight.

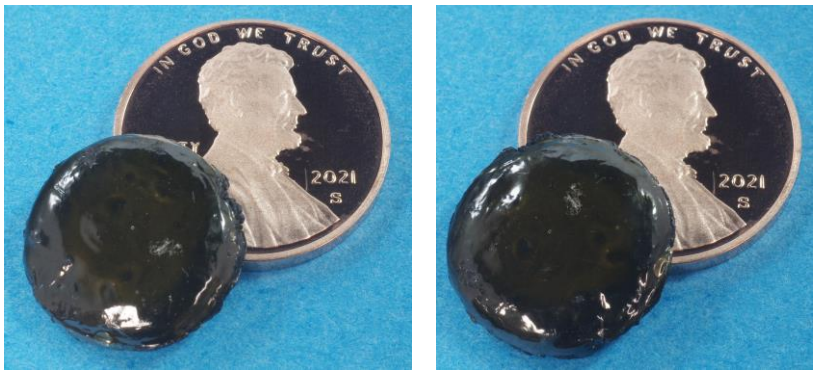



Fig. 3.13: Liquid polyimide thin film coated LC Sensor (left) as fabricated and (right) after 24-hour toluene soak on an US penny.

Table 3.5: Weight of fully packaged LC Sensor during Toluene resistance validation test

| | Weight |
|---|---|
| Before Toluene | 750 mg |
| 1 hour | 750 mg |
| 2 hours | 751 mg |
| 3 hours | 751 mg |
| 20 hours | 755 mg |
| 25 hours | 755 mg |

To determine the necessary thicknesses of the top metal cover and bottom metal substrate stiffener, an FEA model was studied in COMSOL Multiphysics® to understand the stress distribution and deflection of the AlSi10Mg aluminum alloy under high pressure. As shown in Fig. 3.14 (a), the maximum simulated von Mises stress in a 1.2 mm thick AlSi10Mg aluminum alloy top metal cover is 120 MPa at 230 bar applied pressure, permitting a safety factor of >3x for the maximum yield strength of the AlSi10Mg aluminum alloy. The maximum top metal cover deflection was ≈3.6 μm at 230 bar applied pressure. These results suggest an Aluminum top metal cover and bottom metal substrate stiffener with the modeled thicknesses will provide sufficient protection of the transducer under high pressure, while minimizing impact on sensor response.

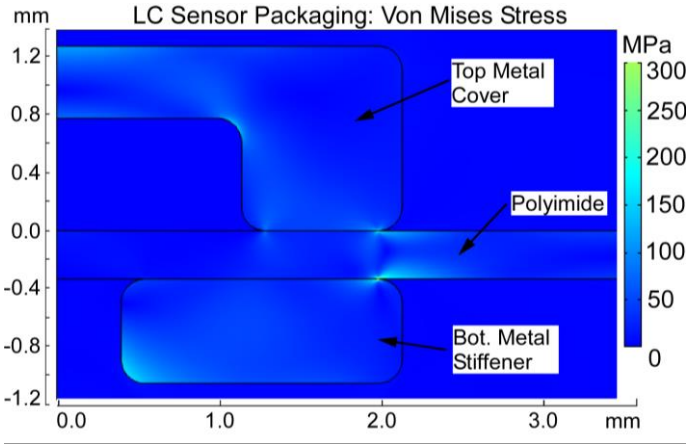



Fig. 3.14: 2D axisymmetric FEA modelling result showing von Mises stress distribution in LC Sensor packaging aluminum top metal cover, polyimide substrate, and aluminum bottom metal substrate stiffener under applied pressure of 230 bar.

It is also important that the top metal cover and bottom metal substrate stiffener are fabricated from materials with as low a relative magnetic permeability ($\mu_r$) as possible. Materials with high $\mu_r$ placed near the inductor will act as a ferrite core; at high frequencies, this will greatly increase the inductor's effective series resistance, reducing $Q$ and $\Delta Z_{in}$, worsening pressure resolution. Results of an LC Sensor without top metal cover and bottom metal substrate stiffener installed (unprotected) and LC Sensors protected with top metal covers and bottom metal substrate stiffeners fabricated from 15-5 stainless steel ($\mu_r \approx 95$), 316L stainless steel ($\mu_r \approx 1.4$), and AlSi10Mg aluminum alloy ($\mu_r \approx 1.0$) are shown in Fig. 3.15. 15-5 stainless steel results in a $Q$ and $\Delta Z_{in}$ reduction of >50% compared to an unprotected LC Sensor; however, the AlSi10Mg aluminum alloy results in a reduction of <10%. It is important to note that these reductions in both $Q$ and $\Delta Z_{in}$ will combine to reduce the pressure resolution dramatically. Given that pressure resolution is indirectly proportional to both $Q$ and $\Delta Z_{in}$, a reduction in these values by >50% will worsen pressure resolution by >4x; however, a reduction of <10% will only cause an increase in resolution of <1.2x.

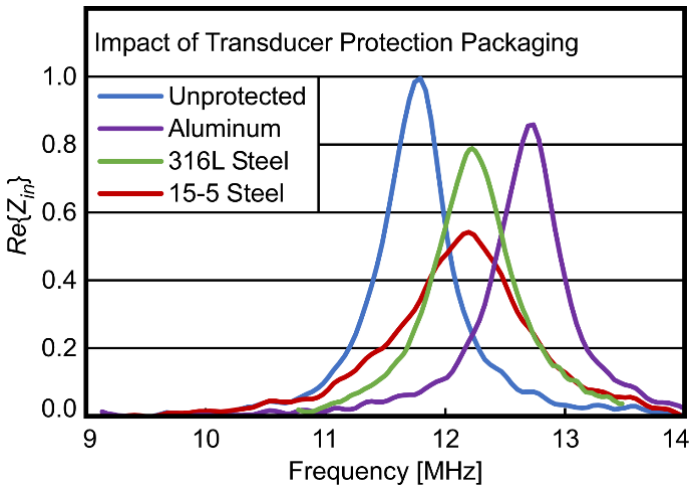



Fig. 3.15: $Re\{Z_{in}\}$ datasets for LC Sensors in unpackaged and packaged configurations with aluminum, magnetic stainless steel (15-5), and non-magnetic stainless steel (316L) top metal cover and bottom metal substrate stiffener.

## 3.4 Software Control and User Interface

Software design for the PGM system has been realized in three stages; 1) state machine for the readout PCB MCUs; 2) software for the External unit back-end to interface with the MCUs; and 3) remote desktop user interface (UI) front-end to interface with the external unit, as shown in Fig. 3.16. The first stage involves state machine design for each microcontroller unit (MCU) for individual readout nodes. The state machine shall enable each MCU to interface with one LC Sensor and its corresponding readout circuit and retrieve sensor data. All MCUs are also configured to be $I^2C$ slave devices with different slave addresses, all connected to the same $I^2C$ bus. The second stage of software design involves configuration of an $I^2C$ master device, a Raspberry Pi® based external unit, *R-Pi* (Raspberry Pi 3, Raspberry Pi Foundation, UK), which interfaces with each individual MCU over the $I^2C$ bus. This external unit back-end is also responsible for processing the sensor data and interfacing wirelessly with a remote desktop-based user interface (UI). The third stage involves design of the user interface front-end which provides an interactive platform to the end user to operate and maintain the PGM system.

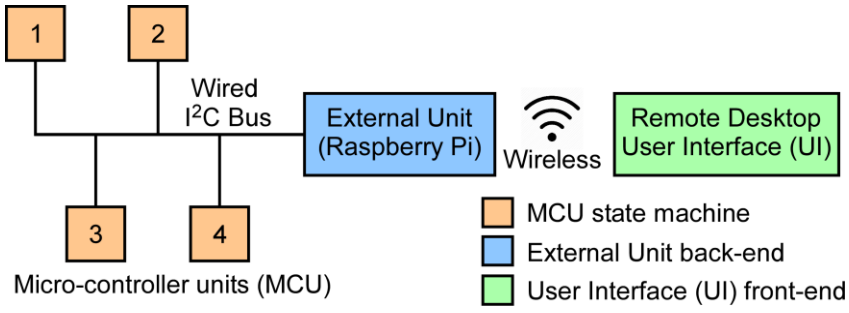



Fig. 3.16: PGM system software requirement.

### 3.4.1 Micro-controller Unit (MCU) State Machine

The software state diagram for the MCUs in each readout node on the flexible readout PCB is shown in Fig. 3.17. The user communicates various commands to the Raspberry Pi external unit through the remote desktop UI over Wi-Fi. The external unit then sends these commands and measurement parameters to each MCU through $I^2C$ protocol. On receiving the commands, the MCU transitions to the required state and performs the requested operation. The functions of individual states of the MCU software are explained below.

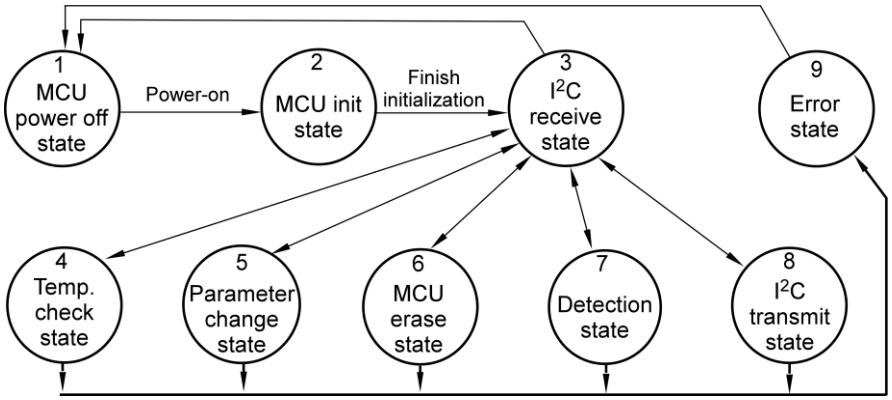



Fig. 3.17: MCU State Diagram.

*State 1, MCU power off state:*

This is the state of the MCU when the system is disconnected from the power supply. The MCU remains off in this state. Data is retained in the MCU flash memory without loss.

*State 2, MCU init state:*

This is a transient state during which the MCU turns on and all global constants and variables are initialized or restored from the flash memory. Registers of pertinent MCU peripherals, e.g. ADC, digital I/O, etc., are initialized for use in later operations.

*State 3, $I^2C$ receive state:*

This is the state in which the MCU receives commands from external unit through I2C protocol. When the user requires sensor measurement, the user communicates this to the Raspberry Pi based external unit through the user interface as the user cannot directly communicate with MCUs. Following this, the external unit initiates a measurement routine by communicating instructions and parameters to each MCU. Depending on the command received, MCU transitions to State 4 (temperature check state), State 5 (parameter change state), State 6 (MCU erase state), State 7 (detection state) or State 8 (I2C transmit state).

*State 4 Temperature check state:*

This state measures system temperature using the MCU internal temperature sensor and stores an integer value in the MCU flash memory.

*State 5, Parameter change state:*

This state allows the external unit to modify system operation parameters such as the range and step size of frequency sweep during detection. Interrogating a large range of frequency would require large step changes in frequency as the total number of frequencies that may be interrogated is fixed; this number is limited by the available MCU flash memory. The parameters are transmitted to the MCU by the external unit using I2C communication.

*State 6, MCU erase state:*

This state allows the MCU to erase the frequency sweep measurement data stored in the flash memory of MCU to open up storage space for new measurements. This state is entered when the MCU flash memory is full and after transferring all stored data to the external unit.

*State 7, Detection state:*

This state performs the pressure sensing function using the LC Sensor and readout PCB. On entering detection state, the MCU triggers the direct digital synthesizer (DDS) frequency generation chip to sweep a range of discrete frequencies based on parameters obtained during the parameter change state. During each frequency step, the MCU samples four voltage values within the readout circuit (used to calculate the $Re\{Z_{in}\}$ level) using a built-in analog to digital converter (ADC). These voltage sets, corresponding to each step of the swept frequency, are then stored in the MCU flash memory to be later retrieved by the external unit during the I2C transmit state.

*State 8, $I^2C$ transmit state:*

This is the state in which the MCU transmits sensor data stored in its flash memory to the external unit using I2C. The external unit is the master and the MCU is the slave for $I^2C$ communication. In this state, the MCU transmits data packets to the external unit. The MCU transitions to this state in two scenarios. The first scenario is when the MCU flash memory is full in the detection state or the frequency sweep has been completed (State 7). The second scenario is when new temperature sensor data is available (State 4). In both scenarios, the external unit sends a trigger to the MCU to transfer the stored sensor data via I2C.

*State 9, Error state:*

This is the state which the MCU enters if the program should fail unexpectedly and stop execution. Once it enters this state, it needs to wait for a power reset. At that point, the MCU goes to State 1 and restarts the program.

### 3.4.2 External Unit Back-end Software

The external unit uses a Raspberry Pi®, *R-Pi* (Raspberry Pi 3, Raspberry Pi Foundation, UK) with a Linux operating system. The software for this external unit was designed using Python programming language. The flowchart for the *R-Pi* software is shown in Fig. 3.18.

After powering on, the software initializes the *R-Pi* system. It then accepts the measurement schedule sent from the remote desktop and starts the periodic measurement cycles. In each cycle, the software checks whether there is any external trigger for instant measurement, and if so, initializes the $I^2C$ bus, and triggers the four sets of MCUs sequentially for measurement with necessary sensing parameters. As the MCUs enter their respective detection states, the external unit waits for the measurements to be completed. Following measurement completion, the external unit reads the measured frequency sweep data from each MCU sequentially over the $I^2C$ bus and runs signal processing algorithm to extract important parameters such as resonant frequency. These extracted parameters are then stored in local nonvolatile memory and is communicated back to the remote desktop to be display to the user in real time. The extracted data can also be uploaded to a cloud storage platform. If there is no external trigger, the software checks the timer for measurement schedule and repeats the above measurement and data handling procedure when the timer is triggered.

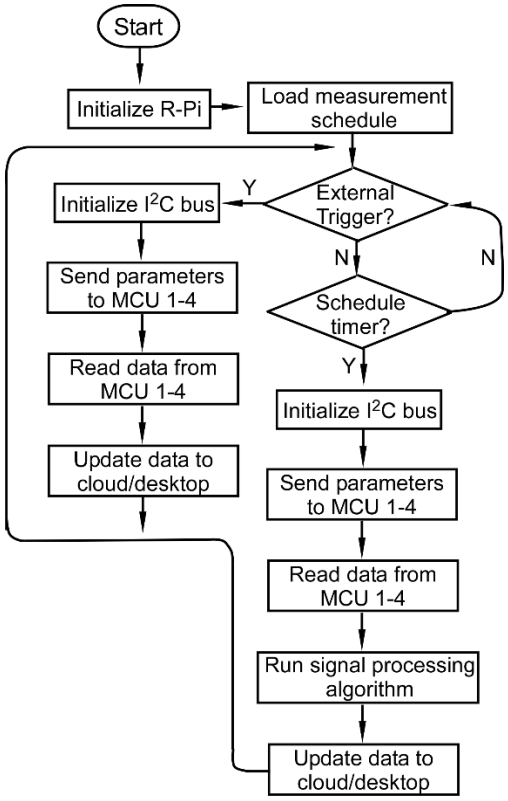



Fig. 3.18: Software flowchart for Raspberry Pi based external unit.

### 3.4.3 Remote Desktop User Interface (UI) Front-end

A custom User Interface (UI) application for the remote desktop, which is wirelessly connected to the external unit (*R-Pi*) over Wi-Fi, has been designed using Python programming language, very similar to the user interface, discussed in Chapter 2 (Fig. 2.7). The UI runs as an executable file on any Windows based system with wireless network connectivity. The interface provides an interactive platform and allows the user to remotely manage the PGM system, select measurement parameters, start and stop scheduled measurement, request an instant measurement, retrieve data from the external unit, plot the data in real time, and store the data in a nonvolatile memory.

### 3.5 System Testing and Validation

As described in Section 3.1, LC Sensors were interrogated with a coupled readout coil and associated readout node. Ideally, each LC Sensor is axially aligned to a readout coil with an *IG* of 4 mm. On receiving a command from the user through the graphical user interface (GUI), the *R-Pi* external unit serially communicates over an $I^2C$ bus with the MCU in each readout node to trigger a measurement cycle. During a measurement cycle, the MCU commands the DDS to supply a sinusoidal excitation signal to the standing wave ratio bridge circuit between the interrogation frequency range, *IFR*, of 11 – 15 MHz with an frequency step size, $f_{ss}$, of 35 kHz. The dwell time at each discrete frequency step is 100 ms, during which the ADC samples the four voltages of the standing wave ratio bridge circuit, collecting and averaging 250 samples to reduce uncorrelated white noise. These four voltages are then used to determine $Re\{Z_{in}\}$ at each discrete interrogation frequency. After completion of each measurement cycle, $Re\{Z_{in}\}$ values stored in the MCU Flash memory are transferred to the *R-Pi*, where a Python-based program extracts $f_0$ by applying a Gaussian fit, $F_{Zin}$, to the $Re\{Z_{in}\}$ dataset. The total time required by the PGM system to trigger four readout nodes into a measurement cycle, interrogate each LC Sensor over the *IFR*, transfer the $Re\{Z_{in}\}$ dataset from the MCU at each node to the R-Pi, and extract $f_0$ by fitting $F_{Zin}$, was 25 sec.

The combined interrogation time for all four nodes was limited by two primary factors: 1) the necessary settling time for the DDS frequency output and standing wave ratio circuit at each interrogation frequency to permit stabilization of the $\overrightarrow{|V_x|}$ values (≈50 ms) before they were digitized and 2) the available MCU Flash storage (<2 kB) of the digitized $\overrightarrow{|V_x|}$ value data. This settling time must be completed at each interrogation frequency; therefore, the total time required to interrogate all 112 frequencies across the full *IFR* was ≈6.5 sec (including an additional ≈5 ms to sample the desired $\overrightarrow{|V_x|}$ values). The limited Flash storage of the MCU required that the digitized

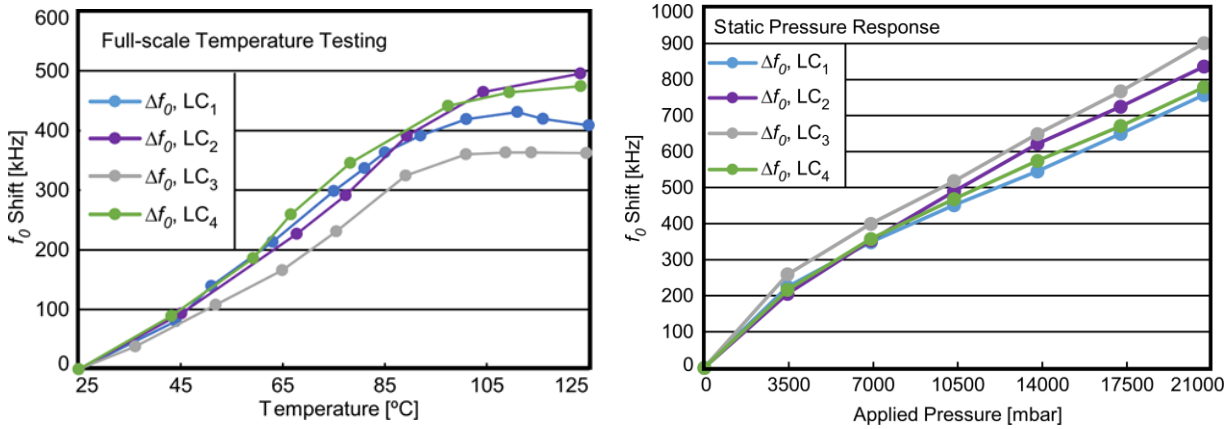
$\overrightarrow{|V_x|}$ values be transferred from the MCU to the external microcomputer after each frequency, taking ≈4.5 sec. Furthermore, data transfer between the readout PCB and microcomputer was limited to a single serial communication bus. As a modular design approach was utilized for the readout circuit (i.e. each readout node contained its own complete circuit), the data transfer speed was further limited, as each of the four individual MCU's was required to wait for the preceding MCU to complete its data transfer to the microcomputer before sending its own data, resulting in a total data transfer period of ≈18.5 sec for all four MCU's. In an alternate application scenario requiring higher operational bandwidth (and where the number of readout nodes is set), further refinement of the standing wave ratio bridge circuit could be completed to reduce settling time and a common excitation and readout electronics platform with a single, higher performance MCU and DDS to control all readout nodes simultaneously may be implemented, which could significantly reduce interrogation time. However, this would come at the cost of reducing the ability to scale the number of readout nodes without major system redesign.

### 3.5.1 Static Pressure and Thermal Response

To verify system operation over the full-scale temperature (25°C – 125°C) and pressure (0 bar – 20 bar) range, LC Sensors were axially aligned to each readout coil on the PCB with an *IG* of 4 mm. The PGM system was placed into an oven (at atmospheric pressure) and the temperature ramped from 25°C to 125°C while readings were continually taken. The system remained fully functional with no change in performance. $f_0$ shift due to temperature (where a shift of "0" refers to $f_0$ at 0 applied pressure and ambient temperature of 25°C) for four LC Sensors ($LC_1$ – $LC_4$) over the full-scale temperature range is shown in Fig. 3.19(a). All four LC Sensors showed a linear shift in $f_0$ of ≈5.3 kHz/°C from 25°C – 100°C, reducing to a shift of approximately 0.0 kHz/°C from 100°C to 125°C.

The PGM system was then placed inside a chamber and pressurized using nitrogen gas. Pressure was raised to 20,700 mbar (300 psi) at 25°C in steps of 3,447 mbar (50 psi). Readings were taken at each pressure step and are shown in Fig. 3.19(b); LC Sensors showed an average response of approximately 38 Hz/mbar from 0 bar to 20.7 bar.

Minor differences in temperature and pressure response between each LC Sensor can be attributed to slight variations in parasitic capacitance, planar coil inductance, and capacitance response of pressure transducers.




(a) (b)

Fig. 3.19: (a) Resonant frequency, $f_0$, shift of four LC Sensors over the full-scale temperature range of 25°C – 125°C, at zero applied pressure. (b) $f_0$ shift of four LC Sensors for an applied static pressure over the full-scale pressure range of 0 – 20 bar, at 25°C.

### 3.5.2 Conversion of Resonant Frequency to Pressure:

In order to convert $f_0$ to applied pressure while also accounting for changes in ambient temperature which also affect $f_0$, multi-dimensional regression (i.e. higher order polynomial curve fitting) [Cra90] was utilized. This approach involves fitting a 3-D polynomial surface to the LC Sensor response, where one dimension is applied pressure, one dimension is ambient temperature, and the third dimension is extracted $f_0$. A third order multi-dimensional polynomial was fit to the static pressure response as measured over the full-scale pressure range of 0 – 20.7 bar and temperature range of 25°C to 125°C. The calibration equation for conversion of the extracted

resonant frequency, $f_0$ and temperature, $T$, to applied pressure, $P_{App}$, is shown in (3.6), where $a_1$ - $a_6$ are fitted coefficients using least squares regression to the static full-scale pressure and temperature test data.

$$P_{App} = a_1(f_0)^3 + a_2(f_0)^2 + a_3(f_0) + a_4 + a_5(f_0 \cdot T) + a_6(T) \tag{3.6}$$

### 3.5.3 Pressure Resolution:

In the context of this work, resolution is defined as the RMS error (*e.g.* ±standard deviation) of at least 50 readings (n≥50) of the LC Sensor taken by the PGM system. The shift in resonant frequency, $\Delta f_0$, with applied pressure, $\Delta P$, (due to the change in capacitance, $\Delta C$, of the pressure transducer over the full-scale pressure range, $\Delta P_{FS}$) is defined as *Absolute Response,* $R_A$, equation (3.7). Pressure resolution was calculated by dividing $R_A$, into the RMS error of $f_0$, converting to units of pressure, equation (3.8).

$$Absolute\ Response, R_A == \frac{\Delta f_0}{\Delta P_{FS}} \approx \frac{\frac{1}{\sqrt{L_S C_S}} - \frac{1}{\sqrt{L_S(C_S + \Delta C)}}}{\Delta P_{FS}} \tag{3.7}$$

$$Pressure\ Resolution\ [mbar] = \frac{RMS\ Error\ of\ f_0\ [Hz]}{R_A \left[{Hz}/{mbar}\right]} \tag{3.8}$$

When this was completed, the resulting instantaneous pressure resolution permitted by the PGM system was found to be 46 mbar. In addition to the instantaneous pressure resolution, oversampling and averaging can be utilized to reduce noise and improve pressure resolution. This is accomplished by lowering in-band noise power without affecting signal power, improving effective resolution. Each quadrupling of the number of averaged samples lowers in-band noise by 6 dB, improving pressure resolution by a factor of two [Opp99]. Fig. 3.20 shows improvement in pressure resolution when oversampling and averaging are used; when 320 samples are averaged, resolution is improved to 1.0 mbar. In core-flood experiments, which operate for up to several

months, high bandwidth measurements are not necessary, permitting a large number of samples to be averaged for resolution improvement without impacting system efficacy.

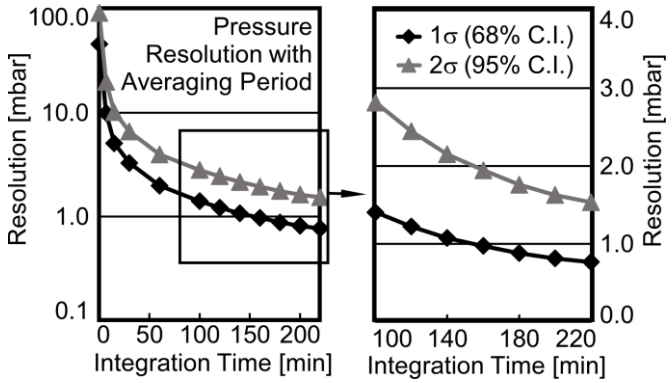
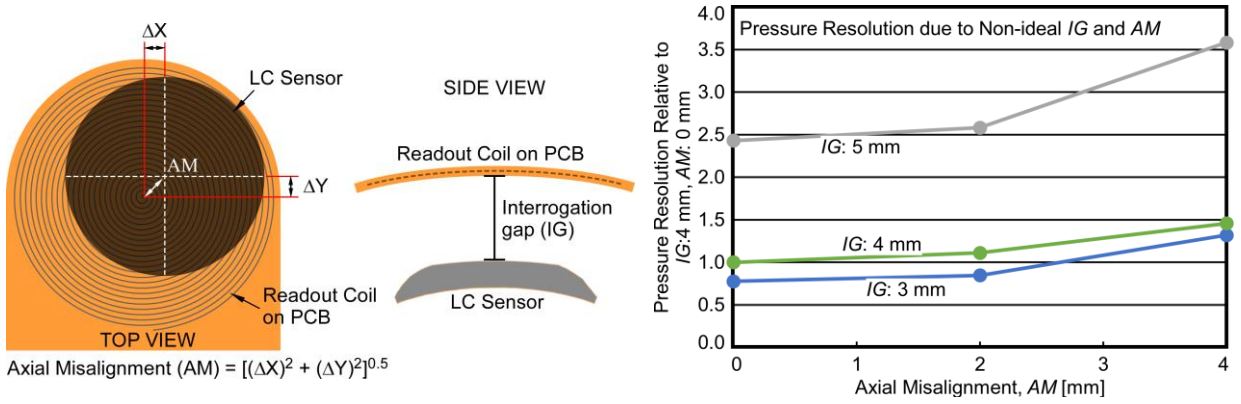



Fig. 3.20: Measured improvement in resolution of integrated Pressure Gradient Measurement (PGM) system when oversampling and averaging is utilized.

The impact of axial misalignment, *AM*, (Fig. 3.21(a)) of up to 4 mm was also studied at an *IG* of 3 mm, 4 mm, and 5 mm. The effect this non-ideal *IG* and *AM* has on pressure resolution has been plotted in Fig. 3.21(b) with respect to the measurement resolution of an LC Sensor with an ideal *AM* of 0 mm and *IG* of 4 mm. As the *IG* between LC Sensor and readout coil increases, the impact of *AM* on pressure resolution increases. The reduction in pressure resolution from 4 mm to 3 mm *IG* (*AM* = 0 mm) is ≈25%; however, the increase in pressure resolution from 4 mm to 5 mm *IG* (*AM* = 0 mm) is ≈145%. These results highlight the significance of considering *AM* and *IG* during the LC Sensor design process to optimize system performance with different deployment requirements. For instance, the optimal LC Sensor and readout coil design (i.e. the design which maximizes *DOF*) for an *IG* of 4 mm is not necessarily the same for an *IG* of 5 mm.




(a) (b)

Fig. 3.21: (a) Illustration of axial misalignment (*AM*) and interrogation gap (*IG*) (b) Measured relative impact on LC Sensor pressure resolution with non-ideal *AM* up to 4 mm and *IG* of 3 mm, 4 mm, and 5 mm.

### 3.5.4 Dynamic Pressure Response and Flow Test:

In order to apply a pressure gradient across multiple LC Sensors through fluid flow, a custom test setup was constructed, shown in Fig. 3.22. The setup consists of a peristaltic pump to generate constant fluid (mineral oil) flow, individual pressure chambers to house each LC Sensor, $LC_n$, (*IG* = 4 mm, *AM* = 0 mm) and Check Valves, $CV_n$, to create a known pressure differential, $\Delta P_{CV}$, between each chamber; commercial Pressure Gauges, $PG_n$, [NPX20] were used to monitor pressure in each LC Sensor chamber. When a flow rate of ≈32 mL/min was applied, $CV_1$ and $CV_3$ provided a $\Delta P_{CV}$ of 60 ± 5 mbar, while $CV_2$ provided a $\Delta P_{CV}$ of 35 ± 5 mbar. Uncertainty in $\Delta P_{CV}$ arises from resolution of the commercial gauges, flow fluctuations due to pulsating action of the peristaltic pump causing ripples in the fluid flow, varying pressure head due to consumption of oil in the upstream reservoir, and PG placement on the opposite side of the pressure chamber relative to the LC Sensor. Furthermore, CV's have a variance in opening pressure of up to 10% [Sma20].

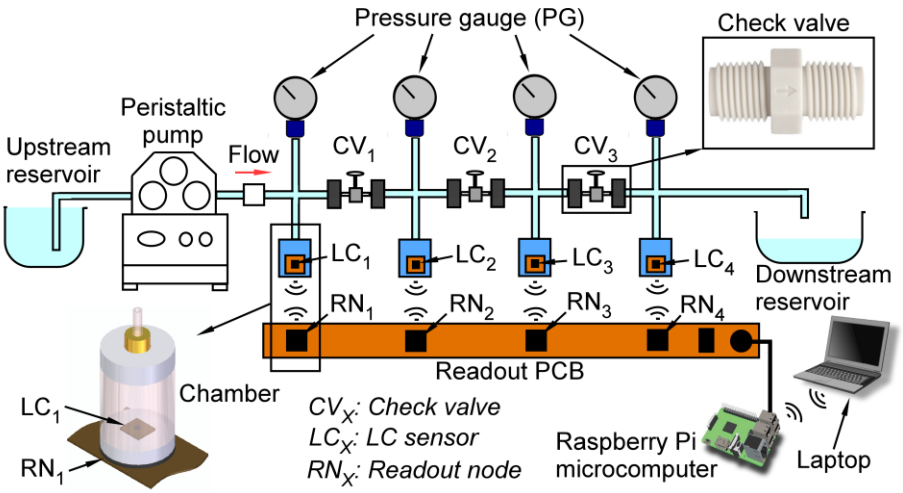



Fig. 3.22: Flow test setup schematic illustrating 4 LC Sensors ($LC_n$) located at 4 different locations along a flow path. 4 wired pressure gauges (PG) are located adjacent to the LC Sensors. Check valves ($CV_n$) create pressure drop along the flow path. Readout nodes ($RN_n$) wirelessly couple with individual LC Sensors for pressure readout.

In a typical experiment, LC Sensors were placed into each pressure chamber and axially aligned (*AM* = 0 mm) to readout coils on the Readout PCB with an *IG* of 4 mm. The test setup was then saturated with mineral oil by initiating fluid flow until steady state flow was established; fluid flow was then ceased and measurements were taken (i.e. pressure readings during a flow rate of 0 mL/min). The fluid flow was restarted and increased in 3 discrete steps of 14 mL/min, 24 mL/min, and 32 mL/min; the flow rate was held constant at each flow step for 225 min. Fig. 3.23(a) and Fig. 3.23(b) shows the raw resonant frequency shift, $\Delta f_0$ and temperature data recorded from the PGM system. Fig. 3.23(c) shows a time-series of pressure measurements from the four LC Sensors; 440 samples were averaged per measurement. The fluid flow rate during the experiment is plotted, shown in a solid red line. In the presence of flow, $LC_1$, being nearest to the pump, recorded the highest pressure head (inlet pressure); as the flow encounters resistance at each check valve, the pressure head drops sequentially from $LC_2$ to $LC_3$ to $LC_4$. Recorded pressure measurements from the commercial pressure gauges ($PG_n$) are shown in Fig. 3.23(d). The LC Sensor measurements are in close agreement with the PG measurements, differing by <5% on average. This difference

in pressure between LC Sensor and commercial PG measurements can be accounted for due to the fact that the LC Sensor and corresponding PG are not exactly collocated; fluctuations in ambient pressure in the room and flow resistance provided by the tube and connectors between the PG and LC Sensor can then result in minor differences between the two pressure levels at the LC Sensor and PG.

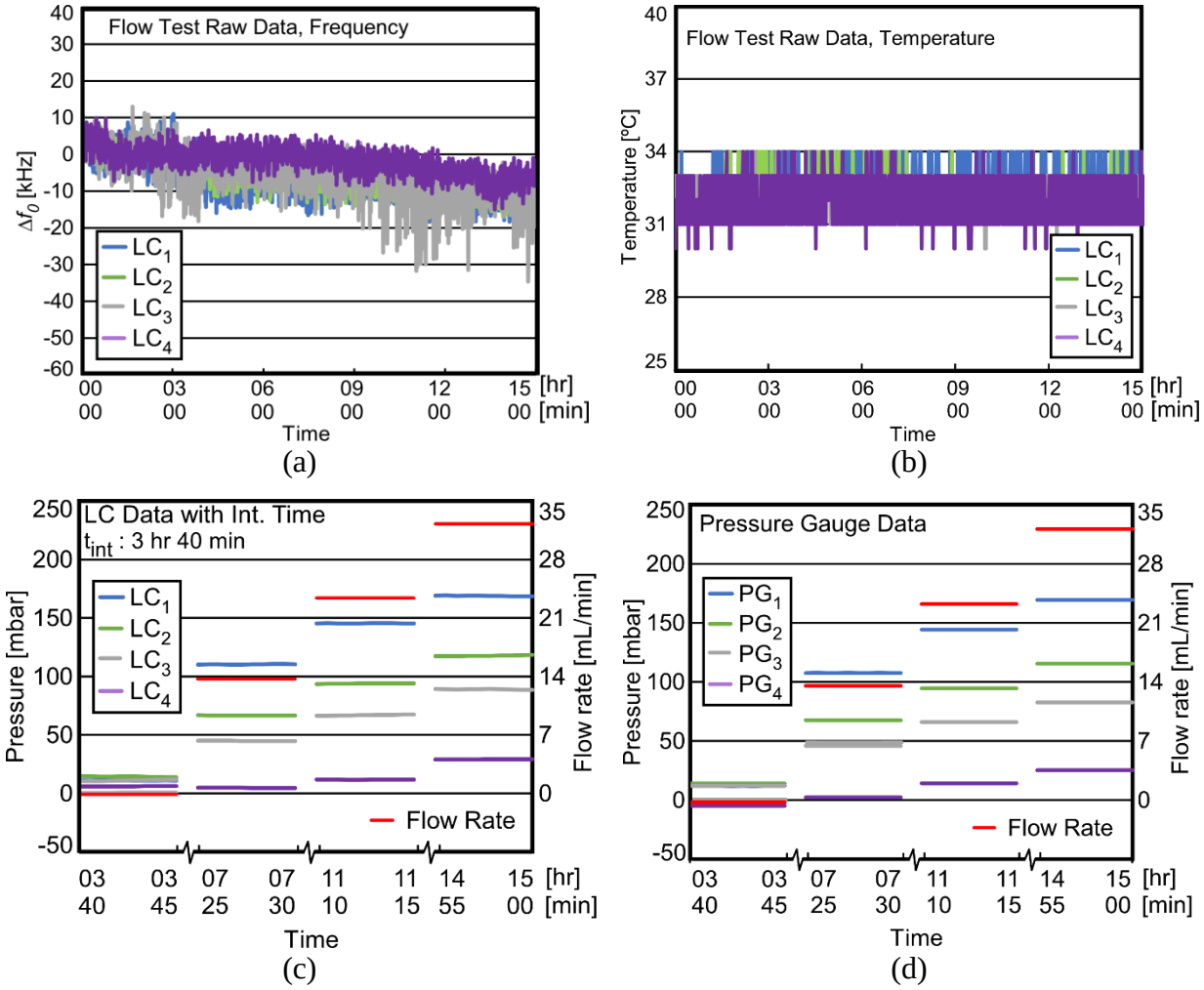



Fig. 3.23: (a) Raw resonant frequency shift, $\Delta f_0$ recorded from the PGM system during flow test (b) Temperature data recorded from PGM system during flow test (c) Pressure recorded by LC Sensors ($LC_n$) during flow experiment in custom setup (Fig. 3.22) at room temperature (25°C). The flow rate is increased in four discrete steps of 0 mL/min, 14 mL/min, 24 mL/min, and 32 mL/min. (d) Pressure measurements recorded by four wired pressure gauges ($PG_n$) during flow experiment, placed adjacent to the LC Sensors.

These results demonstrate the ability of the PGM system to not only measure static pressure with a resolution of up to 1.0 mbar when oversampling and averaging is utilized, but also detect pressure variations due to fluid flow in a dynamic fluid flow environment.

## 3.6 Chapter Summary

A passive wireless pressure measurement system was designed and evaluated to study flow induced pressure gradients. The presented PGM system was designed specifically to enhance core-flood experiments utilized in the energy industry. A surface micromachined pressure transducer was electrically coupled to a planar inductor coil on a flexible polyimide substrate to form a resonant inductor-capacitor (LC) sensor. Physical transducer and coil protection was provided by an enclosure fabricated from an AlSi10Mg aluminum alloy using DMLS 3D printing, which permitted size reduction while retaining structural rigidity. LC Sensor packaging involved encapsulation in Viton$^{TM}$ and thin film polyimide coating, providing chemical protection and permitting pressure transfer to the transducer. The packaged LC Sensor measured <ø15×3.0 mm$^3$.

To passively monitor pressure, the LC Sensor was inductively coupled to a planar readout coil and wirelessly interrogated utilizing inductive coupling telemetry. The pressure dependent resonant frequency, $f_0$, of the LC Sensor was extracted by analyzing the real part of the input impedance, $Re\{Z_{in}\}$, of the readout coil. $Re\{Z_{in}\}$ was computed using a standing wave ratio bridge circuit, where one branch was comprised of the readout coil and coupled LC Sensor. In addition to the standing wave ratio bridge circuit, the interrogation electronics were comprised of a direct digital synthesizer (DDS) to generate a sinusoidal excitation signal, a 12-bit analog to digital converter (ADC) for output signal digitalization, and a microcontroller for data collection and control. The readout circuitry and coil were fabricated on a polyimide substrate using conventional

PCB manufacturing and assembly techniques. Each pressure measurement cycle was completed by determining the magnitude of $Re\{Z_{in}\}$ over a set of discrete frequencies centered near $f_0$.

An external unit, comprised of a Raspberry Pi™ microcomputer and laptop with custom graphical user interface (GUI), was realized to permit data collection and analysis, as well as user control. After each pressure measurement cycle, $Re\{Z_{in}\}$ values stored in the MCU flash memory were transferred to the R-Pi, which applied a Gaussian fit, $F_{Zin}$, to the discrete $Re\{Z_{in}\}$ dataset to extract $f_0$ via interpolation. The laptop was remotely connected to the R-Pi via Wi-Fi for final data collection and user control through the (GUI). Collected sensor data can be uploaded to the cloud for further processing, storage, and analytics.

Based on theoretical analysis in MATLAB (MathWorks, USA) and FEA study in COMSOL Multiphysics® (COMSOL Inc., USA), the final design of the LC Sensor consisted of a two-layer planar inductor coil measuring 13 mm in diameter with trace width and spacing of 0.125 mm and one capacitive pressure transducer. The fully packaged LC Sensor provided an average response of approximately 38 Hz/mbar over a full-scale pressure range of 0 bar – 20.7 bar, resulting in a pressure resolution of up to 1.0 mbar when sample and averaging was utilized. System operation over the full-scale temperature range of 25°C to 125°C was successfully demonstrated, thus achieving all preferred system targets. The impact of *IG* and *AM* on LC Sensor pressure resolution was studied, showing that an *IG* of up to 5 mm and *AM* of up to 4 mm still provide meaningful pressure measurements.

A customized flow test setup was constructed to supply known pressure differentials during fluid flow; it was used to verify system operation and pressure measurement capability in a dynamic fluid flow environment. The PGM system demonstrated pressure measurements in close agreement with commercial PG measurements, differing by <5% on average, which can be

accounted for due to non-ideal collocation of LC Sensor and commercial PG, in which fluctuations in ambient pressure in the room and flow resistance of the tube and connectors between the PG and LC Sensor resulted in minor difference in pressures seen by LC Sensor and PG.

The physically realized passive wireless pressure sensing system was designed for implementation into core-flood experiments. It is a smaller, less costly, and more convenient alternate to CT scan-based fluid saturation estimation techniques, providing continuous, *in situ* pressure distribution measurements. The obtained pressure gradient information can aid in more accurately predicting properties of the geological sample such as porosity and permeability, while improving the overall efficiency and fault detection capability of the core-flood experiment. The flexible PCB design of the LC Sensors, combined with the flexible Viton$^{TM}$ packaging, allows it to conform to tight spaces with minimal disruption to fluid flow. Additionally, the packaging approach is compatible with high pressure, high temperature, and chemically corrosive environments. Four readout nodes (measuring <48×30 mm$^2$) and readout coils (measuring <ø18 mm$^2$) were designed onto a single readout PCB for simultaneous interrogation of four LC Sensors; however, the number of LC Sensors and readout nodes can be scaled up or down to meet the application needs.

# Chapter 4: Optimizing Minimum Resolvable Pressure Resolution in a Wireless LC Sensor System

This Chapter discusses the design principles and methodology for minimizing pressure resolution in a wireless inductor-capacitor (LC) sensor pressure measurement system. As previously described in Chapter 3, an LC Sensor (comprised of a capacitive pressure transducer and inductor coil) can be wirelessly interrogated via an inductively coupled external readout inductor, where the pressure dependent resonant frequency, $f_0$, of the LC Sensor will manifest as a disturbance in the readout inductor coil's complex impedance, $Z_{in}$. When appropriate interrogation circuity is used in conjunction with the readout coil, this pressure dependent $f_0$ disturbance in $Z_{in}$ can be extracted, permitting wireless measurement of the pressure applied to the LC Sensor.

In such a wireless LC Sensor pressure measurement system, four main design "blocks" have been identified, shown in Fig. 4.1, including 1) LC Sensor design, 2) Readout circuit hardware, 3) $Z_{in}$ detection technique, and 4) Control software. While specific design choices can be made for each major block which permit global improvement in pressure resolution regardless of design changes to other block (e.g. utilizing a higher performance ADC), nearly all design choices must be made with the consideration of how interplay between each block can affect parameters (and thus design choices) of adjoining blocks (e.g. how the physical design of LC Sensor and readout coils will affect their coupling, and thus $\Delta Z_{in}$). Design principles for minimizing pressure resolution by considering the complete pressure sensing system are described below.

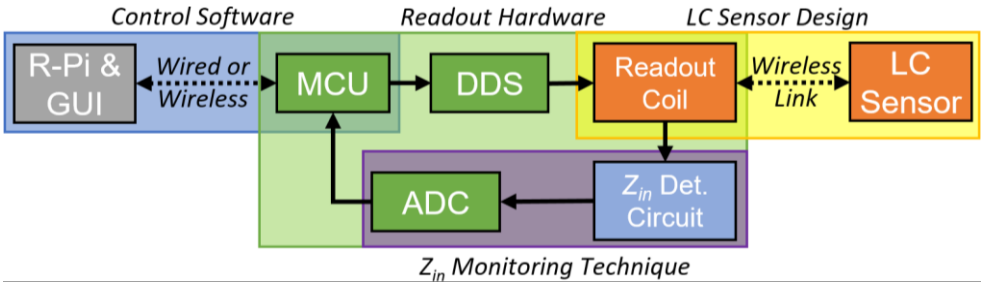



Fig. 4.1: Block diagram of LC Sensor readout system with the four major element blocks highlighted and how most sub-elements overlap within each major block.

## 4.1 Inductor-Capacitor (LC) Sensor Model

The pressure sensing element of a wireless LC Sensor system is the LC Sensor, comprised of a capacitive pressure transducer, $C_{XDCR}$, and inductive coil, $L_S$; a simplified LC Sensor circuit model is shown in Fig. 4.2. The parallel capacitance, $C_{PS}$, is due to any parasitic capacitance of the LC Sensor, as well as additional capacitance added in parallel with $C_{XDCR}$. The parasitic series resistance, $R_S$, is due to resistance of the inductor coil and the equivalent series resistance, $ESR_{XDCR}$, of the capacitive pressure transducer, resulting from the resistance of the thin film metal electrodes.

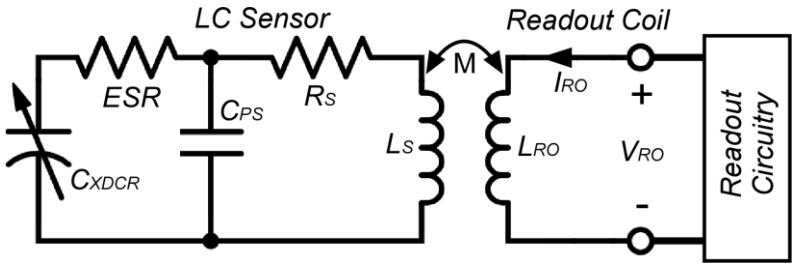



Fig. 4.2: Circuit model illustrating an LC Sensor and Readout coil and circuitry.

When the readout, $L_{RO}$, and LC Sensor, $L_S$, coils are in close proximity, they will become coupled, resulting in a mutual inductance, $M$. The pressure-dependent resonant frequency, $f_0$, of the LC Sensor, equation (4.1), will manifest as a peak in the complex input impedance, $Z_{in}$, of the readout coil, $L_{RO}$, calculated from $V_{RO}$ and $I_{RO}$, equation (2). $Z_{in}$ is monitored by the readout circuitry, described below. An alternate method to interpret $f_0$ involves measuring the phase dip, $\angle Z_{in}$, of the complex input impedance, $Z_{in}$, as described in [Ben19]. The phase dip, however, has a stronger dependence on coupling coefficient, $k$ between the sensor and the readout coil. In a

harsh environment application, where the value of $k$ is largely impacted by packaging materials, coil misalignment, and other environmental factors, the approach with relatively lesser dependence on $k$ was chosen.

$$f_0 \approx \frac{1}{\sqrt{(L_S) \cdot (C_{XDCR} + C_{PS})}} \tag{4.1}$$

$$Z_{in} = \frac{V_{RO}}{I_{RO}} \tag{4.2}$$

The mutual inductance, $M$, between the LC Sensor coil and readout coil is directly proportional to the input impedance magnitude, $\Delta Z_{in}$ (e.g. SNR of measured signal). The LC Sensor itself must be designed to balance the quality factor, $Q$ (peak sharpness) and LC Sensor response, $\Delta f_0/\Delta P$, (resonant frequency shift due to applied pressure). As the $Q$ of the detected signal's waveform increases (for a constant $f_0$, $\Delta f_0/\Delta P$, and $\Delta Z_{in}$), the minimum pressure resolvable by the system will improve due to an improvement in the accuracy with which $f_0$ (and thus applied pressure) can be determined. However, design changes which increase $Q$ will generally cause a reduction in LC Sensor response, potentially degrading the minimum resolvable pressure due to a smaller shift in $f_0$ for the same applied pressure. Additionally, if $M$ is low [Pic04], the input impedance magnitude $\Delta Z_{in}$ will also be small, reducing the SNR and degrading the resolvable pressure due to an increase in $f_0$ uncertainty. In order to minimize resolvable pressure, a balance between these three factors must be determined.

The LC Sensor quality factor, $Q$, [Deh02] and LC Sensor response (resonant frequency shift due to applied pressure, $\Delta f_0/\Delta$P) are dependent on not only the capacitive pressure transducer's ($C_{XDCR}$) capacitance change with pressure ($\Delta$C), but also the total parallel capacitance ($C_{PS} = C_P + C_{DUMMY}$) and the LC Sensor's coil inductance, $L_S$ [Moh99]; $C_P$ is estimated parasitic capacitance, and $C_{DUMMY}$ is any fixed ceramic capacitor placed in parallel with pressure transducer.

The degradation of $Q$ is primarily caused by the total effective series resistance, $R_S$, of the LC Sensor (the summation of the effective series resistance of the inductor coil and the $ESR_{XDCR}$ of the capacitive elements). The AC resistance of the coil, $R_{S,Coil}$, can be easily calculated and will vary depending on the coil trace length, cross-sectional area, and frequency [Whe42]. However, the $ESR_{XDCR}$ of the capacitive transducer is dependent on the specific transducer; it must be physically measured for the chosen transducer (in this instance pressure transducer P. XDCR, used in the PGM system described in Chapter 3, with an $ESR_{XDCR}$ of ≈200 Ω). With the addition of a parallel ceramic capacitor with a near zero series resistance, $C_{DUMMY}$, the total effective series resistance of the capacitive elements of the LC Sensor, $R_{ESR,Eff}$, can be reduced, at the cost of a reduced sensor response, $\Delta f_0/\Delta P$, due to an increase in the total LC Sensor capacitance. Relevant design equations are given below.

$$Q \approx \frac{1}{R_S}\sqrt{\frac{L_S}{(C_{XDCR}+C_{PS})}} == \frac{f_0}{\sigma} \tag{4.3}$$

$$R_{S,Coil} \approx \frac{(\rho)\cdot(Inductor\ Trace\ Length)}{(\delta)\cdot(Inductor\ Trace\ Width)} \tag{4.4}$$

$$Skin\ depth, \delta = \sqrt{\frac{\rho}{\pi\mu f_0}} \tag{4.5}$$

$$R_S = R_{S,Coil} + R_{ESR,Eff} \tag{4.6}$$

$$R_{ESR,Eff} \approx \frac{(ESR_{XDCR})\cdot(C_{XDCR})^2}{(C_{XDCR}+C_{PS})^2} \tag{4.7}$$

$$L \approx (1.94)(d_{out}^{-1.21})(d_{avg}^{2.4})(w^{-0.15})(s^{-0.03})(n^{1.78}) \tag{4.8}$$

$$Mutual\ Inductance, M \approx \left(\frac{\mu_0\pi}{2}\right)(n_{RO}n_S)\frac{(r_{RO}r_S)^2}{(r_{RO}^2+z^2)^{1.5}} \tag{4.9}$$

$$Coil\ Coupling, k = \frac{M}{\sqrt{L_{RO}L_S}} \tag{4.10}$$

σ: Bandwidth of LC Sensor response, defined as $f_0/Q$
$\rho$: Resistivity
$\mu$: Permeability
$d_{out}$: Maximum outer diameter of inductor coil
$d_{avg}$: Average diameter of inductor coil
$w$: Width of inductor coil traces
$s$: Space between each inductor coil trace
$n$: Number of turns in inductor coil
$n_{RO}$, $n_S$: Readout and sensor inductor coil turns
$r_{RO}$, $r_S$: Readout and sensor inductor coil radius

The shift in resonant frequency, $\Delta f_0$, with applied pressure, $\Delta P$, (due to the change in capacitance, $\Delta C$, of the pressure transducer over the full-scale pressure range, $\Delta P_{FS}$) is defined as *Absolute Response*, $R_A$, equation (4.11). $R_A$ is dependent on the choice of $C_{XDCR}$, $C_{PS}$, and $L_S$. The more responsive the transducer is to pressure (*e.g.* a larger $\Delta C/\Delta P_{FS}$, where $\Delta$C is the total change in capacitance over the full-scale pressure range, $\Delta P_{FS}$, of the pressure sensor), the larger the response will be; however, the larger total capacitance ($C_{XDCR} + C_{PS}$) and $L_S$ are (for a constant transducer response), the smaller the response will be.

$$Absolute\ Response, R_A == \frac{\Delta f_0}{\Delta P_{FS}} \approx \frac{\frac{1}{\sqrt{L_S C_S}} - \frac{1}{\sqrt{L_S(C_S + \Delta C)}}}{\Delta P_{FS}} \tag{4.11}$$

Input impedance magnitude, $\Delta Z_{in}$, defined in equation (4.12), is the difference in height between the maximum value of $Re\{Z_{in}\}$, found at approximately $f_0$, and the minimum value of $Re\{Z_{in}\}$, found far away from $f_0$ (at approximately $f_0/10$); it can also be estimated using $M$, $Q$, $L_{RO}$, and $L_S$. Increasing the input impedance magnitude can be accomplished by increasing the coupling, $k$, (and thus Mutual Inductance, $M$) between the readout coil and LC Sensor or increasing the quality factor, $Q$, of the LC Sensor. Coupling is primarily dependent on the physical parameters of $L_S$ (number of turns and diameter) and the spacing and orientation between $L_{RO}$ and $L_S$. For the PGM system discussed in Chapter 3, the maximum physical diameter of $L_S$ and spacing between $L_{RO}$ and $L_S$ are set by the physical boundary conditions of the rock core and required placement of

the LC Sensors. While increasing $Q$ can be accomplished by increasing $L_S$ or decreasing $C_S$, $Q$ is primarily improved by reducing the series resistance, $R_S$.

$$\Delta Z_{in} == Re\{Z_{in}(f_0)\} - Re\left\{Z_{in}\left({}^{f_0}/_{10}\right)\right\} \approx \left(\frac{M^2 Q}{L_{RO} L_S}\right) \tag{4.12}$$

In order to extract the pressure dependent $f_0$ of the LC Sensor, a set of discrete data points is collected, where each data point is the magnitude of $Re\{Z_{in}\}$ at a specific frequency. A typical captured dataset of $Re\{Z_{in}\}$ of the LC Sensor circuit is shown in Fig. 4.3 (duplicated from Fig. 3.3, Chapter 3); a Gaussian curve, referred to as the fitted frequency response waveform, $F_{Zin}$ is fit to each dataset. Bandwidth ($BW = \sigma$) is defined as $f_0/Q$, and mean ($\mu$) is defined as $f_0$. In this work, $\sigma$ is defined as the full width at half maximum (*FWHM*), which is the frequency span of the $Re\{Z_{in}\}$ dataset measured between the points which are half the input impedance magnitude, $\Delta Z_{in}$. By fitting the Gaussian curve, $F_{Zin}$, to the discrete points of the $Re\{Z_{in}\}$ dataset, $f_0$ can be determined through interpolation, vastly improving resolution without requiring collection of an intractably large number of data points. $F_{Zin}$ can be approximated using a Gaussian equation, equation (4.13).

$$F_{Zin} \approx \Delta Z_{in}\, exp\left(\frac{-(f-\mu)^2}{\sigma^2}\right) = \Delta Z_{in}\, exp\left(\frac{-(f-f_0)^2}{\left({}^{f_0}/_{Q}\right)^2}\right) \tag{4.13}$$

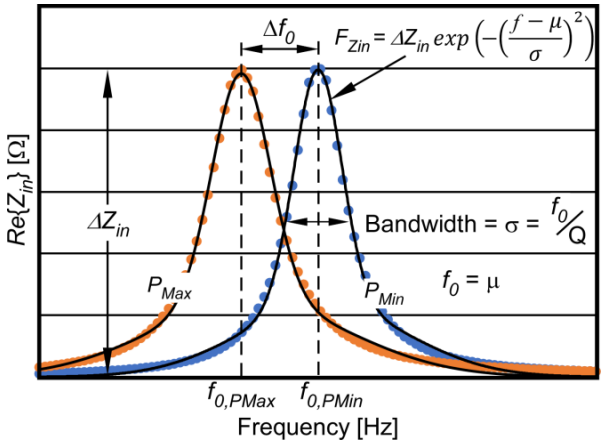



Fig. 4.3: Two $Re\{Z_{in}\}$ datasets at minimum *($P_{Min}$)* and maximum *($P_{Max}$)* applied pressure illustrating important parameters such as bandwidth, $\sigma$, resonant frequency, $f_0$, $f_0$ shift due to applied pressure, $\Delta f_0$, *and* fitted gaussian approximation, $F_{Zin}$, used to extract $f_0$ via interpolation.

## 4.2 Design Refinement Method of LC Sensor

In order to minimize resolvable pressure of the system, a balance between $\Delta Z_{in}$, $Q$, and $R_A$ must be found; furthermore, both readout coil and LC Sensor must be designed in tandem in order to ensure $M$ is large enough such that $\Delta Z_{in}$ is above the minimum detectable signal for the utilized readout electronics. When designing the LC Sensor, there are two main factors which must be considered: 1) $f_0$ is extracted through curve fitting of discrete data points; and 2) $\Delta Z_{in}$, $Q$ and $R_A$ are often in direct conflict – as one is increased, the other is reduced (e.g. $Q$ can be increased by adding parallel ceramic capacitor, $C_{DUMMY}$, to reduce $R_S$ contributed by transducer $ESR_{XDCR}$, but will result in a reduction in $R_A$). Additionally, final design parameters of the LC Sensor must remain within the physical boundary conditions of the specific application; for the core-flood experiment application explored in Chapter 3, Table 3.1.

The LC Sensor captured dataset of $Re\{Z_{in}\}$ is comprised of discrete data points, where each data point is the magnitude of $Re\{Z_{in}\}$ at a specific frequency. The frequency range over which $Re\{Z_{in}\}$ is measured (i.e. interrogation frequency range, $IFR$) must be wide enough so that curve fitting to extract $f_0$ can be completed. To capture >99% of the sensor readout across the full-scale pressure (assuming a Gaussian approximation, described above), a frequency range of approximately $\pm 3\sigma$ plus the span of $f_0$ shift over $\Delta P_{FS}$ is required. In addition to $IFR$, the step size between each discrete data point (frequency step size, $f_{ss}$) must also be carefully chosen. With fewer data points, data collection bandwidth can be improved, but curve fitting performance (and thus resolution) may decrease. Empirical experimentation with the utilized curve fitting algorithm implemented withing the R-Pi microcomputer showed that performance saturated beyond a data density of approximately 10 points within the LC Sensor frequency response bandwidth, $\sigma$ ($f_0/Q$). Therefore, a $f_{ss}$ of $\sigma/10$ ($f_0/10 \cdot Q$) is used.

With the discrete nature of the captured dataset of $Re\{Z_{in}\}$ in mind, it is important to note that, regardless of absolute values of $Q$ and $\sigma$, the $Re\{Z_{in}\}$ datasets for all LC Sensor designs will look identical over their *IFR* (i.e. the dataset will be normalized over its respective bandwidth). However, $Re\{Z_{in}\}$ dataset $f_0$ shift due to applied pressure, when viewed over this bandwidth normalized spectrum, will vary; therefore, it is not $R_A$ which should be examined, but rather $R_A$ *relative* to the LC Sensor bandwidth (i.e. *Relative Response*, $R_R$), defined in equation (4.14).

$$Relative\ Response, R_R == \left(\frac{R_A}{\sigma}\right) = \left(\frac{R_A\, Q}{f_0}\right) \tag{4.14}$$

In addition to $R_R$, input impedance magnitude, $\Delta Z_{in}$, must be considered as well, as it has a direct impact on resolution. $\Delta Z_{in}$ is directly proportional to SNR, assuming a constant white noise across the entire frequency spectrum. Improving $\Delta Z_{in}$ can be accomplished by increasing $M$ or increasing quality factor, $Q$, of the LC Sensor. $M$ is primarily dependent on the physical parameters of the inductors (such as number of turns and diameter) and the spacing and orientation between the coils. While $Q$ can be improved by increasing $L_S$ or decreasing $C_S$, it is primarily improved by reducing the total effective series resistance, $R_S$. $\Delta Z_{in}$ and minimum resolvable pressure are approximately linearly related (*i.e.* a 2x increase in $\Delta Z_{in}$ will improve resolution by ≈2x).

To better illustrate how $Q$, $R_R$, $R_A$, and $\Delta Z_{in}$ are interconnected, Fig. 4.4 shows a SPICE simulation of three $Re\{Z_{in}\}$ datasets for different designs using parameters as listed in Table 4.1, which are plotted over their normalized bandwidth, $\sigma$. The simulation shows the $\Delta f_0$ for an applied pressure of 20 bar; one design maximizes *Absolute Response*, $R_A$ (red), one maximizes *Relative Response*, $R_R$ (orange), and one maximizes a proposed figure of merit in this work, Design Optimization Factor, *DOF* (green), where *DOF* is detailed below.

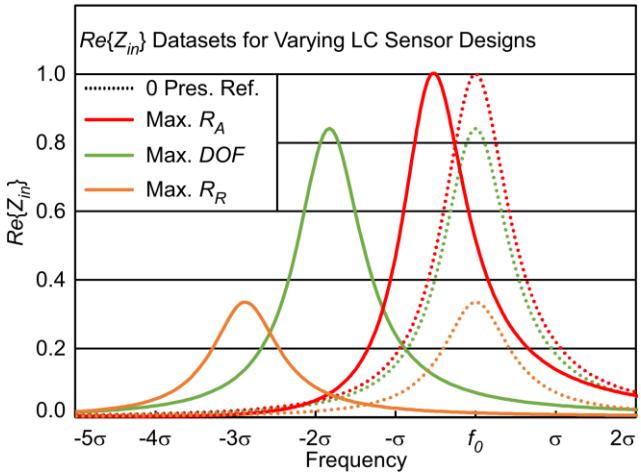



Fig. 4.4: Comparison of example $Re\{Z_{in}\}$ datasets at 0 and 20 bar applied pressure for three different LC Sensor designs with varying absolute and relative LC Sensor Response, $R_A$ and $R_R$, and Design Optimization Factor, *DOF*. All datasets are plotted over their respective bandwidth (i.e. bandwidth normalized); $Re\{Z_{in}\}$ datasets at 0 applied pressure are represented with dashed lines; $Re\{Z_{in}\}$ datasets at 20 bar applied pressure are represented with solid lines.

Table 4.1: LC Sensor specifications used in SPICE circuit simulation of Fig. 4.4.

| | Equ. | Red (Max. $R_A$) | Orange (Max. $R_R$) | Green (Max. *DOF*) |
|---|---|---|---|---|
| **P. XDCR** | --- | 1 Pressure Transducer | | |
| **$L_S$ Diam.** | --- | 13.0 mm | | |
| **Trace Width** | --- | 0.925 mm | 0.125 mm | 0.125 mm |
| **Inductor Layers** | | 2 | 4 | 2 |
| **Inductance** | (4.8) | 0.6 µH | 36.4 µH | 10.5 µH |
| **$f_0$ [MHz]** | (4.1) | 52.8 | 6.7 | 12.5 |
| **σ [kHz]** | --- | 7178 | 167 | 494 |
| ***Q*** | (4.3) | 7.3 | 40.1 | 25.3 |
| **$(\Delta Z_{in})_{norm}$** | --- | 1.00 | 0.35 | 0.88 |
| **$R_A$ [Hz/mbar]** | (4.11) | 0.189 | 0.024 | 0.045 |
| **$R_R$ [ppm/mbar]** | (4.14) | 827 | 4163 | 2662 |
| **$DOF_{norm}$** | (4.15) | 0.33 | 0.63 | 1.00 |

As shown in Table 4.1, the design maximizing $R_A$ has the smallest $R_R$ (as its $\sigma$ is >14x larger than the other designs). The design maximizing $R_R$ results in the smallest $\Delta Z_{in}$ due to the high $R_S$ of its LC Sensor coil. However, the design maximizing *DOF* results in a response with neither the largest $R_R$ or $\Delta Z_{in}$, having $Q$ and $R_A$ values between these two extremes, shown in green.

To identify the ideal balance of absolute frequency response, $R_A$, quality factor, $Q$, and input impedance magnitude, $\Delta Z_{in}$, for any given LC Sensor design, a formula which accounts for the bandwidth normalization due to the discrete nature of the collected data as well as the SNR effect due to $\Delta Z_{in}$ is needed. This figure of merit, referred to the Design Optimization Factor, *DOF*, given in equation (4.15), is relative response, $R_R$, multiplied by input impedance magnitude, $\Delta Z_{in}$. While seemingly simple, this equation accounts for all aspects of the $Re\{Z_{in}\}$ dataset previously described, with the bandwidth normalization effect encompassed within the $R_R$ term and the linear effect of SNR encompassed within the $\Delta Z_{in}$ term. It should be noted that the design with the *maximum* value returned by the *DOF* is the LC Sensor design which will theoretically permit the *minimum* resolvable pressure. Alternatively, the inverse of equation (4.15) will be proportional to pressure resolution. When a proportionality factor, $P$, (a fitted value specific to the noise level in the readout circuit), is multiplied into this equation, simulated pressure resolution values, $Resol_{SIM}$ can be found, shown in equation (4.16).

$$Design\ Optimization\ Factor, DOF == R_R\ \Delta Z_{in} = \left[\frac{R_A\ Q\ \Delta Z_{in}}{f_0}\right] \tag{4.15}$$

$$Simulated\ Pressure\ Resolution, Resol_{SIM} \approx P\left(\frac{f_0}{R_A\ Q\ \Delta Z_{in}}\right) \tag{4.16}$$

Compared to the design with the largest $R_R$ and $Q$ (orange), the design with the largest *DOF* (green) has a relative response ≈40% less; however, it has an input impedance magnitude ≈2.5x larger, resulting in an overall improvement in $Resol_{SIM}$ by ≈1.6x.

An analytical LC Sensor design optimization model was investigated in MATLAB to sweep all physical design parameters of the LC Sensor such as inductor trace width and spacing, number of layers in sensor PCB, number of pressure transducers, necessary adjustments to $C_{PS}$ with use of a dummy capacitor, $C_{DUMMY}$ in parallel with the pressure transducer, etc... in an effort to find the

physical parameter set which results in the highest *DOF*. The studied model has been used in design of the PGM system, described in Chapter 3 of this dissertation.

In addition to optimizing pressure resolution, maximizing the input impedance magnitude, $\Delta Z_{in}$, is necessary beyond a certain threshold value, since it is directly proportional to SNR. Accurate readout of an LC Sensor response with a low $\Delta Z_{in}$, shall be limited by the capabilities of the readout circuitry used and the measured noise floor. For a more intuitive understanding, $\Delta Z_{in}$ can be analytically approximated using equation (4.17), where $f_0$ is LC Sensor resonant frequency, $L_{RO}$ is readout coil inductance, $k$ is coupling coefficient, and $Q$ is quality factor [Nop10]. If we just consider the LC Sensor, not considering $L_{RO}$, $\Delta Z_{in}$ can be increased through increase in parameters, $k$, $M$, and/or $Q$. These three electrical parameters of the LC Sensor may be positively impacted through the four physical design parameters listed below.

$$Input\ Impedance\ Magnitude, \Delta Z_{in} \approx 2\pi f_0 L_{RO} k^2 Q \tag{4.17}$$

*1. Increasing Coil Diameter:*

The coupling between the LC Sensor and readout coil is primarily dictated by the diameter of the coils, i.e., number of turns in the respective inductors and the interrogation gap, *IG* between the two coils. Higher the number of turns, higher the coupling between the coils, at constant *IG*. To understand the impact of coil diameter on *k*, the FEA model described in (Chapter 3, Fig. 3.4) was further analyzed. The improvement in *k* (relative to a coil diameter of 13 mm (1x), as used in the PGM system, at 4 mm *IG*) with a 1.5x and 2x coil diameter has been plotted at different values of *IG*. As shown in Fig. 4.5, a 1.5x coil diameter (19.5 mm) would permit the same coil coupling at 7 mm *IG*, which we observe for the current LC Sensor design at 4 mm *IG*. However, maximum permitted coil diameter and *IG* are often dictated by the application requirement, as it is in case of the PGM system.

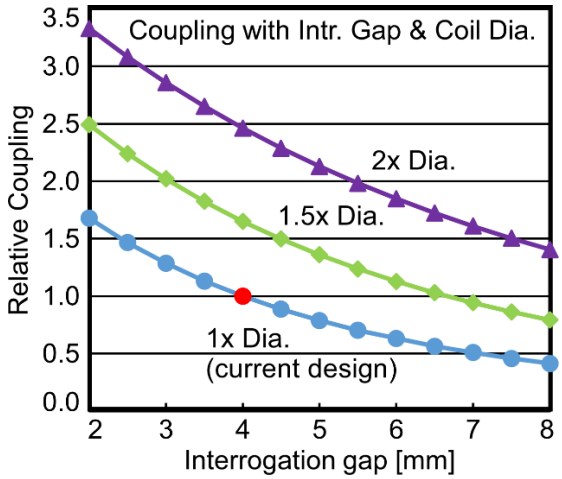



Fig. 4.5: Impact of sensor and readout coil diameter on relative coupling, with varying *IG*.

*2. Increasing PCB layers:*

LC Sensor coil inductance, $L_S$, can be increased by increasing number of turns in the PCB. One way to achieve that would be in the vertical plane by adding more layers to the PCB. A FEA model and SPICE simulation were studied in tandem to understand the impact of increasing number of turns by adding more layers to the PCB. For two, three and four PCB layers using the same trace width and spacing of 0.125 mm, and diameter of 13 mm, estimated LC Sensor coil inductances are 7 µH, 14.5 µH, and 26 µH respectively. However, the coupling coefficient remained unchanged at ≈0.10. These $L_S$ and $k$ values were then input into an LTSPICE circuit model. Although $Q$ of the *captured dataset of* $Re\{Z_{in}\}$ improved slightly in simulation, with additional layers, $\Delta Z_{in}$ stayed unchanged. This effect can be intuitively understood as increasing $Ls$ increases $Q$, (and $\Delta Z_{in}$), equation (4.3), but will reduce $f_0$ (and $\Delta Z_{in}$), equation (4.1), thus balancing out its effect on $\Delta Z_{in}$. In order to gain improvement in $\Delta Z_{in}$ through using more PCB layers, the inductor series resistance, $R_{LS}$ must be reduced by using a thicker inductor trace while also maintaining the same value of coil inductance. In addition, more layers in the PCB will lead to a proximity effect, further increasing the AC effective series resistance of the coil, and degrading $\Delta Z_{in}$.

*3. Modifying $C_{DUMMY}$:*

The main purpose of $C_{DUMMY}$ is to reduce the effective series resistance of the capacitive pressure transducers, $ESR_{XDCR}$, at the cost of increasing the total parallel capacitance, $C_{PS}$ and reducing sensor response ($\Delta C/\Delta P_{FS}$). This approach may work if the intrinsic parasitic capacitance of the circuit is low (<5 pF), while the series resistance is very high (>200 Ω). However, if the parasitic capacitance is already high (as it is in the PGM system, 14 pF measured), the cost of further increasing the capacitance baseline is higher on $\Delta Z_{in}$ as $f_0$ reduces. Hence, the use of $C_{DUMMY}$ must be carefully considered based on the state of other design parameters.

*4. Changing number of capacitive pressure transducers:*

Although it may intuitively seem utilizing more capacitive pressure transducers per LC Sensor should always improve the absolute response, $R_A$ and reduce the series resistance of the LC Sensor, for certain high values of the parasitic capacitance, using equation (4.18), the total transducer and dummy capacitor series resistance, $R_{CS}$ (also illustrated in Fig. 4.8) may increase with increase in number of capacitive pressure transducers, as $C_{XDCR}$ also increases proportionally with the number of transducers. For example, in the absence of any $C_{DUMMY,}$ for a parallel capacitance, $C_{PS}$ of 10 pF, the value of $R_{CS}$ for a two-transducer design (for the LC Sensor coil parameters used in the PGM system) is ≈25 Ω, while for a one-transducer design it is ≈22 Ω, as shown in Table 4.2. In addition to a reduction in series resistance, a lesser transducer design would also reduce the baseline capacitance, increasing $f_0$.

$$R_{CS} = \frac{ESR_{XDCR}C_{XDCR}^2}{(C_{XDCR} + C_{PS})^2} \tag{4.18}$$

Table 4.2: $R_{CS}$ for varying number of transducers, $ESR_{XDCR}$'s, and $C_{PS}$ values.

| | $C_{PS}$ = 3 pF | $C_{PS}$ = 10 pF |
|---|---|---|
| One XDCR, *ESR*=50 Ω | 20 Ω | 5.6 Ω |
| One XDCR, *ESR*=200 Ω | 78 Ω | 22 Ω |
| Two XDCR, *ESR*=50 Ω | 15 Ω | 6.3 Ω |
| Two XDCR, *ESR*=200 Ω | 59 Ω | 25 Ω |

## 4.3 Impact of Packaging Materials on LC Sensor Design

In order to fully utilize the LC Sensor refinement method presented above in section 4.2, electrical characteristics of the LC Sensor were fitted to measured data using a full circuit model representing the LC Sensor in LTSPICE, shown in Fig. 4.6, below. LC Sensors with 2 parallel capacitive pressure transducers and additional parallel ceramic capacitor ($C_{DUMMY}$) of 0 pF, 15 pF, and 47 pF were created (all other parameters unchanged from LC Sensor design proposed in Chapter 3). These LC Sensors were interrogated when packaged with both non-magnetic (316L) and magnetic (15-5) stainless steel top metal covers.

Each capacitive transducer ($C_{XDCR}$) has an equivalent series resistance ($ESR_{XDCR}$) associated with it. The LC Sensor inductor has a parasitic resistance ($R_{LS}$) and capacitance ($C_P$) associated with it. $C_{DUMMY}$ is the added parallel ceramic capacitor, placed in parallel with the pressure transducers.

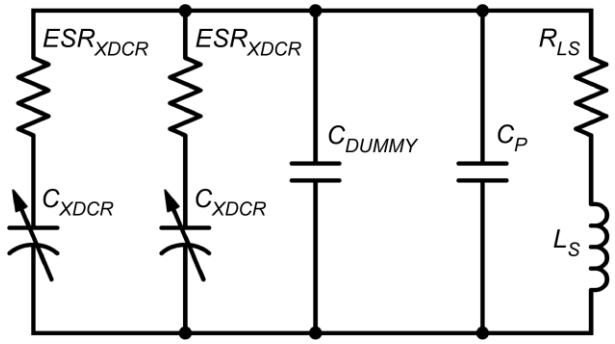
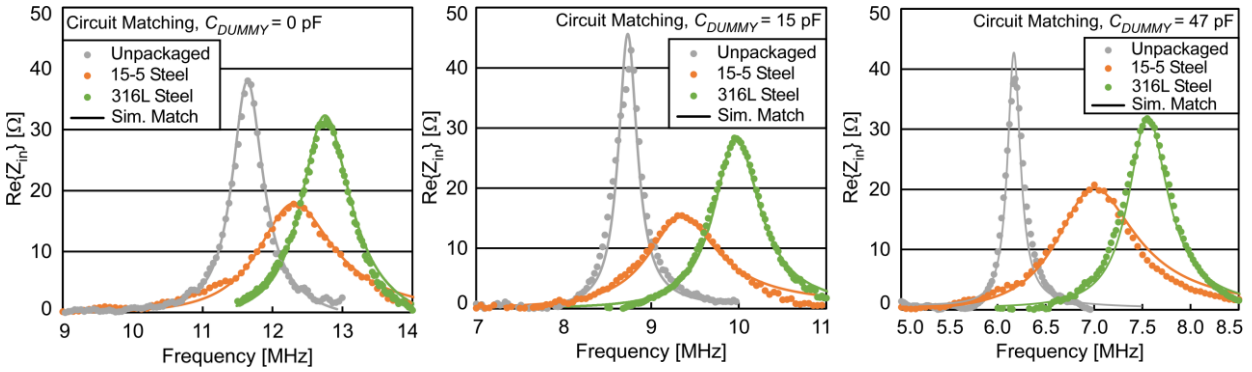


Fig. 4.6: Full circuit model for LC Sensor showing all parasitic resistances and capacitances.

Table 4.3: Fitted component values for measured results.

| Component | Unpackaged | 316L Steel Cover | 15-5 Steel Cover |
|---|---|---|---|
| $C_{XDCR}$ | 4.1 pF | 4.1 pF | 4.1 pF |
| $ESR_{XDCR}$ | 150 Ω | 150 Ω | 150 Ω |
| $L_S$ | 10.5 µH | 10.5 µH | 10.5 µH |
| $R_{LS}$ | 8.5 Ω | 13 Ω | 47 Ω |
| $C_P$ | 8.0 pF | 6.0 pF | 6.0 pF |

As shown in Fig. 4.7(a-c), when the fitted values shown in Table 4.3 are used, the simulation curves fit the measured data exactly. These fitted values are within the range of expected variation for the theoretical expected values. Based on these results, it may be inferred that the packaging material electrically manifests itself as an increase in the parasitic resistance of the inductor ($R_{LS}$). While the unpackaged LC Sensor has the highest $Q$, and $\Delta Z_{in}$ (lowest $R_{LS}$), the more magnetic the top metal cover material is, higher is the deterioration in measured $Q$, and $\Delta Z_{in}$, through a large increase in $R_{LS}$.




(a) (b) (c)

Fig. 4.7: Measured results of LC Sensors unpackaged, packaged with non-magnetic (316L), and packaged magnetic (15-5) stainless steel top metal cover with two parallel pressure transducers and varying dummy ceramic capacitors ($C_{DUMMY}$). Simulation curves are obtained using the circuit from Fig. 4.6 and the values given in Table 4.3.

Based on these findings, a modified LC Sensor circuit model has been shown in Fig. 4.8(a) for the previously simulated circuit model in Fig. 4.6. In this new model, an equivalent series resistance, $R_{COVER}$, has been added in series with the inductor parasitic resistance, $R_{LS}$. $R_{COVER}$

represents the increased AC effective series resistance due to eddy currents formed in the package material (top metal cover) during sensor interrogation.

An analytical circuit simplification for the LC Sensor has been highlighted in Fig. 4.8 (a-d) to reduce the LC Sensor circuit model into a simple R-L-C series circuit. Typical values for each sensor parameter, as discussed in Chapter 3, have been included for better understanding of the simplification steps. The simplified LC Sensor circuit model is composed of two capacitive pressure transducer, $C_{XDCR}$, and inductive coil, $L_S$. The parasitic capacitance, $C_P$, is due to any parasitic capacitance of the LC Sensor, while $C_{DUMMY}$, denotes any additional ceramic capacitor added in parallel to the capacitive pressure transducer. The parasitic series resistance, $R_{EFF}$, is due to the resistance of the inductive sensor coil $R_{LS}$, effective ac resistance of metal covers due to eddy current $R_{COVER}$, and the equivalent series resistance, $R_{CS}$, of the capacitive pressure transducer and parallel capacitor.

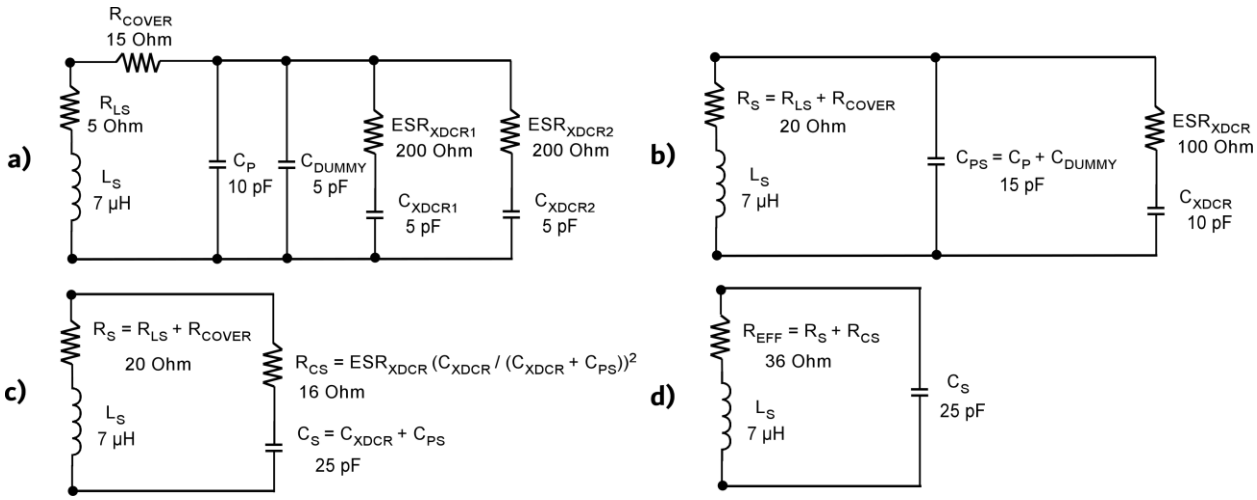
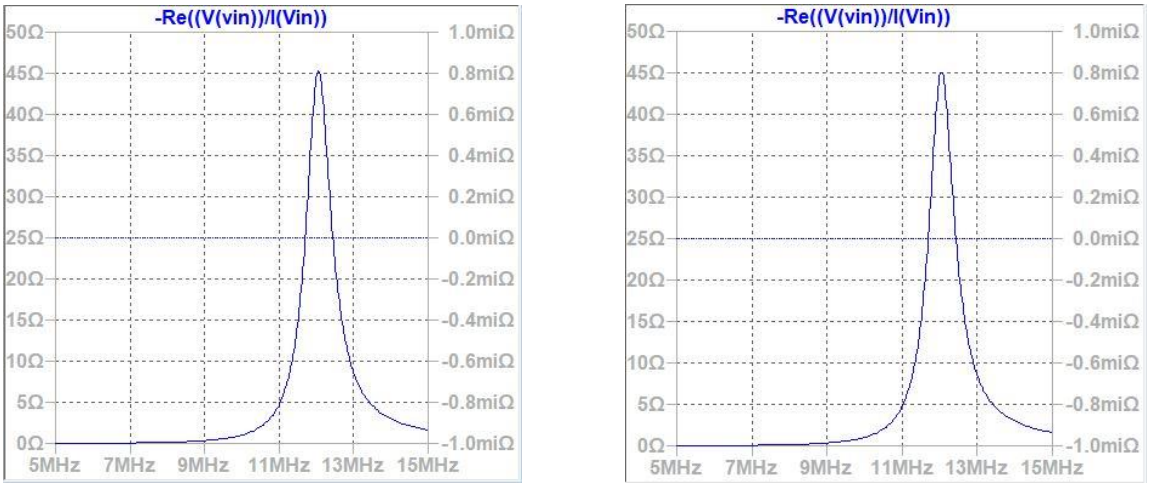



Fig. 4.8: Fig. 1: (a)-(d) Analytical simplification of example LC Sensor circuit model.




(a) (b)

Fig. 4.9: (a) LTSPICE simulated input impedance of circuit model in Fig 4.7(a). (b) LTSPICE simulated input impedance of circuit model in Fig 4.8(d).

The original circuit model (Fig 4.8(a)) and simplified circuit model (Fig 4.8(d)) of the LC Sensor was simulated using LTSPICE to verify accuracy of circuit simplification, and their simulated input impedance waveforms have been shown in Fig 4.9(a) and (b) respectively. Both circuit models produce a near identical $Re\{Z_{in}\}$ output, validating the simplification method.

## 4.4 Verification of Proposed LC Sensor Design Refinement Method

In order to verify the simulated pressure resolution, $Resol_{SIM}$ presented in equation (4.16), the resolution of multiple LC Sensor designs with different parallel capacitances ($C_{PS}$) was measured. A proportionality factor, $P$, is used in equation (4.16) to scale the output to the measured resolution, as the equation returns relative values not representative of an actual pressure resolution.

Measured Pressure Resolution, $Resol_{MEAS}$ is defined as the RMS error (*e.g.* standard deviation) of ≥50 readings ($n$≥50) of the LC Sensor. The RMS error of the set of extracted $f_0$, $(f_0)_{RMS}$ is determined and then divided by the LC Sensor absolute response, $R_A$, equation (4.11), thereby converting to units of pressure, as shown in equation (4.19). The complete readout circuity (including curve fitting to extract $f_0$) is used to evaluate the resolution using the PGM system described in Chapter 3.

$$Pressure\ Resolution,\ Resol_{MEAS}\ [mbar] = \frac{(f_0)_{RMS}[Hz]}{\frac{\Delta f_0}{\Delta P_{FS}}\left[{}^{Hz}/_{mbar}\right]} = \frac{(f_0)_{RMS}[Hz]}{R_A\left[{}^{Hz}/_{mbar}\right]} \quad (4.19)$$

LC Sensors using two parallel pressure transducers with varying values for the additional $C_{PS}$ capacitor were created. Prior to interrogation, the LC Sensor was placed into a sealed chamber composed of non-conductive material (to permit the LC Sensor to be interrogated by the readout coil through the chamber) to eliminate any atmospheric pressure fluctuations that would cause a change in the pressure transducer capacitance and manifest as increased noise. 50 readings were then taken and the instantaneous pressure resolution was calculated as described above in equation (4.19). Resolution measurements of LC Sensors with $C_{PS}$ values of 0 pF, 15 pF, and 47 pF were completed. Unpackaged LC Sensors, LC Sensors with non-magnetic steel (316L) protective caps, and LC Sensors with magnetic stainless steel (15-5) protective top metal covers were tested. Using a proportionality factor of $P$=45, it can be seen in Fig. 4.10 and Table 4.4 that the theoretical simulated pressure resolution, $Resol_{SIM}$ using equation (4.16) matches very closely with the measured pressure resolution, $Resol_{MEAS}$ by the PGM system (<11% mismatch). These measurements validate the proposed design refinement method for the LC Sensor using the new figure of merit (*DOF*) approach to accurately predict LC Sensor pressure resolution.

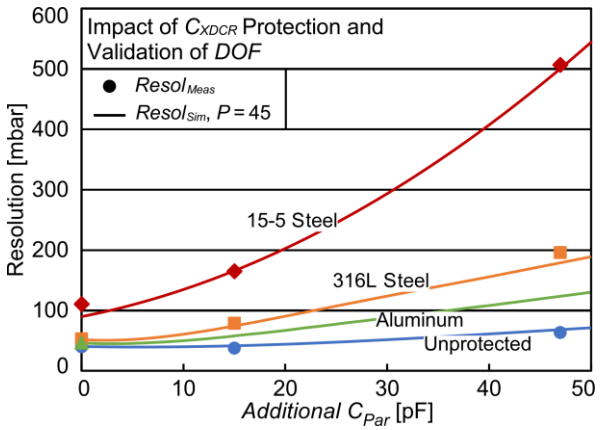



Fig. 4.10: Measured and simulated resolution of LC Sensor with and without top metal covers using equation 4.17 with a proportionality factor, $P$=45, and the fitted LC Sensor values as presented in Table 4.4.

Table 4.4: Resolution results of LC Sensor

| $C_{PS}$ | Packaging | $Resol_{SIM}$, eqn. (4.16) | $Resol_{MEAS}$, eqn. (4.19) |
|---|---|---|---|
| 0 pF | Unpackaged | 24 mbar | 23 mbar |
| 15 pF | Unpackaged | 24 mbar | 22 mbar |
| 47 pF | Unpackaged | 39 mbar | 37 mbar |
| 0 pF | 316L Steel | 29 mbar | 31 mbar |
| 15 pF | 316L Steel | 43 mbar | 46 mbar |
| 47 pF | 316L Steel | 104 mbar | 115 mbar |
| 0 pF | 15-5 Steel | 58 mbar | 65 mbar |
| 15 pF | 15-5 Steel | 103 mbar | 97 mbar |
| 47 pF | 15-5 Steel | 313 mbar | 298 mbar |

## 4.5 Readout Circuitry and Frequency Sweeping Factors Impacting Resolution

Thus far, we have assumed that the LC Sensor response can be perfectly captured and digitized with no noise present. However, this is obviously not true; the choice of analog to digital converter (ADC) will have a large impact on not only the minimum resolvable pressure resolution, but also on the maximum readout bandwidth.

*1. ADC sampling and noise reduction through sample averaging:*

If an ADC with a faster sampling rate is utilized, more samples can be taken and averaged, permitting a reduction in both white noise and quantization error. White noise is reduced by a factor proportional to the number of averaged samples to the one-half power (equation 4.20). The ADC resolution will also impact the noise level, as a lower resolution will result in larger quantization error; however, this effect is minimized with sample averaging (the signal must be oversampled by a factor of 4 for each additional effective bit of resolution) and the RMS white noise on the input signal is typically much greater than the quantization error, even when a relatively low resolution 12-bit ADC is used.

$$Noise\ Reduction\ Factor \propto \sqrt{(No.\ Avg'd\ Samples)} \tag{4.20}$$

*2. Readout circuit noise:*

To calculate $Re\{Z_{in}\}$, for the PGM system, four voltage channels must be sampled by an ADC and the sampled values must be run through equations, as discussed in Chapter 3. The multiplication, division and power raising of these values in equations will increase the effective noise (relative to a single channel being sampled) by a factor of approximately 100x (e.g. a white noise of 100 mV on each channel will create an effective white noise of ≈10 Ω in the output).

*3. Frequency sweep interrogation range and step size:*

What must also be chosen is the interrogated frequency range (*IFR*) and number of discrete frequencies (i.e. frequency step size, $f_{ss}$). The *IFR* selection is simple – it needs only to cover the frequency range over which the input impedance response is evident. The *IFR* is set by assuming that the range must include ±3σ of the response waveform plus the resonant frequency shift due to applied pressure, shown in equation (4.21).

However, determining the number of discrete frequencies is more complex. Interrogating more frequencies will permit more data points to be used by the fitted response curve, potentially improving resolution; however, more interrogated frequencies will reduce the amount of time each frequency can be interrogated (for the same readout bandwidth), reducing the number of samples which can be averaged to reduce noise for a single interrogated frequency point, or the readout bandwidth must be reduced to permit the same number of averaged samples. The frequency range of most interest, of course, is the input impedance response near the resonant frequency. By assuming that a specific number of frequencies (ζ) within the bandwidth ($\sigma$) of the input impedance response must be interrogated for proper curve fitting performance, it is possible to obtain the required frequency step size, as given in equation (4.22). A balance between noise reduction in

individual points and increased noise in curve fitting will need to be found. This frequency interrogation density will depend on the SNR of the signal, the speed and resolution of the ADC, the curve fitting capabilities of the system, and the required output bandwidth. Therefore, it is nearly impossible to fit a mathematical optimization curve as was done for the LC Sensor design above; the optimum step size shall be determined though empirical experimentation.

$$Freq.Range\ (IFR) = 6\sigma + \Delta f_0 = 6\left(\frac{f_0}{Q}\right) + \left(f_{0,max} - f_{0,min}\right) \tag{4.21}$$

$$Freq.Step\ Size,\ f_{ss} = \frac{\sigma}{\zeta} = \frac{f_0}{\zeta \cdot Q} \approx \frac{f_0}{10 \cdot Q} \tag{4.22}$$

*4. Readout Bandwidth:*

With a known *IFR* and $f_{ss}$, the maximum total number of interrogated frequencies can be calculated by dividing *IFR* by $f_{ss}$, equation (4.23). There are methods and algorithms which can be investigated to reduce the number of interrogated frequencies per reading (e.g. using a coarse sweep to identify the approximate $f_0$, then only interrogating near that area with the chosen $f_{ss}$), however, this maximum number is used here, as the benefit of such an algorithm has not been studied. Using the required system readout bandwidth, the maximum amount of time allowed per interrogated frequency can be calculated, equation (4.24). This can then be used to calculate the number samples which can be taken at each frequency, equation (4.25) (and thus the permissible reduction factor in white noise, equation (4.20)).

$$Max.\ No.of\ Interrogated\ Frequencies,\ IF_{Max} = \frac{IFR}{f_{SS}} \tag{4.23}$$

$$Max.Time\ per\ Inter.Freq, \delta_{IF,Max} = \frac{BW_{RO}}{IF_{Max}} \tag{4.24}$$

$$No.of\ ADC\ Samples = \frac{ADC\ Sample\ Rate}{\delta_{IF,Max}} \tag{4.25}$$

However, it is important to note that there will likely be some delays between sampling at each frequency (data transfer, frequency switching, circuit charging / ramp up to steady state, etc…) which will reduce the permitted sampling time at each discrete frequency.

*5. Curve fitting to extract $f_0$:*

Once all the $Re\{Z_{in}\}$ data at each interrogated frequency has been collected, the $f_0$ must be extracted. As was alluded to previously, a curve fitting function should be utilized for this purpose. (If the maximum value was simply picked off, then the resolution would be (at minimum) set by the $f_{ss}$ divided by the LC Sensor absolute response. Additionally, the noise in the system would likely result in erroneous $f_0$ values relatively far from the true $f_0$.) Furthermore, utilizing a curve fitting method to extract the $f_0$ will further improve the minimum resolvable pressure by effectively further reducing the noise in the system.

The curve fitting method utilized in previous work was a Gaussian fit [Ben19]. One of the fitted coefficients is the resonant frequency; this fitted coefficient can simply be output as the resonant frequency (and thus applied pressure) without further effort. A least-squares regression curve fitting method will likely need to be created in the control software run by an external unit, due to limited processing capabilities of the microcontroller in the PGM system (Chapter 3).

## 4.6 Chapter Summary

This Chapter discussed the design methodology of an inductive capacitive (LC) sensing system with the goal to maximize the minimum resolvable pressure resolution of the overall LC tank based sensing system. Various design equations and circuit model representation of the LC Sensor element has been discussed. A new figure of merit termed Design Optimization factor (*DOF*), for estimating the optimum LC Sensor design parameters, when operating under a set of application driven constraints has been proposed. It shows that the parameters which should be

maximized and balanced are the relative LC Sensor response and input impedance magnitude of the digitized signals. This model was implemented in MATLAB, which swept these physical input parameters for all combinations of LC Sensor (e.g. diameter, inductor turn width and spacing, number of coil layers, number of capacitive pressure transducers, etc…) and readout coil (e.g. diameter and inductor turn width and spacing) designs to determine the set of parameters which minimized pressure resolution. This model was experimentally verified through measurements with physically fabricated LC Sensors. The model can also be used to analytically predict pressure resolution of the sensing system. The importance of maximizing input impedance magnitude to maintain a certain threshold value of signal to noise ratio (SNR) has been discussed. LC Sensor physical design parameters which can positively impact input impedance magnitude have been further analyzed.

The impact of packaging material on the LC Sensor circuit model has been analytically and experimentally evaluated. The metal cover causes an increase in effective series resistance of the sensor inductor coil due to developed eddy currents during sensor interrogation. Multiple LC Sensor designs were evaluated to measure their instantaneous pressure resolution. The experimentally obtained values, $Resol_{MEAS}$ were a close match (<11% variation) with analytically simulated values, $Resol_{SIM}$; thus, validating the new figure of merit investigated in this work.

The effects of sample averaging on noise reduction were also discussed. Noise will reduce by a factor proportional to the square root of the number of averaged samples. Therefore, if an ADC with a faster sampling rate is utilized, either the effective noise can be further reduced for the same readout bandwidth, or the readout bandwidth can be improved for the same number of averaged samples (or a combination of both). Using the $Re\{Z_{in}\}$ interrogation method in the PGM

system requires the interrogation of four voltages (multiple noise sources), the effective noise may be further increased due to the use of terms being squared in the utilized equations.

Equations for determining the required frequency sweeping range were also calculated and given. The required frequency sweeping range is set once the LC Sensor design is chosen, determined by the *Q* of and resonant frequency shift (response) with applied pressure of the LC Sensor. However, the chosen number of discrete interrogated frequencies will need to be empirically studied to determine the optimum choice. Interrogating more frequencies will permit more data points for curve fitting, but shorter interrogation time per frequency, effectively increasing the noise of each interrogated point. It is likely that an optimum data density which balances nose reduction on individual frequency points and better curve fitting (effectively reducing noise) can be found, but will likely vary with different input impedance magnitudes, ADC selection, required bandwidth, and curve fitting capabilities of the system.

Finally, it is suggested that curve fitting using a Gaussian equation be utilized to extract the resonant frequency after a full frequency sweep has been performed. Not only is the input impedance waveform (for a $Re\{Z_{in}\}$ measurement) already an approximate Gaussian, but one of the fitted coefficients is the $f_0$, so no further computation is required once this value is calculated. Utilizing a Gaussian curve fit also permits a further reduction in noise and improvement in minimum pressure resolution by effectively "averaging" all discrete interrogated frequencies, but also permitting an interpolation between the discrete frequency points.

# Chapter 5: Environmental Logging Microsystem for Downhole Monitoring

This Chapter investigates the system level design challenges in hardware/software codesign, integration and packaging requirements, and relationship between building blocks of an environment logging microsystem (ELM) for downhole monitoring applications up to 150°C. The proposed microsystem is designed to measure pressure over a full-scale range of 50 MPa with 0.5 kPa measurement resolution. In addition, the microsystem shall be capable of continuously recording temperature (with 0.1°C resolution), geolocation data (acceleration, and magnetic field) at >10 Hz. A power management circuit has been investigated to reduce standby current below 300 nA to improve shelf life to >5 years (governed by self-discharge of primary battery) and increase deployment lifetime. Furthermore, the circuitry automatically transitions microsystem power from primary battery to wireless resonant inductive Qi-power when the microsystem is placed on a commercial Qi wireless power transmitter coil to preserve the battery. Challenges in design of a chemically resistant, high pressure high temperature, and flow compatible microsystem packaging methodology maintaining an overall volume of <48 $cm^3$ and density <1.5 $g/cm^3$ has been investigated.

Downhole monitoring in wellbores provide increased insight and control of reservoir operations, enhanced oil and gas production, and improved employee safety [Cha12, Fin10]. Conventional production logging, wireline, coiled tubing (CT) and other cable-based downhole solutions are bulky, costly, difficult to operate and maintain, and have limited access inside the well. This is particularly true for deviated and horizontal wells. Typical constraints associated with wireline logging include: (i) the mobilization of a rigless team with dedicated equipment for the

gauge, (ii) a production shortfall of several days, and (iii) sensitive slickline interventions ("Fish into the well"), in strongly deviated wells with deposits, often leading to losses of several million dollars for the oil and gas company [Ord20]. However, untethered autonomous microsystems can provide distinct advantages in seamlessness of usage, cost, scalability, and improved sensing in previously unreachable areas of the well by providing better access to horizontal wellbores and fractures. It is envisioned that autonomous microsystems capable of sensing the environment in free-flow deployment can complement wireline monitoring and help to illuminate the region surrounding the wellbore. For this, the microsystems must have form factors that are sufficiently compact to fit within wellbores and must also be density matched to the fluid environment within the well to facilitate recovery through flow back; if these conditions are not met, the microsystems may become lodged in the well, impeding flow, or sinking in the fluid, preventing their recovery.

Temperature and pressure measurements inside energy wells are of high interest for both exploration and production. Temperature measurements provide an indication of fluid viscosity, as well as input for temperature-dependent corrections for measurements of other parameters [Etn89]. Pressure measurements are utilized in a wide range of wellbore assessments, such as in the estimation of recoverable hydrocarbons and determination of over-pressurized regions [Ell07] Additionally, acceleration and magnetic field measurements can help to identify the location of mobile elements and aid in early indications of possible equipment failure (i.e. excessive equipment vibration) [Sco85, Mah20].

For downhole applications, the packaged microsystem size is limited by wellbore size, typically <ø45 mm in diameter. This requires microsystem electronics and power supply to be properly positioned and integrated onto a printed circuit board (PCB) to fit within a package with external dimensions less than that of the wellbore. The density of fracking fluid is typically <1.5

g/cm$^3$ [Bab18, Lia18], indicating that final microsystem density should preferably remain <1.5 g/cm$^3$, as rapid fluid flow within the well will still permit small objects with similar densities to the surrounding fluid to travel with the stream. Other environmental conditions present additional challenges: pressure in a typical reservoir at a depth 4,000 m can be ≥40 MPa (5,800 psi); the chemical environment may impose salinity levels up to 150,000 ppm [Cha12], hydrogen sulfide ($H_2S$) levels up to 2,500 ppm, and contain raw natural gas and oil.

Prior work in which autonomous microsystems for well-deployment were investigated is described in the following paragraphs. Under the platform label of environmental logging microsystem (ELM), the University of Michigan has reported a series of investigations that combined custom sensors with rapidly prototyped commercial electronics, demonstrating operation to 50 MPa pressure and 125°C temperature. These early efforts [Sui21] did not incorporate inertial sensors. More importantly, they used an optical approach for battery recharging and bi-directional communication, requiring a transparent pathway into the package. The materials selected were incompatible with $H_2S$ and diesel fuel, were not density matched to the downhole fluidic environment, and could not provide reusability of the sensors and electronics. Other versions that were reported even earlier [Li17; Cho17] employed steel and glass/ceramic packaging with a rigid exterior that were not well suited for pressure sensing, even though they could be scaled down in size and batch produced [Ma15].

The most recent generation of the ELM prior to this work (ELM7, reported in [Vel22]), incorporates pressure, temperature, and inertial sensors and Bluetooth® Low Energy (BLE, v4.0) communication electronics; power is supplied via secondary battery, recharged using Qi wireless power transfer. The ELM7 microsystem successfully recorded data for >96 hours, measured pressure up to 41.5 MPa, incorporated a 72 kB built in Flash memory for sensor data storage, and

could successfully operate to a temperature of 85°C. The microsystem was packaged in a fluorocarbon elastomer Viton$^{TM}$ shell, filled with low bulk density cenospheres and was successfully deployed in field conditions, in an oil well, to a depth of 1,290 m, recording pressure, temperature, and inertial data.

Although the field deployment of the ELM7 microsystem represented a major achievement in the domain of wireless downhole monitoring, the trial also exposed several operational and design limitations. In addition to being limited in operating temperature at 85°C, a high standby current of >250 µA @ 25°C (rising up to >400 µA @ 85°C), limited size of the available Flash memory for sensor data storage, and reliability issues with the packaging significantly reduced the capability of the microsystem to record data over multiple days in field deployment conditions. Since the full circuit was built on a single PCB, with the secondary battery directly interfaced with the microsystem power bus, temperature induced damage to any component would corrupt the entire PCB, causing microsystem failure, and loss of sensor data stored in the Flash memory. In addition, intrusion of gases through the Viton$^{TM}$ shell causes package swelling, leading to package deformity and damage to electronics.

The goal of this work is to address the above challenges in microsystem design, component integration, and packaging methods to realize a next generation environment logging microsystem (ELM9) to dramatically improve overall microsystem performance. Primary goals include small form factor to access narrow fractures (diameter <ø45 mm), sufficient full-scale range of pressure measurement (≤50 MPa) with an average resolution of <1.5 kPa (≥16 bit), endurance to and measurement of high temperatures (≤150°C), and ability to operate in harsh chemical environments containing high concentrations of brine (≤15%) and $H_2S$ (≤2,500 ppm). Other microsystem capabilities studied include nanowatt power budget (standby current <0.5 µA @

25°C) and power management for extended microsystem deployment lifetime (>5 days @ 100°C), logging of inertial data (acceleration and magnetic field), 100x increase in Flash storage for collected sensor data (>15 MB), and faster data transmission rate over BLE (>100 kbps).

## 5.1 System Design

This section introduces the microsystem design concepts of an environment logging microsystem (ELM9) for downhole monitoring applications up to a temperature of 150°C. The microsystem incorporates both capacitive and piezoresistive pressure sensors to record wellbore pressure over a full-scale range of 50 MPa with 0.5 kPa measurement resolution. Additionally, the microsystem uses Bluetooth® Low Energy (BLE, v5.2) communication module and is capable of continuously recording temperature (with 0.1°C resolution), and inertial measurement data (at >10 Hz bandwidth) while having a low standby current consumption across the full operational temperature range to improve battery-limited microsystem lifetime. A power management unit (PMU) using multiple relay switches is designed to reduce standby current and disconnect the primary battery in the presence of resonant inductive Qi wireless power during sensor interrogation and storage. A microsystem block diagram is shown in Fig. 5.1.

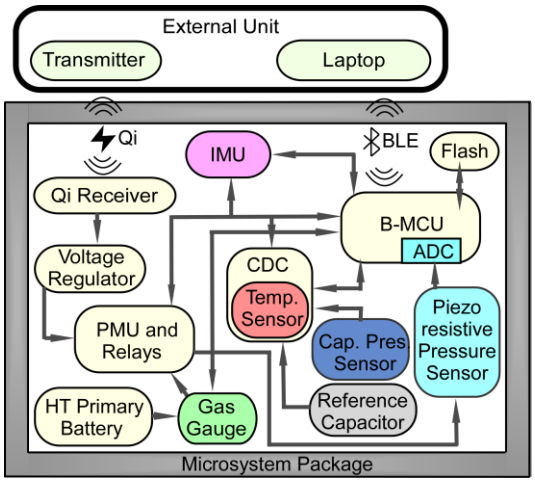



Fig. 5.1: ELM9 Block Diagram.

The autonomous microsystem consists of a BLE microcontroller unit (B-MCU) with an in-built analog to digital converter (ADC), capacitance-to-digital converter (CDC) with in-built temperature sensor, Flash memory, resonant inductive Qi power receiver module, high temperature (HT) primary battery, battery gauge, power management unit (PMU), electronics for accommodating and interrogating a high resolution custom MEMS capacitive pressure sensor or lower performance commercial MEMS piezoresistive pressure sensor, and inertial measurement unit (IMU) consisting of a 3-axis accelerometer and 3-axis magnetometer; the microsystem is then packaged within injection molded hydrogenated nitrile (HNBR). External components consist of a wireless power transmitter kit and Bluetooth® TX/RX module. The PMU is designed to seamlessly toggle between battery and Qi wireless power when the microsystem is placed on a wireless Qi power transmitter coil. The battery gauge continually estimates remaining battery lifetime based on battery power consumption drawn from the HT battery. Sensor data from the CDC, ADC, and IMU is collected and stored in the external Flash memory during deployment. The B-MCU is wirelessly interrogated by the external readout unit using the BLE protocol for data readout post deployment.

### 5.1.1 System Hardware

The ELM9 microsystem electronics are realized on two rigid printed circuit boards (PCBs) using standard PCB manufacturing practices and uses components that have a small footprint and are compatible with high temperature operation (>125°C). Commercial off-the-shelf (COTS) components were chosen to reduce cost and enhance scalability of the proposed solution. Multiple microsystem components, such as the wireless power receiver chip (BQ24083 from Texas Instruments), along with the wireless power transmit and receive coils, has remained unchanged

from ELM7, reported in [Vel20]. However, the wireless power acts as an alternate power source to the primary battery in ELM9, instead of recharging the microsystem battery.

Fig. 5.2 shows overall circuit schematic of the ELM9 microsystem while Table 5.1 summarizes the major components of the ELM9 circuit design with their primary functions. Descriptions of these modules is discussed below.

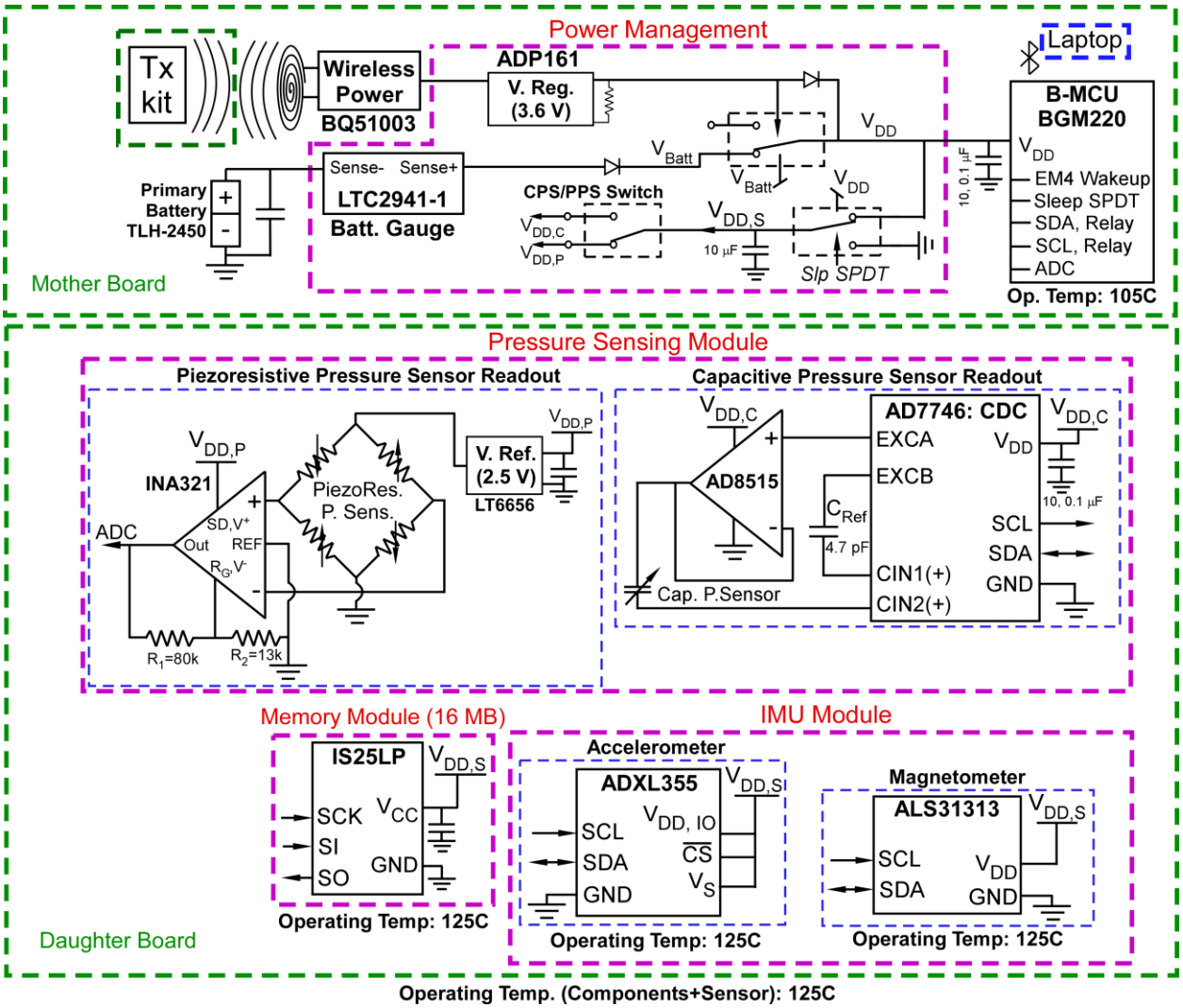



Fig. 5.2: Circuit Schematic of ELM9 microsystem.

Table 5.1: Major ELM9 components.

| Component | Part No. | Footprint [mm] | Device Feature |
|---|---|---|---|
| Wireless power transmitter kit | TYLT Vu-SOLO | 85.0 × 85.0 | Follows Qi protocol |
| Wireless power receiver chip | TI BQ51003 | 1.9 × 3.0 | Follows Qi protocol |
| Voltage regulator | AD ADP161 | 2.9 × 2.8 | Linear Regulator (3.3V) |
| Primary battery | Tadiran TLH-2450 | ø24 × 5.6 | 3.6 V, 550 mAh capacity |
| Battery gas gauge | LT LTC2941-1 | 3.0 × 2.0 | Battery discharge integrator and monitor |
| CDC | AD AD7746 | 5.1 × 6.4 | 2 capacitive input channels, integrated temperature sensor |
| B-MCU | Silicon Labs BGM220 | 6.0 × 6.0 | 1.4 μA deep sleep with RTCC, integrated antenna |
| Accelerometer | AD ADXL355 | 6.0 × 6.0 | 3-axis accelerometer, measurement range ±8 g |
| Magnetometer | Allegro MicroSystems ALS31313 | 6.4 × 3.0 | 3-axis magnetometer, measurement range ±50 mT |
| CMOS SPDT switch | AD ADG819 | 2.2 × 1.1 | CMOS single pole double throw switch |
| CMOS dual SPDT switch | AD ADG836 | 2.0 × 2.0 | Two SPDT switches |
| Instrumentation Amplifier | TI INA321 | 6.4 × 5.0 | Piezoresistive pressure sensor output amplifier |
| Voltage Reference (2.5V) | AD LT6656 | 5.0 × 5.0 | Piezoresistive pressure sensor input volt. ref. |

*Custom MEMS Capacitive Pressure Sensor and CDC:*

The custom capacitive MEMS pressure sensor in ELM9 was realized at the University of Michigan by Dr. Alexander Benken [Ben21]. The sensing diaphragm is composed of a dielectric stack of $SiO_2$, $Si_3N_4$, and $Al_2O_3$ measuring 5 μm thick with an inter-electrode sensing gap of 450 nm. The sensing electrodes are composed of aluminum and insulated with $Si_3N_4$ to permit touch-mode operation. Sapphire was selected as the substrate material due to its good thermal expansion coefficient match with the dielectric diaphragm. The sensors have a typical size of

$1.8 \times 1.5 \times 0.5$ mm$^3$. They show a full-scale range of 0-70 MPa (0-10,000 psi) with an average response of 0.5 fF/kPa (3.3 fF/psi).

The CDC chip (AD7746, Analog Devices) [Ana05] has been proven in Chapter 2 to be functional over the desired operational temperature range (25°C –150°C), and has remained unchanged from ELM7, reported in [Vel20]. The CDC chip has a measurement range of ±4 pF around an adjustable offset of 0-17 pF; however, the capacitive pressure sensor used in this effort has a full-scale capacitance change up to 45 pF and offset capacitance up to 10 pF. Therefore, a range extension circuit is used between the capacitive pressure sensor and the CDC chip to increase its capacitance measurement range (at the cost of reducing the capacitance resolution from 0.04 fF/code to 0.25 fF/code). When the pressure sensor response of 0.5 fF/kPa (3.3fF/psi) is combined with the CDC capacitance resolution of 0.25 fF/code, the average pressure resolution of the ELM9, using the capacitive pressure sensor, becomes approximately 0.5 kPa (0.07 psi, 17 bit).

*Bluetooth Enabled Microcontroller (B-MCU):*

For this work, the BGM220 MCU from Silicon Laboratories, Inc. [Sil22] is selected. It has an integrated antenna and a reasonable footprint ($5.0 \times 5.0$ mm$^2$). Chips without integrated antenna must use commercial antenna or antenna implemented on PCB, typically requiring a larger effective footprint even with a smaller chip size. The BGM220 also offers a low standby current (<1 μA). However, the new B-MCU supports BLE, v5.2, which has a faster data transmission speed and is rated up to 125°C (storage temperature). Table 5.2 compares the key parameters of BGM220 along with other MCUs that were considered.

Table 5.2: Comparison of MCUs for B-MCU.

| **Chip** | TI CC2650 MODA | SiLabs BGM121 (used in ELM7) | Broadcom BCM20737 | SiLabs BGM220 (used in ELM9) |
|---|---|---|---|---|
| **On-Chip Flash** | 128 kB | 128-256 kB | No | 256-512 kB |
| **On-Chip Data Bus** | UART, $I^2C$ | UART, $I^2C$, SPI | UART, $I^2C$ | USART, $I^2C$ |
| **Integrated Antenna** | Yes | Yes | No | Yes |
| **Active Current** | Rx: 6.2 mA<br>Tx : 6.8 mA<br>(0 dBm) | Rx: 9.0 mA<br>Tx: 8.2 mA<br>(0 dBm) | Rx: 9.8 mA<br>Tx: 9.1 mA<br>(0 dBm) | Rx: 4.2 mA<br>Tx: 4.6 mA<br>(0 dBm) |
| **Standby Current (with RTCC active)** | 1.0 µA | 2.5 µA | 12.0 µA | 1.4 µA |
| **Footprint** | 16.9 × 11.0 $mm^2$ | 6.5 × 6.5 $mm^2$ | 5.0 × 5.0 $mm^2$ | 6.0 × 6.0 $mm^2$ |

The selected B-MCU (SiLabs BGM220) can be operated in different energy modes (EM). The energy mode to be used depends on the desired microsystem functionality requirements during that time of operation. The B-MCU is, therefore, placed in the lowest power mode (EM4) when not being actively interrogated or in between sensor measurements. Active mode is required to operate the BLE radio and all the BLE functions; this mode is used during active BLE communication and during sensor interrogation in deployment. The BLE radio is also off in the intervals between the advertising, connection, or data transfer events to further save power. The energy modes with their functions are summarized in Table 5.3.

Table 5.3: Available energy modes during B-MCU operation.

| Energy Mode | Current draw at 25°C (all peripherals disabled) | Function |
|---|---|---|
| EM0 | 27.00 µA/MHz | Fully active state: BLE radio is receiving/transmitting |
| EM1 | 17.00 µA/MHz | Needed when certain peripherals are active (USART) |
| EM2 | 1.40 µA | Needed when certain oscillators are active (LFRCO) |
| EM3 | 1.05 µA | Needed when certain peripherals are active ($I^2C$) |
| EM4 | 0.17 µA | Deep sleep/ hibernate |

*High Temperature (HT) Primary Battery:*

A primary bottleneck in design of an autonomous sensing microsystem for operation beyond 85°C is the battery (the upper operation limit of commercially available secondary

batteries). ELM1-3 used commercially available coin-cell secondary batteries based on manganese silicon lithium chemistry rated for ≤60°C; they exhibited significantly degraded performance at higher temperatures [Sei14]. The ELM7 microsystem permitted the use of a larger battery with thionylchloride ($LiSOCl_2$) chemistry (Tadiran TLI-1020A), which permitted an increase in operational temperature range to 85°C [Vel20]. Typical lithium batteries, when used at temperatures beyond their specifications, will cause the electrolyte inside the battery to degrade, adversely affecting the battery performance, reducing battery lifetime and causing chemical hazards such as leakage or thin-film delamination [Hen98, Dou12, Rob97]. Batteries based on lithium thionylchloride ($LiSOCl_2$) chemistry have been of interest lately for their outstanding performance at high temperature [Hen98]. To this end, a primary coin cell battery based on lithium thionylchloride chemistry has been identified for use in the ELM9 microsystem (TLH-2450, Tadiran Batteries GmbH, Germany) [Tlh20]. The battery has a rated operating temperature up to 150°C and a nominal capacity of 550 mAh. It weighs 8.8 g with a volume of 2.6 $cm^3$ and ø2.4 cm diameter, compatible with the specifications of the ELM9 microsystem.

*Battery Gauge:*

Accurate real-time estimation of remaining microsystem and battery lifetime is critical for autonomous downhole monitoring. For a completely packaged microsystem where the battery is not readily accessible, knowledge of the remaining microsystem battery capacity becomes critical to estimate the length of a subsequent deployment routine, which may last for several days at a time. This prevents any loss of time and valuable data through unexpected microsystem shutdown during deployment. To achieve this goal, a battery gauge (LTC2941-1, Linear Technology Corp. (LT), USA) [Ltc20] has been selected. A precision coulomb counter integrates battery discharge current through an internal sense resistor between the battery's positive terminal and the load. The

measured charge is stored in internal registers. An $I^2C$ (Inter-Integrated Circuit) interface is used by the B-MCU to access battery discharge data and configure the battery gauge. The Linear Technology LTC2941-1 has been chosen over other battery gauges based on high temperature characterization tests, in which the Linear Technology LTC2941-1 chip exhibited a very low quiescent sleep current of 2.3 µA at 150°C (90 µA in active mode). Other tested battery gauges resulted in a high quiescent current, such as the Linear Technology LTC4124 which measured a high active quiescent current of 1.6 mA at 150°C. The quiescent current thermal characteristics recorded in active and sleep modes of operation for Linear Technology LTC2941-1 battery gauge are shown in Fig. 5.3.

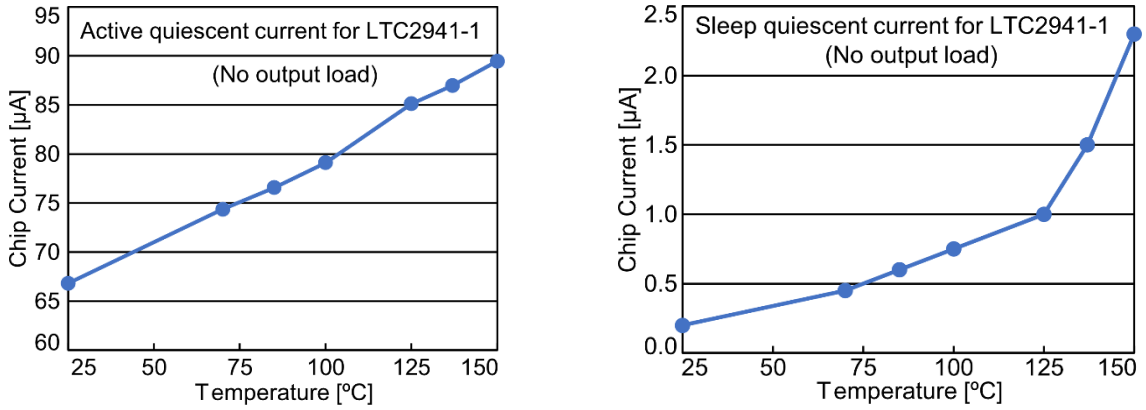



Fig. 5.3: Measured quiescent current variation with temperature for Linear Technology LTC2941-1 battery gauge in (a) Active mode; (b) Sleep mode of operation.

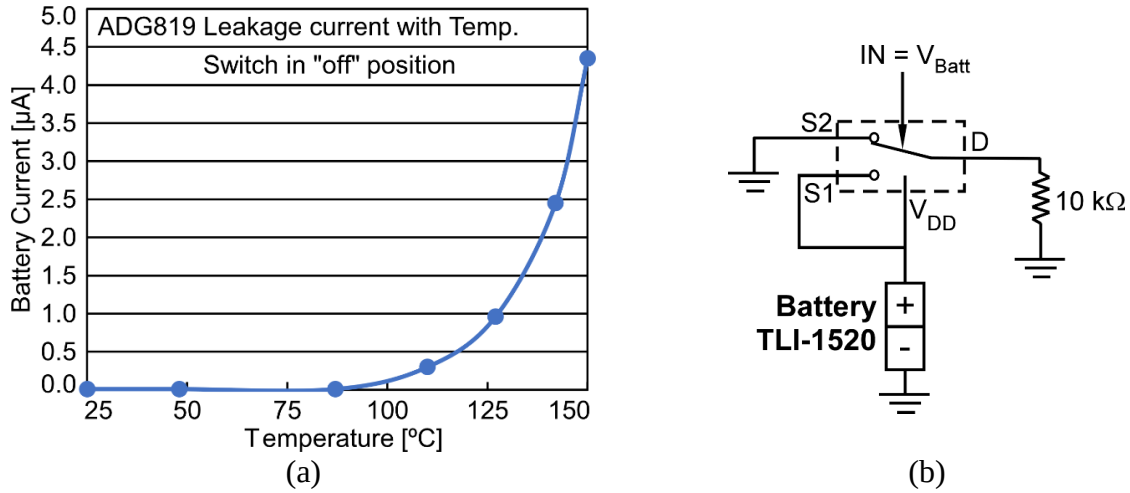
*Inertial Measurement Unit (IMU):*

Inertial sensing is achieved with a 3-axis MEMS accelerometer, ADXL355, from Analog Devices, Inc. [ADX22], and a 3-axis magnetometer, ALS31313, from Allegro MicroSystems [ALS22]. Both sensors can be configured individually using software to be in active or idle state based on measurement necessity. The B-MCU interfaces with the IMU sensors over an $I^2C$ bus. The sensors may be interrogated in either single mode (one set of IMU readings) or burst mode (20 sets of IMU readings collected at ≈10Hz), where a set of IMU reading refers to a single read

of the 3-axis accelerometer and 3-axis magnetometer. The measured acceleration and magnetic field data in single or burst mode, individually or in conjunction with each other, can be used for coarse geolocation and tracking of the ELM9 microsystem. The ADXL355 has a measurement range of ±8 g, with a footprint of 6.0×6.0 $mm^2$, and is rated for operation up to 125°C, with an active current consumption of approximately 200 μA. The ALS31313 has a measurement range of ±50 mT, with a footprint of 6.4×3.0 $mm^2$, and is rated for operation up to 125 °C, with an active current consumption of 15 μA. The ALS31313 also has an in-built temperature sensor with a temperature resolution of ≈0.1°C. While multiple COTS components were considered for the IMU module, in addition to fulfilling microsystem requirements (primarily temperature rating), the final selection of sensors was dependent on chip availability during the COVID-19 pandemic caused world-wide integrated circuit shortage.

*CMOS Relay Switches:*

Several single pole double throw (SPDT) and double pole double throw (DPDT) relay switches controlled by the B-MCU have been included in the design of the ELM9 microsystem to reduce standby current. To realize these relay designs, the ADG819 CMOS SPDT switch and ADG836 CMOS Dual SPDT switch (Analog Devices, Inc., USA) have been used [Adg19, Adg20]. Both CMOS relay switches exhibit a low standby power consumption <0.1 μW and are rated for operation up to 125°C. The temperature induced leakage current through the Analog Devices ADG819 switch in "OFF" state has been characterized in Fig. 5.4(a) while Fig. 5.4(b) shows the relay configuration used for this characterization study. The maximum standby current measured at 150°C is 4.35 μA. Since power to all the microsystem peripherals are routed through SPDT relay switches, this value of leakage current shall be the major contributor of power draw during microsystem standby mode.




(a) (b)

Fig. 5.4: (a) ADG819 leakage current with rising temperature in "OFF" state. (b) Relay configuration used over temperature characterization.

*Flash Memory Chip:*

Using the in-built B-MCU Flash memory (capacity of ≈300 kB) for sensor data storage significantly limits microsystem deployment (i.e. memory-limited) lifetime. For example, if a measurement bandwidth of 10 seconds is chosen using the MEMS capacitive pressure sensor, temperature sensor, and IMU active in burst mode, the memory-limited lifetime is <8 hours. Hence, an external Flash memory chip, IS25LP128F, from Integrated Silicon Solution Inc., with a capacity of 16 MB has been used in ELM9 to store recorded sensor data during deployment [ISS22]. The chosen Flash memory chip has a low standby current draw of 8.0 µA, uses SPI communication protocol to interface with the B-MCU, and has a rated operating temperature up to 125°C. This extra storage capacity permits an increase in the memory-limited lifetime (using the same parameters as above) of the ELM9 microsystem to >435 hours (>18 days).

*MEMS Piezoresistive Pressure Sensor:*

In addition to the custom MEMS capacitive pressure sensor, which provides high resolution pressure measurements, the ELM9 microsystem also incorporates a commercial MEMS piezoresistive pressure sensing interface for pressure measurements up to an applied pressure of

50 MPa, but with a reduced pressure resolution (or reduced sampling bandwidth for higher pressure resolution). For this purpose, a COTS piezoresistive pressure sensor, K1PH-0003-5T, from Merit Sensors, has been used [Mer22]. The sensor is rated for pressure measurement up to 68 MPa with a full-scale output of ≈80 mV with 2.5 V excitation, and rated temperature operation up to 150°C. Fig. 5.5 shows images of the piezoresistive pressure sensor. A voltage reference chip, LT6656, from Analog devices Inc., is used to provide a stable, temperature-independent voltage of 2.5 V to the piezoresistive pressure sensor and is rated for operation up to 125°C [Vre22]. A CMOS instrumentation amplifier, INA321, from Texas Instruments (TI) [Ina22], with a gain factor of 60, has been used to amplify the piezoresistive pressure sensor output, and feed it to the in-built 12-bit (806 μV/code) ADC on the B-MCU. The ADC has been configured to sample at a speed of 2 kHz. With this circuity, the piezoresistive pressure sensor has an instantaneous pressure resolution of 22 kPa. However, by utilizing an oversampling and averaging algorithm, as described in Chapter 4, the effective ADC resolution has been increased to 17-bit (25.2 μV/code) by sampling and averaging 1024 readings, resulting in a measurement bandwidth of ≈0.5 seconds. Assuming noise is limited by digital quantization only, the above algorithm can increase the theoretical pressure measurement resolution by a factor of 30 to ≈0.75 kPa.

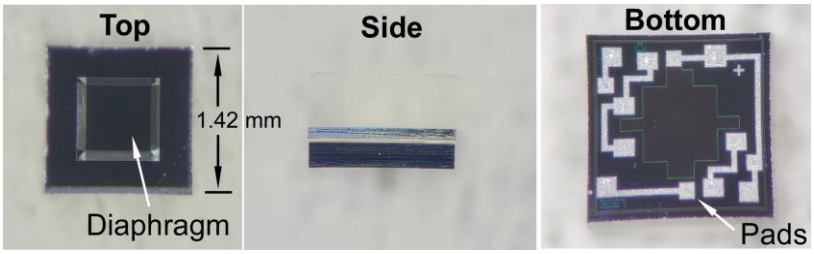



Fig. 5.5: Images of ELM9 piezoresistive pressure sensor [Mer22].

All chosen circuit components in design of the ELM9 microsystem, are temperature rated to ≥125°C. However, with the use of high temperature compatible circuit board materials and packaging, the microsystems can be operated up to 150°C for a finite amount of time. Microsystem

operation at increased temperature, beyond 125°C, will cause a slow, but steady degradation in performance of certain circuit components, such as the microcontroller (B-MCU). During a typical deployment of the ELMs in downhole environment, the microsystem is only subjected to temperatures ≥125°C for a finite amount of time (typically a few hours), while situated at the very depth of the energy well. In addition, given the capacity of the HT primary battery is also limited for operation at 150°C (1-4 days); it is more likely for the microsystem to run out of power first, before any temperature induced failure is encountered if the microsystem is subjected to prolonged exposure at temperatures >125°C.

### 5.1.2 Power Management Unit

Two specific power management features have been designed to increase the operational lifetime of the ELM9 microsystem by reducing the current draw required from the primary battery. One feature is designed to reduce the power budget of the microsystem when in a power-down mode during deployment (i.e. to reduce standby current) while the second is designed to eliminate current draw from the primary battery entirely when wireless power transfer is activated, typically when the BLE radio is active (i.e. when the ELM9 microsystem is utilizing Qi wireless power transfer).

*Power budget reduction in power-down mode:*

When deployed, the ELM9 microsystem is designed to remain in a low power "sleep" state in EM4 when not actively interrogating the sensors. In this state, all components are ideally set into their minimum power consumption mode. However, the microsystem current draw in this power-down state is still not negligible (≈400 μA measured in ELM7 microsystem at 85°C); additionally, some analog components cannot be digitally powered down and will continue to draw a high quiescent current even when not being utilized. Furthermore, the leakage current and current

consumption of nearly all electronic components will increase exponentially with temperature, even when set into a powered down mode, making it imperative that these currents be eliminated to preserve microsystem lifetime in HT environments, such as when deployed downhole.

In order to reduce the power budget of the ELM9 microsystem in power-down mode, electronic SPDT relays are utilized to entirely disconnect all non-essential components (e.g. electronic sensors and sensor readout circuitry) from the microsystem power bus when not in use, permitting an large reduction in current draw, especially at elevated temperatures. The use of these electronic relays can reduce the power-down mode current, improving the operational lifetime of the microsystem when deployed in environments of elevated temperatures. In addition to extending microsystem lifetime when deployed, reducing the power-down current will also permit the shelf life of a fully packaged microsystem (in which the battery cannot be physically disconnected from the electronics) to be greatly extended.

*Use of wireless power transfer during high current draw events:*

In microsystem designs which utilize a primary (non-rechargeable) battery such as ELM9, any power draw, even when the microsystem is not deployed, will reduce its total lifetime (before the package must be opened to replace the battery). Therefore, wireless power transfer is utilized in ELM9 power circuit design not to recharge a battery, but rather to actively supply power to the ELM9 microsystem during high power draw events, such as during device programming, Flash erase, and data transfer over the BLE radio. An electronic SPDT relay is utilized to disconnect the battery and switch the microsystem power to the wireless power transfer circuitry. The switching relay is hardware automated (requires no software trigger); therefore, the microsystem will still operate when being powered through wireless power, even if the packaged battery has been depleted. When the microsystem is not being powered through wireless power transfer, the relay

will automatically and seamlessly switch to battery power without causing a current spike or disruption in microsystem operation, as shown in Fig. 5.6.

Utilizing this design prevents the primary battery from being unnecessarily drained when it is not in a deployment condition. Additionally, if the ELM9 microsystem is kept on a wireless power transfer module when not in use, the battery will remain disconnected from the circuit, further preserving shelf life and battery capacity.

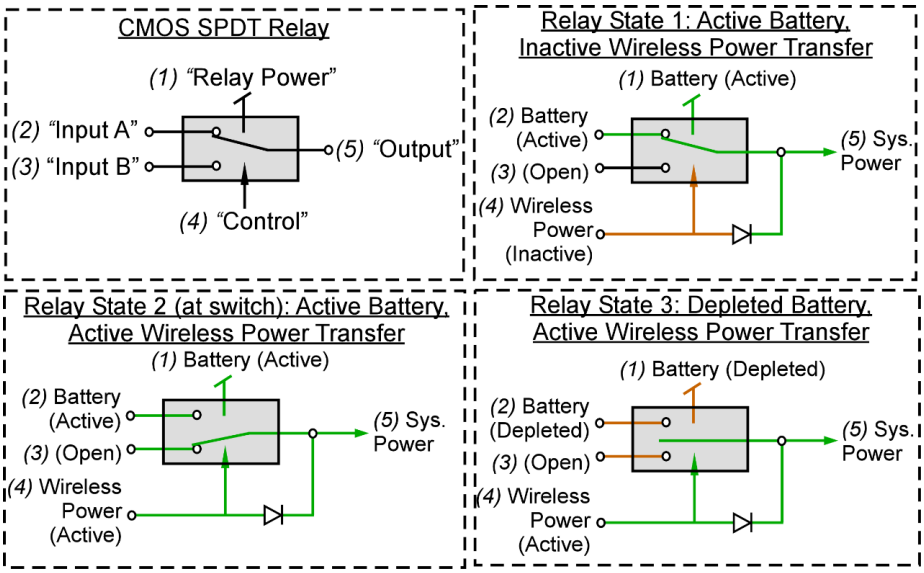



Fig. 5.6: Configuration of designed power switching SPDT relay when wireless power transfer is inactive (state 1, battery power only), during switch to wireless power (state 2, both power sources present) and active (state 3, microsystem recovery with depleted battery).

### 5.1.3 System Software

Software for the ELM9 microsystem involves B-MCU state machine design to implement all microsystem functionalities with reliability in operation and autonomy, reduce microsystem power budget and limit memory usage. The second part involves software for the external computer/laptop, which communicates with the B-MCU using a BLE dongle and operates a graphic user interface (GUI) to interact with the end user for command and data transfer. The typical operation flowchart for the ELM9 microsystem is shown in Fig. 5.7. The B-MCU is

initialized after power on. When the microsystem is ready for deployment, it is placed in the detection state. In the detection state, B-MCU switches with low power state to conserve power when no measurement is to be taken. At the end of the deployment, once the microsystem is retrieved, it is charged and triggered out of the detection state by the user. When the data transfer is requested by the user, B-MCU reports the data to the user through the BLE interface.

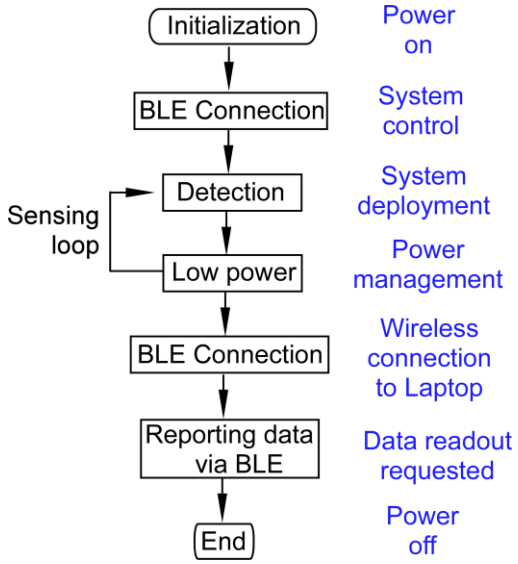



Fig. 5.7: Typical operational flowchart for ELM9.

*B-MCU State Machine:*

The software state diagram for the B-MCU is shown in Fig. 5.8. The B-MCU is powered on, initialized, and moved into the Bluetooth® connection state after initialization. In this state, it is ready to connect to the GUI via BLE and can perform functions determined and sent as commands by the user. The B-MCU then transitions to the state corresponding to the function to be performed. The B-MCU is placed in the EM4 low power state (state 4) when the microsystem is not in use. The functions of the individual states of B-MCU have been described below.

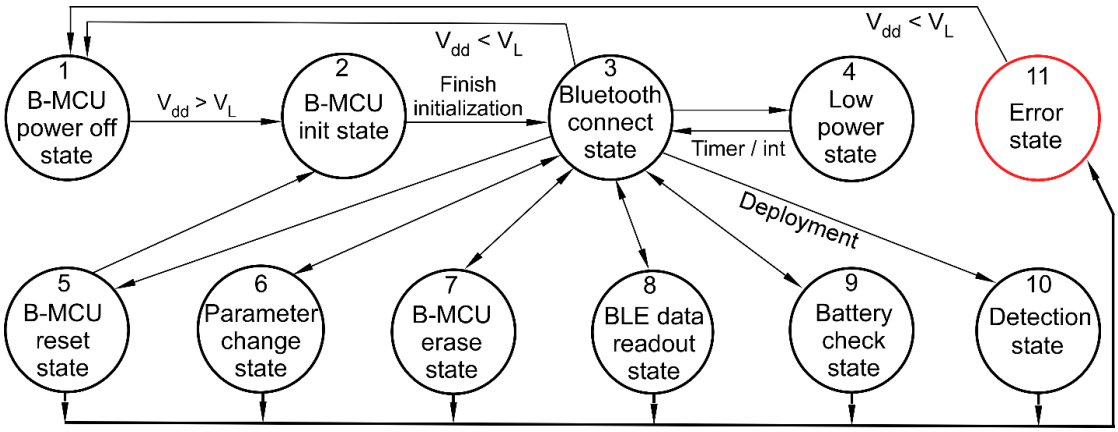



Fig. 5.8: ELM9 B-MCU state machine diagram.

*State 1, B-MCU power off state:*

This is the default state when a sensing program is not running or the battery is discharged, and microsystem voltage ($V_{dd}$) is below a certain threshold voltage, typically <2.4 V ($V_L$). The microsystem typically enters this state after operations. The B-MCU remains off in this state. Data is retained in the external Flash memory without loss.

*State 2, B-MCU init state:*

This is a transient state during which the B-MCU turns on and all global constants and variables are initialized or restored from the Flash memory. Registers of pertinent B-MCU peripherals, e.g. $I^2C$, SPI, digital I/O, ADC, etc., are initialized for use in later operations. The radio is turned on briefly and the Bluetooth® stack is initialized.

*State 3, Bluetooth® connect state:*

This is a transitional state when the B-MCU advertises and waits for Bluetooth® connection request from the laptop. Once connected to the laptop (GUI), the user can choose either to place it in low power state (state 4), reset B-MCU (state 5), sensor parameter update (state 6), erase Flash memory (state 7), transfer data via BLE (state 8), check microsystem battery level (state 9), or place the microsystem in detection mode before deployment (state 10). These states are described below.

*State 4, Low power state:*

This is the state when the B-MCU is on but in EM4 shutoff mode to minimize power consumption[2]. The user places the B-MCU in this state when no active Bluetooth® radio operations are needed. This is also the state the B-MCU goes into when transitioning from detection state to Bluetooth® connect state. In this state, there is no status information retained from the previous operation and the Bluetooth® stack is reinitialized. The B-MCU deactivates all peripherals using the CMOS relays before entering EM4 shutoff mode except a single general purpose input output (GPIO) port to obtain a wakeup interrupt from the wireless power module.

*State 5, B-MCU reset state:*

This state allows the user to manually reset the microsystem should any unexpected behavior occur, such as a clock source oscillating at an unexpected frequency.

[2] B-MCU low power state implemented with support from Mr. Zechao Li, ECE, University of Michigan.

*State 6, Parameter change state:*

The Bluetooth® external interface can be used to set the testing parameters of ELM9. These parameters include selecting time interval definition, sensor selection, IMU operation mode and readout fraction, and sensor periodicity selection.

*State 7, B-MCU erase state:*

This state allows the user to erase the temperature, pressure, and inertial measurement data stored in the external Flash memory to permit collection and storage of new measurements.

*State 8, BLE data readout state:*

This is the state when the B-MCU transmits sensor data to the GUI running on the laptop. The B-MCU reads the stored data from the Flash memory and sends them as data packets to the external unit through the BLE interface. BLE protocol uses CRC error check bit and automatically corrects erroneous data packets by resending. Since the Flash memory on the ELM9 microsystem has a large capacity of 16 MB, the data transfer routine is broken into smaller subroutines, where each subroutine enables transfer of a fixed set of data packets (500 kB)[3]. A custom redundancy check algorithm using two parallel Bluetooth® characteristics has been designed to re-iterate individual subroutines in case of unstable connection and data loss during data transfer as shown in Fig. 5.9. The overall speed of data transfer was measured to be ≈54 kbps with the investigated data transfer algorithm.

[3] BLE data readout state implemented with contribution from Mr. Yifan Yang, ECE, University of Michigan.

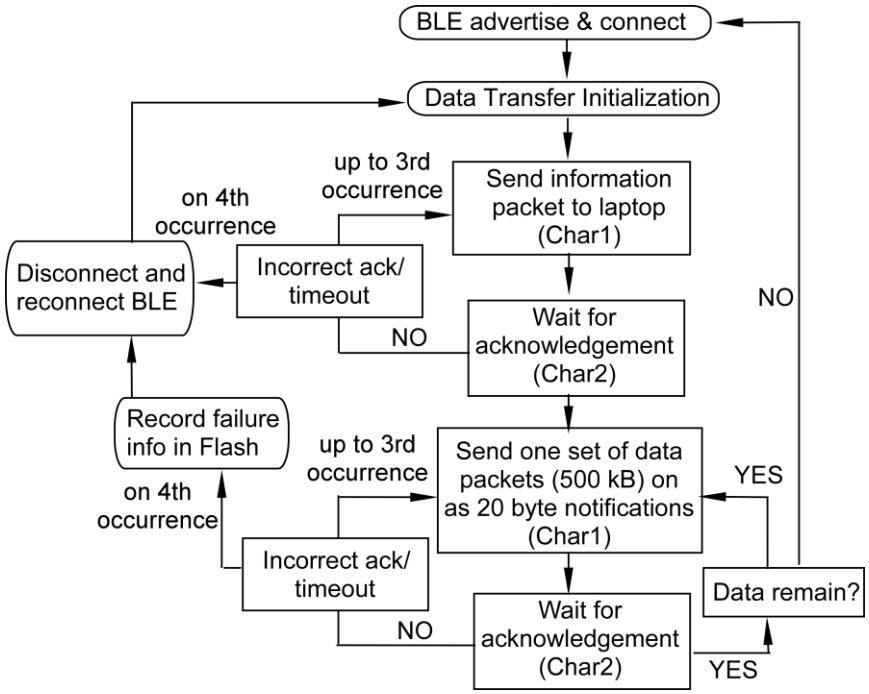



Fig. 5.9: Custom BLE data transfer redundancy check algorithm.

*State 9, Battery check state:*

This is the state when the B-MCU checks for the battery level through the battery fuel gauge and reports it to the user over BLE radio.

*State 10, Detection state:*

This state performs the temperature, pressure, and inertial data measurement, as initially selected by the user, with a predefined schedule. This schedule can be reprogrammed by modifying the global constants in the software through state 6. When the microsystem is placed in detection, it enters the EM4 shutoff mode to conserve microsystem power until a measurement is to be taken. A backup real time clock (BURTC) running from an ultra-low frequency RC oscillator (ULFRCO) in the B-MCU is used to periodically wake up the microsystem according to the predefined schedule. The microsystem on wakeup activates the relay switches that supply power to the necessary sensor peripherals, interrogate sensors based on user defined routines, and store sensor

measurements to the external Flash memory. Following this, all microsystem peripherals are powered down using relay switches before the microsystem enters EM4 shutoff mode. A wakeup interrupt (low signal) on one of the GPIO pins of the B-MCU from the wireless power module triggers the microsystem out of detection state and places it back in low power state followed by Bluetooth® connect state.

*State 11, Error state:*

This is the "catch-all" state which the microsystem enters if the program should fail unexpectedly and stop execution. The microsystem is re-initialized upon entering this state.

Fig. 5.10 lists the different CMOS relays which are controlled by the B-MCU along with their purpose, while Fig. 5.11 shows the operation flowchart of B-MCU in detection state.

All microsystem sensor and time interval selections, along with current iteration information is stored in sector 15 of the external Flash chip, also referred to as the information page, which starts at Flash address 0x00F000.

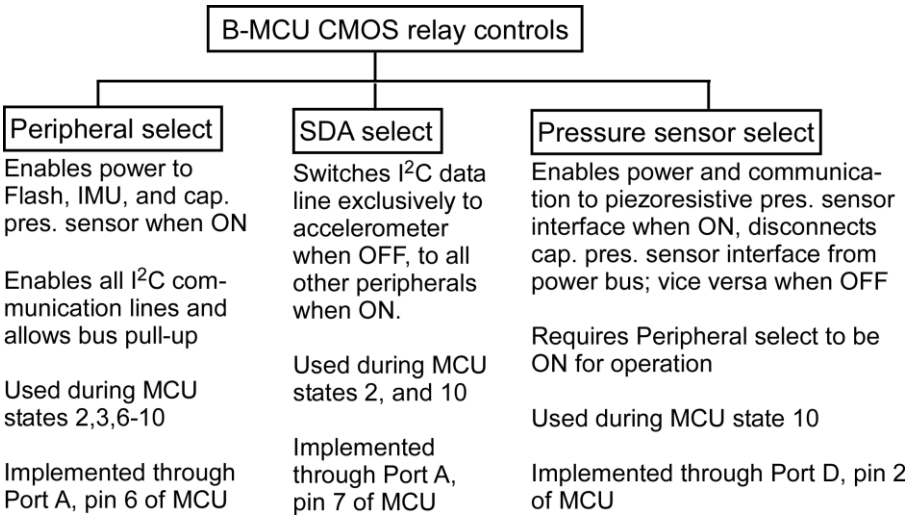



Fig. 5.10: CMOS relays controlled by the B-MCU.

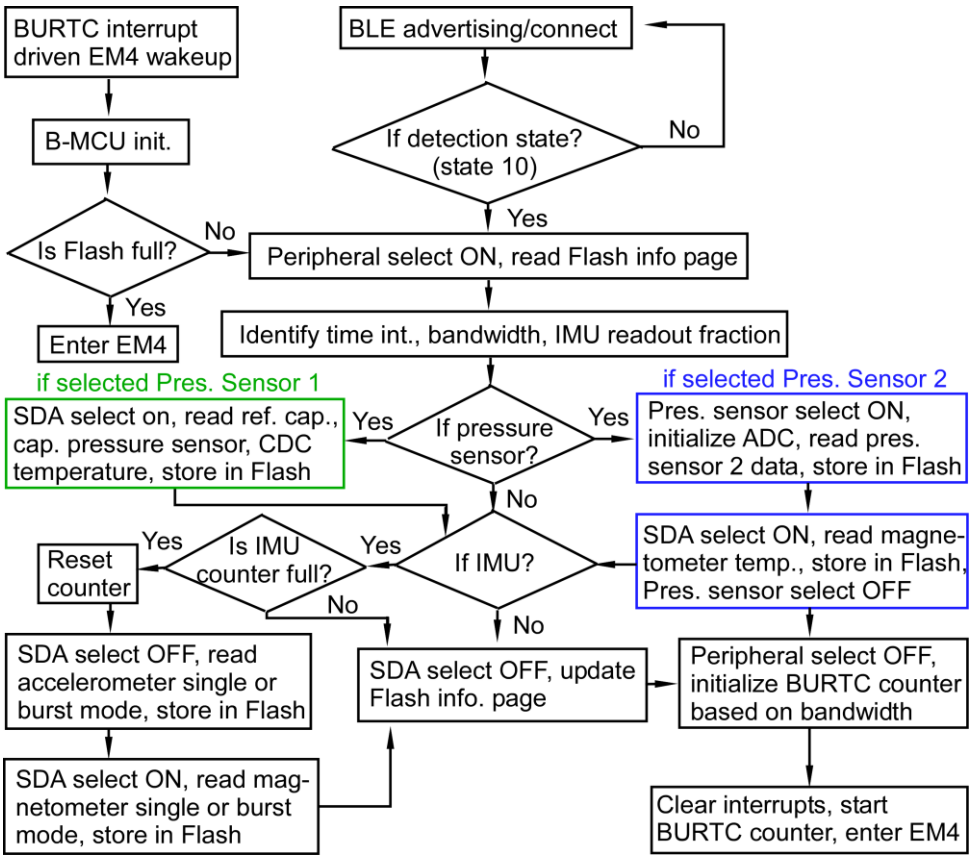



Fig. 5.11: Operation flowchart of B-MCU in detection state.

*Graphic User Interface (GUI):*

The software for the Bluetooth® external unit consists of backend processing and user interface, built using Python programming language. The designed GUI[4] is shown in Fig. 5.12. The GUI software is built using Tkinter package of Python language. The main window of the interface consists of four sections: 1) BLE connection control and status, 2) microsystem information and status, 3) B-MCU commands, 4) other options. The functions of each section are described in Table 5.4.

[4] GUI implemented with contribution from Mr. Ziyan Wang, ECE, University of Michigan.

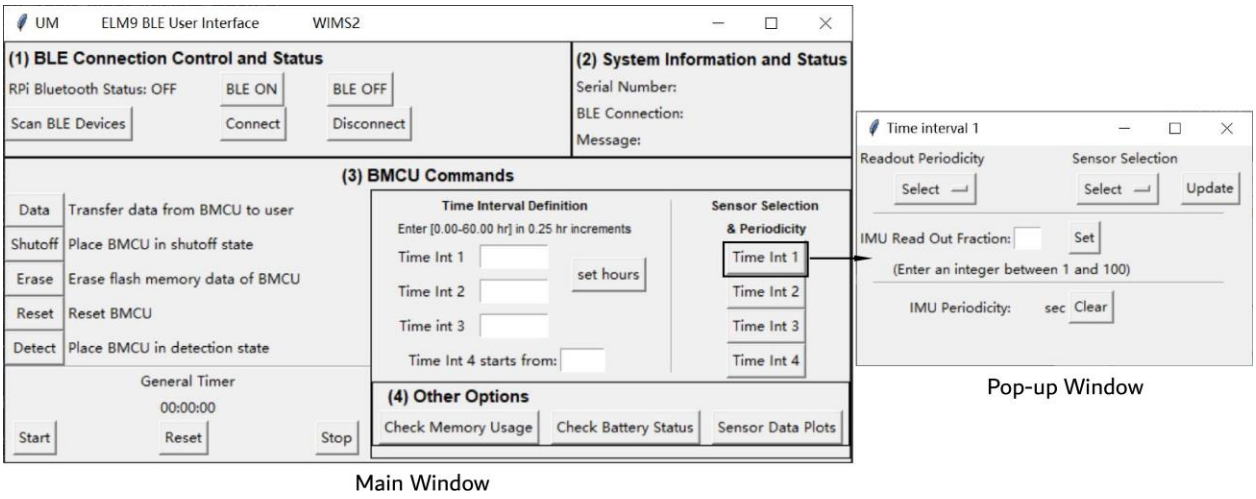



Fig. 5.12: ELM9 Graphical User Interface on laptop.

Table 5.4: List of GUI sections with their functionality.

| No. | Section | Functions |
|---|---|---|
| 1 | BLE Connection Control and Status | • Allows the user to turn on/off Bluetooth interface<br>• Allows the user to scan available BLE devices nearby<br>• Allows the user to select the device for BLE connection and establish/terminate connection |
| 2 | System Information and Status | • Displays the serial number of the connected ELM9 microsystem<br>• Displays the status of BLE connection<br>• Displays the status of the microsystem as a result of any command<br>sent by the user. Contains a “Clear” button to clear the message |
| 3 | B-MCU Commands | • Allows the user to send commands to the B-MCU<br>• Allows the user to provide time interval definition, select the sensors and readout periodicity, and set IMU readout fraction.<br>• Contains a general timer to record the total time in which the system has been in detection state |
| 4 | Other Options | • Interactive tool to estimate memory limited lifetime of microsystem<br>• Displays the battery lifetime of connected ELM9 microsystem<br>• Provides user the graphical plot of sensor data |

A BLE enabled USB dongle, BLED112, from Silicon Laboratories Inc., provides the hardware support (Bluetooth® stack and antenna) for running the GUI on a laptop [Ble20].

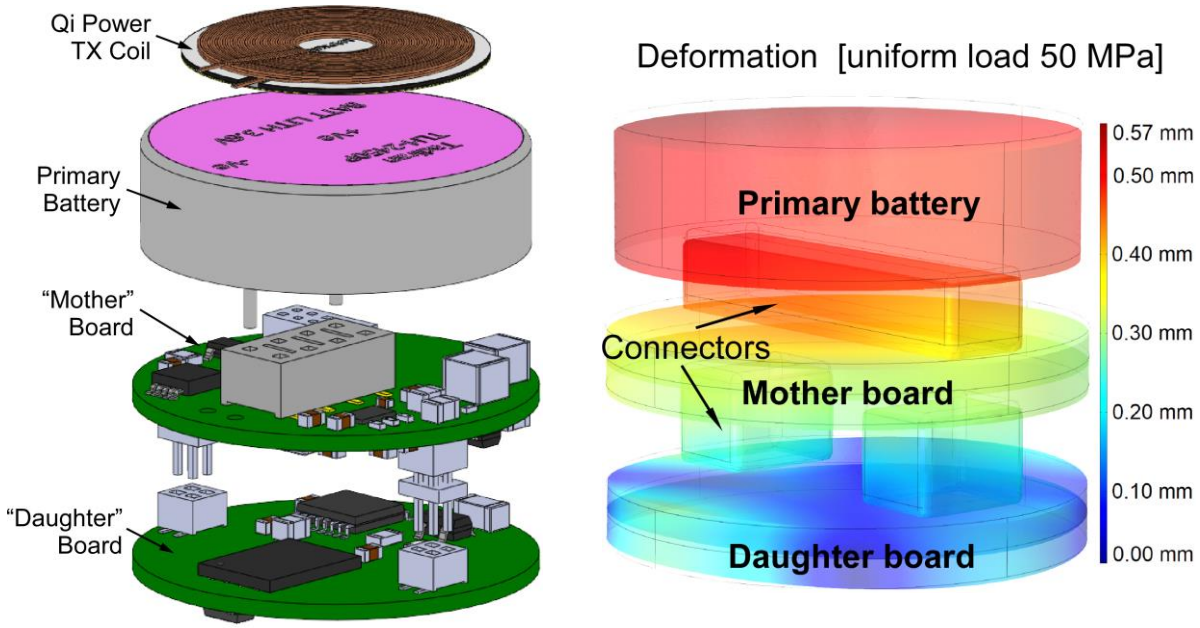
## 5.2 System Integration

The ELM9 microsystem components are integrated on two circular PCBs within the needed form factor to meet the density requirements of the packaged microsystem. A *mother board* houses the wireless power receiver, power management module, B-MCU, and primary battery. A *daughter board* houses all sensor modules and external Flash memory chip. The two-board design enables individual replacement of either board in the event of a failure, promoting reusability of microsystem components and lowering replacement costs. Based on prior efforts, it was observed that the microcontroller and associated passives are more prone to failure induced by prolonged exposure to elevated temperature. A temperature induced failure typically manifests itself by effectively grounding the power bus within the PCB, thus corrupting the entire board. Therefore, the B-MCU and Flash memory chip have been placed on separate PCBs to increase the likelihood of Flash chip data retention in the event of a temperature induced failure during deployment. If a new mother board is attached to the existing sensor board, stored data inside the Flash memory chip can be extracted with ease.

The ELM9 microsystem stack consists of the two PCBs placed on top of each other along with the wireless power receiver coil and primary battery to minimize microsystem form factor, example illustration shown in Fig. 5.13(a)[5]. The PCBs are electrically connected using two sets of a 10-pin male connector (FTSH-105-01-L-DV-K-TR, Samtec Inc.), and 10-pin female connector (CLP-105-02-G-D, Samtec Inc.). The primary battery is connected to the mother board using a female battery connector (HLE-107-02-G-DV-K-TR, Samtec Inc.). The wireless power receiver coil needs to be integrated at one end of the stack, such that the packaged microsystem can be

[5] 3D illustration prepared with contribution from Mr. Hanfei Zheng, ECE, University of Michigan.

placed flat on top of a wireless power transmitter coil. The daughter board also needs to be placed at one end of the stack for ambient pressure to be uniformly transmitted to the pressure sensor diaphragms. To further understand the placement of components, an FEA model with multiple arrangements of the microsystem stack was studied in COMSOL Multiphysics®, where the maximum von Mises stress and deformation of the PCBs was monitored. With a PCB thickness of 3 mm, the stack arrangement shown in Fig. 5.13(b) resulted in the lowest stress and PCB deformation, with the maximum von mises stress at 90 MPa and maximum PCB deflection of 250 µm under an applied compressive load of 50 MPa. For comparison, utilizing PCBs with a thickness of 1.5 mm and poorly oriented connectors, the stress and deformation could increase to 200 MPa and 880 µm, respectively, which may result in microsystem failure at high pressure due to component delamination or destruction.




(a) (b)

Fig. 5.13: (a) Example illustration of ELM9 microsystem stack (b) FEA study showing ELM9 stack arrangement with minimum PCB deformation under uniformly applied load of 50 MPa.

The ELM9 PCBs are fabricated on a 185HR PCB substrate for thermal reliability, which has a glass transition ($T_g$) temperature of 180°C (relative to standard FR4 with a $T_g$ of 130°C). The fabrication and component assembly is performed by Advanced Circuits, Colorado, USA. The capacitive pressure sensor is assembled in-house using conductive Duralco 120 silver epoxy. Fig. 5.14 (a) and (b) shows the PCB design of the mother and daughter boards, respectively. The PCBs are circular in shape with a diameter of ø26.7 mm to fit within the package. Both pressure sensors are placed adjacent to each other, at the edge of the sensor board, close to the package exterior to ensure transmission of exterior pressure with minimal attenuation. An opening is cut on the PCB beneath the capacitive pressure sensor so that the diaphragm is exposed to the exterior pressure, which would be transferred through the packaging elements. The CDC module is placed closed to the pressure sensor to reduce parasitic capacitances.

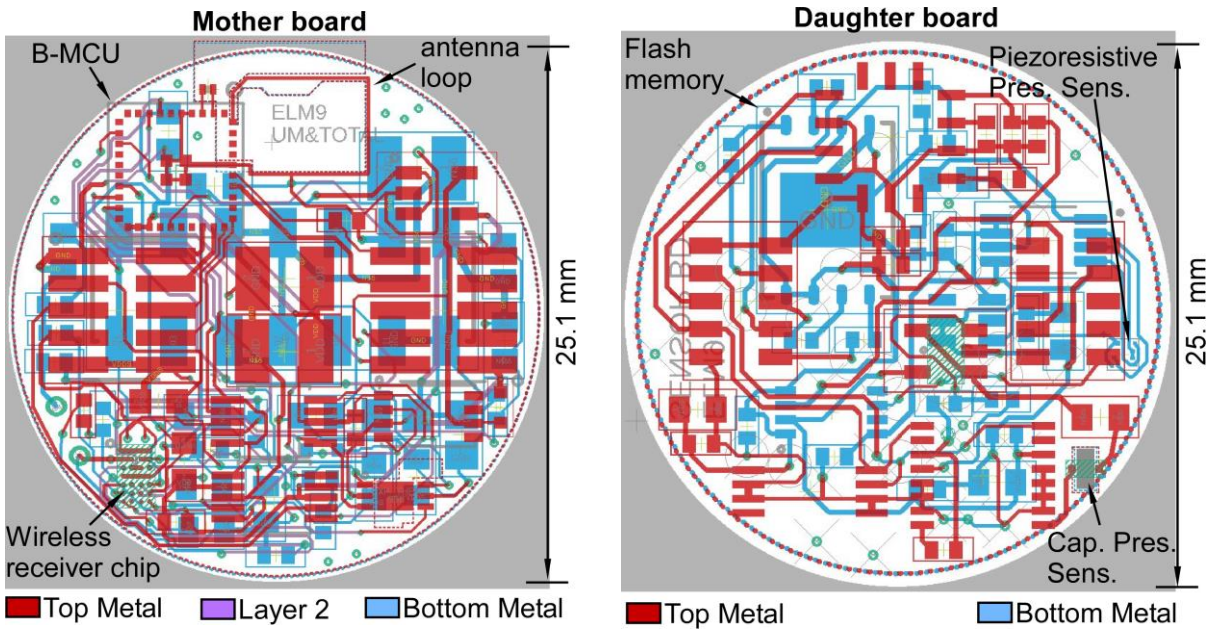


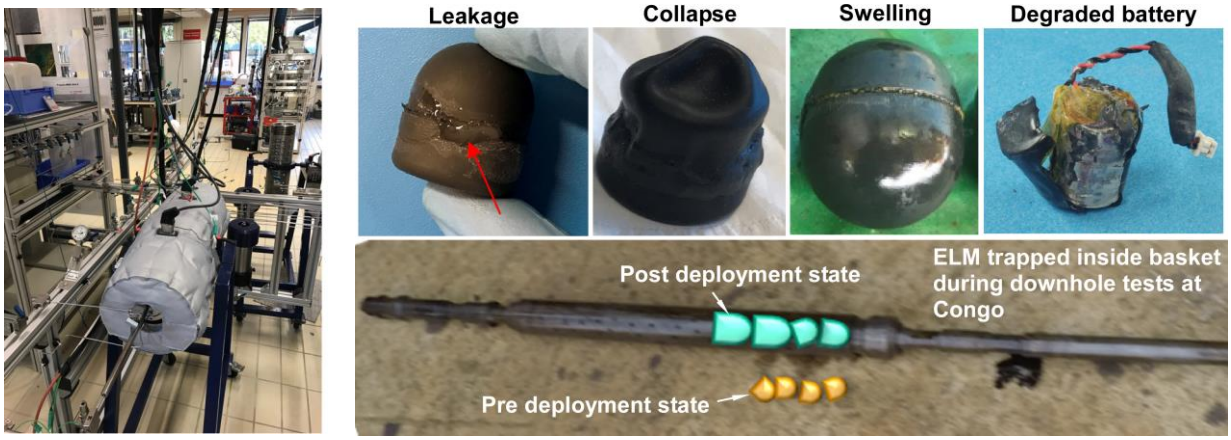

Fig. 5.14: (a) PCB design layout of the mother board with 3 metal layers (top – layer 1, layer 2, and bottom – layer 16) (b) PCB design layout of the daughter board with 2 metal layers (top, and bottom).

## 5.3 System Packaging

For oil reservoirs, which may be as deep as 6 kilometers underground, the typical downhole environment can consist of temperatures of ≤150°C, pressures of ≤50 MPa, salinity of 5-15% (50,000-150,000 ppm), and $H_2S$ concentrations ≤2,500 ppm [Cha12]. The density of downhole fluid is <1.5 g/cm$^3$ [Lia18]. The exterior packaged microsystem size is limited by the size of the well bore, typically <ø45 mm diameter. The package integration approach must permit transfer of external pressure and temperature to the sensors while protecting the electronics from the harsh environment during deployments; between deployments it must allow wireless power transfer and wireless communication, and in certain situations it must also allow the removal of the package and reusability of the microsystem hardware. These goals are achieved by designing the ELM9 microsystem stack to fit within a flow-compatible package designed to operate within oil well bores.

The packaging approach adopted in ELM7 included a two-part injection molded Viton™ shell sealed together with Fluorodyn™ caulk (Thermodyn Corporation, Houston, TX, USA) on the exterior with a low bulk density cenosphere fill on the interior to lower overall microsystem density [Vel20]. The ELM7 package was studied in an acid simulation bench over multiple iterations with simulated oil bore chemical environments at temperature (≈70°C) and pressure (≈35 MPa) conditions in corporate laboratory (TOTAL Energies, Pau, France). Fig. 5.15 (a) shows a picture of the acid simulation bench test setup used for this test. Some of the packages, when subjected to simulated oil wellbore conditions for >4 hours, revealed several issues with package microsystem leakage and rupture of internal support structures. In addition, when the packages were tested in an operational oil well in Congo, Africa, significant package swelling for some

microsystems was observed on retrieval. Pictures of the affected packages have been shown below in Fig. 5.15 (b).




(a) (b)

Fig. 5.15: (a) Picture of acid stimulation bench used to study ELM package in simulated borewell environment at TOTAL Energies, France (b) Pictures of affected ELM7 packages from laboratory and field testing with potential issues identified.

Diffusivity of gases through Viton is exponentially dependent on temperature. As temperature increases with the ELM being lowered into the depth of the energy well, the Viton shell allows increased diffusion of gases like methane, $CO_2$, and $H_2S$ into any interstitial space within the package; the high concentration gradient and high pressure gradient being the driving forces. However, as the ELM is extracted out of the well, the ambient temperature drops quickly, leading to a hysteresis effect caused by rapid drop in diffusivity of the gasses now trapped within the ELM Viton shell. Therefore, while the pressure inside the package is higher, the trapped gas takes a long time to diffuse out of the package (often being multiple days). Any loss in package integrity may disrupt proper functioning of the ELM microsystem and expose the sensors or electronics to harsh environments.

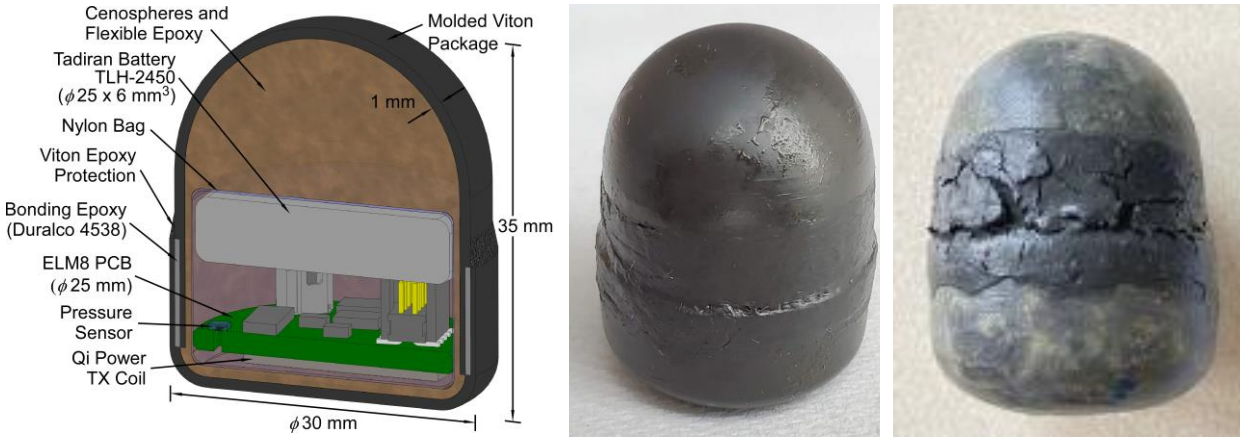
Therefore, an improved approach to microsystem packaging has been investigated in this work to preserve ELM9 microsystem operation in downhole environments.

In order to improve the packaging approach, three primary findings from the ELM7 package were identified[6]: 1) As the outer Viton™ shell allowed gas intrusion under pressure, the large interstitial space in the cenosphere filling allowed this gas to be trapped, causing package swelling when the package undergoes quick depressurization (i.e. retrieved from oil well), as the trapped gas cannot escape, 2) since two separate Viton™ shells are being bonded manually with Fluorodyn™ caulk, the smooth surface of Viton™ makes it very difficult to attain a leakage free seal, and 3) any 3D printed support structure should be sufficiently rigid to bear a large compressive stress.

Based on these learnings, an intermediate ELM microsystem package (ELM8) was designed and tested. The design included mixing the cenosphere filler with a low-density flexible epoxy (Duralco 4538, Brooklyn, NY, USA). This approach eliminated the interstitial space within the cenosphere filler, minimizing trapped gas (1), and the epoxy core would provide mechanical support to the electronics, eliminating the need for a support structure (3). Additionally, a surface treatment of Viton™ in FlouroEtch solvent was performed prior to bonding to chemically activate the surface for a better seal, addressing (2). Fig. 5.16(a) shows an illustration of the packaging approach for ELM8. Fig. 5.16(b) shows an ELM8 microsystem after 72 hour testing at HPHT conditions in an oil bath, shows no degradation in package. However, when a package was tested for gas intrusion in a $CH_4$ environment at a pressure of 34 MPa and temperature of 90°C for 6 hours, ≈109% volumetric swelling was observed in the package. The package after the gas intrusion test is shown in Fig. 5.16(c). The Viton™ shell tends to delaminate from the epoxy and

[6] ELM microsystem packaging effort is led by Dr. Alexander Benken, University of Michigan.

cenosphere core, causing a ballooning effect of the Viton$^{TM}$ with gas intrusion and cracks at the bonded interface of the two Viton$^{TM}$ shells.




(a) (b) (c)

Fig. 5.16: (a) Illustration showing ELM8 packaging approach (b) ELM8 package after 72 hour in HPHT oil bath (c) ELM8 dummy package (no electronics) after $CH_4$ gas intrusion test at 34 MPa, 90°C for 6 hours.

It is now evident, to successfully package ELM9 microsystem to prevent gas intrusion, the Viton$^{TM}$ shell should be eliminated, as it is permeable to gases when pressurized, especially at high temperatures. The proposed approach for packaging the ELM9 microsystem consists of directly molded the electronics stack into a low-density polymer to eliminate the layering of different materials. The chosen material when cured, must be flexible to allow transmission of pressure to the sensor diaphragms, and the molding process must be compatible with the microsystem electronics (molding/curing temperature <150°C). Viton$^{TM}$ has a density of 1.84 g/cm$^3$; the low density cenospheres and epoxy mix was necessary to reduce overall ELM8 density to <1.5 g/cm$^3$. Therefore, an alternate polymer or composite must be identified, which is compatible with the HPHT chemical environment, and has a sufficiently low density to permit the the ELM9 microsystem density to remain <1.5 g/cm$^3$. A number of materials were analyzed from literature for resistance to brine (15%), diesel (100%), $H_2S$ (0.25%), and $CH_4$ (100%); the findings are listed in Table 5.5.

Table 5.5: Potential options for ELM9 package material.

| Material | Molding Method | Brine (15%) | Diesel (100%) | $H_2S$ (0.25%) | $CH_4$ (100%) | Max. Temp. | Density [g/cm$^3$] | ELM9 Density (ø39 mm) | Cost |
|---|---|---|---|---|---|---|---|---|---|
| **Kalrez (FFKM)** | Injection Molding | Good | Good | Good | Good | 250°C | 2.10 | 2.03 | $$$$$ |
| **Viton (FKM)** | Injection Molding | Good | Good | Fair | Good | 200°C | 1.84 | 1.86 | $$$ |
| **Viton+Cenosphere** | Injection Molding | Good | Good | Fair | Good | 200°C | 1.83 | 1.72 | $$$ |
| **Nitrile (NBR)** | Injection Molding | Good | Good | Good | Good | 120°C | 1.25 | 1.46 | $ |
| **Hydrogenated Nitrile (HNBR)** | Injection Molding | Good | Good | Good | Good | 170°C | 1.18 | 1.39 | $$ |
| **Silicone (VMQ) (Sylgard 170)** | Vacuum Molding | Good | Incom. | Poor | Incom. | 200°C | 1.30 | 1.50 | $$ |
| **VMQ+Cenosphere** | Vacuum Molding | Good | Incom. | Poor | Incom. | 200°C | 0.91 | 1.16 | $$ |

Good / compatible response
Fair response / minor or reversable issues
Incompatible / Poor response

The above findings suggest hydrogenated nitrile (HNBR) may be a good fit, as it is resistant to the chemical environment, has a low density of 1.18 g/cm$^3$, and can sustain temperatures of ≤170°C. In order to further understand the applicability of HNBR, a Viton$^{TM}$ shell ELM8 dummy package, along with two injection molded solid cylinders of HNBR and Viton$^{TM}$ were simultaneously studied in the gas migration test setup in a $CH_4$ environment, described in Fig. 5.15(a) at Total Energies, France; the results from the test have been summarized in Table 5.6.

Table 5.6: Dimensional and weight changes of Viton and HNBR, after $CH_4$ migration test[7].

| | Diameter (L x W) [mm] | Height [mm] | Volumetric Expansion | Weight [g] | Weight Expansion |
|---|---|---|---|---|---|
| ***Viton-Shell,*** Initial | ø33.6 | 30.5 | --- | 24.34 | --- |
| ***Viton-Shell,*** Post-Test | ø37.1 | 44.5 | 109% | 24.4 | 0.24% |
| ***Viton-Solid,*** Initial | 21.32 x 21.48 | 0.50 | --- | 1.594 | --- |
| ***Viton-Solid,*** Post-Test | 21.57 x 22.12 | 0.51 | 6.3% | 1.584 | 0.64% |
| ***HNBR-Solid,*** Initial | 20.66 x 19.80 | 0.50 | --- | 1.020 | --- |
| ***HNBR-Solid,*** Post-Test | 20.86 x 20.15 | 0.51 | 4.1% | 1.011 | -0.88% |

Although the Viton™ solid structure performed better than its shell counterpart in the volumetric expansion study (suggesting solid molding is the path forward for ELM9 packaging), the results suggest that HNBR (4.1%) outperforms Viton™ (6.3%) with a lower volumetric expansion after the gas migration test. In addition, the low density of HNBR (1.18 g/cm$^3$) permits a low compact microsystem size, while retaining a low overall microsystem density <1.4 g/cm$^3$. Hence as illustrated in Fig. 5.17, the ELM9 microsystem stack, injection molded with HNBR into a flow compatible spherical ball, with ø39.0 mm diameter, and estimated density of 1.39 g/cm$^3$, is the chosen packaging approach for the ELM9 microsystem. The injection molding of HNBR was performed commercially through TMI Rubber, Youngstown, OH, USA.

[7] Gas migration tests of ELM package performed at Total Energies, France.

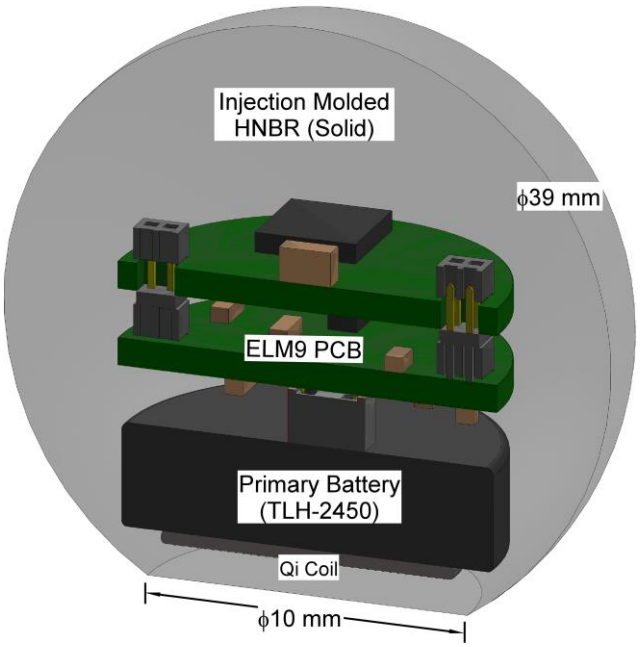



Fig. 5.17: Packaging concept of ELM9 microsystem – includes ELM9 microsystem stack injection molded into a sphere of HNBR with small flat area for placement onto Qi wireless power transfer pad.

## 5.4 System Fabrication and Testing

### 5.4.1 ELM8 Fabrication

The ELM microsystem fabrication and testing has been performed in two steps. In the first implementation (ELM8), only the HT primary battery and the Power management module described in section 5.1, were added to the existing design of the ELM7 microsystem, keeping all other design elements unchanged. The updated circuit design (ELM8) was fabricated on a single PCB as illustrated in Fig. 5.18, by Advanced Circuits, Colorado. This intermediate microsystem (ELM8) was used to validate operation of the new power system, autonomous control of CMOS relays by the B-MCU, lead software state machine design, and contribute to packaging studies for HPHT operation. Physical specifications for the ELM8 microsystem are given in Table 5.7; descriptions of all major components and sensors contained with the ELM8 microsystem are given in Table 5.8.

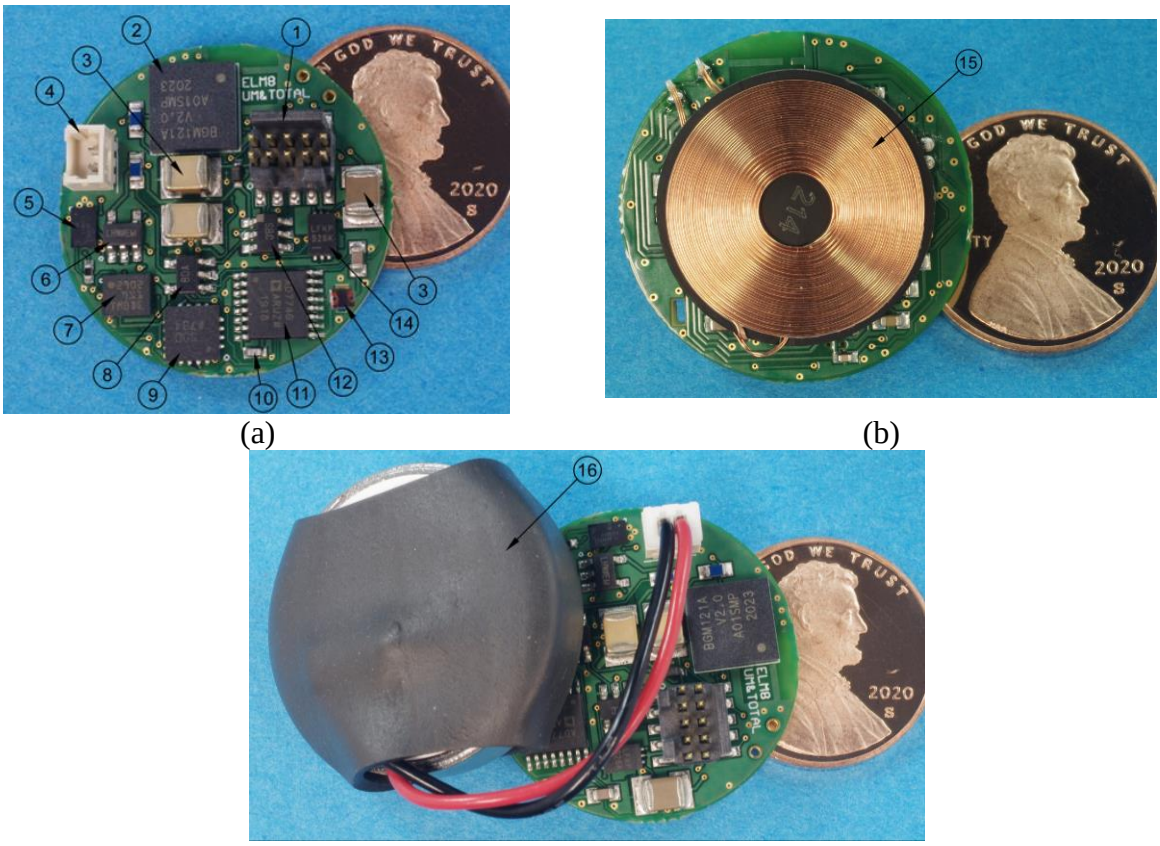



Fig. 5.18: Unpackaged Environmental Logging Microsystem 8 (ELM8): (a) top and (b) bottom view (without primary battery) and (c) HT primary battery connected to ELM8 microsystem. Major components labelled are detailed in Table 5.8.

Table 5.7: ELM8 microsystem specifications

| Specification | Value | | |
|---|---|---|---|
| | Min. | Typ. | Max. |
| Unpackaged PCB dimension | - | ≈ø25 mm$^2$ | - |
| Packaged microsystem dimension | - | - | ø30 x 35 mm$^3$ |
| Packaged microsystem mass | 26.8 g | 29.1 g | 32.4 g |
| Packaged microsystem density | 1.3 g/cm$^3$ | 1.45 g/cm$^3$ | 1.6 g/cm$^3$ |
| Typical battery voltage | - | - | 3.55 V |
| Microsystem pressure range | - | - | 7.3 kpsi |
| Operational temperature range | 20°C | - | 85°C |
| Pressure sensor resolution | 0.04 psi | 0.08 psi | 0.15 psi |
| Sensor data storage capacity | - | 76 kB | - |

Table 5.8: Descriptions of major components of ELM8.

| Item | Component | Description | Dimension (L×W×H mm$^3$) | Manufacturer Part Number |
|---|---|---|---|---|
| 1 | Debug Connector | Used for programming the B-MCU | 6.4 × 5.8 × 6.0 | FTSH-105-01-L |
| 2 | Bluetooth-Microcontroller Unit (B-MCU) | Controls ELM8 microsystem, stores sensor data, and communicates with External Unit using BLE protocol | 6.5 × 6.5 × 1.4 | BGM121 |
| 3 | Bypass Capacitors | Used to smooth high current spikes required during flash data writing and data transfer. | 3.2 × 2.5 × 2.5 | GRM32EC7 |
| 4 | Battery Connector | Used for connecting the battery to the PCB | 4.3 × 3.2 × 4.2 | 0530470210 |
| 5 | Wireless Power Receiver Chip | Receives power wirelessly using Qi protocol | 1.9 × 3.0 × 0.5 | BQ51003 |
| 6 | Voltage Regulator | Used to convert 5 V received from wireless power to 3.6 V for use by the circuity | 2.9 × 2.8 × 1.0 | ADP161 |
| 7 | Inertial Measurement Unit (IMU) | Consists of an accelerometer and magnetometer for measuring internal data | 3.5 × 3.0 × 1.0 | LSM9DS1 |
| 8 | Capacitive Extension Op. Amp. | Used for increasing the capacitive range of the CDC to permit up to 10.0 kpsi full-scale range | 3.0 × 3.0 × 1.5 | AD8515 |
| 9 | Low Power Disconnect Relay | Disconnects power from unused components during sleep-mode to reduce current draw | 4.0 × 4.0 × 0.8 | ADG888 |
| 10 | Reference Capacitor | Capacitor with negligible temperature coefficient for temperature compensation. | 1.0 × 0.5 × 0.6 | GCM1555C1H |
| 11 | Capacitance to Digital Converter | Used to interface with pressure sensor and provide temperature sensing using an internal circuit | 5.1 × 6.4 × 1.2 | AD7746 |
| 12 | Switching Relay | Switches power draw of ELM8 from battery to wireless power when available. | 3.0 × 3.0 × 1.4 | ADG819 |
| 13 | MEMS Pressure Sensor | Capacitive pressure sensor [Ben21] | 1.8 × 1.5 × 0.5 | Model 85C56-92 |
| 14 | Battery Gauge | Coulomb counter for battery lifetime estimation | 3.0 × 2.0 × 0.8 | LTC2941-1 |
| 15 | Wireless Power Coil | Used for Qi wireless power transfer | ø19.0 × 0.8 | 760308101214 |
| 16 | Primary Battery | Primary (non-rechargeable) Tadiran TLH-2450 battery | ø25 × 10 | TLH-2450 |

### 5.4.2 Laboratory Testing of Packaged ELM8 microsystem

The fabricated ELM8 microsystem electronics were packaged using the flexible epoxy and cenosphere filler, described in section 5.3, and evaluated in a controlled HPHT chamber filled with mineral oil. A second ELM8 microsystem electronics packaged using the ELM7 packaging approach [Vel20], with the microsystem electronics placed in an oil filled nylon bag for transmission of external pressure to the sensor diaphragm, was parallel evaluated to understand any differences in sensed parameter transmission through the package. Both package designs transmitted all sensing parameters well, with near identical performance, thus eliminating the need for packaging the electronics in a custom oil filled nylon bag. The 4-hour HPHT test results from the two packaged ELM8 microsystems, with applied pressure up to 7,250 psi and temperature up to 100°C have been shown below in Fig. 5.19(a) and (b), respectively. The experiment resulted in a <1% reduction of the primary battery capacity, verifying correct operation of the power management module. The microsystem standby current during EM4 shutoff was measured to be 0.6 µA @ 25°C, which is a two order of magnitude reduction when compared to the ELM7 microsystem.

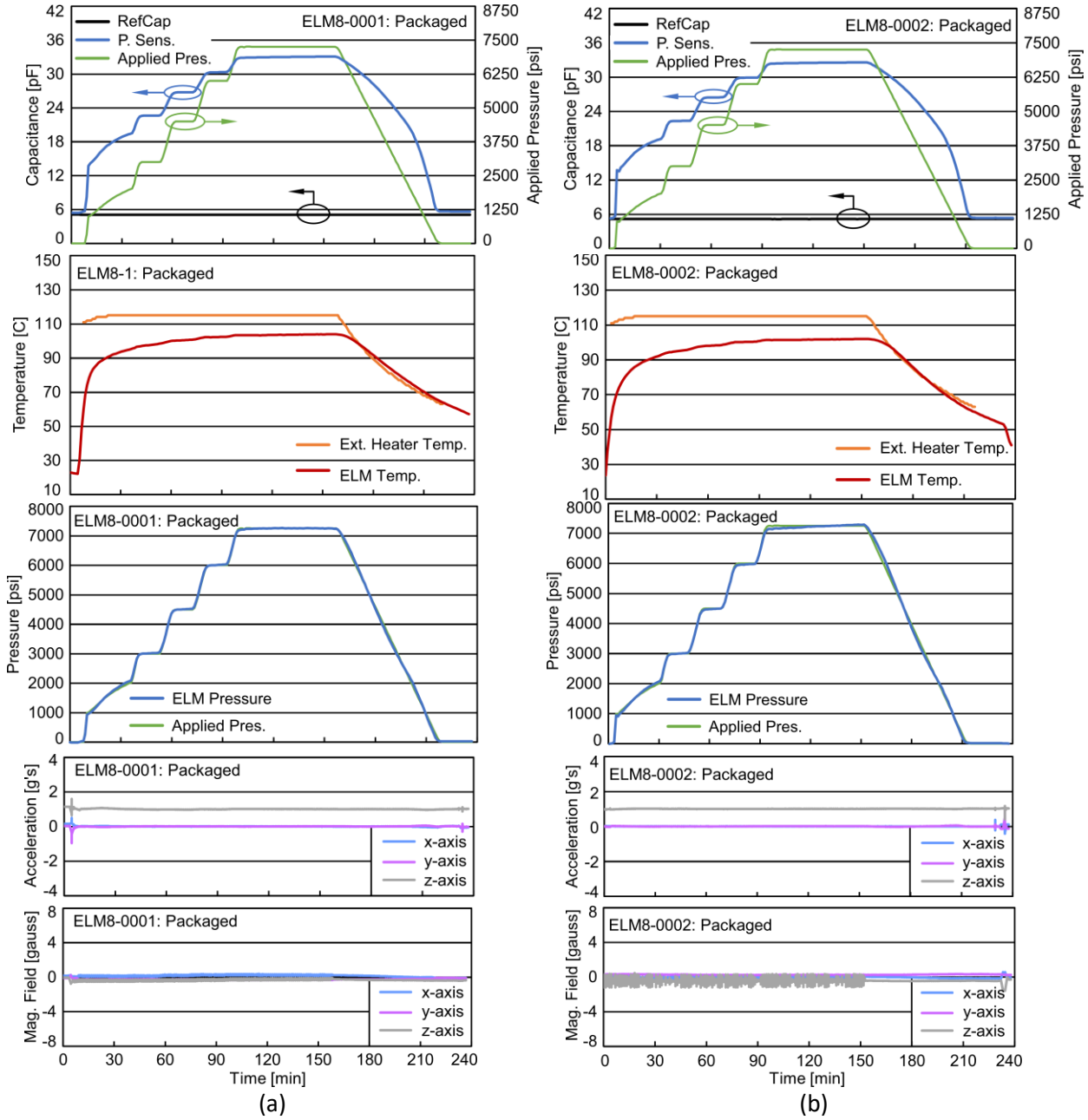



Fig. 5.19: Collected data from packaged ELM8 microsystems (up to 7,250 psi and 100°C). (a) ELM8-0001 is packaged using flexible epoxy and cenosphere composite. (b) ELM8-0002 is packaged in oil filled nylon bag [Vel20].

### 5.4.3 Functionality and Current Characterization of ELM9 microsystem

In the ELM9 implementation, all microsystem design elements discussed in section 5.1, and 5.2 were realized onto two PCBs, fabricated by Advanced Circuits, Colorado. Functional characterization of a proto-board design of the full ELM9 microsystem was used to validate the

state machines. The $I^2C$ and SPI communication was successfully tested between the B-MCU, sensor interfaces, and external Flash memory chip. The Bluetooth® functionality of the B-MCU was successfully verified; the remaining battery lifetime of ELM9 was accurately read out. The temperature, pressure, and inertial sensor data was successfully collected and readout using BLE. The B-MCU current consumption during BLE communication was characterized. A detailed analysis of the current consumption of B-MCU along with other microsystem components was carried out during the investigation of previous ELM generations [Sui17, Vel20]. The current consumption of B-MCU during BLE communication was experimentally measured at 25°C by sending data from the B-MCU. These tests were performed at 25°C to match the intended application scenario where the user only needs the BLE communication after the microsystem is retrieved from deployment for data readout. The transient current of the B-MCU was measured using the Silicon Labs energy profiler, in-built within the Simplicity Studio Integrated Development Environment, using a CORTEX debug interface [Aem22]. The measured transient current of the B-MCU during a typical BLE advertising mode and handshaking mode are plotted in Fig. 5.20(a) and (b), respectively. Fig. 5.20(c) and (d) shows one sensor measurement cycle during BMCU detection state. In Fig. 5.20(c) only the capacitive pressure sensor is active, while in Fig. 5.20(d), the IMU is also active in single readout mode. Fig. 5.20(e) shows the current draw during a Flash erase operation, typically performed before every deployment routine. The continuous high current draw of 20 mA over ≈25 sec, suggests this operation is performed when wireless power is available. Fig. 5.20(f) shows the ELM9 current draw profile in standby mode, when the B-MCU is placed in EM4 shutoff. The average current is measured at 0.27 µA at 25ºC, which is below the preferred design target of <0.5 µA.

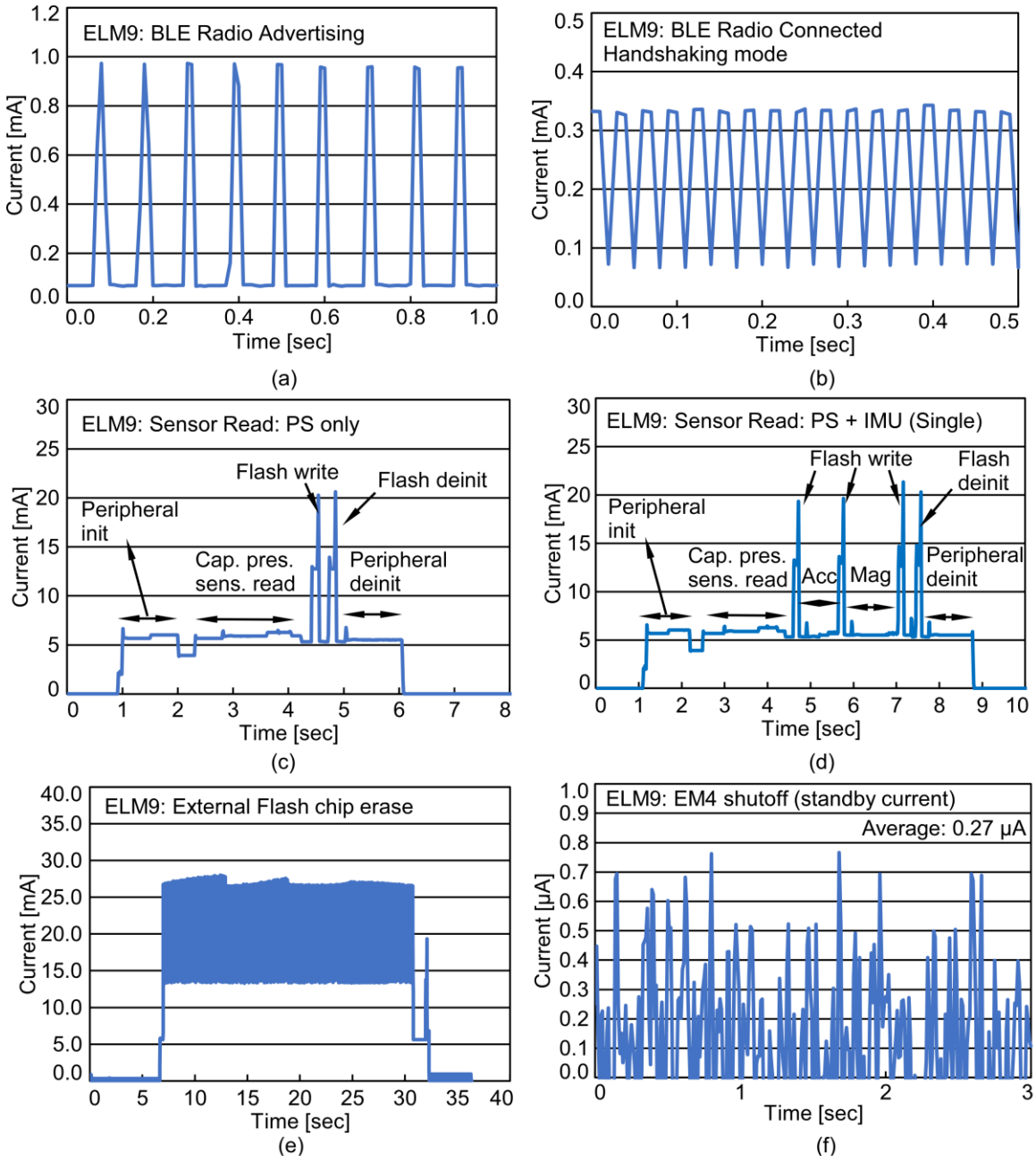



Fig. 5.20: (a) ELM9 current draw during BLE radio advertising (b) ELM9 current draw during BLE connection and handshaking with GUI (c) ELM9 current draw during one sensor measurement routine in B-MCU detection state with only capacitive pressure sensor active (d) ELM9 current draw during one sensor measurement routine in B-MCU detection state with capacitive pressure sensor and IMU active in single mode (e) ELM9 current draw during external Flash erase operation (f) ELM9 current draw during standby mode/B-MCU placed in EM4 shutoff; average current is 0.27 µA. All measurements performed at 25°C.

The low standby current of 0.27 µA permits an ELM9 lifetime of >5 days at 100ºC and >1 day at 150ºC, determined by the chosen sensors and measurement bandwidth. Designed ELM9 microsystem specifications are listed in Table 5.9.

Table 5.9: ELM9 microsystem specifications.

| Specification | Value | | |
|---|---|---|---|
| | Min. | Typ. | Max. |
| Unpackaged PCB dimension (Mother + Daughter board) | - | ≈ø25 $mm^2$ | - |
| Packaged microsystem dimension | - | - | ø39 $mm^3$ |
| Packaged microsystem mass (est.) | - | 29.1 g | - |
| Packaged microsystem density (est.) | - | 1.39 $g/cm^3$ | - |
| Typical battery voltage | - | - | 3.55 V |
| Microsystem pressure range | - | - | 50 MPa |
| Operational temperature range | 20°C | 125°C | 150°C |
| Capacitive pressure sensor resolution | 0.3 kPa | 0.5 kPa | 1.0 kPa |
| Piezoresistive pressure sensor resolution (est.) | 1 kPa* | - | 44 kPa# |
| Sensor data storage capacity | - | 16 MB | - |

** Utilizing oversampling and averaging, 2 Hz BW*
*# Instantaneous resolution, 2 kHz BW*

## 5.5 Chapter Summary

This Chapter discussed the system design of an environment logging microsystem (ELM9) for autonomous buoyant downhole monitoring application. The microsystem was designed to achieve a pressure measurement full-scale range of 50 MPa with operating temperatures up to 150°C. Multiple high temperature compatible commercial off-the-shelf (COTS) components were chosen in microsystem design, to reduce cost and enhance scalability of the solution. Most components were selected based on features, minimum package footprint, and operational capability at high temperatures. The ELM9 houses both a capacitive and piezoresistive pressure sensor interface. While the custom capacitive pressure sensor [Ben21] provides high resolution pressure measurement at an increased cost, the COTS piezoresistive pressure sensor provides a

low cost, and easy to scale alternate and can be used to sample pressure at a frequency of 2 kHz with lower pressure resolution.

Two specific power management features were designed to increase the operational lifetime of the ELM9 microsystem by reducing the current draw required from the primary battery, with a measured standby current of 0.27 µA @ 25°C. One feature was designed to reduce the current consumption of the microsystem when in a power-down mode during deployment while the second was designed to eliminate current draw from the primary battery entirely when wireless power is available during data interrogation and storage.

Software for the ELM9 microsystem first included Bluetooth® microcontroller (B-MCU) state machine to reliably implement all microsystem functionalities, reduce microsystem power budget and limit Flash memory usage. The second part involved graphic user interface (GUI) design for the external computer/laptop, which interfaces with the B-MCU using a BLE wireless dongle and interacts with the end user for command and data transfer.

A finite element analysis (FEA) model was studied to determine the integration of multiple microsystem components into a low form factor and mechanically robust microsystem stack. A packaging approach was investigated, using injection molded hydrogenated nitride (HNBR) to reduce the impact of gas intrusion while protecting the microsystem in a HPHT chemical environment. The new packaging approach also eliminated any custom integration and assembly steps, improving overall scalability of the microsystem.

An intermediate version of the ELM microsystem (ELM8) was investigated, fabricated, packaged, and tested in a controlled HPHT test setup. The results verified successful operation of the power management module, and primary battery, along with making positive strides toward

realization of an improved packaging approach for ELM9 microsystem. The final version of the ELM microsystem (ELM9) was fully investigated and characterized on protoboard. The PCBs for the proposed ELM9 microsystem are currently under fabrication at Advanced Circuits, Colorado, and shall be tested in both laboratory and field environments on arrival.

# Chapter 6: Conclusions and Future Work

This Chapter summarizes the efforts which investigated critical elements of building pressure sensing microsystems with applications in the energy industry. Major contributions to the microsystems field in design, integration, and packaging of such microsystems are listed. Future work regarding (i) passive wireless pressure gradient measurement for fluid flow analysis, and (ii) environment logging microsystem for downhole operation up to 150°C has been proposed.

## 6.1 Summary and Major Contributions

This dissertation advances the knowledge in building volume scalable, low-cost, modular sensing microsystems, focusing on applications in the energy industry. The specific goals of this dissertation were to 1) investigate new system and packaging technologies for deploying multiple pressure sensor nodes in a space constrained chemical environment, measure very low pressure gradients (<100 Pa) induced by fluid transport through a porous material over a large baseline pressure for application within core flood experiments; 2) investigate design methodologies and investigate pathways to minimize pressure measurement resolution of a LC Sensor with design constraints governed by the specific application requirements; 3) investigate microsystem level design challenges in dimensional scaling, relationships between interconnected design blocks, and environment specific performance limits of an autonomous environment logging microsystem for downhole application; and 4) investigate a microsystem package (maximum diameter ø45 mm) to enable deployment into narrow wellbores and fractures.

This work highlighted pressure sensing microsystem opportunities across the four sectors of the energy industry, namely upstream, midstream, downstream, and analytical/support technology. Two pertinent opportunities for pressure sensing microsystems have been addressed within the upstream and analytical sectors, which have a compelling need for such research and investigation. The first application involved deploying pressure sensing technology inside high pressure high temperature (HPHT) laboratory equipment, namely for core-flood experiments. The second application involved deploying autonomous buoyant environment logging microsystems (ELM) for monitoring downhole pressure and temperature within energy wells. The two chosen applications posed several contrasting requirements; the laboratory application posed strict requirements on sensor size and equipment compatibility and high pressure measurement resolution (<100 Pa) over a more limited full-scale pressure measurement range (2 MPa); the energy well application requirements included microsystem robustness, small form factor, and large full-scale pressure measurement range (50 MPa). The accomplishment of each specific goal has been discussed in the following paragraphs.

Toward the first specific goal, two approaches in deploying multiple pressure sensor nodes along the seam of a rock core in a core flood experiment setup were investigated. In the first approach, a wired feedthrough technology was investigated to provide lead transfer to MEMS capacitive pressure sensors, housed across a polymer sheath, with a 230-bar (23 MPa) pressure difference across the sheath. In a second approach, passive wireless inductive capacitive (LC) sensors (dia. <ø15 mm, thickness <3 mm) were investigated to eliminate the requirement of a wired feedthrough. In both approaches, the readout electronics are placed exterior to the rock core and interfaced with the sensors using a feedthrough (in approach 1) or wireless inductive coupling (in approach 2). The first approach, discussed in Chapter 2, was successfully tested in both an

academic laboratory using a custom flow test setup which provides pressure differentials during fluid flow, mimicking the rock core, and in an industry laboratory via integration into a core flood experiment test cell, demonstrating a pressure resolution of 0.3 mbar (30 Pa), over a full-scale pressure measurement range of 20 bar (2 MPa). The second approach, discussed in Chapter 3, was successfully tested in academic laboratory in the custom flow test setup and demonstrated a pressure measurement resolution of <1 mbar (100 Pa), over the same full-scale pressure range of 20 bar (2 MPa). Both microsystems were tested for temperature operation up to 125°C.

Toward the second specific goal, an LC Sensor design model and figure of merit, termed Design Optimization Factor (*DOF*), was proposed in Chapter 4, which aimed to encompasses all major design dependencies of the LC Sensor and its readout microsystem which may be in direct conflict with one another (e.g. interrogation gap, inductor coil diameter, capacitive pressure transducer response, etc…), into a single global equation, used to aid in the design to minimize final pressure measurement resolution of the microsystem, in context of unique challenges posed by the application (robust packaging, flexible PCB substrate, custom pressure transducers with unique $\Delta C/C_0$ response, misalignment tolerance, interrogation gap, etc.). Methods to increase the LC Sensor input impedance magnitude and signal to noise ratio (*SNR*), were evaluated. The *DOF* design model has been studied in MATLAB (MathWorks, USA) with the use of closed form analytical equations from literature, finite element analysis (FEA) studies performed using COMSOL Multiphysics® (Comsol Inc., USA), and SPICE circuit model evaluations. The *DOF* generated pressure resolution predictions were experimentally verified using the fabricated passive LC Sensor based microsystem discussed in Chapter 3.

Toward the third specific goal, the microsystem design and integration concepts of an environment logging microsystem (ELM) were investigated and reported in Chapter 5. For

downhole monitoring, the sensing targets include operating temperatures up to 150°C, full-scale pressure measurement range up to 50 MPa (500 bar) with a preferred resolution of <1.5 kPa, and inertial data (acceleration and magnetic field) logging (at >10 Hz frequency to extract meaningful geolocation information); the ELM9 microsystem was designed to meet these targets successfully. The microsystem size was limited by the size of the well bore and chosen integration and packaging methodology. Between deployments, the microsystem accommodated wireless power transfer as well as wireless communication with the external user.

ELM9 microsystem hardware and software were codesigned for dynamic control of oscillators and sensor hardware peripherals based on microsystem performance necessities and configurable duty cycles. The implemented microsystem demonstrated a low standby current consumption (0.27 µA @ 25°C) enabling multiday deployment (>5 days @ 100ºC), and accommodated recovery of sensor data stored in the Flash memory should the primary battery become depleted, through operation on wireless power. Fig. 6.1 shows the operation regime of the ELM8 and ELM9 microsystems in this work, in comparison to prior effort (ELM7) [Vel20].

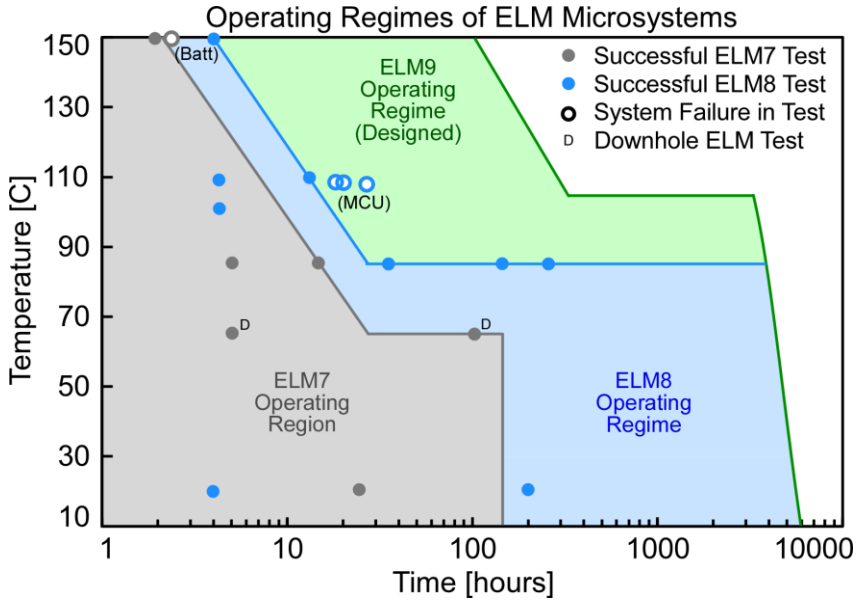



Fig. 6.1: Operating regimes of ELM microsystems.

Toward the fourth specific goal of investigating packaging materials and integration concepts for deployment and retrieval of environment logging microsystems, a new ELM microsystem package design using commercially injection molded hydrogenated nitrile (HNBR) was discussed in Chapter 5. The new material was tested to verify the impact of gas intrusion, compared to other potential materials such as Viton$^{TM}$. The package integration approach protected the electronics from the harsh environment while permitting transfer of external pressure and temperature to the sensors during deployments; between deployments it allowed wireless power transfer and wireless communication. These goals were achieved by designing the ELM9 microsystem stack, with all microsystem electronics on two separate PCBs, power source, and sensors, integrated into a low form factor, to fit within a flow-compatible package (maximum diameter ø39 mm, overall packaged microsystem density 1.39 g/cm$^3$).

Table 6.1 summarizes the key system functional thresholds and preferred design targets of this dissertation along with achieved results in this work.

Table 6.1: Comparison of results with design targets of this dissertation.

| Goals | Tasks | Parameters | Functional Threshold | Preferred Target | This work |
|---|---|---|---|---|---|
| Design in situ distributed pressure measurement microsystem to record pressure gradients and flow characteristics along the seam of a rock core | Investigate system hardware, automation, and integration strategies | Max. operating pressure | 15 MPa | 25 MPa | 25 MPa |
| | | Max. operating temperature | 100°C | 125°C | 125°C |
| | | Max. full-scale pres. range with offset | 1 MPa | 2 MPa | 2 MPa |
| | | Pres. Meas. resolution | <1 kPa | <100 Pa | <100 Pa |
| | Investigate wired feedthrough technology | Upper limit of feedthrough pressure difference | 15 MPa | 25 MPa | 23 MPa |
| | Investigate passive wireless LC sensing technology | Max. LC Sensor package thickness | 4 mm | 3 mm | 3 mm |
| | | Max. LC Sensor package diameter | ø20 mm | ø15 mm | ø15 mm |
| Design of an autonomous environment logging microsystem for downhole monitoring application | Investigate system level design challenges, and performance limits | Max. operating pressure | 40 MPa | 70 MPa | 50 MPa |
| | | Max. operating temperature | 100°C | 150°C | >125°C |
| | | Pressure measurement resolution | <7 kPa | <1.5 kPa | 0.5 kPa |
| | | Max. standby current | <5.0 µA @ 25°C | <0.5 µA @ 25°C | 0.27 µA @ 25°C |
| | | Min. deployment lifetime | 5 days (100°C) 1 day (150°C) | 10 days (100°C) 2 days (150°C) | >5 days (100°C) >1 day (150°C) |
| | Investigate an autonomous ELM package | Packaged system diameter | <ø45 mm | ø25 mm | ø39 mm |
| | | Packaged system volume | <48.0 $cm^3$ | 8.2 $cm^3$ | <32 $cm^3$ |
| | | Packaged system density | <1.5 $g/cm^3$ | 1.0 $g/cm^3$ | 1.39 $g/cm^3$ |

## 6.2 Future Work

This dissertation provides the path forward for research work in broadly three areas: (i) new applications of pressure sensing microsystems; (ii) microsystem design, integration, and packaging methods for HPHT chemical environments; and (iii) application specific optimization of passive LC Sensor based pressure sensing technology. The various aspects of microsystems presented in Chapters 2, 3, and 5, including power management, sensing, automation, microsystem integration, and packaging can be adapted for sensing microsystems applications such as aerospace, biomedical, consumer, food, and marine, to name only a few. With the advancement of battery technology and high temperature compatible electronics, the microsystem design and integration challenges investigated in this dissertation, may be extended to deploy MEMS sensors in harsher

environments, such as geothermal sensing, requiring microsystem operation at temperature up to 500ºC. Some alternate applications of a passive wireless pressure sensing system for fluid flow analysis have been discussed in section 6.2.1 while section 6.2.2 proposes a node to node acoustic communication methodology using the designed hardware and software capabilities of the ELM9 microsystem.

### 6.2.1 Alternate Applications of Passive Wireless Pressure Gradient Measurement system for Fluid Flow Analysis

In addition to core flood experiments discussed in this dissertation, study and measurement of small flow induced pressure gradients in a high pressure, space constrained environment may be critical in many engineering systems such as high performance liquid chromatography (HPLC) columns [Pod19], and navigation of unmanned underwater vehicles [Dev15]. The passive wireless LC Sensor based technology for fluid flow analysis in Chapter 3, can be extended to these fluidic systems, in which sensors have a minimal effect on flow.

HPLC is a critical analytical tool applied at all stages of drug discovery, development, and production in the pharmaceutical industry [Kaz07]. In a typical HPLC setup, a liquid mobile phase carries a test sample through a separation column filled with a porous packing material (i.e. stationary phase). Physiochemical interactions along the length of the separation column determine the eluting order of separated components, which are recorded by a detector. During the experimental procedure, adsorption of biomolecules in the separation column can lead to blockage and changes in column viscosity. In order to maintain a compact, homogeneous packing inside the HPLC separation column with unaltered performance metrics, any sensor placement must be confined to the inner wall of the column, with a very thin form factor so as to minimally impact flow of the mobile phase; wireless sensor technology using a thin, flexible substrate may fulfil

such a requirement. Pressure gradient measurements along an HPLC separation column can provide important information about the performance of chromatographic process such as the flow regime, sample and mobile phase properties, and organization or microstructure of chromatographic media. Pressure gradient information can then serve as a powerful process analytic and technology parameter during chromatography process development and routine runs for improvements in system monitoring and control [Pod19].

In oceanography, pressure gradient measurements are utilized to study fluid flow dynamics around the perimeter of a boat or submerged vehicle to detect the presence of upstream obstacles [Dev15]. A set of distributed pressure sensors can mimic bioinspired artificial lateral lines for improved navigation and control of aquatic vehicles, complementing existing vision sensing modules such as sonar and camera [Sha18]. A pressure sensor array has previously been used to control the angle of attack of an underwater vehicle with respect to freestream flow [Gao12]. This system used macro-scale wired commercial pressure gauges with readout electronics on a rail mounted carriage external to the submerged test vehicle. A passive wireless measurement system with miniaturized sensing elements and a compact readout system could improve such artificial lateral line navigation systems by minimizing the size of the equipment and permitting an increase in the number of distributed pressure sensors.

### 6.2.2 Node to Node Acoustic Communication

The ELM9 microsystem, discussed in this dissertation, can be extended to investigate an acoustic communication infrastructure in downhole environments using the capacitive and piezoresistive pressure measurement interface. Acoustic signals may be generated locally by each microsystem node using an acoustic actuator integrated within each node. A combination of high resolution, but low bandwidth capacitive pressure sensor measurements along with the high

bandwidth, but lower measurement resolution piezoresistive pressure sensor measurements can be used to record AC seismic pressure waves up to 2 kHz (bandwidth of piezoresistive pressure sensor in ELM) in the presence of a DC pressure bias up to 50 MPa (maximum operating pressure of ELM microsystem). An illustration of the proposed acoustic communication between microsystem nodes with multiple tethered acoustic transponders has been shown below in Fig. 6.2. Acoustic communication protocols may be investigated for decoding transmitted acoustic signals. However, the impact of system packaging on range of communication, system power draw, impact of external noise sources, and signal processing with noise filtering algorithms shall need further evaluation.

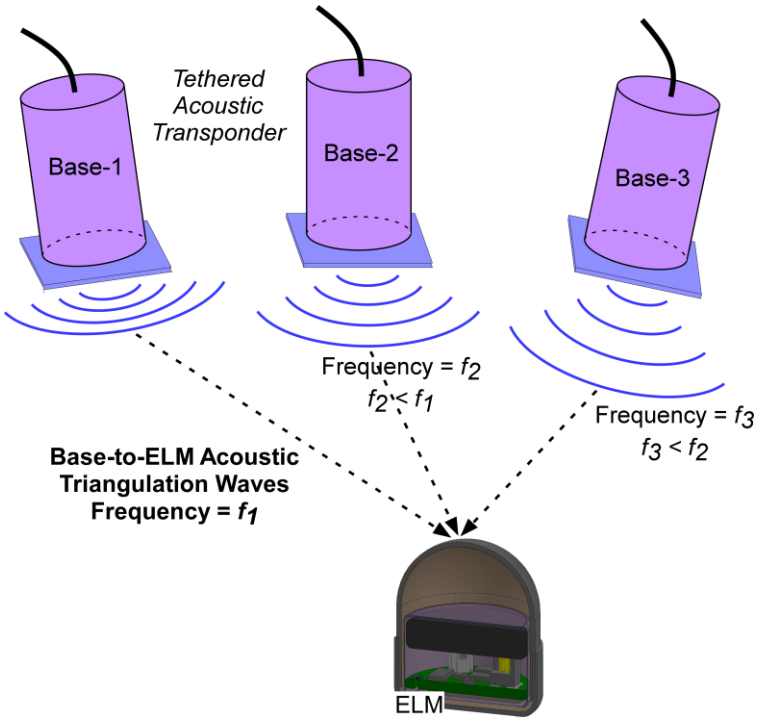



Fig. 6.2: Illustration of acoustic communication between sensing nodes with a multiple tethered acoustic transponder.

# REFERENCES


[Aal18] M. Y. Aalsalem, W. Z. Khan, W. Gharibi, M. K. Khan, Q. Arshad, "Wireless Sensor Networks in energy industry: Recent advances, taxonomy, requirements, and open challenges," Journal of Network and Computer Applications, vol. 113, pp. 87-97, 2018.

[Adg19] Analog Devices, Inc., USA, "ADG819 CMOS 2.1 Mux/SPDT switch," [Online]. Available: www.analog.com/media/en/technical-documentation/data-sheets/ADG819.pdf, accessed July 2022.

[Adg20] Analog Devices, Inc., USA, "ADG888 CMOS Dual DPDT switch," [Online]. Available: www.analog.com/media/en/technical-documentation/data-sheets/ADG888.pdf, accessed July 2022.

[ADX22] Analog Devices Inc., "Low Noise, Low Drift, Low Power, 3-axis MEMS Accelerometers ADXL355," [Online]. Available: https://www.analog.com/media/en/technical-documentation/data-sheets/ADXL354_355.pdf, accessed July 2022.

[Aem22] Silicon Laboratories Inc., "UG172-BRD4320a-User Guide," [Online]. Available: https://www.silabs.com/documents/public/user-guides/ug172-brd4320a-user-guide.pdf, accessed July 2022.

[Aka01] O. Akar, T. Akin, K. Najafi, "A wireless batch sealed absolute capacitive pressure sensor," Sensors and Actuators A: Physical, vol. 95, no. 1, pp. 29-38, 2001.

[ALS22] Allegro MicroSystems, "ALS31313 Automotive grade, 3D Linear Hall-Effect Sensor with I2C output and advanced low power management," [Online]. Available: https://www.allegromicro.com/-/media/files/datasheets/als31313-datasheet.pdf, accessed July 2022.

[Bab18] M.B. Babenkov, "Temperature of Rock Formation and Fracturing Fluid During the Hydraulic Fracturing Process," IOP Conf. Series: Earth and Environ. Science, 2018.

[Bag01] S. Bagci, M. V. Kok, U. Turksoy, "Effect of brine composition on oil recovery by waterflooding," Petroleum Science and Technology, vol. 19, pp. 359−372, 2001.

[Bal14] A. Baldygin, D. S. Nobes, S. K. Mitra, "New laboratory core flooding experimental system," Industrial & Engineering Chemistry Research, vol. 53, no. 34, pp. 13497-13505, 2014.

[Ben19] A. Benken, Y. Gianchandani, “Passive Wireless Pressure Sensing for Gastric Manometry,” MDPI Micromachines; Section B: Biology; Implantable Microdevices, vol. II, micromachines-647439, vol. 10, Issue 12, 2019.

[Ben21] A. Benken and Y. B. Gianchandani, “A High-Yield Microfabrication Process for Sapphire Substrate Capacitive Pressure Sensors Providing 70 MPa Range and 0.5 kPa Resolution,” IEEE Sensors Journal, vol. 21, no. 24, pp. 27315-27324, Dec.15, 2021.

[Bha13] K. N. Bhat, M. M. Nayak, “MEMS pressure sensors-an overview of challenges in technology and packaging,” Journal of Smart structures and systems, vol. 2, pp. 1-10, 2013.

[Bla14] D. Blaauw, D. Sylvester, P. Dutta, Y. Lee, I. Lee, S. Bang, Y. Kim, “IoT design space challenges: Circuits and systems,” Proc. Symposium on VLSI Technology, Digest of Technical Papers, pp. 1-2, 2014.

[Ble20] Silicon Laboratories Inc., “BLED112 Bluetooth Low Energy Dongle Datasheet,” [Online]. Available: https://www.silabs.com/documents/public/data-sheets/BLED112-DataSheet.pdf, accessed July 2022.

[Buz20] E. Buzi, H. R. Seren, M. Deffenbaugh, “Sensor Ball: An Autonomous Untethered Logging Platform,” Offshore Technology Conference, Houston, 2020.

[Cai16] F. Cai, C. Yi, S. Liu, Y. Wang, L. Liu, X. Liu, X. Xu, L. Wang, “Ultrasensitive, passive and wearable sensors for monitoring human muscle motion and physiological signals,” Biosens. Bioelectron., no. 77, pp. 907–913, 2016.

[Cer20] CERE core flooding equipment, “ Flooding system in connection with CT-scanner,” [Online]. Available: www.cere.dtu.dk/expertise/laboratories/core-flooding-equipment/flooding-system-in-connection-with-ct-scanner, accessed July 2020.

[Cha01] A. V. Chavan, K. D. Wise, “Batch-processed vacuum-sealed capacitive pressure sensors,” Journal of Microelectromechanical Systems, vol. 10, pp. 580-588, 2001.

[Cha12] D. Chapman, W. Trybula, “Meeting the Challenges of Oilfield Exploration using Intelligent Micro and Nano-Scale Sensors,” Proc. IEEE 12th International Conf. on Nanotechnology (IEEE-NANO), pp. 20-23, 2012.

[Cha87] H. L. Chau, K. D. Wise, “Scaling limits in batch-fabricated silicon pressure sensors,” IEEE Transactions on Electron Devices, vol. 34, no. 4, pp. 850-858, 1987.

[Cha88] H. L. Chau and K. D. Wise, “An ultraminiature solid-state pressure sensor for a cardiovascular catheter,” IEEE transactions on Electron Devices, vol. 35, pp. 2355-2362, 1988.

[Cha94] S. H. Chang, R. Grigg, “Laboratory flow tests used to determine reservoir simulator foam parameters for EVGSAU CO2 foam pilot,” Proc. Permian Basin Energy Recovery Conf., Paper SPE-27675-MS, pp. 483−492, 1994.

[Che08] P. J. Chen, D. Rodger, S. Saati, M. Humayun, Y. C. Tai, “Microfabricated Implantable Parylene-Based Wireless Passive Intraocular Pressure Sensors,” J. Microelectromech. Syst., vol. 17, pp. 1342–1351, 2008.

[Che14] Chen, J. H. Chung, T. E. Standaert, E. Alptekin, T. A. Spooner, V. Paruchuri, “Interconnect performance and scaling strategy at 7 nm node,” Proc. IEEE International Interconnect Technology Conf., pp. 93-96, 2014.

[Cho92] S. T. Cho, K. Najafi, C. L. Lowman, K. D. Wise, “An Ultrasensitive Silicon Pressure-Sensor Based Microflow Sensor,” IEEE Electron Devices, ED-39, pp. 825–835, 1992.

[Col67] C.C. Collins, “Miniature passive pressure transensor for implanting in the eye,” IEEE Trans. Biomed. Eng., vol. 2, pp. 74–83, 1967.

[DeH02] A. DeHennis, K.D. Wise, “A double-sided single-chip wireless pressure sensor,” Proceedings of the IEEE/ASME International Conference on Micro Electro Mechanical Systems (MEMS ’02), Las Vegas, NV, USA, 24 January 2002.

[Dev15] L. DeVries, F.D. Lagor, H. Lei, X. Tan, D.A. Paley, “Distributed flow estimation and closed-loop control of an underwater vehicle with a multi-modal artificial lateral line,” Bioinspiration & Biomimetics, vol. 10, no. 2, 2015.

[Dou12] D. Doughty and E.P. Roth, “A General Discussion of Li Ion Battery Safety,” The Electrochemical Society Interface, Vol. 21, No. 2, pp. 37-44, Jun. 2012.

[Dut19] P. P. Dutta, T. Li, and Y. B. Gianchandani, “A Sensing Microsystem for High Resolution Pressure Gradient Measurement in Core-Flood Experiments,” Proc. IEEE SENSORS, pp. 1-4, 2019.

[Eat97] W. P. Eaton, J. H. Smith, “Micromachined pressure sensors: Review and recent developments,” Smart Mater. Struct., vol. 6, pp. 530, 1997.

[Ell07] D. Ellis, J. Singer, “Well Logging for Earth Scientists,” Springer, 2007.

[Etn89] L.M. Etnyre, “Finding oil and gas from well logs,” Springer, 1989.

[Far91] T.M. Farabee, “Spectral features of wall pressure fluctuations beneath turbulent boundary layers,” Physics of Fluids A: Fluid Dynamics, vol. 3, no. 10, pp. 2410-2420, 1991.

[Fin10] J. Finger, D. Blankenship, “Handbook of best practices for geothermal drilling,” Sandia Nat. Labs., Albuquerque, NM, USA, and Livermore, CA, USA, Dec. 2010.

[Fle01] W. Fleming, “Overview of automotive sensors,” IEEE Sens. J., vol. 1, pp. 296–308, 2001.

[Fon02] M. A. Fonseca, J. English, M. Arx, M. G. Allen, “Wireless micromachined ceramic pressure sensor for high-temperature applications,” J. of Microelectromechanical Systems, vol. 11, no. 4, pp. 337-343, 2002.

[Fra18] SBS News Article, “Fracking: Hydraulic Fracturing,” [Online]. Available: www.sbs.com.au/news/what-is-fracking-and-why-is-it-dividing-australia, accessed June 2022.

[Gao12] A. Gao and M. Triantafyllou, “Bio-inspired pressure sensing for active yaw control of underwater vehicles,” 2012 Oceans, pp. 1-7, 2012.

[Gia06] Y.B. Gianchandani, C.G. Wilson, J.-S. Park, “Micromachined pressure sensors: Devices, interface circuits, and performance limits,” The MEMS Handbook, ed: M. Gad-el-Hak, CRC Press, pp. 3.1-3.44, 2006.

[Gia83] J. M. Giachino, R. J. Haeberle, J. W. Crow, “Method for manufacturing variable capacitance pressure transducers,” U. S. Patent 4,386,453, Jun. 7, 1983.

[Gil94] R.E. Gilliland, Apparatus and Method for Measuring Relative Permeability and Capillary Pressure of Porous Rock, U.S. Patent No. 5,297,420, 1994.

[Glo17] A. Glória, F. Cercas, N. Souto, “Comparison of communication protocols for low cost Internet of Things devices,” Proc. IEEE South Eastern European Design Automation, Computer Engineering, Computer Networks and Social Media Conference (SEEDA-CECNSM), pp. 1-6, 2017.

[Gop93] S. P. Gopinath, L. Cherian, C. S. Robertson, R. K. Narayan, R. G. Grossman, “Evaluation of a microsensor intracranial pressure transducer,” J. Neurosci. Methods, no. 49, pp. 11–15, 1993.

[Gri01] C. A. Grimes, M. K. Jain, R. S. Singh, Q. Cai, A. Mason, K. Takahata, Y.B. Gianchandani, “Magnetoelastic microsensors for environmental monitoring,” Proc. IEEE/ASME 14th International Conf. on Micro Electro Mechanical Systems (MEMS 01), pp. 278-281, 2001.

[Hea08] M. Healy, T. Newe, E. Lewis, “Wireless Sensor Node Hardware: A Review,” IEEE Sensors Conference, pp.621-624, 2008.

[Hen05] J. A. Henao-Sepulveda, M. Toledo-Quinones, Y. Jia, “Contactless monitoring of ball bearing temperature,” Proc. IEEE Instrum. Meas. Technol. Conf., Ottawa, ON, Canada, pp. 1571–1573, 2005.

[Hen98] D. Hensley, M. Milewits, W. Zhang, “The Evolution of Oil Field Batteries,” Oil Field Review, vol. 10, no. 3, pp. 42-57, Oct. 1998.

[Hes17] J. Hester, J. Sorber, “The future of sensing is batteryless, intermittent, and awesome,” Proc. 15th ACM Conf. on Embedded Network Sensor Systems, pp. 1-6, 2017.

[Hor07] S. Horowitz, T. Nishida, L. Cattafesta, M. Sheplak, “Development of a micromachined piezoelectric microphone for aeroacoustics applications,” J. Acoust. Soc. Am., no. 122, pp. 3428, 2007.

[Hor87] V. Hornof, N. Morrow, “Gravity effects in the displacement of oil by surfactant solutions,” SPE Reservoir Eng., vol. 2, pp. 627−633, 1987.

[Hua16] Q. A. Huang, L. Dong, L. F. Wang, “LC passive wireless sensors toward a wireless sensing platform: status, prospects, and challenges,” J. of Microelectromechanical Systems, vol. 25, no. 5, pp. 822-841, 2016.

[Huy09] B. Huyghe, J. Vanfleteren, J. Doutreloigne, “Design of Flexible, Low-Power and Wireless Sensor Nodes for Human Posture Tracking Aiding Epileptic Seizure Detection,” *IEEE Sensors Conference*, pp.1963-1966, 2009.

[Hyd19] The Engineering Toolbox, “Hydrostatic Pressure”, [Online]. Available: https://www.engineeringtoolbox.com/hydrostatic-pressure-water-d_1632.html, accessed June 2022.

[IGN21] INGU Pipers Technical specifications. INGU, Apr-2021. [Online]. Available: ingu.com/technical-specifications/, accessed Aug. 2021.

[Ina22] Texas Instruments, “INA321 microPower, Single-Supply, CMOS Instrumentation Amplifier,” [Online]. Available: https://www.ti.com/lit/ds/symlink/ina2321.pdf?HQS=dis-dk-null-digikeymode-dsf-pf-nullwwe&ts=1657977229015&ref_url=https%253A%252F%252Fwww.ti.com%252Fgeneral%252Fdocs%252Fsuppproductinfo.tsp%253FdistId%253D10%2526gotoUrl%253Dhttps%253A%252F%252Fwww.ti.com%252Flit%252Fgpn%252Fina2321, accessed July 2022.

[ISS22] Integrated Silicon Solution Inc., “IS25LP128F 128Mb Serial Flash Memory Datasheet,” [Online]. Available: https://www.issi.com/WW/pdf/25LP-WP128F.pdf, accessed July 2022.

[Ji92] J. Ji, S. T. Cho, Y. Zhang, K. Najafi, “An Ultraminiature CMOS Pressure Sensor for a Multiplexed Cardiovascular Catheter,” IEEE Trans. Electron. Devices, 39, pp. 2260–2267, 1992.

[Kam15] F. Kamali, F. Hussain, Y. Cinar, "A laboratory and numerical-simulation study of co-optimizing CO 2 storage and CO 2 enhanced oil recovery," SPE Journal, vol. 20, no. 06, pp. 1-227, 2015.

[Kan82] Y. Kanda, "A Graphical Representation of the Piezoresistive Coefficients in Si," IEEE Trans. Electron. Devices, 29, pp. 64–70, 1982.

[Kaz07] Y.V. Kazakevich, R. Lobrutto, "HPLC for pharmaceutical scientists," John Wiley & Sons, 2007.

[Kha16] W. Z. Khan, M. Y. Aalsalem, W. Gharibi, Q. Arshad, "Energy monitoring using Wireless Sensor Networks: Requirements, issues and challenges," Proc. IEEE International Conference on Radar, Antenna, Microwave, Electronics, and Telecommunications (ICRAMET), pp. 31-35, 2016.

[Ko14] K. M. Ko, B. H. Chon, S. B. Jang, H. Y. Jang, "Surfactant flooding characteristics of dodecyl alkyl sulfate for enhanced oil recovery," J. Ind. Eng. Chem, vol. 20, pp. 228−233, 2014.

[Koh15] K. Kohyama, "Oral sensing of food properties," J. of Texture Studies, vol. 46, no. 3, pp. 138-151, 2015.

[Kon10] X. Kong, M. Ohadi, "Applications of micro and nano technologies in the energy industry-overview of the recent progress," Proc. SPE Abu Dhabi international petroleum exhibition and conference, 2010.

[Kre01] E. Kress-Rogers, C. JB. Brimelow, "Instrumentation and sensors for the food industry," vol. 65, Woodhead Publishing, 2001.

[Lec01] D. Leclercq, M. Jacob, A. Louisot, C. Talotte, "Forward-backward facing step pair-Aerodynamic flow, wall pressure and acoustic characterization," AIAA/CEAS 7th Aeroacoustics Conf. and Exhibit, pp. 2249, 2001.

[Lee14] S. Lee, A.P. Chandrakasan, H. S. Lee, "A 1 GS/s 10b 18.9 mW time-interleaved SAR ADC with background timing skew calibration," IEEE J. Solid State Circuits, no. 49, pp. 2846–2856, 2014.

[Lia18] T. Liang, L. Shao, E. Yao, et al., "Study on Fluid-Rock Interaction and Reuse of Flowback Fluid for Gel Fracturing in Desert Area," Geofluids, 2018.

[Lia22] X. Liao, B. Li, J. Li, "Impacts of Apple's M1 SoC on the Technology Industry," 7th International Conference on Financial Innovation and Economic Development (ICFIED 2022), pp. 355-360, Atlantis Press, 2022.

[Lin05] Linear Technology Corp., "LTC4306 Datasheet," [Online]. Available: www.analog.com/media/en/technical-documentation/data-sheets/4306.pdf, accessed July 2022.

[Ltc20] Linear Technology Corp., “LTC2941-1 1A I2C Battery Gas Gauge Datasheet,” [Online]. Available: www.analog.com/media/en/technical-documentation/data-sheets/29411f.pdf, accessed July 2022.

[Lou99] C. Loudon, K. McCulloh, “Application of the Hagen—Poiseuille Equation to Fluid Feeding through Short Tubes”, Annals of the Entomological Society of America, vol. 92, no. 1, pp. 153-158, 1999.

[Mah91] J.R. Mahan, A. Karchmer, “Aeroacoustics of flight vehicles: Theory and practice; volume 1: noise sources,” NASA TR903052 edited by H.H. Hubbard, pp. 504-507, Aug. 1991.

[Mah20] M. Mahjoub, K. Nguyen, S. Menand, et al., “Dynamics Vibration Prediction and Comparison with Downhole Data Measurements in Unconventional Wells,” IADC/SPE Int’l Drilling Conference and Exhibition, OnePetro, 2020.

[Man10] A. Mandal, A. Samanta, A. Bera, K. Ojha, “Role of oil-water emulsion in enhanced oil recovery,” Intl. Conf. on Chemistry and Chemical Engineering, pp. 190−194, 2010.

[Mar20] Markets and Markets research report, “Pressure sensor market report, 2021,” [Online]. Available: www.marketsandmarkets.com/Market-Reports/pressure-sensor-market-871.html, accessed June 2022.

[Mat14] V. Matko, M. Milanovi´c, “Temperature-compensated capacitance-frequency converter with high resolution,” Sens. Actuators A Phys., no. 220, pp. 262–269, 2014.

[Mer22] Merit Medical Systems, Inc., “Merit Sensor K Series Datasheet,” [Online]. Available: https://www.mouser.com/datasheet/2/764/K_series-769895.pdf, accessed July 2022.

[Mic08] Microfab Service GmbH, “E8.0T Datasheet,” [Online]. Available: http://www. microfab.de/downloads/200080109datasheete8.0ta4.pdf, accessed July 2022.

[Moh99] S. Mohan, M. Hershenson, S. Boyd, T.H. Lee, “Simple accurate expressions for planar spiral inductances,” IEEE J. Solid-State Circuits, vol. 34, pp. 1419–1424, 1999.

[Mon17] J. A. Montiel-Nelson, J. Sosa, R. Pulido, A. Beriain, H. Solar, R. Berenguer, “Digital output MEMS pressure sensor using capacitance-to-time converter,” IEEE Des. Circuits Integr. Syst., pp. 1–4, 2017.

[Mur13] Murata Manufacturing, “SCB10H-B250 Datasheet,” [Online]. Available: https://www.murata.com/-/media/webrenewal/products/sensor/pressure/product-family-speficifation-scb10h-pressure-elements82125000b.ashx?la=en&cvid=20150130114557054200, accessed July 2022.

[Mus43] M. Muskat, “Fluid Flow Through Porous Media,” Proc. Sec. Hydraulic Conference, Bull, vol. 27, 1943.

[Nas11] R. Nasralla, M. Alotaibi, H. Nasr-El-Din, “Efficiency of oil recovery by low salinity water flooding in sandstone reservoirs,” Proc. SPE Western North American Region Meeting, Paper SPE- 144602-MS, 2011.

[Noa19] NOAA National Data Buoy Center, “What is air pressure?”, [Online]. Available: https://www.ndbc.noaa.gov/educate/pressure.shtml, accessed July 2022.

[Nob07] M. Nobakht, S. Moghadam, Y. Gu, “Effects of viscous and capillary forces on CO2 enhanced oil recovery under reservoir conditions,” Energy Fuels, vol. 21, pp. 3469−3476, 2007.

[Nop10] R. Nopper, R. Niekrawietz, and L. Reindl, “Wireless Readout of Passive LC Sensors,” IEEE Transactions on Instrumentation and Measurement, 59(9), September 2010.

[NPX20] NXP Semiconductors Inc., “50 kPa On-Chip Temperature Compensated and Calibrated Silicon Pressure Sensors Datasheet”, [Online]. Available: https://www.nxp.com/docs/en/ data-sheet/MPX2053.pdf, accessed July 2022.

[Oil14] IEA, “Oil market report,” [Online]. Available: https://www.iea.org/topics/oil-market-report, accessed July 2022.

[One99] C. B. O'Neal, A. P. Malshe, S. B. Singh, W. D. Brown, W. P. Eaton, “Challenges in the packaging of MEMS,” Proc. International Symposium on Advanced Packaging Materials, Processes, Properties and Interfaces, Cat. No. 99TH8405, pp. 41-47, 1999.

[Ope14] Openfield ¾” Pressure and Temperature Micro-Recorder for Drill Stem Testing, 2014. [Online]. Available: https://www.openfield-technology.com/wp-content/uploads/2019/06/Open Field_ThreeQuarterInch_Brochuregages.pdf, accessed Aug. 2021.

[Opp99] A. Oppenheim, J. Buck, R. Schafer, Discrete-Time Signal Processing, New Jersey: Prentice Hall, 1999.

[Ord20] J.R. Ordonez Varela, J.G. Boero Rollo, A.L. Beulze, J. Ochi, N. Vellaluru, P.P. Dutta, A. Benken, Y. Gianchandani, “Wireless Advanced Nano-Devices for Well Monitoring,” Abu Dhabi International Petroleum Exhibition & Conference, OnePetro, 2020.

[Ott12] H. Ott, K. de Kloe, M. van Bakel, A. van Pelt, P. Legerstee, A. Bauer, K. Eide, A. van der Linden, S. Berg, A. Makurat, “Core-flood experiment for transport of reactive fluids in rocks,” Review of Scientific Instruments, vol. 83, no. 8, 084501, 2012.

[Par00] J. S. Park and Y. Gianchandani, “A capacitive absolute-pressure sensor with external pick-off electrodes,” Journal of Micromechanics and Microengineering, vol. 10, p. 528, 2000.

[Par99] J. S. Park, Y.B. Gianchandani, “A low cost batch-sealed capacitive pressure sensor,” Proc. IEEE/ASME 12th International Conf. on Micro Electro Mechanical Systems (MEMS 99), pp. 82-87, 1999.

[Ped97] M. Pedersen, M. G. H. Meijerink, W. Olthuis, P. Bergveld, “An IC-compatible polyimide pressure sensor with capacitive readout,” Sensors and Actuators A: Physical, vol. 63, no. 3, pp. 163-168, 1997.

[Pet05] V. P. Petkov, B. E. Boser, “A fourth-order Delta Sigma interface for micromachined inertial sensors,” IEEE J. Solid State Circuits, no. 40, pp. 1602–1609, 2005.

[Pet08] E. B. Petersen, A. Lohne, J. O. Helland, G. Virnovsky, “Relative permeabilities for two- and three- phase flow processes relevant to the depressurization of the Statfjord field,” Intl. Symposium of the Society of Core Analysis, Paper SCA2008-23, pp. 1-12, 2008.

[Phi14] N. Philip, N. George, “Design and analysis of a dual-slope inductance-to-digital converter for differential reluctance sensors,” IEEE Trans. Instrum. Meas., no. 63, pp. 1364–1371, 2014.

[Pic04] S. Pichorim, P. Abatti, “Design of coils for millimeter-and submillimeter-sized biotelemetry,” IEEE Trans. Biomed. Eng, , vol. 51, pp. 1487–1489, 2004.

[Pin13] R. Pini, S.M. Benson, “Simultaneous determination of capillary pressure and relative permeability curves from core-flooding experiments with various fluid pairs,” Water Resources Research, vol. 49, no. 6, pp. 3516-3530, 2013.

[Pod19] A. Podgornik, “Pressure drop in liquid chromatography,” Journal of Separation Science, vol. 42, no. 1, pp. 72-88, January 2019.

[Puy17] G. Puyou, M. N’Guyen, S. Savin, “CXBOX: An Innovative Tool For Fluid Dynamic Quantification During Corefloods,” Proc. SCA International Symposium, 2017.

[Slf19] Sensirion, “SLF3S-1300F Liquid Flow Sensor Datasheet”, [Online]. Available: https://www.sensirion.com/fileadmin/user_upload/customers/sensirion/Dokumente/0_Datasheets/Liquid_Flow/Sensirion_Liquid_Flow_Sensor_SLF3S-1300F_Datasheet_EN_D1.pdf, accessed July 2022.

[Rob97] A.D. Robertson, A.R. West, and A.G. Ritchie, “Review of Crystalline Lithium-ion Conductors Suitable for High Temperature Battery Applications,” Solid State Ionics, vol. 104, no. 1, pp. 1-11, Dec. 1997.

[Sam73] Samaun, K. D. Wise, J. B. Angell, “An IC piezoresistive pressure sensor for biomedical instrumentation,” IEEE Transaction on Biomedical Engineering, vol. 20, no. 2, pp. 101–109, 1973.

[Sam12] A. Samanta, A. Bera, K. Ojha, A. Mandal, “Comparative studies on enhanced oil recovery by alkali surfactant and polymer flooding,” J. Pet. Explor. Prod. Technol., vol. 2, pp. 67−74, 2012.

[San80] S. Sander, J. W. Knutti, J. D. Meindl, “A monolithic capacitive pressure sensor with pulse-period output,” IEEE Transactions on Electron Devices, vol. 27, no. 5, pp. 927-930, 1980.

[Sav13] S. Savazzi, S. Guardiano, U. Spagnolini, “Wireless sensor network modeling and deployment challenges in energy refinery plants,” Int. J. Distributed Sens. Netw, 2013.

[Sco85] J. Scott, G. Olson, “A Three-Component Borehole Magnetometer Probe for Mineral Investigations and Geologic Research,” SPWLA 26th Annual Logging Symposium, Dallas, Texas, 1985.

[Sei14] Seiko Instruments Inc., “Micro Battery Product Catalogue,” [Online]. Available: https://www.seiko-instruments.de/fileadmin/Editors/COMP/PDF/MicroBattery_catalogue_ E_2018A_forWeb.pdf, accessed July 2022.

[Ser17] H.R. Seren, E. Buzi, L. Al-Maghrabi, “An Untethered Sensor Platform for Logging Vertical Wells,” IEEE Transactions on Instrumentation and Measurement, vol. 67, no. 4, pp. 798-803, 2017.

[Sha18] M.A. Sharif, X. Tan, “A pressure gradient sensor inspired by the canal neuromasts of fish,” Electroactive Polymer Actuators and Devices (EAPAD) XX, International Society for Optics and Photonics, Vol. 10594, pp. 105941P, 2018.

[Shi15] Z. Shi, Y. Chen, M. Yu, S. Zhou, N. Al-Khanferi, “Development and Field Evaluation of a Distributed Microchip Downhole Measurement System,” SPE Digital Energy Conference and Exhibition, The Woodlands, Texas, Mar. 2015.

[Sil19] Silicon Laboratories Inc., “BGM121 Datasheet,” [Online]. Available: www.silabs.com/documents/public/data-sheets/bgm12x-datasheet.pdf, accessed July 2022.

[Sil22] Silicon Laboratories Inc., “BGM220S Wireless Gecko Bluetooth® Module Data Sheet,” [Online]. Available: https://www.silabs.com/documents/public/data-sheets/bgm220s-datasheet .pdf, accessed July 2022.

[Sma20] Smart Products USA, Inc., “Check/Pressure Relief Valves Product Catalog, Series 200, Model #214,” [Online]. Available: https://www.smartproducts.com/docs/Smart_ Products_ Product_Catalog.pdf, accessed July 2022.

[Sta20] Statistica, “US gas and oil industry expenditures on exploration and development,” [Online]. Available: www.statista.com/statistics/294604/us-gas-and-oil-industry-expenditures-on-exploration-and-development/, accessed July 2022.

[Sol04] S. Sola, “Feasibility experimental investigation of steam/methane flooding in a heavy oil reservoir,” Proc. SPE Intl. Petroleum Conf., Paper SPE-91968-MS, 2004.

[Son20] P. Song, Z. Ma, J. Ma, L. Yang, J. Wei, Y. Zhao, M. Zhang, F. Yang, X. Wang, “Recent progress of miniature MEMS pressure sensors,” Micromachines, vol. 11, no. 1, pp. 56, 2020.

[Stm20] STMicroelectronics, “LSM9DS1, iNEMO inertial module,” [Online]. Available: https://www.st.com/resource/en/datasheet/lsm9ds1.pdf, accessed July 2022.

[Sui17] Y. Sui, Low Power Autonomous Microsystem for Oil Well Logging Applications, Ph.D. dissertation, Univ. Michigan, An Arbor, MI, USA, 2017.

[Sun16] Y. Sun, Q. Li, D. Yang, X. Liu, “Laboratory core flooding experimental systems for CO2 geosequestration: An updated review over the past decade,” Journal of Rock Mechanics and Geotechnical Engineering, vol. 8, no. 1, pp. 113-126, 2016.

[Tak04] K. Takahata, A. DeHennis, K.D. Wise, Y.B. Gianchandani, “A wireless microsensor for monitoring flow and pressure in a blood vessel utilizing a dual-inductor antenna stent and two pressure sensors,” Proc. IEEE/ASME 17th International Conf. on Micro Electro Mechanical Systems (MEMS 04), pp. 216-219, 2004.

[Tiw12] M. I. Tiwana, S. J. Redmond, N. H. Lovell, “A review of tactile sensing technologies with applications in biomedical engineering,” Sensors and Actuators A: physical, vol. 179, pp. 17-31, 2012.

[Tlh20] Tadiran Batteries GmBh, “Tadiran TLH-2450 Datasheet,” [Online]. Available: www.tadiranbat.com/assets/tlh-2450.pdf, accessed July 2022.

[Vel20] N. Vellaluru, Microsystem Design and Package Integration Concepts for Pipeline and Downhole Monitoring, Ph.D. dissertation, Univ. Michigan, An Arbor, MI, USA, 2020.

[Vel22] N. Vellaluru, P. Dutta, A. Benken, JG. Boero-Rollo, JR. Ordonez-Varela, Y. Gianchandani, “Autonomous Sensing Microsystem with H2S Compatible Package and Enhanced Buoyancy for Downhole Monitoring,” SPE Journal, pp. 1-12, 2022.

[Vre22] Analog Devices Inc., “LT6656 1μA Precision Series Voltage Reference,” [Online]. Available: https://www.analog.com/media/en/technical-documentation/data-sheets/lt6656.pdf, accessed July 2022.

[Wan97] Y. Wang, M. Esashi, “A novel electrostatic servo capacitive vacuum sensor,” International Conference on Solid-State Sensors, Actuators, and Microsystems (Transducers), pp. 1457–1460, 1997.

[Whe42] H. Wheeler, “Formulas for the skin effect,” Proc. IRE, vol. 30, pp. 412–424, 1942.

[Whi86] S. Whitaker, “Flow in porous media I: A theoretical derivation of Darcy's law,” Transport in porous media, vol. 1, no. 1, pp. 3-25, 1986.

[Wij20] N. Wijaya, J. J. Sheng, “Controlling Water Blockage Using Surfactant Into Fracturing Fluid: Optimum Interfacial Tension and Wettability Criteria,” AADE, Paper AADE-20-FTCE-SPP-10, 2020.

[Wod11] S. Wodin-Schwartz, M. W. Chan, K. R. Mansukhani, A. P. Pisano, D. G. Senesky, “MEMS sensors for down-hole monitoring of geothermal energy systems,” in Proceedings of the ASME 2011 5th International Conference on Energy Sustainability, Washington, DC, USA, 2011.

[Wu06] C. H. Wu, C. Zorman, M. Mehregany, “Fabrication and testing of bulk micromachined silicon carbide piezoresistive pressure sensors for high temperature applications,” IEEE Sens. J., vol. 6, pp. 316–324, 2006.

[Yam92] M. Yamada, T. Takebayashi, S. Notoyama, K. Watanabe, “A switched-capacitor interface for capacitive pressure sensors,” IEEE Trans. Instrum. Meas, no. 41, pp. 81–86, 1992.

[Yan14] X. C. Yang, “Method and structure of monolithically integrated pressure sensor using IC foundry-compatible processes,” U.S. Patent 8,796,746, Aug. 5, 2014.

[Yu12] M. Yu, S. He, Y. Chen, N. Takach, P. LoPresti, S. Zhou, N. Al-Khanferi, “A Distributed Microchip System for Subsurface Measurement,” SPE Annual Technical Conference and Exhibition, San Antonio, Texas, Oct. 2012.

[Zha20] C. Zhang, R. Gallichan, D. M. Budgett, D. McCormick, “A Capacitive Pressure Sensor Interface IC with Wireless Power and Data Transfer,” Micromachines 11, no. 10, pp. 897, 2020.

[Zou16] L. Zou, “A resistive sensing and dual-slope ADC based smart temperature sensor,” Analog Integr. Circuits Signal Process., no. 87, pp. 57–63, 2016.